PAVOL JOZEF ŠAFÁRIK UNIVERSITY IN KOŠICE
JOHANNES GUTENBERG UNIVERSITY IN MAINZ

Numerical Modelling of Fluid-Structure Interaction with Application in Hemodynamics

"Co-Tutelle de Thèse"
Dissertation Thesis

KOŠICE / MAINZ
2012

GABRIELA RUSNÁKOVÁ

Numerical Modelling of Fluid-Structure Interaction with Application in Hemodynamics

A DISSERTATION
"CO-TUTELLE DE THÈSE"

SUBMITTED TO
THE FACULTY OF SCIENCE
OF PAVOL JOZEF ŠAFÁRIK UNIVERSITY IN KOŠICE
AND
THE FACULTY 08 - PHYSICS, MATHEMATICS AND COMPUTER SCIENCE
OF JOHANNES GUTENBERG UNIVERSITY IN MAINZ
IN PARTIAL FULFILLMENT OF THE REQUIREMENTS

FOR THE DEGREE OF
DOCTOR OF PHILOSOPHY / DOKTOR DER NATURWISSENSCHAFTEN

by

Gabriela Rusnáková

Abstract

The thesis deals with numerical algorithms for fluid-structure interaction problems with application in blood flow modelling. It starts with a short introduction on the mathematical description of incompressible viscous flow with non-Newtonian viscosity and a moving linear viscoelastic structure. The mathematical model consists of the generalized Navier-Stokes equation used for the description of fluid flow and the generalized string model for structure movement. The arbitrary Lagrangian-Eulerian approach is used in order to take into account moving computational domain. A part of the thesis is devoted to the discussion on the non-Newtonian behaviour of shear-thinning fluids, which is in our case blood, and derivation of two non-Newtonian models frequently used in the blood flow modelling. Further we give a brief overview on recent fluid-structure interaction schemes with discussion about the difficulties arising in numerical modelling of blood flow. Our main contribution lies in numerical and experimental study of a new loosely-coupled partitioned scheme called the kinematic splitting fluid-structure interaction algorithm. We present stability analysis for a coupled problem of non-Newtonian shear-dependent fluids in moving domains with viscoelastic boundaries. Here, we assume both, the nonlinearity in convective as well is diffusive term. We analyse the convergence of proposed numerical scheme for a simplified fluid model of the Oseen type. Moreover, we present series of experiments including numerical error analysis, comparison of hemodynamic parameters for the Newtonian and non-Newtonian fluids and comparison of several physiologically relevant computational geometries in terms of wall displacement and wall shear stress. Numerical analysis and extensive experimental study for several standard geometries confirm reliability and accuracy of the proposed kinematic splitting scheme in order to approximate fluid-structure interaction problems.

Keywords: fluid-structure interaction, non-Newtonian fluids, stability, convergence, hemodynamic wall indices, stenosis, bifurcation

Kurzfassung

Die Arbeit befasst sich mit numerischen Algorithmen zur Berechnung des Problems der Wechselwirkung von Fluid und Struktur mit Anwendungen in Modellierung der Blutströmung. Zuerst wird die Strömung der inkompressiblen viskosen Flüssigkeiten mit nicht-Newtonscher Viskosität in beweglichen viskoelastischen Gittern mathematisch beschrieben. Das mathematische Modell besteht aus der verallgemeinerten Navier-Stokes Gleichungen zur Beschreibung der Fluidströmung und des sogenannten "generalized string" Modells, womit man die Bewegung einer elastischen Körper beschreibt. Der "Arbitrary Lagrangian-Eulerian" Ansatz wird verwendet, um die Bewegung des Berechnungsgebietes zu berücksichtigen und folgen. Ein Teil der Arbeit widmet sich der Diskussion über das nicht-Newtonsche Verhalten scherverdünnenden Flüssigkeiten, wobei wir uns auf den Fall des Blutes beschränken. Darüber hinaus präsentieren wir eine Ableitung von zwei nicht-Newtonschen Modelle, die häufig in der Blutströmungmodellierung eingesetzt sind. Wir geben einen Überblick über die aktuellen Fluid-Struktur Interaktion Algorithmen und diskutieren über die in der Modellierung der Blutströmung auftretenden Schwierigkeiten. Unser Hauptbeitrag liegt in der numerischen und experimentellen Studie eines neuen schwach gekoppelten partitionellen Algorithmus, dem sogenannten "kinematic splitting" Fluid-Struktur Interaktion Algorithmus. Wir präsentieren Stabilitätsanalyse unseres gekoppelten Problems mit scherabhängigen Flüssigkeiten in bewegten Gebieten mit viskoelastischen Ränden. Wir gehen davon aus, dass die Nonlinearitäten sowohl in dem konvektiven und auch dem diffusiven Term auftreten. Die Konvergenz des entwickelten Algorithmus wird für ein vereinfachtes Fluidmodell von dem Oseen-Typ vorgestellt. Wir stellen Reihe von Experimenten einschließlich numerischer Fehler-Analyse, Vergleich der hämodynamischen Parameter für die Newtonschen und nicht-Newtonschen Flüssigkeiten und Vergleich mehrerer physiologisch relevanten Berechnungsgebieten in Bezug auf die Strukturverschiebung und Wandschubspannung. Numerische Analyse und umfangreiche experimentelle Studie für mehrere Standard-Geometrien zeigen Zuverlässigkeit und Genauigkeit des vorgeschlagenen "kinematic splitting" Algorithmus geeignet zur numerischen Approximation des Fluid-Struktur Interaktion Problems.

Schlüsselwörter: Fluid-Struktur Interaktion, nicht-Newtonsche Flüssigkeiten, Stabilität, Konvergenz, hämodynamische Parameter, Stenose, Bifurkation

Contents

1 Introduction **1**
- 1.1 Preliminaries . . . 4
  - 1.1.1 Useful functional spaces . . . 4
  - 1.1.2 Useful inequalities . . . 7
  - 1.1.3 Useful theorems . . . 8

2 Mathematical Model **11**
- 2.1 Governing equations . . . 11
- 2.2 Arbitrary Lagrangian-Eulerian mapping . . . 14
- 2.3 Structure equation . . . 16

3 Non-Newtonian rheology **23**
- 3.1 Newtonian versus non-Newtonian material . . . 23
- 3.2 Blood as a non-Newtonian fluid . . . 24
  - 3.2.1 Shear thinning models for blood viscosity . . . 26
  - 3.2.2 Viscoelastic models for blood viscosity . . . 28

4 Fluid-structure interaction problem **35**
- 4.1 Boundary, initial and coupling conditions . . . 35
- 4.2 Weak formulation of the model . . . 36
- 4.3 Numerical resolution of fluid-structure interaction problem . . . 39
- 4.4 Kinematic splitting algorithm . . . 41
- 4.5 Weak formulation for the kinematically splitted FSI problem . . . 41

5 Stability analysis **43**
- 5.1 A priori estimates for the continuous problem . . . 43
  - 5.1.1 A priori estimate for the operator A . . . 43
  - 5.1.2 A priori estimate for the operator B . . . 46
  - 5.1.3 A priori estimate of the coupled problem . . . 47
- 5.2 Stability analysis of semi-discrete problem . . . 49
  - 5.2.1 Energy estimate for the operator A . . . 51
  - 5.2.2 Energy estimate for the operator B . . . 54
  - 5.2.3 Energy estimate of the coupled problem . . . 55

6 Convergence analysis **59**
- 6.1 Mathematical model . . . 59
- 6.2 Weak formulation . . . 60
- 6.3 Kinematic splitting of the continuous problem (6.1)-(6.9) . . . 60
- 6.4 Finite element discretization and approximation errors . . . 61
- 6.5 Finite element weak formulation . . . 66
- 6.6 Kinematic splitting of the semi-discrete problem (6.43)-(6.51) . . . 67
- 6.7 Error analysis . . . 67

6.7.1 Error analysis for the operator A 68
6.7.2 Error analysis for the operator B 75
6.7.3 Error estimate of the coupled problem 77

7 Numerical experiments **85**
7.1 Discretization methods 86
7.2 Finite volume approximation of the fluid equations in the ALE frame 87
7.3 Finite difference approximation of the structure equation 94
7.4 Computational geometry and parameter setting 95
7.5 Experiments 99
7.6 Experimental order of convergence 111
7.6.1 Experimental order of convergence in space 111
7.6.2 Experimental order of convergence in time 113
7.7 Hemodynamic wall indices 116

8 Conclusions and future works **125**

Bibliography **129**

List of Figures

2.1 ALE mapping $\mathcal{A}_t$ with a moving boundary and a symmetry axis. 14
2.2 2D domain geometry and 1D compliant wall obtained by intersecting the cylindrical tube with the plane $\theta = \bar{\theta}$. Without loss of generality, we assume here that $R_0 = \text{const}$. 18

3.1 Couette flow experiment. 23
3.2 Shear rate versus shear stress for the Newtonian and some non-Newtonian fluids. 24
3.3 Viscosity versus shear rate for power-law fluids which are shear thinning (dash line), shear thickening (dash-dot line) or have constant viscosity (solid line). 27
3.4 Viscosity function for non-Newtonian models (3.19) and (3.20) and asymptotic viscosities μ_∞ for (3.19) and (3.20) fit for the physiological data from Tab. 7.2. 32

4.1 Computational domain geometry. 35

7.1 A possible grid arrangement for the FVM. Each control volume is represented by a grid point (gp) and a set of integration points (ip). 88
7.2 Symmetric non-stenosed computational geometry. 95
7.3 Stenotic reference geometry. 96
7.4 Bifurcation reference geometry, see [85]. 96
7.5 Inflow rate $Q(t)$ in iliac artery (left) and in common carotid artery (right), see [85, 101]. 97
7.6 Evolution of domain deformation η along Γ^0_{wall} at several time instants; Carreau viscosity function; non-stenosed geometry, see Fig. 7.2. 100
7.7 Velocity streamlines and pressure isolines for non-stenosed geometry at several time instants. 101
7.8 Streamlines, velocity vector field, pressure isolines and u_1-velocity isolines for bifurcation from Fig. 7.4 at two time instants; mean Reynolds number Re $\approx$ 304. 102
7.9 Streamlines, velocity vector field, pressure isolines and u_1-velocity isolines for bifurcation from Fig. 7.4 at two time instants; mean Reynolds number Re $\approx$ 304. 103
7.10 Streamlines, velocity vector field, pressure isolines and u_1-velocity isolines for bifurcation from Fig. 7.4 at two time instants; mean Reynolds number Re $\approx$ 152. 104
7.11 Streamlines, velocity vector field, pressure isolines and u_1-velocity isolines for bifurcation from Fig. 7.4 at two time instants; mean Reynolds number Re $\approx$ 152. 105
7.12 The evolution of η along the moving boundary Γ^m_{wall} for bifurcation geometry. Mean prescribed Reynolds number Re $\approx$ 304. Left: comparison at different time instants, right: comparison of constitutive models at $t = 0.36$ s. 107
7.13 The evolution of η along the moving boundary Γ^m_{wall} for bifurcation geometry. Mean prescribed Reynolds number Re $\approx$ 152. Left: comparison at different time instants, right: comparison of constitutive models at $t = 0.36$ s. 107
7.14 Streamlines, pressure isolines, velocity vector field and u_1-velocity isolines for stenosed vessel at two time instants. 108

7.15 Streamlines, pressure isolines, velocity vector field and u_1-velocity isolines for stenosed vessel at two time instants. 109
7.16 The evolution of η along the line $x_2 = R_0$ for stenosed vessel. Mean prescribed Reynolds number Re $\approx$ 195. Left: comparison at several time instants, right: comparison of constitutive models at $t = 0.36\,\mathrm{s}$. 110
7.17 The evolution of η along the line $x_2 = R_0$ for stenosed vessel. Mean prescribed Reynolds number Re $\approx$ 98. Left: comparison at several time instants, right: comparison of constitutive models at $t = 0.36\,\mathrm{s}$. 110
7.18 Comparison of the wall deformation η in stenosed vessel for the global iterative method and the explicit kinematic splitting; Carreau model: $\mu_0 = 1.26\mathrm{P}$, $\mu_\infty = 2.53\mathrm{P}$, $\Lambda = 1$, $q = 1.356$. 110
7.19 WSS along Γ_{wall} for stenotic vessel geometry at several time instants; mean Reynolds number Re $\approx$ 195. 117
7.20 WSS along Γ_{wall} for stenotic vessel geometry at several time instants; mean Reynolds number Re $\approx$ 98. 117
7.21 WSS along Γ^m_{wall} for bifurcation geometry at several time instants; mean Reynolds number Re $\approx$ 304. 118
7.22 WSS along Γ^m_{wall} for bifurcation geometry at several time instants; mean Reynolds number Re $\approx$ 152. 119
7.23 WSS at five different positions along Γ^m_{wall} for the period of one heart beat; bifurcation geometry; mean Reynolds number Re $\approx$ 304. 120
7.24 WSS at five different positions along Γ^m_{wall} for the period of one heart beat; bifurcation geometry; mean Reynolds number Re $\approx$ 152. 121
7.25 WSS at three different positions along Γ^m_{wall} for the period of one heart beat; stenotic geometry; mean Reynolds number Re $\approx$ 195. 122
7.26 WSS at three different positions along Γ^m_{wall} for the period of one heart beat; stenotic geometry; mean Reynolds number Re $\approx$ 98. 122
7.27 OSI along Γ_{wall}. Left: stenosed geometry (mean Re $\approx$ 304), right: bifurcation geometry (mean Re $\approx$ 195). 123
7.28 OSI along Γ_{wall}. Left: stenosed geometry (mean Re $\approx$ 152), right: bifurcation geometry (mean Re $\approx$ 98). 123

List of Tables

3.1 Examples of some non-Newtonian fluids. 25
3.2 Some of the representative generalized Newtonian models for blood viscosity with corresponding material constants. Data are obtained from the blood of a 25 year old female donor with Ht=40%, $T = 23$ °C, cf. [45]. 28
3.3 Examples of some viscoelastic models. 30

7.1 Fluid and structure model parameters. 98
7.2 Non-Newtonian model parameters. 98
7.3 Reynolds numbers for physiological data and physiological pulses for the common carotid artery. 99
7.4 Reynolds numbers for physiological data and physiological pulses for the iliac artery. 99
7.5 Convergence rates in space; rigid tube, Newtonian viscosity. 111
7.6 Convergence rates in space; rigid tube, Carreau viscosity. 112
7.7 Convergence rates in space; strong coupling scheme, Carreau viscosity. 112
7.8 Convergence rates in space; kinematic splitting scheme, Carreau viscosity. . . 112
7.9 Convergence rates in space; kinematic splitting scheme, Newtonian viscosity. 112
7.10 Convergence rates in space; explicit kinematic splitting scheme, Carreau viscosity. 113
7.11 Convergence rates in space; implicit kinematic splitting scheme, Carreau viscosity. 113
7.12 Convergence rates in space; explicit Strang splitting scheme, Carreau viscosity. 113
7.13 Convergence rates in space; implicit Strang splitting scheme, Carreau viscosity. 113
7.14 Convergence rates in time; rigid domain, Newtonian viscosity. 114
7.15 Convergence rates in time; rigid domain, Carreau viscosity. 114
7.16 Convergence rates in time; explicit kinematic splitting, Newtonian viscosity. . 114
7.17 Convergence rates in time; explicit kinematic splitting, Carreau viscosity. . . 115
7.18 Convergence rates in time; implicit kinematic splitting, Carreau viscosity. . . 115
7.19 Convergence rates in time; explicit Strang splitting, Carreau viscosity. 115
7.20 Convergence rates in time; implicit Strang splitting, Carreau viscosity. 115

Chapter 1

Introduction

The study of blood circulation in human body is of great interest for physicians and biologists because it allows to understand better the cardiovascular system and it helps to prevent serious diseases such as thrombosis or atherosclerosis. Such pathologies are the main cause of illnesses and death in western countries. Hence the questions like, e.g. "how the arteries become damaged?", "how the local hemodynamics looks like?" and "how plaque develops and changes over time?" are of high interest. For this reason this field is an active and challenging area of medical research [53].

In the recent decades a big progress has been done in clinical studies also thanks to the mathematical modelling. Geometric reconstruction techniques and medical imaging give us key information about the shape of different blood vessels that is crucial to bring mathematical modelling closer to the real applications [9, 10, 20, 16, 21, 42, 65, 100, 101, 104, 89]. Furthermore, promising results from numerical studies, confirmed by in vivo experiments, have encouraged the use of more sophisticated numerical methods to simulate the blood flow in mostly abnormal blood vessels and have provided useful informations about regions with increased plaque danger or thrombosis occurrence [2, 85, 95, 99].

Blood is usually considered to be an incompressible viscous fluid. Therefore conservations laws, i.e. the Navier-Stokes equations, can well describe its flow in the cardiovascular system. However, it is necessary to point out that blood itself is a very complex fluid. Roughly speaking, it is a mixture of red blood cells in plasma. Hence, it belongs to the class of the non-Newtonian fluids. Here it is important to point out that importance of the non-Newtonian blood rheology is a frequently discussed topic. In large arteries of healthy people blood is typically modelled as a Newtonian fluid [45]. Thus the Cauchy stress tensor depends linearly on the rate of the deformation tensor. However, in small vessels or in patients with cardiovascular disease, the more appropriate non-Newtonian models for blood viscosity should be considered [14, 45, 61, 105, 106]. The non-Newtonian rheology of blood is included in the fluid model in the non-constant viscosity. In particular, we assume a shear thinning viscosity function instead of a single constant value. In this case, the governing equations are called the generalized Navier-Stokes equations.

In the real physiological situations, the pulsatile flow causes the vessel walls to move. In addition, blood interacts mechanically as well as chemically with the vessel tissue. From the mathematical point of view, this mutual interaction leads to the so-called fluid-structure interaction. The complexity of this problem depends basically on the fluid model, on the structural model and on the coupling between them. For simplicity of presentation we will work in this thesis with a simple structural model, i.e. the generalized string model, which allows us however to study a non-constant radius vessel like in the case of stenotic occlusion. The theoretical results presented in this work can be generalized to a more complex linear structures, such as those used in [21, 37, 81]. On the other hand, our aim is to emphasize the non-Newtonian blood rheology and to consider the shear thinning behaviour of blood. The

coupled fluid-structure interaction model presented here is simple enough to performed a detailed numerical analysis, but it inherits the most important difficulties that are necessary to understand the complex physiological behaviour of three-dimensional vascular flow.

In the recent years, there has been an increasing interest in developing of efficient numerical algorithms for fluid-structure interaction in hemodynamics, see, e.g. [18, 21, 22, 37, 41, 50, 61, 80, 81, 83, 89] just to mention some of them. In general, there are two ways of constructing a numerical scheme for coupled fluid-structure interaction problems. Monolithic algorithms solve the whole fully coupled problem at once. This requires a new coupled solver and the algorithms are consequently less modular. They belong to the class of strongly coupled schemes. An alternative and quite popular approach is the one of sequential algorithms. Those methods allow the use of different solvers for different physical subproblems. Among the sequential (or partitioned) algorithms we may distinguish between strongly and weakly coupled methods. If the weak coupling is used, a possible imbalance of coupling conditions and the corresponding artificial added mass effects may cause instability; in particular for the problems arising in hemodynamics. One way to overcome the stability issue is to realize sub-iterations per each time step (implicit or strong coupling) that balance out the coupling conditions, see [18, 37, 41, 58, 89]. Recently, some new loosely coupled schemes (explicit coupling) have been proposed in [37, 50, 81].

The main goal of this work is to analyse theoretically as well as experimentally a new loosely coupled kinematic splitting algorithm. In the choice of partitioned strategy we were inspired by the recent paper of Guidoboni et al. [50], where a novel way to avoid instabilities and the necessity to stabilize the fluid-structure interaction algorithm has been presented. However, our approach is more general than the one considered in [50]. Indeed, we allow the use of the second order splitting methods and we analyse theoretically the fully nonlinear coupling between the non-Newtonian fluid and linear structure. The stability analysis is performed on the semi-discrete problem using the implicit Euler discretization in time. This type of discretization was chosen for convenience. In the derivation of the energy estimates the so-called geometric conservation law condition plays a crucial role. We analyse two possible time discretizations of the convective term with a domain velocity. In case of the explicit discretization, we derive the corresponding stability condition for the time step. However, if the midpoint rule is used to approximate the domain velocity convective term, then the kinematic splitting algorithm is unconditionally stable (see an analogous result obtained for the partitioned scheme by Formaggia and Nobile [41], where stability of a linear convection-diffusion problem with a given evolution of the domain boundary is analysed.) We point out that the position of moving wall is treated in an explicit way. More precisely, it means that the fluid equations are solved on the domain computed in the previous time step. Finally, let us also recall that we consider the non-Newtonian shear-dependent fluids and thus our nonlinearities arise not only through geometry and convective term, but also in the viscous fluid term.

The convergence analysis is presented for a simplified fluid model of the Oseen type. The extensions to the fully nonlinear generalized Navier-Stokes equations would be analogous, but will include some technical steps. We sum up these additional difficulties in several remarks. However, even in this general case the main idea of convergence analysis for the fluid-structure interaction problem based on the kinematic splitting approach remains the same.

Our fluid-structure interaction problem is studied also experimentally. We perform the numerical analysis using the UG software toolbox [7, 76], where the generalized Navier-Stokes equation in moving domains with a simple structure solver has been already implemented by Broser and Hundertmark-Zaušková [17, 107]. We have extended the software to the case of kinematic splitting scheme with the operator splitting of the first order (Marchuk-Yanenko splitting scheme) and the second order (Strang splitting scheme). One of our aims was to

analyse the experimental order of convergence for pulsatile inflow assuming the Newtonian as well as non-Newtonian rheology. Moreover, the reliability of our scheme is proved on series of numerical experiments for a non-stenosed, a stenotic and a bifurcation geometry. Here we focus in particular on the wall shear stress distribution along the moving boundary as well as the corresponding oscillatory shear index.

The outline of the thesis is organized as follows:

In Chapter 2 we will describe the mathematical model of blood flow in compliant vessels. We use the conservation laws for incompressible fluids, which will be rewritten for the moving domains using the so-called arbitrary Lagrangian-Eulerian approach. Derivation of the generalized string model describing the elastic movement of structure will be presented in Section 2.3.

The Chapter 3 is devoted to the non-Newtonian rheology. At the beginning we recall the characteristic features of Newtonian and the non-Newtonian materials. In Section 3.2 two models suitable for description of blood viscosity will be derived. The first one, the Carreau model, is the power-law-type model. The second one, the Yeleswarapu model, is a viscoelastic model, where the shear thinning viscosity function is in relation to the extra stress tensor (and its objective choices). Since we are concerned in particular with modelling of shear-dependent fluids, we will omit this the dependence of the generalized viscosity function on the extra stress tensor. Thus, the Yeleswarapu model in our analysis will be represented only by the shear thinning viscosity function.

The fluid-structure interaction problem will be introduced in Chapter 4. We summarize the common strategies used to solve the fluid-structure interaction problem and discuss the difficulties that are connected to the numerical treatment of the schemes. We will be focused on the kinematic splitting technique and introduce the weak formulation of our loosely-coupled scheme.

Chapter 5 deals with the numerical analysis of stability of the loosely-coupled fluid-structure interaction algorithm based on the kinematic splitting. This part will be divided in two main sections. In Section 5.1 we will establish the functional setting for the stability analysis using the a priori estimates for the continuous problem. Then, in Section 5.2 we will derive an energy estimate for discrete coupled fluid-structure interaction problem that includes nonlinearities in both the convective and the diffusive terms as well as in the geometric coupling.

In Chapter 6 we will present the convergence analysis. For the sake of simplicity we will use a linearized fluid model of the Oseen type. The analysis will start with presenting of the general concept of finite element method. Here we will assume that the triangulations are regular. In order to find out the error estimates we will define the interpolation operator for both, the fluid and the structure. The analysis presented in Section 6.7 will be based on the weak formulation for the exact solutions and their numerical counterparts. We will show the convergence of the first order in space. The extensions to the fully nonlinear generalized Navier-Stokes equations will be discussed in several remarks. The generalized Navier-Stokes model causes only technical difficulties due to the model nonlinearities and the pressure contribution. However, the kinematic splitting strategy will influence the convergence in the way that is analogous to the Oseen type of the problem.

In the last part, Chapter 7, we will present results of numerical experiments. Since we are interested in modelling of blood flow in stenosed regions, we will consider preferably non-Newtonian constitutive models. They will be compared with the results obtained for the Newtonian fluid. A comparison will be done for different types of geometry such as a single artery with a stenotic occlusion as well as a carotid arterial bifurcation. Numerical experiments will be realized for simplified two-dimensional domains representing cuts of compliant vessels. A generalization for more realistic three-dimensional geometries is a subject of our future study. The numerical error analysis will be performed for a simplified geometry

and compared with the so-called global iterative approach [58]. Moreover, a comparison in terms of the hemodynamic wall parameters such as the wall-shear stress and the oscillatory shear index will be presented. The experimental analysis of convergence in both space and time confirms stability and high resolution of the proposed scheme (the convergence rates are typically close to the second order).

1.1 Preliminaries

This section gives a brief overview of preliminaries from functional analysis needed for the mathematical model of fluid-structure interaction. It consists of three parts that collect several definitions of functional spaces as well as useful inequalities and theorems that will be needed in the analysis later. For more details see e.g. [1, 33, 36, 78, 91].

Let d represents the space dimension. Let u, v be the scalar-valued functions, $\boldsymbol{u} = (u_1, \ldots, u_d)^T$, $\boldsymbol{v} = (v_1, \ldots, v_d)^T$ be the vector-valued functions and $\mathbf{A} = \{A_{ij}\}$, $\mathbf{B} = \{B_{ij}\}$ for $i, j = 1, \ldots, d$ be the $d \times d$ tensors. We will use the following notation

$$(\bigtriangledown u)_i := \frac{\partial u}{\partial x_i}, \qquad \bigtriangledown \cdot \boldsymbol{u} := \sum_{i=1}^{d} \frac{\partial u_i}{\partial x_i}, \tag{1.1}$$

$$\bigtriangledown u \cdot \bigtriangledown v \ := \ \sum_{i=1}^{d} \frac{\partial u}{\partial x_i} \frac{\partial v}{\partial x_i}, \qquad | \bigtriangledown u |^2 \ := \ \sum_{i=1}^{d} \left| \frac{\partial u}{\partial x_i} \right|^2, \tag{1.2}$$

$$\bigtriangledown \boldsymbol{u} \cdot \bigtriangledown \boldsymbol{v} \ := \ \sum_{i=1}^{d} \sum_{j=1}^{d} \frac{\partial u_i}{\partial x_j} \frac{\partial v_i}{\partial x_j}, \qquad \mathbf{A} : \mathbf{B} := \sum_{i=1}^{d} \sum_{j=1}^{d} A_{ij} B_{ij}, \tag{1.3}$$

$$| \bigtriangledown \boldsymbol{u} |^2 \ := \ \bigtriangledown \boldsymbol{u} : \bigtriangledown \boldsymbol{u}, \qquad (\boldsymbol{u} \otimes \boldsymbol{v})_{ij} := u_i v_j \tag{1.4}$$

Moreover, let α be the multiindex defined by $\alpha := (\alpha_1, \ldots, \alpha_d) \in \mathbb{N}^d$ such that $|\alpha| = \sum_{i=1}^{d} \alpha_i$. Then we will denote by D^α the α-th partial derivative defined by

$$D^0 v = v \quad \text{and} \quad D^\alpha \ = \frac{\partial^{|\alpha|}}{\partial x_1^{\alpha_1} \ldots \partial x_d^{\alpha_d}}, \quad \text{if} \ \ |\alpha| \geq 1. \tag{1.5}$$

In what follows we will assume that $\Omega \in \mathbb{R}^d$ is a bounded domain with a Lipschitz-continuous boundary. We will denote by $\overline{\Omega}$ its closure and by Γ its boundary. Moreover we will use a shorter notation $f_{x_1} := \partial f / \partial x_1$ and $f_{x_1 x_1} := \partial^2 f / \partial x_1^2$.

1.1.1 Useful functional spaces

- **The space $C^k(\Omega)$**

  For $k \geq 0$ we denote by $C^k(\Omega)$ the space of k-times continuously differentiable functions in Ω, i.e.

  $C^k(\Omega) \ = \ \{v |\ v \ \text{ and all its partial derivatives up to the order } k \text{ are continuous in } \Omega\}.$

  For $0 \leq k < \infty$ is the space $C^k(\Omega)$ equipped with the norm

  $$||v||_{C^k(\Omega)} \ = \ \max_{0 \leq |\alpha| \leq k} \ \sup_{x \in \Omega} \ |D^\alpha v|,$$

  where D^α denotes the α-th partial derivative defined in (1.5).

  For $k = \infty$ the space $C^\infty(\Omega)$ denotes the space of all functions with continuous derivatives of all orders, i.e. $C^\infty(\Omega) = \bigcup_{k=1}^{\infty} C^k(\Omega)$. Furthermore, $C^\infty(\overline{\Omega}) = \bigcup_{k=1}^{\infty} C^k(\overline{\Omega})$.

- **The space $L^p(\Omega)$**

  For $1 \leq p < \infty$ we will denote by $L^p(\Omega)$ the space of all measurable functions whose p-th power is Lebesgue integrable in a domain Ω, i.e.

$$L^p(\Omega) \;=\; \left\{v|\; v : \Omega \to \mathbb{R};\; \int_\Omega |v(\boldsymbol{x})|^p \;\mathrm{d}\boldsymbol{x} < \infty,\; 1 \leq p < \infty\right\}$$

  and by $L^\infty(\Omega)$ the space of essentially bounded functions in Ω, i.e.

$$L^\infty(\Omega) = \{v|\; v : \Omega \to \mathbb{R};\; |v(\boldsymbol{x})| < \infty \;\text{ for almost each }\; \boldsymbol{x} \in \Omega\}.$$

  The spaces $L^p(\Omega)$ and $L^\infty(\Omega)$ are normed spaces equipped with the following norms

$$\begin{aligned} ||v||_{L^p(\Omega)} &:= \left(\int_\Omega |v(\boldsymbol{x})|^p \;\mathrm{d}\boldsymbol{x}\right)^{1/p}, && \text{if }\; 1 \leq p < \infty, \\ ||v||_{L^\infty(\Omega)} &:= \operatorname{ess}\sup_{\boldsymbol{x}\in\Omega} |v(\boldsymbol{x})|, && \text{if }\; p = \infty, \end{aligned}$$

  respectively. If $p = 2$, then $L^2(\Omega)$ is a Hilbert space with the scalar product $(v, w)_{L^2(\Omega)}$ and the induced norm $||v||_{L^2(\Omega)}$ given by

$$(v, w)_{L^2(\Omega)} \;:=\; (v, w) = \int_\Omega v(\boldsymbol{x}) w(\boldsymbol{x}) \;\mathrm{d}\boldsymbol{x}, \quad ||v||_{L^2(\Omega)} \;:=\; (v, v)^{\frac{1}{2}},$$

  respectively.

- **The spaces with compact support $C_0^\infty(\Omega)$, $C_{0,\mathrm{div}}^\infty(\Omega)$**

  $C_0^\infty(\Omega)$, $C_{0,\mathrm{div}}^\infty(\Omega)$ denote the following spaces

$$\begin{aligned} C_0^\infty(\Omega) &:= \{v|\; v \in C^\infty(\Omega),\; v \text{ has a compact support in } \Omega\}, \\ C_{0,\mathrm{div}}^\infty(\Omega) &:= \{v|\; v \in C_0^\infty(\Omega),\; \bigtriangledown \cdot v = 0\}, \end{aligned}$$

  respectively.

- **The Sobolev space $H^1(\Omega)$**

  $H^1(\Omega)$ will denote the following Sobolev space

$$H^1(\Omega) = \left\{v|\; v \in L^2(\Omega),\; \frac{\partial v}{\partial x_i} \in L^2(\Omega),\; \forall i = 1, \ldots d\right\} \tag{1.6}$$

  equipped with the scalar product $(v, w)_{H^1(\Omega)}$ and the norm $||v||_{H^1(\Omega)}$ defined by

$$(v, w)_{H^1(\Omega)} := \int_\Omega (vw + \bigtriangledown v \cdot \bigtriangledown w) \;\mathrm{d}x, \quad ||v||_{H^1(\Omega)} := \left(\int_\Omega (|v|^2 + |\bigtriangledown v|^2) \;\mathrm{d}x\right)^{1/2}, \tag{1.7}$$

  respectively. The derivatives in (1.6) are in the distributional sense, i.e.

$$\int_\Omega \frac{\partial v}{\partial x_i} \;\varphi \;\mathrm{d}x = -\int_\Omega \frac{\partial \varphi}{\partial x_i} \;v \;\mathrm{d}x, \quad \forall \varphi \in C_0^\infty(\Omega).$$

  Moreover, let us define the seminorm over $H^1(\Omega)$ by $|v|_{H^1(\Omega)} := \left(\int_\Omega |\bigtriangledown v|^2 \;\mathrm{d}x\right)^{1/2}$.

- **The Sobolev space $H_0^1(\Omega)$**

  $H_0^1(\Omega)$ is the Sobolev space defined as a completion of $C_0^\infty(\Omega)$ in the space $H^1(\Omega)$, i.e. $H_0^1(\Omega) := \overline{C_0^\infty(\Omega)}^{\,||\cdot||_{H^1(\Omega)}}$. It holds

$$H_0^1(\Omega) = \{v|\ v \in H^1(\Omega),\ v|_\Gamma = 0\}.$$

  Moreover $H_0^1(\Omega)$ is closed subspace of $H^1(\Omega)$ and therefore a Hilbert space with the scalar product and norm as defined in (1.7). Here $v|_\Gamma$ denotes a trace of v on $\partial\Omega =: \Gamma$, see also (1.18).

- **The Sobolev space $W^{k,p}(\Omega)$**

  Let $W^{k,p}(\Omega)$ denote a class of spaces with $k \in \mathbb{N}$ or $k = 0$ and $p \geq 1$. If $k = 0$, then $W^{0,p}(\Omega) = L^p(\Omega)$. If $k \in \mathbb{N}$, then

$$W^{k,p}(\Omega) = \{v|\ D^\alpha v \in L^p(\Omega), \forall \alpha = (\alpha_1, \ldots, \alpha_d) \in \mathbb{N}^d \text{ such that } |\alpha| \leq k\},$$

  where D^α denotes the α-th partial derivative defined in (1.5) and taken in the sense of distributions. The space $W^{k,p}(\Omega)$ is the Banach space equipped with the norm

$$||v||_{W^{k,p}(\Omega)} := \left(\sum_{0 \leq |\alpha| \leq k} ||D^\alpha v||^p_{L^p(\Omega)} \right)^{1/p}, \qquad 1 \leq p < \infty, \tag{1.8a}$$

$$||v||_{W^{k,\infty}(\Omega)} := \max_{0 \leq |\alpha| \leq k} ||D^\alpha v||_{L^\infty(\Omega)}, \qquad p = \infty. \tag{1.8b}$$

  If $p = 2$, we write $H^k(\Omega)$ instead of $W^{k,2}(\Omega)$. The space $H^k(\Omega)$ is the Hilbert space with the scalar product $(v, w)_{H^k(\Omega)} = \sum_{0 \leq |\alpha| \leq k} \int_\Omega D^\alpha v\ D^\alpha w\ \mathrm{d}x$. The norm is defined in (1.8a).

- **The Sobolev space $W_0^{k,p}(\Omega)$**

  For $1 < k \leq \infty$ we define the Sobolev space $W_0^{k,p}(\Omega)$ by

$$W_0^{k,p}(\Omega) := \{v|\ v \in W^{k,p}(\Omega),\ D^\alpha v = 0 \text{ on } \Gamma,\ \forall \alpha :\ 0 \leq |\alpha| \leq k-1\}$$

  or for $1 < k < \infty$ as completion of $C_0^\infty(\Omega)$ in the space $W^{k,p}(\Omega)$, i.e. $W_0^{k,p}(\Omega) := \overline{C_0^\infty(\Omega)}^{\,||\cdot||_{W^{k,p}(\Omega)}}$. From the definition of $W_0^{k,p}(\Omega)$ we see that this space consists of functions from $W^{k,p}(\Omega)$ which have zero trace on the boundary Γ.

- **The Bochner space $L^p(I; X)$**

  Let $I = (0, T)$, $1 \leq p \leq \infty$ and X be a Banach space equipped with the norm $||\cdot||_X$. Let $g(\boldsymbol{x}, t)$ be a function defined in space-time domain $\Omega \times I$. Let us denote by $g(t) := g(\boldsymbol{x}, t)$ the space-time function that attains for each $t \in I$ a value belonging to the space $X(\Omega)$. Then we will denote by $L^p(I; X)$ the space

$$L^p(I; X) := \left\{ g|\ g(t) : I \to X(\Omega), \int_0^T ||g(\boldsymbol{x}, t)||^p_X\ \mathrm{d}t < \infty,\ \ 1 \leq p < \infty \right\},$$

$$L^\infty(I; X) := \left\{ g|\ g(t) : I \to X(\Omega),\ \operatorname{ess}\sup_{t \in\ I} ||g(\boldsymbol{x}, t)||_X < \infty \right\}, \quad \text{if } \ p = \infty.$$

  equipped with the following norm

$$||g||_{L^p(I;X)} := \left(\int_0^T ||g(\boldsymbol{x}, t)||^p_X\ \mathrm{d}t \right)^{1/p}, \quad 1 \leq p < \infty,$$

$$||g||_{L^\infty(I;X)} := \operatorname{ess}\sup_{t \in I} ||g(\boldsymbol{x}, t)||_X, \qquad p = \infty.$$

1.1.2 Useful inequalities

- **The Young inequality.** Let $a, b \in \mathbb{R}^+$ and $\varepsilon, \varepsilon_1, \varepsilon_2 > 0$ are small constants. Then

$$ab \;\leq\; \frac{a^2}{4\varepsilon} + \varepsilon b^2. \tag{1.9}$$

For $p, q \in (1, \infty)$ such that $1/p + 1/q = 1$ it holds

$$ab \;\leq\; C_1\varepsilon\; a^p + \frac{C_2}{\varepsilon^{q/p}}\; b^q, \quad \text{where} \quad C_1 := \frac{1}{p}, \quad C_2 := \frac{1}{q}. \tag{1.10}$$

- **The Hölder inequality.** Let $u, v \in L^p(\Omega)$ and $p, q \in [1, \infty]$ such that $1/p + 1/q = 1$. Then $uv \in L^1(\Omega)$ and

$$\int_\Omega |uv| \; \mathrm{d}\boldsymbol{x} \;\leq\; ||u||_{L^p(\Omega)}\; ||v||_{L^q(\Omega)}. \tag{1.11}$$

- **The Sobolev imbedding theorems [1, 33, 78].** Let V be a suitable Banach space such that the following imbedding $W^{k,p}(\Omega) \hookrightarrow V$ holds. Then there exists a positive constant $C = C(\Omega)$ such that

$$||v||_V \;\leq\; C\; ||v||_{W^{k,p}(\Omega)}, \quad \forall\; v \in W^{k,p}(\Omega). \tag{1.12}$$

The validity of (1.12) depends on the choice of the space V, the dimension d and the domain Ω. In particular, it holds

$$H^1(\Omega) \subset C^0(\overline{\Omega}) \qquad \text{if} \;\; d = 1, \tag{1.13}$$

$$H^1(\Omega) \subset L^p(\Omega), \quad \forall p \in [1, \infty) \qquad \text{if} \;\; d = 2, \tag{1.14}$$

$$H^1(\Omega) \subset L^p(\Omega), \quad \forall p \in \left[1, \tfrac{2d}{d-2}\right] \qquad \text{if} \;\; d \geq 3, . \tag{1.15}$$

- **The Poincaré and the Korn inequalities [13, 79].** Let $d \geq 2$ and $p \in (1, \infty)$. Then there exists a positive constant C such that

$$||\boldsymbol{v}||_{H^1(\Omega)} \;\leq\; C\; \Big\{||\boldsymbol{v}||^2_{L^2(\Omega)} + ||\mathbf{D}(\boldsymbol{v})||^2_{L^2(\Omega)}\Big\}^{1/2}, \quad \forall\; \boldsymbol{v} \in H^1(\Omega),$$

$$||\boldsymbol{v}||_{W^{1,p}(\Omega)} \;\leq\; C\; \Big\{||\boldsymbol{v}||^p_{L^p(\Omega)} + ||\mathbf{D}(\boldsymbol{v})||^p_{L^p(\Omega)}\Big\}^{1/p}, \quad \forall\; \boldsymbol{v} \in W^{1,p}(\Omega),$$

where $(\mathbf{D}(\boldsymbol{v}))_{ij} := \dfrac{1}{2}\Big(\dfrac{\partial v_i}{\partial x_j} + \dfrac{\partial v_j}{\partial x_i}\Big)$ denotes the symmetrized gradient of $\boldsymbol{v}$, $i = 1, \cdots, d$. If $\boldsymbol{v}$ equals to zero on $\Gamma_0 \subset \Gamma$ with $\mathrm{meas}(\Gamma_0) > 0$, then

$$||\boldsymbol{v}||_{H^1(\Omega)} \;\leq\; C\; ||\mathbf{D}(\boldsymbol{v})||_{L^2(\Omega)}, \quad \forall\; \boldsymbol{v} \in H^1(\Omega), \tag{1.16}$$

$$||\boldsymbol{v}||_{W^{1,p}(\Omega)} \;\leq\; C\; ||\mathbf{D}(\boldsymbol{v})||_{L^p(\Omega)}, \quad \forall\; \boldsymbol{v} \in W^{1,p}(\Omega). \tag{1.17}$$

The inequalities (1.16) and (1.17) are called the Poincaré and the Korn inequality, respectively.

- **The trace theorem.** Let $\mathrm{T} : W^{1,p}(\Omega) \to L^p(\Gamma)$, $p \geq 1$ be the trace operator. Then there exists a constant $C = C(\Omega)$ such that

$$||\mathrm{T}v||_{L^p(\Gamma)} \;\leq\; C\; ||v||_{W^{1,p}(\Omega)}, \quad \forall\; v \in W^{1,p}(\Omega). \tag{1.18}$$

In the following we will use especially in the boundary integrals the notation $\mathrm{T}v = v$ or $v|_\Gamma$.

- **Trilinear form estimate.** Let $\boldsymbol{u}, \boldsymbol{v}, \boldsymbol{w} \in H^1(\Omega)$, $d = 2$. Then there exists a positive constant such that

$$\int_\Omega (\boldsymbol{u} \cdot \bigtriangledown)\; \boldsymbol{v} \cdot \boldsymbol{w} \; \mathrm{d}x \;\leq\; C\; ||\boldsymbol{u}||_{H^1(\Omega)} ||\boldsymbol{v}||_{H^1(\Omega)} ||\boldsymbol{w}||_{H^1(\Omega)}. \tag{1.19}$$

1.1.3 Useful theorems

- **The divergence (or the Gauss) theorem.** Let $\boldsymbol{v} \in C^1(\overline{\Omega})$ be a vector field. Then it holds

$$\int_\Omega \bigtriangledown \cdot \boldsymbol{v} \ \mathrm{d}x = \int_{\partial\Omega} \boldsymbol{v} \cdot \boldsymbol{n} \ \mathrm{d}S, \tag{1.20}$$

where $\mathrm{d}S$ denotes a boundary element and $\boldsymbol{n}$ stays for the outward normal vector. Componentwisely we can rewrite (1.20) as

$$\int_\Omega \sum_{i=1}^{d} \frac{\partial u_i}{\partial x_i} \mathrm{d}x = \int_{\partial\Omega} \sum_{i=1}^{d} u_i n_i \mathrm{d}S, \quad i = 1, \ldots, d.$$

- **The Green theorem.** Let $u, v \in H^1(\Omega)$. Then applying the Gauss theorem on the scalar function uv we obtain

$$\int_\Omega \frac{\partial u}{\partial x_i} \ v \ \mathrm{d}\omega \ = \ -\int_\Omega u \frac{\partial v}{\partial x_i} \ \mathrm{d}\omega + \int_{\partial\Omega} u \ v \ n_i \ \mathrm{d}S, \quad i = 1, \ldots, d. \tag{1.21}$$

From (1.21) it follows easily that for $u \in H^1(\Omega)$ and $v \in H^2(\Omega)$ we have

$$\int_\Omega \sum_{i=1}^{d} \frac{\partial u}{\partial x_i} \ \frac{\partial v}{\partial x_i} \ \mathrm{d}\omega \ = \ -\int_\Omega u \ \frac{\partial^2 v}{\partial x_i^2} \ \mathrm{d}\omega + \int_{\partial\Omega} \frac{\partial u}{\partial x_i} \ v \ n_i \ \mathrm{d}S, \quad i = 1, \ldots, d. \tag{1.22}$$

- **The Reynold transport theorem in the Lagrangian frame [36].** Let Ω_t be a time-dependent domain and Ω_0 a reference domain corresponding to the time instant t_0. Let $\mathcal{V}_0 \subset \Omega_0$ be occupied by a fixed set of material particles. We denote by $\mathcal{V}_t$ a time-dependent region in Ω_t, which is in general different than a material region $\mathcal{V}_0$, but contains the same material points. Let ϕ be any scalar or tensor-valued field with the representation

$$\phi = \bar{\phi}(\boldsymbol{Y}, t) = \hat{\phi}(\boldsymbol{x}, t), \quad \text{with} \quad \boldsymbol{Y} \in \Omega_0, \ \boldsymbol{x} \in \Omega_t \tag{1.23}$$

and let $\mathcal{I}$ denotes a volume integral of ϕ over $\mathcal{V}_t$ as well as a volume integral of ϕ over $\mathcal{V}_0$

$$\mathcal{I} \ := \ \int_{\mathcal{V}(t)} \hat{\phi}(\boldsymbol{x}, t) \mathrm{d}v = \int_{\mathcal{V}_0} \bar{\phi}(\boldsymbol{Y}, t) \ DJ \mathrm{d}V,$$

where the infinitesimal material volume $\mathrm{d}v$ from $\mathcal{V}_t$ is transformed into the corresponding infinitesimal material volume $DJ\mathrm{d}V$ from $\mathcal{V}_0$, where DJ denotes the determinant of the Jacobian of transformation. Then the Reynold transport theorem states that

$$\frac{\mathrm{d}\mathcal{I}}{\mathrm{d}t} = \int_{\mathcal{V}_t} \left[\frac{D\hat{\phi}}{Dt} + \hat{\phi}(\boldsymbol{x}, t) \ \bigtriangledown \cdot \hat{\boldsymbol{u}}(\boldsymbol{x}, t) \right] \mathrm{d}v, \tag{1.24}$$

where $\dfrac{D\hat{\phi}}{Dt}$ denotes the Lagrangian (or material) derivative defined by

$$\frac{D\hat{\phi}}{Dt} := \frac{\partial \hat{\phi}}{\partial t} + (\boldsymbol{u} \cdot \bigtriangledown)\hat{\phi}$$

Alternatively we can write

$$\frac{\mathrm{d}\mathcal{I}}{\mathrm{d}t} = \int_{\mathcal{V}_t} \frac{\partial \hat{\phi}(\boldsymbol{x}, t)}{\partial t} + \int_{\partial\mathcal{V}_t} \hat{\phi}(\boldsymbol{x}, t) \hat{\boldsymbol{u}}(\boldsymbol{x}, t) \cdot \boldsymbol{n} \ \mathrm{d}S, \tag{1.25}$$

where $\boldsymbol{n}$ is the outward unit normal vector to $\partial\mathcal{V}(t)$ and $\mathrm{d}S$ denotes an infinitesimal surface area related to the infinitesimal volume $\mathrm{d}v$.

- **The Gronwall lemma [91].** Let $f \in L^1(t_0, T)$ be a non-negative function, g and ψ be continuous functions on $[t_0, T]$. If ψ satisfies

$$\psi(t) \leq g(t) + \int_{t_0}^{t} f(\tau)\psi(\tau)\ \mathrm{d}\tau,\ t \in [t_0, T], \tag{1.26}$$

then

$$\psi(t) \leq g(t) + \int_{t_0}^{t} f(s)g(s) \exp\left(\int_{s}^{t} f(\tau)\ \mathrm{d}\tau\right)\ \mathrm{d}s,\ t \in [t_0, T]. \tag{1.27}$$

If moreover g is non-decreasing, then

$$\psi(t) \leq g(t) \exp\left(\int_{t_0}^{t} f(\tau)\ \mathrm{d}\tau\right),\ t \in [t_0, T]. \tag{1.28}$$

- **The discrete Gronwall lemma [91].** Let $\Delta t, g_0, a_n, b_n, c_n, \gamma_n$ be sequences of non-negative numbers for $n \geq 0$. If the following inequality holds

$$a_n + \Delta t \sum_{i=0}^{n}\ b_i \leq \Delta t \sum_{i=0}^{n} \gamma_i a_i + \Delta t \sum_{i=0}^{n} c_i + g_0, \tag{1.29}$$

then for all $n \geq 0$ we have

$$a_n + \Delta t \sum_{i=0}^{n}\ b_i \leq \left[\Delta t \sum_{i=0}^{n} c_i + g_0\right] \exp\left\{\Delta t \sum_{i=0}^{n} \sigma_i \gamma_i\right\}, \tag{1.30}$$

where $\Delta t \leq \dfrac{1}{\gamma_i}$ and $\sigma_i := \dfrac{1}{1 - \gamma_i \Delta t}$ for $i = 0, \ldots, n$.

Chapter 2

Mathematical Model

This chapter is devoted to the description of a mathematical model for our fluid-structure interaction problem. Firstly, we introduce the governing equations for fluid flow and discuss their well-posedness. Then we look more precisely on the arbitrary Lagrangian-Eulerian mapping that helps us to rewrite our fluid model for the moving meshes. Finally, we focus on derivation of the generalized string model, which is a structural model that describes viscoelastic movement of structure.

2.1 Governing equations

In what follows we introduce basic conservation laws for continuum mechanics. Firstly, we recall some relevant notations. Material points in a fluid (generally called the body) can be identified by specifying their location in some reference configuration. In our analysis the reference configuration, denoted by Ω_0, represents a configuration of the fluid at time instant t_0, which is usually considered to be equal zero. First, assume that each fluid quantity φ, for example velocity, pressure, fluid's density and so on, can be written either as a function of $\boldsymbol{Y}$ (position of an arbitrary material particle in Ω_0) and t or as a function of $\boldsymbol{x}$ and t. The configuration of the domain of interest at time instant t is denoted by Ω_t, where $t \in [t_0, T]$. The couple of variables $(\boldsymbol{X}, t)$ represents the so-called referential or *Lagrangian description* of a body, while $(\boldsymbol{x}, t)$ denotes the spatial or *Eulerian description*. Thus, similarly as in (1.23), we can write

$$\varphi = \bar{\varphi}(\boldsymbol{Y}, t) = \hat{\varphi}(\boldsymbol{x}, t). \tag{2.1}$$

The relation between the referential and the actual configuration can by expressed as follows

$$\boldsymbol{x} = \chi_{\Omega_0}(\boldsymbol{Y}, t) \quad \text{or} \quad \boldsymbol{Y} = \chi_{\Omega_0}^{-1}(\boldsymbol{x}, t),$$

where the function $\chi_{\Omega_0}(\boldsymbol{X}, t)$ providing the mapping between these two frames is differentiable as many times as necessary both, in space and in time.

Let us denote by $\boldsymbol{u} = (u_1, \ldots, u_d)^T$ the fluid velocity field. For the viscous fluids a fundamental kinematic variable is represented by the *velocity gradient vector* $\bigtriangledown \boldsymbol{u}$. On the other hand, the main kinematic properties for elastic solids are expressed by means of the *deformation gradient tensor* $\mathbf{F}$, which is defined by

$$\mathbf{F} = \frac{\partial \chi_{\Omega_0}(\boldsymbol{Y}, t)}{\partial \boldsymbol{Y}}.$$

It holds that the Jacobian of transformation J is equivalent to the determinant of $\mathbf{F}$, i.e. $J := \det \mathbf{F}$. Measures of deformation and strain for elastic materials are represented by the *left Cauchy-Green tensor* $\mathbf{B}$ and the *right Cauchy-Green tensor* $\mathbf{C}$ defined by

$$\mathbf{B} = \mathbf{F} \cdot \mathbf{F}^T, \quad \mathbf{C} = \mathbf{F}^T \cdot \mathbf{F},$$

respectively. In the case of viscous fluids, the *rate of the deformation tensor* $\mathbf{D}$ plays a significant role. It is defined by

$$\mathbf{D} = \frac{1}{2}\Big(\bigtriangledown \boldsymbol{u} + \bigtriangledown \boldsymbol{u}^T \Big).$$

For simplicity of presentation, we will omit the "hat" notation in what follows. Using the Reynold transport theorem (1.25) for the fluid quantity $\varphi = \rho_f(\boldsymbol{x}, t)$ we obtain the **principle of conservation of mass** in the local Eulerian and the Lagrangian form

$$\frac{\partial \rho_f}{\partial t} + \bigtriangledown \cdot (\boldsymbol{u}\rho_f) = 0 \quad \text{and} \quad \frac{D\rho_f}{Dt} + \rho_f \ \bigtriangledown \cdot \boldsymbol{u} = 0, \tag{2.2}$$

respectively. Applying (1.25) on the quantity $\varphi = \rho_f(\boldsymbol{x}, t)\boldsymbol{u}(\boldsymbol{x}, t)$ we obtain the **balance of linear momentum**. In the local Eulerian and the Lagrangian form it can be written as

$$\frac{\partial(\rho_f \boldsymbol{u})}{\partial t} + \bigtriangledown \cdot (\rho_f \boldsymbol{u} \otimes \boldsymbol{u}) = \bigtriangledown \cdot \mathbf{T} + \mathbf{b} \quad \text{and} \quad \frac{D(\rho_f \boldsymbol{u})}{Dt} + \rho_f \boldsymbol{u} \ \bigtriangledown \cdot \boldsymbol{u} = \bigtriangledown \cdot \mathbf{T} + \mathbf{b}, \tag{2.3}$$

respectively. The term $\mathbf{b}$ from (2.3) represents the vector of body forces and $\mathbf{T}$ is the *Cauchy stress tensor*. For inviscid fluids the stress tensor $\mathbf{T}$ is defined by

$$\mathbf{T} = -p\mathbf{I},$$

where p denotes the dynamic pressure and $\mathbf{I}$ is the identity matrix. In the case of viscous fluids $\mathbf{T}$ is defined in the following way

$$\mathbf{T} = -p\mathbf{I} + \mathbf{S}^{(v)}(\boldsymbol{u}), \quad \text{i.e.} \quad T_{ij} = -p\delta_{ij} + S_{ij}^{(v)}, \quad i, j = 1, \ldots, d, \tag{2.4}$$

where δ_{ij} denotes the Kronecker delta function and $\mathbf{S}^{(v)}$ is the viscous part of the so-called *extra stress tensor* $\mathbf{S}$ (which corresponds to the deviatoric part of $\mathbf{T}$). The so-called viscoelastic fluids have the stress tensor of the form

$$\mathbf{T} = -p\mathbf{I} + \mathbf{S}(\boldsymbol{u}), \quad \text{i.e.} \quad T_{ij} = -p\delta_{ij} + S_{ij}, \quad i, j = 1, \ldots, d,$$

with viscous as well as elastic part included in the extra stress tensor tensor $\mathbf{S}(\boldsymbol{u})$, i.e.

$$\mathbf{S}(\boldsymbol{u}) = \mathbf{S}^{(v)}(\boldsymbol{u}) + \mathbf{S}^{(e)}(\boldsymbol{u}) \quad \text{i.}e. \quad S_{ij} = S_{ij}^{(v)} + S_{ij}^{(e)}. \tag{2.5}$$

The **balance of energy** in the local forms states

$$\rho_f \frac{\partial E}{\partial t} + \bigtriangledown \cdot (E\boldsymbol{u}) \ = \ \mathbf{b} \cdot \boldsymbol{u} + \bigtriangledown \cdot (\mathbf{T} \cdot \boldsymbol{u}) - \bigtriangledown \cdot \boldsymbol{q} + \rho_f Q \tag{2.6}$$

or

$$\rho_f \frac{DE}{Dt} + \bigtriangledown E \cdot \boldsymbol{u} \ = \ \mathbf{b} \cdot \boldsymbol{u} + \bigtriangledown \cdot (\mathbf{T} \cdot \boldsymbol{u}) - \bigtriangledown \cdot \boldsymbol{q} + \rho_f Q. \tag{2.7}$$

Here the scalar function $E = E(\boldsymbol{x}, t)$ is the specific energy per unit mass, $\boldsymbol{q}$ denotes the thermal energy per unit surface area, $Q = Q(\boldsymbol{x}, t)$ is the specific heat supply per unit time.

In this work we are focused on the incompressible fluid flow. Due to the assumption of incompressibility, i.e. $D\rho_f/Dt = 0$, we consider only balance of mass (2.2) and balance of linear momentum (2.3). The energy balance (2.6)-(2.7) represents an additional constraint on temperature and energy, if necessary. Therefore, the mathematical model is given by the so-called generalized Navier-Stokes equations (NSE), i.e. the momentum and the continuity equation, and reads as follows

$$\rho_f \left[\frac{\partial \boldsymbol{u}}{\partial t} + (\boldsymbol{u} \cdot \bigtriangledown)\boldsymbol{u} \right] - \bigtriangledown \cdot \Big[\mathbf{S}(\bigtriangledown \boldsymbol{u}) \Big] + \bigtriangledown \ p \ = \boldsymbol{f}, \qquad \text{in} \quad \Omega_t, \tag{2.8a}$$

$$\bigtriangledown \cdot \boldsymbol{u} \ = 0, \qquad \text{in} \quad \Omega_t, \tag{2.8b}$$

where $\boldsymbol{f} = (f_1, \ldots, f_d)^T$ represents possible forcing term for velocity and ρ_f denotes the fluid density that is assumed to be a constant. The form of the extra stress tensor depends on the type of fluid one is working with. Relevant constitutive equations for non-Newtonian fluids, in particular for blood, will be discussed in Chapter 3. In our numerical modelling and theoretical analysis we assume that the extra stress tensor $\mathbf{S}$ obeys a constitutive equation of the type

$$\mathbf{S} \;=\; 2\mu(|\mathbf{D}(\boldsymbol{u})|)\mathbf{D}(\boldsymbol{u}),$$

where $\mu(|\mathbf{D}(\boldsymbol{u})|)$ represents the viscosity function depending on the rate of the deformation tensor. In what follows, the explicit dependence of $\mathbf{S}$ on $\mathbf{D}(\boldsymbol{u})$ will be emphasized using the notation $\mathbf{S}(\mathbf{D}(\boldsymbol{u}))$. We note, that if $\mu = \text{const}$ the equations (2.8a)-(2.8b) are called the Navier-Stokes equations.

The generalized Navier-Stokes equations represent an initial boundary valued problem, which consists in finding the velocity field $\boldsymbol{u}(\boldsymbol{x}, t)$ and the pressure field $p(\boldsymbol{x}, t)$, which obey certain initial and boundary conditions. Moreover, while working with moving domains, also the coupling conditions providing a matching at the interfaces of moving boundaries should be carefully prescribed. A suitable boundary, initial and coupling conditions will be discussed in Section 4.1.

Remark 2.1 (Well-posedness of NSE in rigid domains) *The study of the existence and uniqueness of the Navier-Stokes equations distinguishes between the strong (i.e. classical) and the weak solutions. Here we assume that domains through which a fluid flow does not change in time.*
Considering weak solutions $\boldsymbol{u} \in L^\infty(0, T; H) \cap L^2(0, T; V)$*, where*

$$H := \{\boldsymbol{u}|\ \boldsymbol{u} \in L^2(\Omega)\}, \quad \text{and} \quad V := \{\boldsymbol{u}|\ \boldsymbol{u} \in H_0^1(\Omega) :\ \bigtriangledown \cdot \boldsymbol{u} = 0 \text{ in } \Omega\},$$

the following results has been obtained:

- **Two-dimensions:** *In 1933 Leray proved the existence and uniqueness for all time in the whole space [66, 67]. The proof of uniqueness for bounded as well as unbounded domains was given 1959 by Lions and Prodi [71]. In 1963, Serrin formulated a sufficient condition for a weak solution to be unique, which gave a proof of uniqueness of a weak solution in two dimensions [94].*

- **Three-dimensions:** *The proof of global long-time and large-data existence was given in 1934 by Leray [67] and in 1951 extended by Hopf for bounded domains with no-slip boundary conditions [56]. The existence was furthermore extended to the so-called suitable weak solutions in 1982 by Caffarelli, Kohn and Nirenberg [19]. Since the Serrin condition does not hold for three dimensions and no counter examples has been constructed so far, the question of uniqueness of a weak solution for three dimensions is still an open problem [35]. It means that the uniqueness of weak solutions for which the existence in guaranteed has not been shown yet. Hence, it was proved only that* $\boldsymbol{u} \in L^{8/3}(0, T; L^4(\Omega))$*. However, it it possible to show that there exists at most one weak solution in the following class of functions:* $\boldsymbol{u} \in L^8(0, T; L^4(\Omega))$*, see, e.g. [102].*

In the case of classical strong solutions it has been shown:

- **Two-dimensions:** *The existence and uniqueness has been proved in 1962 by Ladyzhenskaya [63].*

- **Three-dimensions:** *Local existence on a time interval* $(0, T^*)$*,* $T^* < T$ *and uniqueness in whole domain was proved in 1934 by Leray [67]. However, the uniqueness in general has not been proved yet, see, e.g. [102].*

2.2 Arbitrary Lagrangian-Eulerian mapping

As already mentioned above, we are focused on time-dependent domains. This will be emphasized by adding a subscript t to the domain of interest Ω, i.e. Ω_t. Moreover, as it is common in the field of blood flow modelling, we assume that several boundaries are rigid (the inflow and the outflow) while the others are allowed to move. Hence, we need a special technique to treat the motion of moving domain Ω_t.

In general, there are several methods used to solve problems on deformable meshes. The most suitable for fluid-structure interaction problems and problems with large deformations in solid mechanics, e.g. blood flow circulation [50, 58, 90], airfoil vibrations [68, 98] etc., is the Arbitrary Lagrangian-Eulerian (ALE) approach. From the other adaptive techniques we mention for instance the dynamic mesh method, the co-rotational approach and space-time configurations, see, e.g. [32, 34] and references therein.

We are working with the ALE method. It takes the advantages of both classical kinematic descriptions, the Eulerian and the Lagrangian, and combines them into one. Hence, when it is necessary, the mesh moves with the material (Lagrangian description), otherwise the mesh remains fixed and the material can flow through it (Eulerian description). In order to describe the movement of domain, we introduce, in addition to the material and the spatial domain, a reference domain. Then, the dynamic mesh movement, either a priori prescribed or given by a physical law, can be easily computed with respect to the reference domain.

In what follows we rewrite the Navier-Stokes equations (2.8a)-(2.8b) using the ALE mapping $\mathcal{A}_t$, see Fig. 2.1.

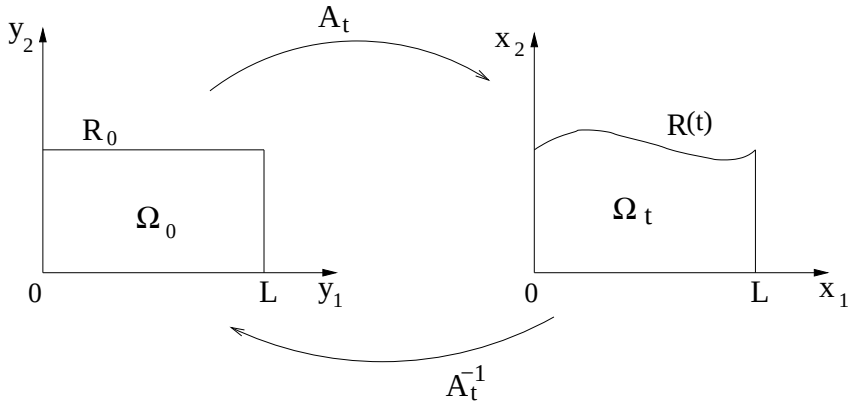

Figure 2.1: ALE mapping $\mathcal{A}_t$ with a moving boundary and a symmetry axis.

Throughout this work we will assume that the ALE mapping is enough smooth. In particular we assume that $\mathcal{A}_t \in W^{1,\infty}(\Omega_0)$, $\mathcal{A}_t^{-1} \in W^{1,\infty}(\Omega_t)$, $\forall t \in I$, where Ω_0 is a two-dimensional bounded reference domain with the Lipschitz continuous boundary and $\Omega_t := \mathcal{A}_t(\Omega_0)$ is bounded and $\partial\Omega_t$ is Lipschitz continuous. Indeed, one can construct analogously as in [80] the ALE mapping obeying the above regularity and show that $\mathcal{A}_t \circ v$ is an isomorphism from $L^q(0,T;W^{1,q}(\Omega_0))$ onto $L^q(0,T;W^{1,q}(\Omega_t))$ and from $L^\infty(0,T;L^2(\Omega_0))$ onto $L^\infty(0,T;L^2(\Omega_t))$. We will present one such example in Section 5.2.

Introducing the so-called ALE derivative

$$\frac{\mathcal{D}^{\mathcal{A}}\boldsymbol{u}(\boldsymbol{x},t)}{\mathcal{D}t} := \frac{\partial \boldsymbol{u}(\boldsymbol{Y},t)}{\partial t}\bigg|_{\boldsymbol{Y}=\mathcal{A}_t^{-1}(\boldsymbol{x})} = \frac{\partial \boldsymbol{u}(\boldsymbol{x},t)}{\partial t}\bigg|_{\boldsymbol{x}} + \boldsymbol{w}(\boldsymbol{x},t)\cdot\nabla\boldsymbol{u}(\boldsymbol{x},t) \quad \text{for } \boldsymbol{x}\in\Omega_t,\ \boldsymbol{Y}\in\Omega_0 \tag{2.9}$$

we can define the domain velocity

$$\boldsymbol{w}(\boldsymbol{x},t) := \left.\frac{\partial \mathcal{A}_t(\boldsymbol{Y})}{\partial t}\right|_{\boldsymbol{Y}=\mathcal{A}_t^{-1}(\boldsymbol{x})} = \frac{\partial \boldsymbol{x}}{\partial t} \quad \text{for} \quad \boldsymbol{x} \in \Omega_t,\ \boldsymbol{Y} \in \Omega_0 \tag{2.10}$$

and rewrite the governing equations (2.8a)-(2.8b) into the form that takes into account specific time-dependent behaviour of the domain, i.e.

$$\rho_f \left[\frac{\mathcal{D}^{\mathcal{A}}\boldsymbol{u}}{\mathcal{D}t} + ((\boldsymbol{u}-\boldsymbol{w})\cdot \bigtriangledown)\boldsymbol{u} \right] - \bigtriangledown \cdot \left[2\mu(|\mathbf{D}(\boldsymbol{u})|)\ \mathbf{D}(\boldsymbol{u}) \right] + \bigtriangledown\, p = \boldsymbol{f}, \qquad \text{in } \Omega_t, \tag{2.11a}$$

$$\bigtriangledown \cdot \boldsymbol{u} = 0, \qquad \text{in } \Omega_t,\ t \in I. \tag{2.11b}$$

Now we give a proof of the Reynolds transport theorem for the case of arbitrary Lagrangian-Eulerian description.

Theorem 2.2 (Reynold's transport theorem in the ALE frame) *Let $\mathcal{A}_t$ be the ALE mapping, $\mathcal{D}^{\mathcal{A}}/\mathcal{D}t$ the ALE derivative defined in (2.9) and $\boldsymbol{w}$ the domain velocity defined in (2.10). Moreover, let us denote by $J_{\mathcal{A}}$ the Jacobian of the ALE mapping and by $DJ_{\mathcal{A}}$ the determinant of the Jacobian $J_{\mathcal{A}}$ defined by*

$$(J_{\mathcal{A}})_{ij} = \left(\frac{\partial \mathcal{A}_t(Y_i)}{\partial Y_j} \right)_{1\le i,j\le d}, \quad DJ_{\mathcal{A}} = \det\ J_{\mathcal{A}},$$

respectively. Then for a function $f(\boldsymbol{x},t)$ defined in Ω_t it holds

$$\begin{aligned} \frac{\mathrm{d}}{\mathrm{d}t}\int\limits_{\Omega_t} f(\boldsymbol{x},t)\mathrm{d}\omega &= \int\limits_{\Omega_t} \left[\frac{\partial f(\boldsymbol{x},t)}{\partial t} + \bigtriangledown \cdot (f\ w)(\boldsymbol{x},t) \right] \mathrm{d}\omega \\ &= \int\limits_{\Omega_t} \left[\frac{\mathcal{D}^{\mathcal{A}} f(\boldsymbol{x},t)}{\mathcal{D}t} + f(\boldsymbol{x},t) \bigtriangledown \cdot\ \boldsymbol{w}(\boldsymbol{x},t) \right] \mathrm{d}\omega. \end{aligned} \tag{2.12}$$

Proof. Let us firstly transform the integral over $\Omega_t = \mathcal{A}_t(\Omega_0)$ to the integral over the reference domain Ω_0. Hence, it holds

$$\frac{\mathrm{d}}{\mathrm{d}t}\int\limits_{\Omega_t} f(\boldsymbol{x},t)\mathrm{d}\omega = \frac{\mathrm{d}}{\mathrm{d}t}\int\limits_{\Omega_t} f(\mathcal{A}_t(\boldsymbol{Y},t),t)\ \mathrm{d}\omega = \frac{\mathrm{d}}{\mathrm{d}t}\int\limits_{\Omega_0} f(\mathcal{A}_t(\boldsymbol{Y},t),t)\ DJ_{\mathcal{A}}(\boldsymbol{Y},t)\ \mathrm{d}\omega_0,$$

where $\mathrm{d}\omega$ and $DJ_{\mathcal{A}}(\boldsymbol{Y},t)\mathrm{d}\omega_0$ denotes differential volume element from Ω_t and Ω_0, respectively. Being on the reference frame, we can come with the time derivative inside the integral. This yields

$$\frac{\mathrm{d}}{\mathrm{d}t}\int\limits_{\Omega_t} f(\boldsymbol{x},t)\mathrm{d}\omega = \int\limits_{\Omega_0} \left[\frac{\partial f(\mathcal{A}_t(\boldsymbol{Y},t),t)}{\partial t}\ DJ_{\mathcal{A}}(\boldsymbol{Y},t) + f(\mathcal{A}_t(\boldsymbol{Y},t),t)\frac{\partial DJ_{\mathcal{A}}(\boldsymbol{Y},t)}{\partial t} \right] \mathrm{d}\omega_0. \tag{2.13}$$

Denoting by M_{ik} the minors of $(J_{\mathcal{A}})_{ik}$ and writing the determinant of the Jacobian of the ALE mapping as

$$DJ_{\mathcal{A}} = \sum_{k=1}^{n} (J_{\mathcal{A}})_{ik}(-1)^{i+k} M_{ik}$$

we obtain

$$\begin{aligned}
\frac{\partial\ (DJ_{\mathcal{A}})}{\partial t} &= \sum_{i,j=1}^{n} \frac{\partial(DJ_{\mathcal{A}})}{\partial(J_{\mathcal{A}})_{ij}}\ \frac{\partial(J_{\mathcal{A}})_{ij}}{\partial t} = \sum_{i,j}^{n} \frac{\partial\Big(\sum_{k=1}^{n}(J_{\mathcal{A}})_{ik}(-1)^{i+k}M_{ik}\Big)}{\partial(J_{\mathcal{A}})_{ij}}\ \frac{\partial(J_{\mathcal{A}})_{ij}}{\partial t} \\
&= \sum_{i,j=1}^{n} (-1)^{i+j}M_{ij}\ \frac{\partial^2\mathcal{A}_t(Y_i)}{\partial t\partial Y_j} = \sum_{i,j=1}^{n} (-1)^{i+j}M_{ij}\ \frac{\partial \boldsymbol{w}_i}{\partial Y_j} \\
&= \sum_{i,j=1}^{n} (-1)^{i+j}M_{ij}\ \frac{\partial \boldsymbol{w}_i}{\partial x_k}\ \frac{\partial x_k}{\partial Y_j} = \sum_{i,j=1}^{n} (-1)^{i+j}M_{ij}\ \frac{\partial \boldsymbol{w}_i}{\partial x_k}\ \frac{\partial \mathcal{A}_t(Y_k)}{\partial Y_j} \\
&= \sum_{i,j=1}^{n} (-1)^{i+j}M_{ij}(J_{\mathcal{A}})_{kj}\ \frac{\partial \boldsymbol{w}_i}{\partial x_k} = \sum_{i=1}^{n} (DJ_{\mathcal{A}})\ \delta_{ik}\ \frac{\partial \boldsymbol{w}_i}{\partial x_k} \\
&= (DJ_{\mathcal{A}})\ \frac{\partial \boldsymbol{w}_i}{\partial x_i} = (DJ_{\mathcal{A}})\ \bigtriangledown\cdot\boldsymbol{w}. \qquad (2.14)
\end{aligned}$$

Inserting (2.14) into (2.13) we have

$$\begin{aligned}
\frac{\mathrm{d}}{\mathrm{d}t}\int\limits_{\Omega_t} f(\boldsymbol{x},t)\mathrm{d}\omega &= \int\limits_{\Omega_0}\Bigg[\left(\frac{\partial f(\mathcal{A}_t(\boldsymbol{Y},t),t)}{\partial\mathcal{A}_t}\ \frac{\partial\mathcal{A}_t}{\partial t} + \frac{\partial f(\mathcal{A}_t(\boldsymbol{Y},t),t)}{\partial t}\ \frac{\partial t}{\partial t}\right) \\
&\qquad + f(\mathcal{A}_t(\boldsymbol{Y},t),t)\bigtriangledown\cdot\boldsymbol{w}(\mathcal{A}_t(\boldsymbol{Y},t),t)\Bigg](DJ_{\mathcal{A}})(\boldsymbol{Y},t)\ \mathrm{d}\omega_0 \\
&= \int\limits_{\Omega_0}\left[\frac{\partial f}{\partial t} + \bigtriangledown f\cdot\boldsymbol{w} + f\bigtriangledown\cdot\boldsymbol{w}\right](\mathcal{A}_t(\boldsymbol{Y},t),t)(DJ_{\mathcal{A}})(\boldsymbol{Y},t)\ \mathrm{d}\omega_0 \\
&= \int\limits_{\Omega_0}\left[\frac{\partial f}{\partial t} + \bigtriangledown\cdot(f\boldsymbol{w})\right](\mathcal{A}_t(\boldsymbol{Y},t),t)(DJ_{\mathcal{A}})(\boldsymbol{Y},t)\ \mathrm{d}\omega_0 \\
&= \int\limits_{\Omega_t}\left[\frac{\partial f}{\partial t} + \bigtriangledown\cdot(f\boldsymbol{w})\right](\boldsymbol{x},t)\ \mathrm{d}\omega = \int\limits_{\Omega_t}\left[\frac{\mathcal{D}^{\mathcal{A}}f}{\mathcal{D}t} + f\bigtriangledown\cdot\boldsymbol{w}\right](\boldsymbol{x},t)\ \mathrm{d}\omega.
\end{aligned}$$

■

2.3 Structure equation

Mathematical modelling of blood vessel walls is a complicated task. It is due to the fact that vascular wall has a very complex nature and its structure depends on many mechanical characteristics. Therefore it is necessary to find simplifying assumptions which preserve the main physical features and still reasonably describe the behaviour of physiological vessel walls. The main difference between solids and fluids is in the kinematic quantity which entries into the constitutive relation. In the case of fluids, the constitutive equation links the Cauchy stress tensor $\mathbf{T}$ with the velocity gradient $\bigtriangledown\boldsymbol{u}$ or with the rate of the deformation tensor $\mathbf{D}$. The situation is different for the case of solids, where the Cauchy stress tensor $\mathbf{T}$ is expressed in terms of the deformation gradient $\mathbf{F}$ or the right (left) Cauchy-Green tensor $\mathbf{B}$ ($\mathbf{C}$). However, there is a large variety of materials that behave both as a liquid and as a solid. For example, if the material is viscoelastic the constitutive law can be expressed in the form

$$\mathbf{T} = \mathbf{T}(\mathbf{D},\mathbf{F}).$$

In literature several models describing the deformation of a moving structure can be found. They can be divided into two main groups. The first group is represented by the so-called **shell models**, e.g. the Koiter shell model, cf. [21, 26, 27]. They arise from the general theory of elastic shells. The second group contains simplified structural models, e.g. the **membrane models**, cf., [84, 86, 90]. The simplified reference models are derived for cylindrical geometry allowing only axially symmetric flow. The moving surface is defined in the cylindrical coordinate system by

$$\Gamma = \{(r, \theta, z) : r = R_0,\ \theta \in [0, 2\pi),\ z = [0, L]\}, \tag{2.15}$$

where R_0 denotes the radius of reference surface, r denotes the radial variable, θ denotes the angle, z the longitudinal variable and L is the length of the vessel tube. Assuming that the reference geometry is cylindrical, wall thickness h_s is small, longitudinal and angular displacement are neglectable, we obtain the simplest 1D model called the **simple algebraic model**, i.e.

$$\eta = k(p - P_{ext}), \tag{2.16}$$

where k is a positive constant related to the mechanical and geometric properties, p denotes the fluid pressure, P_{ext} the external pressure acting on the wall and η is the radial displacement with respect to the reference surface R_0 defined by

$$\eta(\theta, z, t) = R(\theta, z, t) - R_0(\theta, z). \tag{2.17}$$

Here, R denotes the current radius of vessel. Adding an inertia term to the model (2.16) we obtain the **independent ring model**

$$\frac{\partial^2 \eta}{\partial t^2} + b\eta = H_1, \quad \text{where} \quad H_1 = \frac{p - P_{ext}}{\rho_s h_s}. \tag{2.18}$$

Here b is a constant and ρ_s the structure density. The model (2.18) does not guarantee the smoothness of η, but it can be improved by adding a term describing the wall deformation along the z-direction. The resulting model is called the **generalized ring model**

$$\frac{\partial^2 \eta}{\partial t^2} - a\frac{\partial^2 \eta}{\partial z^2} + b\eta = H_2, \quad \text{where} \quad H_2 = \frac{-\mathbf{T} \cdot \boldsymbol{n} \cdot \boldsymbol{e}_r - P_{ext}}{\rho_s h_s}. \tag{2.19}$$

Here a is the constant for longitudinal rigidity and H_2 accounts full contribution of the Cauchy stress tensor. The vector $\boldsymbol{n}$ is the outward unit normal vector to the wall surface and $\boldsymbol{e}_r$ denotes the radial coordinate vector. The model (2.19) can be extended by adding a viscoelastic term. The structural model including viscoelastic nature of biological material is called the **generalized (vibrating) string model**. It reads

$$\frac{\partial^2 \eta}{\partial t} - a\frac{\partial^2 \eta}{\partial z^2} + b\eta - c\frac{\partial^3 \eta}{\partial t \partial z^2} = H_2, \tag{2.20}$$

where c is a positive constant. The derivation of the model (2.20) can be found in [89]. Let us point out here, that the model (2.20) is valid only for $R_0 = \text{const}$. For our applications, in particular considering stenotic vessels, the model (2.20) needs to be extended also for the case $R_0 \neq \text{const}$. In what follows we present the derivation of the generalized string model for a stenotic compliant vessel, cf. also in [60].

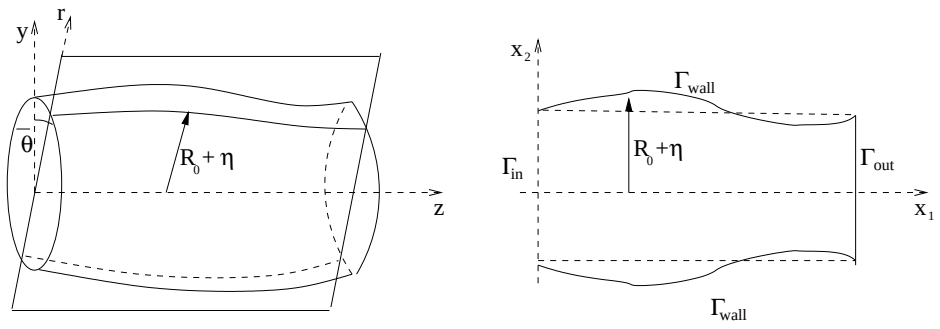

Figure 2.2: 2D domain geometry and 1D compliant wall obtained by intersecting the cylindrical tube with the plane $\theta = \bar{\theta}$. Without loss of generality, we assume here that $R_0 = \text{const}$.

All assumptions used in the derivation of the generalized string model for non-constant reference radius can be summarized in the following list:

(A1) *Cylindrical geometry without branching.*

(A2) *Homogeneous material.*

(A3) *"Small" displacements*, i.e. the wall displacement function $\eta = (\eta_r, \eta_\theta, \eta_z)$ corresponding to the cylindrical coordinates (r, θ, z) is small.

(A4) *"Small" deformation gradient with respect to the direction z and the angle θ*, i.e. $\partial\eta/\partial z$ and $\partial\eta/\partial\theta$ are small. This assumption together with (A2) and (A3) allow us to consider only linear elasticity.

(A5) *"Small" thickness of the wall h_s*, i.e. reduction from 3D shell models to 2D shell models and consequently from $\eta = (\eta_r, \eta_\theta, \eta_z)$ to $\eta = (\eta_r, \eta_z)$. Hence, the geometry can be approximated by a surface by introducing the function $R(z, t)$, which provides at each time instant radial coordinate of the wall surface.

(A6) *The surface stresses, i.e. the longitudinal stress σ_z and the circumferential stress σ_θ, are directed along the normal to the longitudinal $z = \text{const}$ and transversal $\theta = \text{const}$ cross sections, respectively*, i.e. together with (A2) it gives $\partial\sigma_\theta/\partial r = 0$.

(A7) *The circumferential stress $|\sigma_\theta|$ is constant along the θ-direction*, i.e. $\partial\sigma_\theta/\partial\theta = 0$. This assumption together with (A6) helps to reduce the model from the shell to a membrane model.

(A8) *Wall displacement only in the radial direction*, i.e. the axial symmetry in assumed and $\eta = (0, \eta_r)$. For simplification, we denote the wall displacement in the radial direction by $\eta := \eta_r$. However, we will have in mind that η stays for unknown radial displacement.

In what follows let us denote the longitudinal coordinate z by x_1 and the radial coordinate r by x_2, see Fig. 2.2, right. Structural model is derived from the balance of internal and external forces, the Newton law of motion and linear elasticity (see assumptions (A2)-(A4)). Let us consider for instance a three-dimensional radially symmetric tube (see Fig. 2.2, left) with deformations only in the radial direction. Thus, the wall displacement is constant with respect to the angle θ. Hence, the unknown wall displacement function $\eta(x_1, t)$ is at each time step defined as difference between the actual radius $R(x_1, t)$ and the reference one $R_0(x_1)$, i.e.

$$\eta(x_1, t) \;:=\; R(x_1, t) - R_0(x_1), \quad \text{for} \quad x_1 \in [0, L],\ t \in [0, T].$$

Let us now derive briefly the balance of forces on the infinitesimal surface element

$$d\sigma \;:=\; dc\ dl \in [0, 2\pi\ R) \times \Gamma_{wall}(t),$$

where $dc := Rd\theta$ with $\theta \in [0, 2\pi)$ is the arc length, $dl \in \Gamma_{wall}$ is the length of element along x_1-direction and $\Gamma_{wall}(t)$ is defined by

$$\Gamma_{wall}(t) := \left\{(x_1, x_2) \in \mathbb{R}^2,\ t \in [0,T] :\ 0 < x_1 < L,\ x_2 = \eta(x_1, t) + R_0(x_1)\right\}.$$

The second Newton law implies that the force applied on $d\sigma$ is equal to the time rate of change of its linear momentum, i.e.

$$\mathbf{F}_{mass} = \text{mass} \times \frac{\partial^2 R}{\partial t^2}, \quad \text{where} \quad \text{mass} := \rho_s h_s\ dcdl, \tag{2.21}$$

Note that $\partial^2 R/\partial t^2 = \partial^2 \eta/\partial t^2$. Clearly, $\mathbf{F}_{mass}$ is balanced with internal forces $\mathbf{F}_{int}$ and the external forces $\mathbf{F}_{ext}$, i.e.

$$\mathbf{F}_{mass} = \mathbf{F}_{int} + \mathbf{F}_{ext}. \tag{2.22}$$

The external forces applied on $d\sigma$ from the fluid are represented by the Cauchy stress tensor and external pressure forces, i.e.

$$\mathbf{F}_{ext} = (-P_{ext}\mathbf{I} - \mathbf{T}) \cdot \boldsymbol{n} \cdot \boldsymbol{e}_r\ Rd\theta dl + \mathcal{O}(d\theta dl). \tag{2.23}$$

Here $\boldsymbol{n}$ is the outward unit normal vector on $d\sigma$ defined by

$$\boldsymbol{n} = \left(-\frac{\partial R}{\partial x_1}, 1\right)^T \left[1 + \left(\frac{\partial R}{\partial x_1}\right)^2\right]^{-1/2} \tag{2.24}$$

and $\boldsymbol{e}_r = (0,1)^T$. The internal forces are caused by the circumferential and longitudinal stress σ_θ and σ_{x_1}, respectively. These are applied inside of internal tissue in normal direction. Taking into account the assumptions (A4), (A6)-(A7), we can write

$$\begin{aligned}
\mathbf{F}_{int} &= (\mathbf{F}_{\sigma_\theta} + \mathbf{F}_{\sigma_{x_1}}) \cdot \boldsymbol{e}_r \\
&= \left\{ -\frac{Eh_s\eta}{(1-\tilde{\xi}^2)R_0 R} + |\sigma_{x_1}| h_s \frac{\partial^2 R}{\partial x_1^2} \left[1 + \left(\frac{\partial R_0}{\partial x_1}\right)^2\right]^{-3/2} \boldsymbol{n} \cdot \boldsymbol{e}_r \right\} Rd\theta dl \\
&\quad + \mathcal{O}(d\theta dl),
\end{aligned} \tag{2.25}$$

where E denotes the Young modulus of elasticity, $|\sigma_{x_1}| = G\kappa$ is the longitudinal stress, $G = E/(2(1+\tilde{\xi}))$ denotes the shear modulus, $\tilde{\xi}$ is the Poisson ratio and κ is the Timoshenko shear correction factor.

By approximating $\boldsymbol{n} \cdot \boldsymbol{e}_r \approx [1 + (\partial_{x_1} R_0)^2]^{-1/2}$ and $\eta/R \approx \eta/R_0$ for $|\eta| < |R_0|$ we can rewrite (2.25) as

$$\mathbf{F}_{int} = \left\{ -\frac{Eh_s\eta}{(1-\tilde{\xi}^2)R_0^2} + |\sigma_{x_1}| h_s\ \frac{\partial^2 R}{\partial x_1^2} \left[1 + \left(\frac{\partial R_0}{\partial x_1}\right)^2\right]^{-2} \right\} Rd\theta dl + \mathcal{O}(d\theta dl). \tag{2.26}$$

Altogether, inserting (2.21),(2.23) and (2.26) into (2.22) we obtain

$$\begin{aligned}
\Bigg\{ \rho_s h_s\ \frac{\partial^2 \eta}{\partial t^2} + \frac{Eh_s\eta}{(1-\tilde{\xi}^2)R_0^2} - |\sigma_{x_1}| h_s\ \frac{\partial^2 R}{\partial x_1^2} \left[1 + \left(\frac{\partial R_0}{\partial x_1}\right)^2\right]^{-2} \\
+ \Big((P_{ext}\mathbf{I} + \mathbf{T})\boldsymbol{n}\Big) \cdot \boldsymbol{e}_r \Bigg\} Rd\theta dl = \mathcal{O}(d\theta dl).
\end{aligned} \tag{2.27}$$

Adding a damping viscoelastic term $-\gamma \dfrac{\partial^3 \eta}{\partial t \partial x_1^2}$, where γ is a viscoelastic constant and passing the measure of infinitesimal surface element $d\sigma$ to zero, i.e. $d\theta \to 0$ and $dl \to 0$, we obtain the so-called **generalized string model for non-constant reference radius**

$$\frac{\partial^2 \eta}{\partial t^2} - a\frac{\partial^2(\eta + R_0)}{\partial x_1^2} + b\eta - c\frac{\partial^3 \eta}{\partial t \partial x_1^2} = H(\boldsymbol{u}, p) \quad \text{on} \quad [0, 2\pi R) \times \Gamma_{wall}, \tag{2.28}$$

where $H(\boldsymbol{u},p)$ represents the forces exhibited by the normal fluid stress acting on the elastic vessel wall

$$H(\boldsymbol{u},p) = -\frac{\Big((\mathbf{T}+P_{ext}\ \mathbf{I})\boldsymbol{n}\Big)\cdot \boldsymbol{e}_r}{\rho_s h_s} \tag{2.29}$$

and a,b,c are the structure parameters defined by

$$a = \frac{|\sigma_{x_1}|}{\rho_s}\left[1+\left(\frac{\partial R_0}{\partial x_1}\right)^2\right]^{-2}, \quad b = \frac{E}{\rho_s(1-\tilde{\xi}^2)R_0^2}, \quad c = \frac{\gamma}{\rho_s h_s}. \tag{2.30}$$

Let us point out that the unknown wall displacement represents the movement of structure with respect to the reference configuration, i.e. the wall motion is referred to a material domain $[0,2\pi R_0)\times\Gamma^0_{wall}$. Therefore, in what follows, we transform the right hand side of the structure equation (2.28) from the Eulerian frame into the Lagrangian frame. To this end let us rewrite the balance of forces (2.28) for an element $d\sigma_0 := R_0 d\theta dl_0$, $(\theta, dl_0)\in(0,2\pi]\times\Gamma^0_{wall}$, where Γ^0_{wall} denotes the boundary of radially symmetric reference domain Ω_0, i.e.

$$\Gamma^0_{wall} \ := \ \big\{(x_1,x_2)\in\ \mathbb{R}^2:\ 0<x_1<L,\ x_2=R_0(x_1)\big\}\ .$$

Due to the incompressibility is the volume of an element, on which internal and mass forces are applied, the same in both, the reference configuration and the current configuration. This allows us to write

$$h_s d\sigma = h_0 d\sigma_0 \quad \text{for} \quad \mathbf{F}_{int},\ \mathbf{F}_{mass}, \tag{2.31}$$

where h_0 is the wall thickness at the time instant t_0. An element area $d\sigma\in[0,2\pi R)\times\Gamma_{wall}$ on which external forces are applied can be transformed directly on $d\sigma_0\in[0,2\pi R_0)\times\Gamma^0_{wall}$ in the following way

$$d\sigma = \frac{R}{R_0}\left[1+\left(\frac{\partial R}{\partial x_1}\right)^2\right]^{1/2}\left[1+\left(\frac{\partial R_0}{\partial x_1}\right)^2\right]^{-1/2} d\sigma_0 \quad \text{for} \quad \mathbf{F}_{ext}.$$

The factor

$$\tilde{g} := \left[1+\left(\frac{\partial R}{\partial x_1}\right)^2\right]^{1/2}\left[1+\left(\frac{\partial R_0}{\partial x_1}\right)^2\right]^{-1/2} \tag{2.32}$$

corresponds to the Jacobian of transformation between the Eulerian framework ($dl\in\Gamma_{wall}$) used for the description of fluid and the Lagrangian framework ($dl_0\in\Gamma^0_{wall}$) used for the structure. Assuming that $h_0\approx h_s$, then the transformation of forces from $[0,2\pi R)\times\Gamma_{wall}$ to $[0,2\pi R_0)\times\Gamma^0_{wall}$ reads as follows

$$\left\{\rho_s h_s\frac{\partial^2\eta}{\partial t^2}+\frac{Eh_s\eta}{(1-\tilde{\xi}^2)R_0^2}-|\sigma_{x_1}|h_s\left[1+\left(\frac{\partial R_0}{\partial x_1}\right)^2\right]^{-2}-\gamma\frac{\partial^3\eta}{\partial t\partial x_1^2}\right.$$
$$\left.+\ \Big((P_{ext}\mathbf{I}+\mathbf{T})\boldsymbol{n}\Big)\Big|_{\Gamma^0_{wall}}\cdot\boldsymbol{e}_r\tilde{g}\frac{R}{R_0}\right\}R_0 d\theta dl_0 = \mathcal{O}(d\theta dl_0). \tag{2.33}$$

For $d\sigma_0\to 0$ we obtain from (2.33) the **generalized string model for non-constant reference radius** expressed in the coordinates for the reference surface, i.e.

$$\frac{\partial^2\eta}{\partial t^2}-a\frac{\partial^2(\eta+R_0)}{\partial x_1^2}+b\eta-c\frac{\partial^3\eta}{\partial t\partial x_1^2} = H(\boldsymbol{u},p) \quad \text{on} \quad [0,2\pi R_0)\times\Gamma^0_{wall}, \tag{2.34}$$

where $H(\boldsymbol{u},p)$ represents the forces exhibited by the normal fluid stress acting on the elastic vessel wall transformed to the reference surface

$$H(\boldsymbol{u},p) = -\frac{\Big((\mathbf{T}+P_{ext}\ \mathbf{I})\boldsymbol{n}\Big)\Big|_{\Gamma^0_{wall}}\cdot\boldsymbol{e}_r}{\rho_s h_s}\frac{R}{R_0}\frac{\sqrt{1+(\partial_{x_1}R)^2}}{\sqrt{1+(\partial_{x_1}R_0)^2}}, \quad R=R_0+\eta. \tag{2.35}$$

From (2.34) we see that the fluid stresses provide the forcing term for the structure movement, whereas the structure gives a boundary condition for the fluid problem.

In what follows we consider a two-dimensional fluid domain

$$\Omega_t := \left\{(x_1, x_2) \in \mathbb{R}^2, t \in I : \ 0 < x_1 < L, \ 0 < x_2 < R_0(x_1) + \eta(x_1, t)\right\}$$

with a given reference radius $R_0(x_1)$ and unknown wall displacement function $\eta(x_1, t)$. We assume that the upper boundary Γ_{wall} is deformable and the lower one Γ_{sym} is the axis of symmetry, cf. Fig. 4.1.

We point out that for realistic hemodynamic simulations fully three-dimensional vascular flow should be considered. However, the main aim of this paper is to analyse theoretically as well as experimentally recent loosely coupled kinematic splitting technique and apply it to fully nonlinear coupling between the non-Newtonian shear-dependent fluid and a linear structure. Thus, for simplicity of presentation and in order to point out clearly the conceptual difficulties appearing in hemodynamic flows we will consider a simplified structural model (2.34), which has been derived for axially symmetric configurations.

Remark 2.3 (Well-posedness of NSE in moving domains) *The question of existence and uniqueness discussed in Remark 2.1 will be now extended to the case of moving domains. We assume that the movement of a domain is caused by an elastic or viscoelastic structure and leads to a fluid-structure interaction problem. Due to the structure movement is the analysis much more complicated and results depend on a concrete functional settings for both, the fluid and structure, and the initial geometry of the domain. Considering flow of a viscous incompressible fluid, which interacts with a thin viscoelastic structure, the global existence in time of a weak solution was proved assuming the following restrictions: the structure is typically regularized by the higher order terms (e.g.* $\frac{\partial^5 \eta}{\partial t \partial x_1^4}$*) and either initial data approach equilibrium or the structure is not allowed to touch the rigid bottom, see works of Guidorzi et al., Chambolle et al., Grandmont [49, 23, 39]. The local existence of strong solution in two dimensions was proved by Beirao da Veiga [11]. He assumes one-dimensional generalized string model for the structure. We mention also the work of Cheng and Shkoller [24], where the existence and uniqueness of regular solutions in three dimensions was studied. Here, a Koiter shell model without the inertial term was considered.*

Chapter 3

Non-Newtonian rheology

In order to close the system of governing equations (2.11a)-(2.11b) we need to select a constitutive model, which characterizes material properties of a particular fluid. The choice of a suitable constitutive equation should cover the most important features of the fluid we are particularly interested in. The models presented in this chapter are derived from the continuous mechanical theory, see, e.g. [82, 103]. We begin with explanation of the notions of the Newtonian and non-Newtonian fluid. Then we focus on blood as a non-Newtonian fluid, see, e.g. [45]. Finally, several significant constitutive models relevant for blood flow modelling, i.e. the Carreau model and the Yeleswarapu model, will be introduced.

3.1 Newtonian versus non-Newtonian material

We start this section with definitions of some important physical quantities describing the flow of viscous materials, namely viscosity, shear stress and shear rate. *Viscosity* is a material property that expresses a fluid's internal resistance to flow. It can be measured for example between two parallel plates, one of which moves relative to the other (see Fig. 3.1).

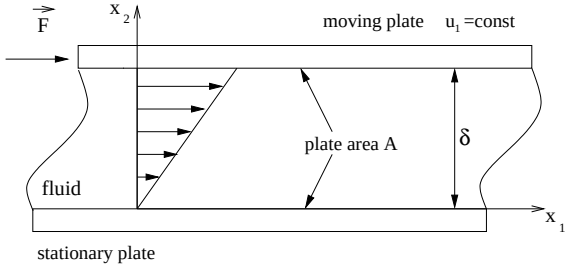

Figure 3.1: Couette flow experiment.

The *shear stress*, in the case of planar Couette flow, is defined as the ratio of tangential force F needed to keep the plate moving at a constant velocity u_1 to the plate area A. The *shear rate* denotes velocity gradient in direction perpendicular to the layers. Again, in the case of Couette flow it is the ratio of horizontal velocity component u_1 and distance δ between the plates. Then viscosity (also called shear viscosity or simplified viscosity) can be defined by

$$\mu \ := \ \frac{\text{shear stress}}{\text{shear rate}} = \frac{F/A}{u_1/\delta} \tag{3.1}$$

and it expresses the ratio between pressure exerted on the surface of a fluid (in the lateral or horizontal direction) to the velocity gradient. Depending on the change of shear rate versus shear stress inside a material the viscosity can be categorized by having linear or non-linear (e.g. plastic, dilatant) response. A material for which the shear stress is linearly proportional

to the shear rate is called the **Newtonian material**, see Fig. 3.2. In general, Newtonian materials obey the Newtonian criterion, which in one dimension reads as follows

$$S = \mu \frac{\partial u_1}{\partial x_2}. \tag{3.2}$$

Comparing relations (3.1) and (3.2) we see that S denotes the shear stress between the layers and $\partial u_1/\partial y$ expresses a differential form of shear rate. From (3.2) it is clear that the shear stress S expresses the T_{12} component of the Cauchy stress tensor (2.4).

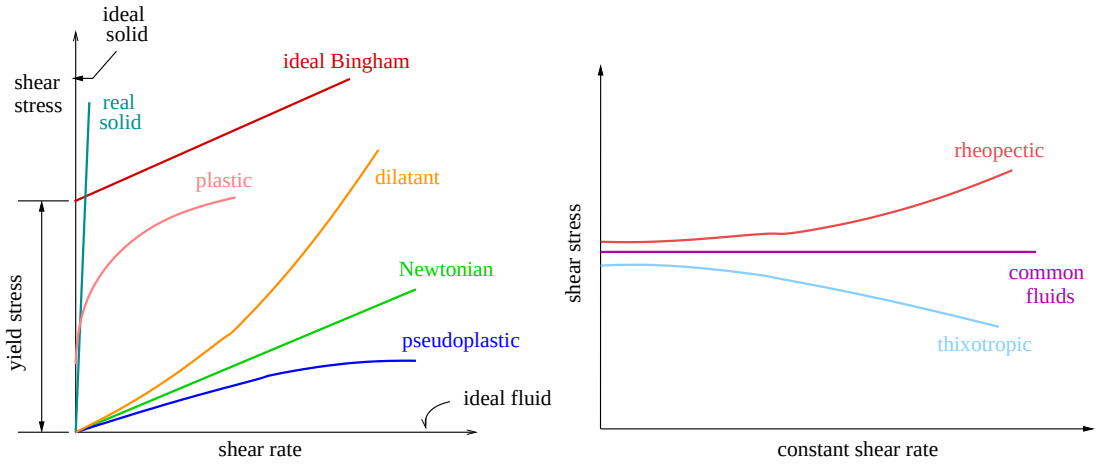

Figure 3.2: Shear rate versus shear stress for the Newtonian and some non-Newtonian fluids.

In the case, when material exhibits a non-linear response of the shear stress to the shear rate, i.e. it does not satisfy the Newtonian criterion (3.2), it is categorized as a **non-Newtonian material.** The non-Newtonian materials can have a complex relationship between the shear stress and the rate rate, see Fig.3.2. A brief overview of main types of non-Newtonian materials is presented in Tab. 3.1.

3.2 Blood as a non-Newtonian fluid

Blood is a suspension of red blood cells, white blood cells, platelets and other particles in plasma. The non-Newtonian rheology of blood is influenced the most by the red blood cells due to their deformability and their specific behaviour at low and at high shear rate. The low shear rate regions are characterized by red blood cells aggregation and formation of branched three-dimensional nanostructures. On the other hand, high shear rate areas force them to align with the flow field. Thanks to these characteristic features the blood is considered to be a shear thinning fluid with nonlinear viscoelastic behaviour. However, there are cases, when also the Newtonian viscosity is a good approximation of the viscosity model. Mainly, working with large and medium vessels, the simple Newtonian model is widely acceptable. However, considering small vessels or dealing with patients with a cardiovascular disease, this is no more the case and a more reasonable and precise model includes the non-Newtonian feature.

Working with the notion "viscosity", we need to point out that the terminology in the literature on blood rheology is not unified. The notion "viscosity" usually means material viscosity, which is a material property. However, for the purposes of concrete applications and studies, many others viscosities has been defined [45]. To the most common "viscosities" belong: shear viscosity, volume (bulk) viscosity, extensional viscosity, apparent viscosity, relative viscosity. Moreover, we would like to point out that experiments on blood at low shear rates are difficult to perform. In the case of absent yield stress, viscosity would tend

I. Power-Law Fluids		
shear thinning (pseudoplastic) fluids	the apparent viscosity decreases with an increase in shear rate	paints, some emulsions, milk, clay, cement, ...
shear thickening (dilatant) fluids	the apparent viscosity increases with an increase in shear rate	printing inks, clay slurries, starches, ...
II. Plastic materials		
perfectly plastic materials	strain does not result in opposing stress, pass after the yield point	ductile metals, ...
Bingham plastic materials	linear shear stress/shear rate relationship; require a finite yield stress before they begin to flow	toothpaste, slurry, mud, mayonnaise, ...
III. Viscoelastic fluids		
Maxwell materials	exhibit elastic and viscous properties	dough, silly putty, ...
Oldroyd-B fluids	linear combination of Maxwell and Newtonian behaviour	
Anelastic materials	return to its original shape on the removal of load	
Kelvin materials	a special case of the Maxwell fluid material	
IV. Fluids with time-dependent viscosity		
Rheopectic materials	time dependent dilatant behaviour; the apparent viscosity increases with duration of stress, i.e. shaking for a time brings solidification	gypsum paste, printers ink, body armour applications, footwear applications, ...
Thixotropic materials	time dependent pseudoplastic behaviour; the apparent viscosity decreases with duration of stress, i.e. shaking changes the stable form, at rest to the liquid form	drilling mud, some clay, ground substance, many paints, ...
IV. Fluids with the time- and pressure- dependent viscosity		
generalized Newtonian fluids	shear stress depends on the shear rate, it can also depend on the pressure applied on it	blood, custard, ...

Table 3.1: Examples of some non-Newtonian fluids.

to a finite value denoted by μ_0. The behaviour of viscosity for shear rates of the order of $1\,s^{-1}$ and larger is less controversial. As the shear rate increases above this range, viscosity steeply decreases until a plateau in viscosity is apparently reached. This plateau value is often called the asymptotic blood viscosity denoted by μ_∞. For the mathematical purposes the asymptotic viscosities μ_0 and μ_∞ are defined as follows

$$\mu_0 = \lim_{\dot{\gamma}\to 0} \mu(\dot{\gamma}), \quad \mu_\infty = \lim_{\dot{\gamma}\to \infty} \mu(\dot{\gamma}), \tag{3.3}$$

where $\dot{\gamma}$ denotes the shear rate. In practice, μ_0 is obtained from the experimental data and μ_∞ is only a mathematical construct. Alternatively, the value of μ_∞ can be obtained from measurements of plateau viscosity at sufficiently high shear rates. General constitutive models for blood viscosity include both mentioned constants. For normal red blood cells in

plasma, the majority of the drop in viscosity (approximately 95 %) occurs in the following low shear stress range $\dot{\gamma} \leq [0.01, 6]$ s^{-1}, where aggregation plays an important role.

In order to obtain a constitutive model that is physically reasonable some requirements have to be set up. Here, we consider models arising from pure mechanical theory. We neglect the other effects, like, e.g. temperature variation. The restrictions on constitutive equation can be summarized in the following list of principles:

(P1) *Principle of coordinate invariance*, i.e. independence of the coordinate system used to describe the motion of the fluid.

(P2) *Principle of the stress determinism*, i.e. the stress of a fluid at the current time instant is determined only by the history of motion of the fluid and independent of the future behaviour of the fluid.

(P3) *Principle of local action*, i.e. the stress for a given particle in a fluid depends only on the motion inside a small neighbourhood of that particle, cf. [82].

(P4) *Principle of equipresence*, i.e. a quantity which appears as an independent variable in one constitutive equation should be present in all the others for the same material, cf. [103].

(P5) *Principle of material frame indifference*, i.e. the mechanical response of a fluid is considered to be unchanged under a superposed rigid body motion of a body (this holds in the case of the change in orientation and position of the fluid).

An important restriction arises also from the thermodynamics, which says that the total entropy of thermodynamical processes can never be negative. Neglecting thermal effects, it can be expressed as

$$\mathbf{T} : \mathbf{D} = 2\mu \mathrm{tr}(\mathbf{D}^2) \geq 0,$$

which implies that $\mu \geq 0$.

Arising from the principles (P1)-(P6) and using the nonlinear field theory in mechanics the following constitutive model can be derived

$$\mathbf{T} = -p\mathbf{I} + 2\mu(\dot{\gamma})\mathbf{D}. \tag{3.4}$$

Here $\dot{\gamma}$ is a positive metric of $\mathbf{D}$ called the **shear rate** that is in the two-dimensional case defined by

$$\dot{\gamma} := \sqrt{2\ \mathrm{tr}(\mathbf{D}^2)} = \sqrt{2\ \mathbf{D} : \mathbf{D}} = \sqrt{-4\mathrm{II}_\mathrm{D}}, \tag{3.5}$$

where II_D denotes the second principal invariant of the rate of deformation tensor $\mathbf{D}$, cf. [14, 15, 45, 105]. The formula (3.4) describes the stress tensor of generalized Newtonian fluids, see [82, 103]. Models of the type (3.4) differ only in the choice of a suitable viscosity function $\mu(\dot{\gamma})$.

In the following sections we focus of the choice of viscosity function $\mu(\dot{\gamma})$. In particular, we look more precisely on viscosity functions suitable for shear thinning and viscoelastic fluids. Other models, like, e.g. the yield stress models, which are also relevant for modelling the non-Newtonian behaviour of blood, will be omitted in our analysis.

3.2.1 Shear thinning models for blood viscosity

The shear thinning nature of normal blood plays a minor role in majority of the arterial circulation and it is incorrect to use strongly shear thinning viscosity models to study the circulatory system in healthy patients. For this reason blood viscosity is often approximated to be constant. On the other side, shear thinning may be important in a stable vortex downstream of a stenosis, in a stable vortex inside a saccular aneurysm or in some anastomoses of the cerebral vasculature. And as it was mentioned already before, shear thinning behaviour

of viscosity plays a significant role in the circulatory system of the patients with pathological conditions that increases the strength of red blood cells to aggregates.

There are several important time intervals for human blood, which can help to identify the aggregate formation, the aggregate disaggregation and the recovery time for red blood cells deformation. Schmid-Schönbein et al. [96] found the half-time for aggregate formation in blood to be $3 - 5\,\mathrm{s}$ for normal blood and $0.2 - 1.5\,\mathrm{s}$ for pathological blood samples. Disaggregation is expected to be much more rapid and the half-time for a mechanically deformed red blood cells to relax to half its initial stretch is estimated to be on the order of $0.06\,\mathrm{s}$.

The statistically most significant variable for shear thinning models is the shear rate. However, blood viscosity is sensitive also to other factors besides shear rate, e.g. the hematocrit, temperature. For example, under the temperature drop of 15 °C, e.g. from body temperature to room temperature, the blood viscosity can increase in 66% [45]. The variation in plasma viscosity and its composition on blood viscosity is observed even in the healthy population and escalates by some diseases. In what follows we present some one-variable models, where shear-rate plays the crucial role.

The simplest one-variable model frequently used for blood viscosity is called the **power-law model**

$$\mu(\dot{\gamma}) = K\dot{\gamma}^{(n-1)}, \tag{3.6}$$

where n and K is the power-law index and consistency coefficient, respectively.

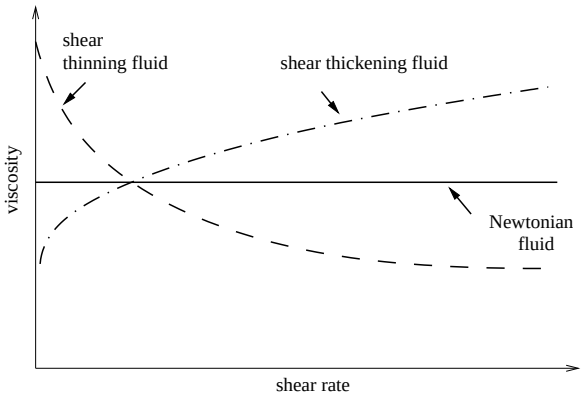

Figure 3.3: Viscosity versus shear rate for power-law fluids which are shear thinning (dash line), shear thickening (dash-dot line) or have constant viscosity (solid line).

For $n = 1$ the power-law model describes the flow of a Newtonian fluid. In the case of $n < 1$ we have the **shear thinning** power-law model, while for $n > 1$ the model is **shear thickening**, both cases are shown in Fig. 3.3. The shear thinning power-law model is often used to describe the viscous behaviour of blood, even though it predicts zero viscosity as the shear rate tends to infinity and an unbounded viscosity at zero shear rate. The diminishing viscosity with increasing shear rate is the most well-studied non-Newtonian characteristic of blood.

Most of the models of power-law type contains viscosity function of the form

$$\mu(\dot{\gamma}) = \mu_\infty + (\mu_0 - \mu_\infty) f(\dot{\gamma}), \tag{3.7}$$

where the asymptotic viscosities $\mu_\infty,\ \mu_0$ are considered to have finite values and $f(\dot{\gamma})$ is a suitable polynomial function. The viscosity function for the **Carreau-Yasuda model** can be written as

$$\mu(\dot{\gamma}) = \mu_\infty + (\mu_0 - \mu_\infty)\left[1 + (\lambda\dot{\gamma})^a\right]^{\frac{n-1}{a}}, \tag{3.8}$$

where $n < 1$ for a shear thinning fluid. In the zero-shear-rate region (when values of $(\lambda\dot{\gamma})^a$ are small), the viscosity tends to a plateau constant μ_0 and exhibits a Newtonian behaviour. On the other hand, in the power-law region (for large values of $(\lambda\dot{\gamma})^a$), power-law-type model with non-zero μ_∞ is obtained. This is the reason why the constant n from (3.6) is called the "power-law exponent". The parameter a denotes the size of transition region between the zero-shear rate and power-law regions. The equation (3.8) was firstly proposed (for $a = 2$) by Pierre Carreau and the fluids with such a viscosity function

$$\mu(\dot{\gamma}) = \mu_\infty + (\mu_0 - \mu_\infty)\left[1 + (\lambda\dot{\gamma})^2\right]^{\frac{n-1}{2}} \tag{3.9}$$

are often called the **Carreau fluids**. In Tab. 3.2 several shear thinning models as special cases of the Carreau-Yasuda model with an appropriate viscosity function $f(\dot{\gamma})$ are presented. The values of the parameters μ_0 and μ_∞ are usually obtained from the least square analysis of measured data.

Shear thinning model	viscosity function $f(\dot{\gamma})$	material constants
Carreau-Yasuda	$[1 + (\lambda\dot{\gamma})^a]^{\frac{n-1}{a}}$	$\mu_0 = 65.7\,\text{mPa.s}$ $\mu_\infty = 4.47\,\text{mPa.s}$, $\lambda = 10.4\,\text{s},\ n = 0.34,\ a = 1.76$
Carreau (a=2)	$[1 + (\lambda\dot{\gamma})^2]^{\frac{n-1}{2}}$	$\mu_0 = 63.9\,\text{mPa.s}$ $\mu_\infty = 4.45\,\text{mPa.s}$, $\lambda = 10.3\,\text{s},\ n = 0.35$
Cross (a=n-1)	$[1 + (\lambda\dot{\gamma})^m]^{-1}$	$\mu_0 = 87.5\,\text{mPa.s}$ $\mu_\infty = 4.70\,\text{mPa.s}$, $\lambda = 8.00\,\text{s},\ m = 0.801$
Simplified Cross (a=1, n=0)	$(1 + \lambda\dot{\gamma})^{-1}$	$\mu_0 = 73.0\,\text{mPa.s}$ $\mu_\infty = 5.18\,\text{mPa.s}$, $\lambda = 4.84\,\text{s}$

Table 3.2: Some of the representative generalized Newtonian models for blood viscosity with corresponding material constants. Data are obtained from the blood of a 25 year old female donor with Ht=40%, $T = 23$ °C, cf. [45].

3.2.2 Viscoelastic models for blood viscosity

Viscoelastic materials exhibit both, elastic properties of solids and viscous properties of fluids. In response to a small, rapidly applied and removed strain, they may deform and then return to their original shape. A special feature is the ability to store and release energy. In the case of blood this behaviour is provided by three-dimensional branched aggregates of red blood cells.

Before introducing the viscoelastic models for blood we firstly turn our attention on the so-called simple fluids (or generally called simple materials). The main reason to do so is that viscoelastic models are special cases of incompressible simple fluids constitutive models. The notion simple material, originally developed by Noll, cf. [82], denotes a body in which the stresses for a material element depend on the cumulative history of the deformation gradient of this element. An important class of simple fluids are simple fluids with fading memory. This is connected with the fact that they have ability to partly forget their initial state. The characteristic time for this memory effect is denoted by α. For a purely elastic material $\alpha = 1$ (the material never forgets its initial shape). Otherwise for a purely viscous material

the characteristic time is $\alpha = 0$. Linear viscoelastic fluids are special case of incompressible simple fluids with fading memory, where α coefficient is from the range: $0 < \alpha < 1$.

Reference configuration for viscoelastic fluids with fading memory is chosen to be a configuration at the current time instant t, denoted by κ_t. An arbitrary material point in the body is identified by its position $\boldsymbol{x}$ in κ_t. The position of the same material points at the time instant $\tilde{t}$ prior to time t, i.e. $\tilde{t} \leq t$, will be denoted by $\tilde{\boldsymbol{x}}$ and expressed as $\tilde{\boldsymbol{x}} = \chi_t(\boldsymbol{x}, \tilde{t})$, for $\tilde{t} \in (-\infty, 0]$. Let $\mathbf{G}_t$ denote the Cauchy strain tensor defined in terms of the relative deformation gradient $\mathbf{F}_t$ and the right relative Cauchy-Green tensor $\mathbf{C}_t$ by

$$\mathbf{G}_t = \mathbf{C}_t - \mathbf{I}, \quad \text{where} \quad \mathbf{C}_t = \mathbf{F}_t^T . \mathbf{F}_t. \tag{3.10}$$

The strain measure $\mathbf{G}_t$ is defined so that it is equal to zero at the current time instant t.

Then the constitutive equation for a **simple material** is defined by

$$\mathbf{T} = \mathfrak{H}_{s=0}^{\infty}[\mathbf{F}_t(s); \rho], \tag{3.11}$$

where $\mathfrak{H}_{s=0}^{\infty}[.]$ denotes a second-order tensor-valued functional of the history of a relative deformation gradient and $s = t - \tilde{t}$ is the converted time scale. In the following we will call the function $\mathbf{G}_t(s)$, defined for $s \geq 0$ with values which are symmetric tensors, a history. Restricting our attention to the finite and infinitesimal linear viscoelasticity we assume that the strain relative to the rest history is small, cf. [82]. Using the first-order approximation for incompressible, simple fluids with fading memory we can rewrite the Cauchy stress tensor (3.11) into the form

$$\mathbf{T} = -p\mathbf{I} - \int_0^{\infty} m(s)\mathbf{G}_t(s)ds \quad \text{with} \quad \|\mathbf{G}_t(s)\| \to 0. \tag{3.12}$$

The norm $\|\cdot\|$ is $\mathcal{L}_{h(s),p}-$ norm of the Banach space $\mathcal{L}$ proposed by Coleman and Noll [28] and used to measure the distance of a given history $\mathbf{G}_t(s)$ from the so-called rest history $\mathbf{G}_t = 0$. It is characterized by a real constant p, $1 \leq p \leq \infty$ and an the so-called influence function $h(s)$ and it is defined by

$$\begin{aligned} \|\mathbf{G}_t(s)\|_{h(s),p} &= \sqrt[p]{\textstyle\int_0^{\infty} h(s)\,|\mathbf{G}_t(s)|^p\,ds} \qquad \text{if} \quad 1 \leq p < \infty, \\ \|\mathbf{G}_t(s)\|_{h(s),\infty} &= \sup_{s \geq 0} \left\{ h(s)\,|\mathbf{G}_t(s)| \right\} \qquad \text{if} \quad p = \infty. \end{aligned}$$

The function $m(s)$ from (3.12) denotes the memory function satisfying the following assumptions

$$\lim_{s \to \infty} m(s) = 0 \quad \text{and} \quad \int_0^{\infty} \frac{|m(s)|^2}{h^2(s)} ds < \infty.$$

Memory function $m(s)$ can be associated with the so-called relaxation function $\mathcal{G}(s)$ through the relation

$$\mathcal{G}(s) = \int_s^{\infty} m(u)du.$$

An example of the relaxation modulus is the modulus of Maxwell type $\mathcal{G}(s) = \mathcal{G}_0 e^{-s/\alpha}$. Constitutive equation (3.12) is an example of the viscoelastic **model of integral type**. If the extra stress tensor can be written as an explicit function of an appropriate strain measure $\mathbf{G}_t$ (and the finite number of its time derivatives), the model is classified to be of the **differential type**. Rate-type constitutive models are the most often used ones. They contain one or more derivatives of the extra stress tensor. An example is the class of the **quasi-linear rate-type viscoelastic models** called the Maxwell models. They have extra stress tensor of the form

$$\mathbf{S} + \alpha \frac{\mathcal{D}\mathbf{S}}{\mathcal{D}t} = 2\mu\mathbf{D}, \tag{3.13}$$

Viscoelastic model	rate-type form of the model
Johnson-Segalman model	$\mathbf{S} + \alpha \overset{\square}{\mathbf{S}} = 2(\mu_1 + \mu_2)\left(\mathbf{D} + \frac{\alpha\mu_2}{\mu_1+\mu_2} \overset{\square}{\mathbf{D}}\right)$
Lower convected Maxwell $(\zeta = 2, \mu_2 = 0)$	$\mathbf{S} + \alpha \overset{\triangle}{\mathbf{S}} = 2\mu\mathbf{D}$ or $\mathbf{S} = \int_0^\infty \frac{\mu}{\alpha^2} \mathrm{e}^{-s/\lambda}(\mathbf{I} - \mathbf{C}_t)\mathrm{d}s$
Upper convected Maxwell $(\zeta = 0, \mu_2 = 0)$	$\mathbf{S} + \alpha \overset{\triangledown}{\mathbf{S}} = 2\mu\mathbf{D}$ or $\mathbf{S} = \int_0^\infty \frac{\mu}{\alpha^2} \mathrm{e}^{-s/\lambda}(\mathbf{C}_t^{-1} - \mathbf{I})\mathrm{d}s$
Oldroyd-A $(\zeta = 2)$	$\mathbf{S} + \alpha \overset{\triangle}{\mathbf{S}} = 2(\mu_1 + \mu_2)\left(\mathbf{D} + \frac{\alpha\mu_2}{\mu_1+\mu_2} \overset{\triangle}{\mathbf{D}}\right)$
Oldroyd-B $(\zeta = 0)$	$\mathbf{S} + \alpha \overset{\triangledown}{\mathbf{S}} = 2(\mu_1 + \mu_2)\left(\mathbf{D} + \frac{\alpha\mu_2}{\mu_1+\mu_2} \overset{\triangledown}{\mathbf{D}}\right)$

Table 3.3: Examples of some viscoelastic models.

where the definition of operator $\dfrac{\mathcal{D}\mathbf{S}}{\mathcal{D}t}$ can be chosen from the following objective choices

$$\overset{\triangledown}{\mathbf{S}} = \frac{D\mathbf{S}}{Dt} - \mathbf{L}\cdot\mathbf{S} - \mathbf{S}\cdot\mathbf{L}^{\mathrm{T}}, \quad \text{i.e.} \quad \overset{\triangledown}{S}_{ij} = \frac{\partial S_{ij}}{\partial t} + \sum_{k=1}^{d}\left(v_k\frac{\partial S_{ij}}{\partial x_k} - \frac{\partial v_i}{\partial x_k}S_{kj} - S_{ik}\frac{\partial v_j}{\partial x_k}\right), \tag{3.14a}$$

$$\overset{\triangle}{\mathbf{S}} = \frac{D\mathbf{S}}{Dt} + \mathbf{S}\cdot\mathbf{L} + \mathbf{L}^{\mathrm{T}}\cdot\mathbf{S}, \quad \text{i.e.} \quad \overset{\triangle}{S}_{ij} = \frac{\partial S_{ij}}{\partial t} + \sum_{k=1}^{d}\left(v_k\frac{\partial S_{ij}}{\partial x_k} + S_{ik}\frac{\partial v_k}{\partial x_j} + \frac{\partial v_k}{\partial x_i}S_{kj}\right), \tag{3.14b}$$

$$\overset{\circ}{\mathbf{S}} = \frac{1}{2}(\overset{\triangledown}{\mathbf{S}} + \overset{\triangle}{\mathbf{S}}), \tag{3.14c}$$

where $L := \triangledown\boldsymbol{v}$ denotes the velocity gradient. Tensors $\overset{\triangledown}{\mathbf{S}}$, $\overset{\triangle}{\mathbf{S}}$ and $\overset{\circ}{\mathbf{S}}$ are called the upper convected derivative, the lower convected derivative and the co-rotational derivative, respectively. Any superposition of the operators (3.14a)- (3.14b) is also an objective operator and the resulting second-order tensor is symmetric. If we use the operator

$$\overset{\square}{\mathbf{S}} = \left(1 - \frac{\zeta}{2}\right)\overset{\triangledown}{\mathbf{S}} + \frac{\zeta}{2}\overset{\triangle}{\mathbf{S}} \quad \text{with} \quad \zeta = \text{const} \tag{3.15}$$

and express the extra stress tensor $\mathbf{S}$ as a sum of the viscous $\mathbf{S}^{(v)}$ and the constant elastic $\mathbf{S}^{(e)}$ part

$$\mathbf{S} = \mathbf{S}^{(v)} + \mathbf{S}^{(e)}, \quad \mathbf{S}^{(e)} + \alpha\overset{\square(e)}{\mathbf{S}} = 2\mu_1\mathbf{D}, \quad \mathbf{S}^{(v)} = 2\mu_2\mathbf{D}$$

we obtain from (3.13) the four-constant **Johnson-Segalman model**

$$\mathbf{S} + \alpha\overset{\square}{\mathbf{S}} = 2(\mu_1 + \mu_2)\left(\mathbf{D} + \frac{\alpha\mu_2}{\mu_1 + \mu_2}\overset{\square}{\mathbf{D}}\right). \tag{3.16}$$

In Tab. 3.3 several special cases of the Johnson-Segalman model are shown. It is common to rewrite the viscoelastic models using relaxation time function λ_1 and retardation time function λ_2 defined by

$$\lambda_1 := \alpha, \quad \lambda_2 := \frac{\alpha\mu_2}{\mu(\dot\gamma)}, \quad 0 \le \lambda_2 \le \lambda_1. \tag{3.17}$$

From (3.17) is it clear that λ_1 and λ_2 are functions of shear rate $\dot\gamma$. Adopting the notation (3.17) we obtain a commonly used form of the **Oldroyd-B model**, i.e.

$$\mathbf{S} + \lambda_1\overset{\triangledown}{\mathbf{S}} = 2\mu(\dot\gamma)\left(\mathbf{D} + \lambda_2\overset{\triangledown}{\mathbf{D}}\right),$$

see for example [106]. The lower and upper convected Maxwell model are two-constant models and the Oldroyd-A and the Oldroyd-B are three-constant models. An important type of viscoelastic constitutive models for blood is the **Yeleswarapu model**. It is a five-constant generalization of the Oldroyd-B model (see Tab. 3.3), where the constant viscosity $\mu = \mu_1 + \mu_2$ is replaced with a generalized Newtonian viscosity $\mu(\dot{\gamma})$ defined by

$$\mu(\dot{\gamma}) = \mu_\infty + (\mu_0 - \mu_\infty)\left[\frac{1 + \ln(1 + \Lambda\dot{\gamma})}{1 + \Lambda\dot{\gamma}}\right]. \tag{3.18}$$

Here Λ is a material constant. The last model presented here is a model employed by Deutsch and Phillips [29]. This model includes viscoelastic as well as shear thinning effects

$$\mathbf{S} + \lambda_1 \overset{\triangledown}{\mathbf{S}} + t_0(\mathrm{tr}\mathbf{S})\mathbf{D} = 2\mu_0(\mathbf{D} + \lambda_2 \overset{\triangledown}{\mathbf{D}}).$$

Here t_0 is a time constant and μ_0 denotes the zero shear rate viscosity.

In our study we consider that blood behaves like a shear thinning fluid. Here we do not take into account the viscoelasticity of blood. We will assume that the viscosity function $\mu(\dot{\gamma})$ is given by the Carreau model (3.9) or by the generalized Newtonian viscosity function appearing in the viscoelastic Yeleswarapu model (3.18). In our analysis the models for the viscosity function $\mu(\dot{\gamma})$ from (3.9) and (3.18) will be scaled accordingly to the work of Yeleswarapu, see [105, 106]. Moreover, to show the dependence of the viscosity function on the positive metric of the rate of the deformation tensor, we will write the Carreau model and the Yeleswarapu model as follows

$$\mu(|\mathbf{D}(\boldsymbol{u})|) = \mu_\infty + (\mu_0 - \mu_\infty)\left[1 + 2(\lambda|\mathbf{D}(\boldsymbol{u})|)^2\right]^{\frac{q-2}{2}} \tag{3.19}$$

and

$$\mu(|\mathbf{D}(\boldsymbol{u})|) = \mu_\infty + (\mu_0 - \mu_\infty)\left[\frac{1 + \ln(1 + \sqrt{2}\Lambda|\mathbf{D}(\boldsymbol{u})|)}{1 + \sqrt{2}\Lambda|\mathbf{D}(\boldsymbol{u})|}\right], \tag{3.20}$$

respectively. Here μ_∞ and μ_0 are the asymptotic values of viscosity, i.e.

$$\mu_\infty := \lim_{|\mathbf{D}(\boldsymbol{u})|\to\infty} \mu(|\mathbf{D}(\boldsymbol{u})|), \qquad \mu_0 := \lim_{|\mathbf{D}(\boldsymbol{u})|\to 0} \mu(|\mathbf{D}(\boldsymbol{u})|).$$

The parameters λ, Λ and q are given constants [105], see also Tab. 7.2 for typical physiological values used for blood and Fig. 3.4 for the corresponding graphs. From the definition (3.19) we see that for $q > 2$ viscosity increases with increasing shear rate ($\mu_0 < \mu_\infty$), while for $q < 2$ viscosity decreases with increasing shear rate ($\mu_0 > \mu_\infty$). The first situation describes the so-called shear thickening fluids and the second situation represents the so-called shear thinning fluids. If $q = 2$, then we obtain the simplest behaviour corresponding to Newtonian fluids. The Yeleswarapu model (3.20) describes only the shear thinning behaviour.

Remark 3.1 *Soulis et al. [97] studied the non-Newtonian behaviour of blood with respect to a cardiac cycle. They found the non-Newtonian rheology to be relevant for approximately* 30% *of one cardiac cycle. However, both models, the Newtonian as well as the non-Newtonian, predicted crucial areas with low wall shear stress at the same positions. Ardakani et al. [3] focused on viscosity blood models in modelling of blood flow in stenosed carotid bifurcations. They showed that the non-Newtonian effect is more visible dealing with ideal model geometries than with geometries obtained from real patients. Moreover, considering real geometries, difference between the Newtonian and the non-Newtonian constitutive blood model depends on the position in the vessel. Especially in a carotid bifurcation, differences are more visible in the sinus bulb area than in other parts of artery, see also Section 7.5.*

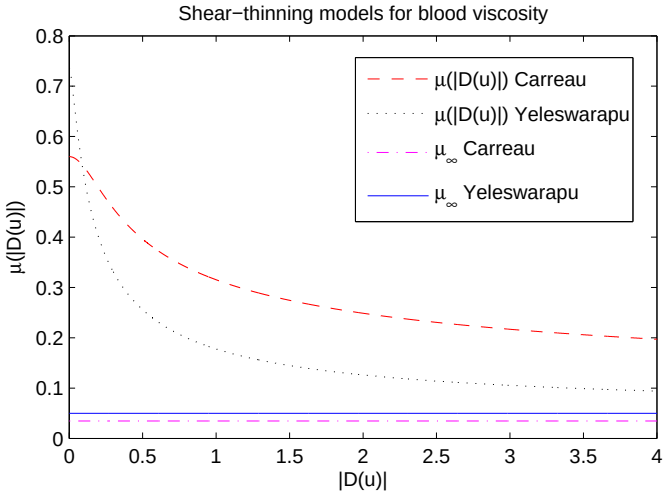

Figure 3.4: Viscosity function for non-Newtonian models (3.19) and (3.20) and asymptotic viscosities μ_∞ for (3.19) and (3.20) fit for the physiological data from Tab. 7.2.

Remark 3.2 (Well-posedness of the generalized NSE in rigid and moving domains) *Studying the flow of shear dependent fluids described by a power-law type model we distinguish between two basic groups: shear thinning fluids, i.e. $q \in (1,2)$, and shear thickening fluids, i.e. $q > 2$. The results on existence and uniqueness for both, rigid as well as moving domains, depend on the power-law exponent q. In our analysis we focus in particular on blood flow modelling with the power-law exponents $q = 1.6$ and $q = 1.356$, see Section 7. In what follows we briefly summarize main results on existence of shear thinning and shear thickening fluids.*

Considering no movement of domain, the following results have been obtained:

- **Two-dimensions:** *First results on existence of weak solution for shear-thickening fluids, i.e. $q \geq 2$, was proved in 1969 by Ladyzhenskaya [63] for both, the space-periodic as well as Dirichlet boundary problem. Concerning the spatially-periodic problem, the existence was extended also for the shear-thinning fluids. The largest interval for power-law constant q, i.e. $q > 1$, including also the shear thinning fluids, was obtained by Málek, Nečas, Rokyta, Růžička [73] for spatially-periodic boundary conditions. Assuming homogeneous Dirichlet boundary conditions Diening, Růžička and Wolf used in [31] the Lipschitz truncation method on the local pressure method to prove the existence of weak solution in $L^q(I; W^{1,q}(\Omega))$ for $q > \frac{2d}{d+2}$.*

  Summarizing the results on existence of strong solutions, i.e.

$$\boldsymbol{u} \in L^\infty(I; W^{2,\tilde{q}}(\Omega)) \cap L^2(I; V_q), \quad \text{where} \quad \tilde{q} := \min(2, q)$$

  and

$$V_q := \overline{V}^{\,||\cdot||_{L^q(\Omega)}} \quad \text{with} \quad V := \{\boldsymbol{v} |\ \boldsymbol{v} \in C_0^\infty(\Omega),\ \bigtriangledown \cdot \boldsymbol{v} = 0\},$$

  it has been shown the global existence for $q > 2$, i.e. for shear thickening fluids. Moreover, the local in time existence and global existence for small initial data were proved also for shear thinning fluids, i.e. $q > 1$, see e.g. [12, 73].

- **Three-dimensions:** *In 1969, Ladyzhenskaya [63] and Lions [70] showed existence for the certain shear thickening fluids with $q \geq \frac{3d+2}{d+2}$ assuming the Dirichlet boundary conditions, see also [64]. This result has been improved in [31] for $q > \frac{2d}{d+2}$, i.e. $q > \frac{3}{2}$. Assuming a spatially-periodic problem it was possible to extend the existence results to the case $q \geq \frac{2(d+1)}{d+2}$,i.e. $q \geq \frac{8}{5}$. This was done by Frehse, Málek and Steinhauer [44].*

The existence of strong solution was proved for some shear thickening fluid with $q > \frac{3d+2}{d+2}$ *which yields the following bound:* $q > \frac{11}{5}$*, see the work of Málek, Nečas and Růžička [74]. Similarly as in the two-dimensional case, this result can be extended assuming small initial data to* $q > \frac{3d-4}{d}$*, i.e.* $q > \frac{5}{3}$*, cf. Málek, Rajagopal and Růžička [75]. In [75] also local in time existence of a strong solution has been proved for* $q > \frac{3d-4}{d}$*.*

The situation is more complicated considering a fluid-structure interaction problem between a non-Newtonian (e.g. shear-dependent) fluid and a moving structure. The global existence of weak solution of fully unsteady fluid-structure interaction problem for shear thickening fluids, i.e. $q \geq 2$*, was shown by Hundertmark, Lukáčová and Nečasová [59].*

Chapter 4

Fluid-structure interaction problem

In this chapter we look more precisely on the fluid-structure interaction problem given by the generalized Navier-Stokes equations (2.11b)-(2.11a) and the generalized string model (2.34). Firstly, we present boundary, initial and coupling conditions. Then we give a general overview on numerical techniques proposed in literature. Here, we will be focused in particular on the kinematic splitting approach, which is used in our numerical study. Finally, the weak formulation of our fluid-structure interaction will be introduced.

4.1 Boundary, initial and coupling conditions

Let us assume two-dimensional domain Ω_t as it is depicted on Fig. 4.1. The boundary of Ω_t consists from one moving boundary Γ_{wall} (upper boundary), a symmetric boundary Γ_{sym} (lower boundary), inflow boundary Γ_{in} and outflow boundary Γ_{out}.

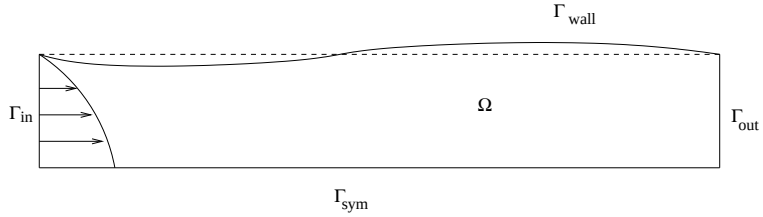

Figure 4.1: Computational domain geometry.

The coupled fluid-structure interaction problem

$$\rho_f \left[\frac{\mathcal{D}^{\mathcal{A}} \boldsymbol{u}}{\mathcal{D}t} + ((\boldsymbol{u} - \boldsymbol{w}) \cdot \bigtriangledown)\boldsymbol{u} \right] - \bigtriangledown \cdot \Big[2\mu(|\mathbf{D}(\boldsymbol{u})|)\, \mathbf{D}(\boldsymbol{u}) \Big] + \bigtriangledown\, p = \boldsymbol{f}, \quad \text{in} \quad \Omega_t, \tag{4.1a}$$

$$\bigtriangledown \cdot \boldsymbol{u} = 0, \quad \text{in} \quad \Omega_t,\ t \in I. \tag{4.1b}$$

$$\frac{\partial^2 \eta}{\partial t^2} - a \frac{\partial^2 (\eta + R_0)}{\partial x_1^2} + b\eta - c \frac{\partial^3 \eta}{\partial t \partial x_1^2} = H(\boldsymbol{u}, p) \quad \text{on} \quad \Gamma^0_{wall}\ , \tag{4.2}$$

where $\mu(|\mathbf{D}(\boldsymbol{u})|)$ is defined in (3.19) and

$$H(\boldsymbol{u}, p) = - \frac{\Big((\mathbf{T} + P_{ext}\ \mathbf{I})\boldsymbol{n} \Big)\Big|_{\Gamma^0_{wall}} \cdot \boldsymbol{e}_r}{\rho_s h_s} \frac{R}{R_0} \frac{\sqrt{1 + (\partial_{x_1} R)^2}}{\sqrt{1 + (\partial_{x_1} R_0)^2}}, \quad R = R_0 + \eta. \tag{4.3}$$

is equipped with the following initial conditions

$$\boldsymbol{u}(\cdot,t_0)=\boldsymbol{u}_0 \qquad \text{in} \quad \Omega_0 \tag{4.4}$$

$$\eta(\cdot,t_0)=0, \quad \frac{\partial\eta(\cdot,t_0)}{\partial t}=\boldsymbol{u}_0|_{\Gamma^0_{wall}}\cdot\boldsymbol{e}_r \qquad \text{on} \quad \Gamma^0_{wall}\ . \tag{4.5}$$

Boundary conditions read as follows

$$\left(\mathbf{T}(\boldsymbol{u},p)-\frac{\rho_f}{2}|\boldsymbol{u}|^2\mathbf{I}\right)\cdot\boldsymbol{n}=-(P_{in}\ \mathbf{I})\cdot\boldsymbol{n}, \qquad \text{on} \quad \Gamma_{in},\ t\in I, \tag{4.6}$$

$$\left(\mathbf{T}(\boldsymbol{u},p)-\frac{\rho_f}{2}|\boldsymbol{u}|^2\mathbf{I}\right)\cdot\boldsymbol{n}=-(P_{out}\ \mathbf{I})\cdot\boldsymbol{n}, \qquad \text{on} \quad \Gamma_{out},\ t\in I, \tag{4.7}$$

$$\frac{\partial u_1}{\partial x_2}=0, \quad u_2=0, \qquad \text{on} \quad \Gamma_{sym},\ t\in I, \tag{4.8}$$

$$\eta(0,t)=\eta_1, \quad \eta(L,t)=\eta_2, \qquad \text{for} \quad t\in I. \tag{4.9}$$

Conditions (4.6) and (4.7) are called the kinematic pressure conditions. They are a variant of the well-known "do nothing" boundary conditions in the case that the Bernoulli pressure $p+\rho_f|\boldsymbol{u}|^2/2$ is taken into account, cf. [45, 52, 58].

The fluid and the structure are coupled through the matching conditions. The **kinematic coupling condition** represented by

$$\boldsymbol{u}=\boldsymbol{w}:=\left(0,\frac{\partial\eta}{\partial t}\right)^T \quad \text{on} \quad \Gamma_{wall}(t) \tag{4.10}$$

describes the continuity of fluid and structure velocities on $\Gamma_{wall}(t)$. Moreover, the balance of forces and the continuity of fluid and structure stresses is provided by the **dynamic coupling condition**, which is given by the structure equation in the Lagrangian frame (4.2).

Remark 4.1 *Since the structure variables, i.e. the wall displacement η and wall velocity ξ, are at each time instant defined for the points $x_1\in[0,L]$, we will in what follows equivalently use the notation*

$$\int_0^L(\cdot)\ \mathrm{d}\gamma=\int_{\Gamma_{wall}}(\cdot)\ \mathrm{d}\gamma \quad \text{for} \quad t\in I, \quad \text{and} \quad \int_0^L(\cdot)\ \mathrm{d}\gamma=\int_{\Gamma^0_{wall}}(\cdot)\ \mathrm{d}\gamma \quad \text{for} \quad t=t_0,$$

where the integrand $(\cdot)$ contains structure variables. Moreover, in the functional space settings for η and ξ and their derivatives, we will use preferably the notation $(0,L)$ instead of Γ_{wall} and Γ^0_{wall}.

4.2 Weak formulation of the model

Before presenting the splitting algorithm and analyzing its stability and convergence let us write down the weak formulation of the model (4.1a)-(4.10). Let the test functions $\boldsymbol{v}$ and $\tilde{q}$ belong to the following spaces

$$V := \{\boldsymbol{v}|\ \boldsymbol{v}\in W^{1,q}(\Omega_t):\ v_1|_{\Gamma_{wall}}=0, v_2|_{\Gamma_{sym}}=0\}, \quad \text{a.e. } t\in I, \tag{4.11}$$

$$Q := L^2(\Omega_t)\ , \quad \text{a.e.} \quad t\in I, \tag{4.12}$$

respectively. Then we are looking for functions

$$\boldsymbol{u} \in V^F := L^q(I;V)\cap L^\infty(I;L^2(\Omega_t)), \tag{4.13}$$

$$\eta \in V^S := H^1(I;H^1_0(0,L))\cap W^{1,\infty}(I;L^2(0,L)), \tag{4.14}$$

such that for a.e. $t \in (0,T)$

$$\begin{aligned}
&\int_{\Omega_t} \frac{\mathcal{D}^{\mathcal{A}}\boldsymbol{u}}{\mathcal{D}t} \cdot \boldsymbol{v}\ \mathrm{d}\omega + \frac{2}{\rho_f}\int_{\Omega_t} \mu(|\mathbf{D}(\boldsymbol{u})|)\ \mathbf{D}(\boldsymbol{u}) : \mathbf{D}(\boldsymbol{v})\ \mathrm{d}\omega - \frac{1}{\rho_f}\int_{\Omega_t} p\ \bigtriangledown \cdot \boldsymbol{v}\ \mathrm{d}\omega \\
&+ \int_{\Omega_t} \left[(\boldsymbol{u}-\boldsymbol{w})\cdot\bigtriangledown\boldsymbol{u}\right]\cdot\boldsymbol{v}\ \mathrm{d}\omega \quad = \quad \frac{1}{\rho_f}\int_{\Omega_t} \boldsymbol{f}\cdot\boldsymbol{v}\ \mathrm{d}\omega + a\frac{\rho_s h_s}{\rho_f}\int_{\Gamma^0_{wall}} \frac{\partial^2 R_0}{\partial x_1^2}\ v_2|_{\Gamma^0_{wall}}\ \mathrm{d}l_0 \\
&- \frac{\rho_s h_s}{\rho_f}\int_{\Gamma^0_{wall}} \left(\frac{\partial^2\eta}{\partial t^2} - a\frac{\partial^2\eta}{\partial x_1^2} + b\eta - c\frac{\partial^3\eta}{\partial t\partial x_1^2}\right) v_2|_{\Gamma^0_{wall}}\ \mathrm{d}l_0 - \frac{1}{\rho_f}\int_{\Gamma_{wall}} \frac{P_{ext}\ v_2}{\sqrt{1+(\partial_{x_1}R)^2}}\ \mathrm{d}l \\
&+ \int_{\Gamma_{in}} \left(\frac{1}{\rho_f}P_{in} - \frac{1}{2}|\boldsymbol{u}|^2\right) v_1\ \mathrm{d}x_2 - \int_{\Gamma_{out}} \left(\frac{1}{\rho_f}P_{out} - \frac{1}{2}|\boldsymbol{u}|^2\right) v_1\ \mathrm{d}x_2, \quad \forall \boldsymbol{v}\in V, \\
&\int_{\Omega_t} \bigtriangledown\cdot\ \boldsymbol{u}\ \tilde{q}\ \mathrm{d}\omega = 0, \quad \forall \tilde{q}\in Q,
\end{aligned} \tag{4.15}$$

where $\mathrm{d}l$ and $\mathrm{d}l_0$ denote the lengths of elements from Γ_{wall} and Γ^0_{wall} along the x_1-direction, respectively. Here the boundary integral $\int_{\partial\Omega_t} (\mathbf{T}\ \boldsymbol{n})\cdot\boldsymbol{v}\ \mathrm{d}\gamma$ has been replaced by given boundary data and the structure equation. We note that the spaces V and Q defined in (4.11)-(4.12) depend on time.

In what follows we will show how the corresponding boundary integrals are obtained. Note that all derivations are formal, i.e. we assume enough smooth functions, such that the corresponding integrals exist. Hence, we have

$$\begin{aligned}
\int_{\partial\Omega_t} (\mathbf{T}\ \boldsymbol{n})\cdot\ \boldsymbol{v}\ \mathrm{d}\gamma \ &= \int_{\Gamma_{wall}} (\mathbf{T}\ \boldsymbol{n})\cdot\ \boldsymbol{v}\ \mathrm{d}l + \int_{\Gamma_{sym}} (\mathbf{T}\ \boldsymbol{n})\cdot\ \boldsymbol{v}\ \mathrm{d}\gamma \\
&+ \int_{\Gamma_{in}} \left(-P_{in} + \frac{\rho_f}{2}|\boldsymbol{u}|^2\right) \underbrace{\boldsymbol{n}\cdot\boldsymbol{v}}_{-v_1}\ \mathrm{d}x_2 + \int_{\Gamma_{out}} \left(-P_{out} + \frac{\rho_f}{2}|\boldsymbol{u}|^2\right) \underbrace{\boldsymbol{n}\cdot\boldsymbol{v}}_{v_1}\ \mathrm{d}x_2,
\end{aligned} \tag{4.16}$$

Note that

$$(\mathbf{T}\ \boldsymbol{n})\cdot\boldsymbol{v} = (T_{11}n_1 + T_{12}n_2)\ v_1 + (T_{21}n_1 + T_{22}n_2)\ v_2.$$

The boundary term over Γ_{sym} disappears due to boundary condition (4.8), the definition of the normal vector on this boundary, i.e. $\boldsymbol{n} = (0,-1)^T$, and the condition enforced to the test function, i.e. $v_2|_{\Gamma_{sym}} = 0$. Hence, it yields

$$\int_{\Gamma_{sym}} (\mathbf{T}\ \boldsymbol{n})\cdot\ \boldsymbol{v}\ \mathrm{d}\gamma = -\int_{\Gamma_{sym}} \frac{\partial u_1}{\partial x_2}\ v_1\ \mathrm{d}\gamma = 0. \tag{4.17}$$

In order to rewrite the integral over Γ_{wall} we can proceed in the following way: we transform the external forces from Γ_{wall} to Γ^0_{wall} and for each surface element $\mathrm{d}\sigma_0 \in [0,2\pi)\times\Gamma^0_{wall}$ we use the structure equation

$$\frac{\partial^2\eta}{\partial t^2} - a\frac{\partial^2\eta}{\partial x_1^2} + b\eta - c\frac{\partial^3\eta}{\partial t\partial x_1^2} = -\frac{(\mathbf{T}+P_{ext}\ \mathbf{I})\boldsymbol{n}\cdot\boldsymbol{e}_r}{\rho_s h_s}\frac{R}{R_0}\frac{\sqrt{1+(\partial_{x_1}R)^2}}{\sqrt{1+(\partial_{x_1}R_0)^2}} + a\frac{\partial^2 R_0}{\partial x_1^2} \tag{4.18}$$

with parameters a, b, c defined in (2.30). Consecutively, we have

$$\begin{aligned}
\int\limits_{\Gamma_{wall}} (\mathbf{T}\ \boldsymbol{n})\cdot\ \boldsymbol{v}\ \mathrm{d}l &= \frac{1}{2\pi}\int\limits_0^{2\pi}\int\limits_{\Gamma_{wall}} \frac{(\mathbf{T}\ \boldsymbol{n})\cdot \boldsymbol{e}_r\ v_2}{R}\ \mathrm{d}\sigma \\
&= \frac{1}{2\pi}\int\limits_0^{2\pi}\int\limits_{\Gamma^0_{wall}} \frac{(\mathbf{T}\ \boldsymbol{n})\cdot \boldsymbol{e}_r\ v_2}{R_0}\frac{R}{R_0}\frac{\sqrt{1+(\partial_{x_1}R)^2}}{\sqrt{1+(\partial_{x_1}R_0)^2}}\ \mathrm{d}\sigma_0 \\
&= -\frac{\rho_s h_s}{2\pi\rho_f}\int\limits_0^{2\pi}\int\limits_{\Gamma^0_{wall}} \frac{1}{R_0}\left(\frac{\partial^2\eta}{\partial t^2} - a\frac{\partial^2\eta}{\partial x_1^2} + b\eta - c\frac{\partial^3\eta}{\partial t\partial x_1^2}\right)v_2\ \mathrm{d}\sigma_0 \\
&\quad - \frac{1}{2\pi}\int\limits_0^{2\pi}\int\limits_{\Gamma^0_{wall}} \frac{(P_{ext}\mathbf{I}\ \boldsymbol{n})\cdot \boldsymbol{e}_r\ v_2}{R_0}\frac{R}{R_0}\frac{\sqrt{1+(\partial_{x_1}R)^2}}{\sqrt{1+(\partial_{x_1}R_0)^2}}\ \mathrm{d}\sigma_0 \\
&\quad + a\ \frac{\rho_s h_s}{2\pi\rho_f}\int\limits_0^{2\pi}\int\limits_{\Gamma^0_{wall}} \frac{1}{R_0}\frac{\partial^2 R_0}{\partial x_1^2}\ v_2\ \mathrm{d}\sigma_0. \qquad (4.19)
\end{aligned}$$

Here $\mathrm{d}\sigma \in [0,2\pi)\times\Gamma_{wall}$ and $\mathrm{d}\sigma = R\mathrm{d}\theta\mathrm{d}l$. In (4.19) we have used the following equality: $(\mathbf{T}\ \boldsymbol{n})\cdot\boldsymbol{v} = (\mathbf{T}\boldsymbol{n})\cdot\boldsymbol{e}_r\ v_2$ on Γ_{wall}. The term containing external pressure can be transformed back to the Γ_{wall} as follows

$$\begin{aligned}
-\frac{1}{2\pi}\int\limits_0^{2\pi}\int\limits_{\Gamma^0_{wall}} \frac{(P_{ext}\mathbf{I}\ \boldsymbol{n})\cdot \boldsymbol{e}_r\ v_2}{R_0}\frac{R}{R_0}\frac{\sqrt{1+(\partial_{x_1}R)^2}}{\sqrt{1+(\partial_{x_1}R_0)^2}}\ \mathrm{d}\sigma_0 &= -\frac{1}{2\pi}\int\limits_0^{2\pi}\int\limits_{\Gamma_{wall}} \frac{(P_{ext}\mathbf{I}\ \boldsymbol{n})\cdot \boldsymbol{e}_r\ v_2}{R}\ \mathrm{d}\sigma \\
&= -\int\limits_{\Gamma_{wall}} \frac{P_{ext}\ v_2}{\sqrt{1+(\partial_{x_1}R)^2}}\ \mathrm{d}l. \qquad (4.20)
\end{aligned}$$

To simplify the model for analysis we will moreover assume that $\boldsymbol{n}\cdot\boldsymbol{e}_r \approx [1+(\partial_{x_1}R_0)^2]^{-1/2}$. Hence, the term with external pressure will be written as

$$-\int\limits_{\Gamma_{wall}} \frac{P_{ext}\ v_2}{\sqrt{1+(\partial_{x_1}R)^2}}\ \mathrm{d}l\ \approx\ -\int\limits_{\Gamma_{wall}} \frac{P_{ext}\ v_2}{\sqrt{1+(\partial_{x_1}R_0)^2}}\ \mathrm{d}l. \qquad (4.21)$$

Altogether, summing up the contributions (4.17), (4.19)-(4.20) and inserting them into (4.16) we can rewrite the boundary term as follows

$$\begin{aligned}
\int\limits_{\partial\Omega} (\mathbf{T}\ \boldsymbol{n})\cdot\ \boldsymbol{v}\ \mathrm{d}l\ &= \int\limits_{\Gamma_{in}}\left(P_{in} - \frac{\rho_f}{2}|\boldsymbol{u}|^2\right)v_1\ \mathrm{d}x_2 - \int\limits_{\Gamma_{out}}\left(P_{out} - \frac{\rho_f}{2}|\boldsymbol{u}|^2\right)v_1\ \mathrm{d}x_2 \\
&\quad - \frac{\rho_s h_s}{\rho_f}\int\limits_{\Gamma^0_{wall}} \frac{1}{R_0}\left(\frac{\partial^2\eta}{\partial t^2} - a\frac{\partial^2\eta}{\partial x_1^2} + b\eta - c\frac{\partial^3\eta}{\partial t\partial x_1^2}\right)v_2\ \mathrm{d}l_0 + a\ \frac{\rho_s h_s}{\rho_f}\int\limits_{\Gamma^0_{wall}} \frac{\partial^2 R_0}{\partial x_1^2}\ v_2\ \mathrm{d}l_0 \\
&\quad - \int\limits_{\Gamma_{wall}} \frac{P_{ext}\ v_2}{\sqrt{1+(\partial_{x_1}R_0)^2}}\ \mathrm{d}l.
\end{aligned}$$

The well-posedness of this coupled fluid-structure interaction problem has been studied in [59] for $q \geq 2$, cf. (3.19).

4.3 Numerical resolution of fluid-structure interaction problem

One of the most important numerical difficulties arising in the analysis of fluid-structure interaction problem (4.1a)-(4.1b), (4.2) is the non-linear character of coupling. Further, nonlinearities appear in the convective term and since we are focused on shear thinning fluids also the viscous term is nonlinear. Another peculiarity that occurs especially in the modelling of blood flow is caused by the comparable magnitude of blood density with the one of vessel's tissue. This in contrast to other mechanical applications commonly used in sequential coupling schemes, e.g. in aeroelasticity, where the density of structure is in general much larger than the one of the fluid, exhibits instabilities due to the artificial added mass effect, cf. [22, 37, 39]. As a consequence even small perturbations may cause large numerical instabilities.

- **Added mass effect**

  The added mass effect is a physical phenomenon affected most of the physical equations. It is observed in those situations, when a body moves thought a fluid and shifts some portion of volume of this fluid. As a consequence, a virtual mass created on the interface of body and a fluid is added to the system. The added mass effect is in general very strong, when the density of fluid is comparable to the density of structure as well as in the case of slender domains. Interestingly, this happens irrespectively on the time step size. In order to minimize the added mass effect in the design of fluid-structure interaction schemes based on partitioned methods a criterion on physical parameters can be derived. It gives a condition on the ratio between the fluid and structure densities and pure geometrical quantities. In [22] Causin, Gerbeau and Nobile examined explicit and implicit partitioned schemes applied on a reduced problem, i.e. a linear, incompressible and inviscid model, and tried to associate numerical instabilities with a concrete choice of physical and geometric quantities. They found out that in the case of weakly-coupled schemes the problems occur, when the structure density is lower than a threshold or the length of a domain is greater than a threshold. Note that considering explicit schemes no iterations between the fluid and the structure subproblem are used. A drawback is the problem with the exact energy balance. On the other hand, considering strongly coupled schemes no problems due to the balance of energy occur, but several iterations between the fluid and the structure are necessary. It has been observed that when iterations are based on the relaxed fixed-point method, the smaller is the structure density and the larger the length of the domain, the more relaxation in iterations is needed. The analysis of the added mass effect deals with the spectrum of the added mass operator. In [22] the corresponding conditions on unconditional stability of explicit schemes and convergence of iterative methods are derived. The artificial added mass effect has been studied also in the framework of sequential staggered fluid-structure schemes by Förster, Wall and Ramm [43].

In literature various approaches have been proposed in order to solve the fluid-structure interaction problems [6, 18, 22, 37, 39, 41, 83, 89]. In what follows we give a brief overview of possible numerical methods applicable on the discretization and coupling of the fluid and the structure. Focusing on the strategy how the numerical solution is obtained the fluid-structure interaction schemes can be categorized in the following three groups: **implicit** (i.e. fully, strongly coupled), **explicit** (i.e. weakly, loosely coupled) and **semi-implicit schemes**. Moreover, the fluid-structure interaction techniques can be divided into two group with respect to the numerical treatment of the coupling. In particular, if the solution of the fluid-structure interaction problem is based on one solver or if there is possibility to solve the

fluid and the structure part using two different solvers, then we distinguish the **monolithical** and **partitioned methods**, respectively.

- **Implicit, explicit and semi-implicit schemes**

  The simplest strategy represents the explicit method, see e.g. [18, 50, 80]. The main idea of this method lies on the explicit coupling between the fluid and the structure, which allows to solve the fluid and the structure equations at each time step only once and independently. This kind of schemes is cheap in terms of computational costs, but generally unstable, because of the added mass effect [22]. Therefore a stabilization technique is necessary, see, e.g. [18].

  The implicit coupling schemes, see, e.g. [6, 40, 47, 57], overcome the instability problems of the explicit ones and are stable in the energy form. Due to the use of the fixed-point or the Newton method additional computational time is required. Moreover, the coupling conditions are treated implicitly at each time step.

  The semi-implicit schemes combines the advantages of the explicit and the implicit methods. They remain stable for a reasonable range of discretization parameters. Usually, they treat the interface condition and the convective term in an explicit way, see, e.g. [4, 38, 39, 88].

- **Monolithical and partitioned schemes**

  Monolithical methods, see, e.g. [55, 57], often called the fully-coupled methods, are based on implicit scheme implemented in one single software. They are quite expensive concerning computational costs but typically robust. The coupling between the fluid and the structure is highly nonlinear.

  Besides the monolithical methods there is a big group of partitioned schemes applicable on the fluid-structure interaction problem, see for example [6, 18, 41, 83, 89]. Numerically, the solving of the fluid-structure interaction problem with a partitioned method can be split in two parts, the fluid subproblem and the structure subproblem and the fluid-structure interaction problem is solved subsequently. At each time step the fluid determines the forcing term for structure, while structure gives the boundary condition on moving boundary. The connection between these two part is given by the coupling (matching) conditions. An advantage of the partitioned procedure is that the fluid and the structure subproblems can be solved separately with two different codes. The scheme can be used for the strongly as well as the weakly coupled scheme although it is preferable to use it more in the loosely coupled schemes.

Numerical solution of the fluid-structure interaction problem is often based on the operator splitting approach. The classical operator splitting approach distinguishes between the fluid and the structure subproblem and uses the Dirichlet-Neumann transmission condition. In this case each subproblem is solved by an iteration between these two parts until convergence is obtained [6]. A novel way of solving the fluid-structure interaction problem introduced by Guidoboni et al. [50, 51] is given by a partitioned algorithm based on a time-discretization of structure equation via **non-standard operator splitting technique**. More precisely, the splitting approach is applied on the second-order time derivative of unknown function, see Section 4.4 for more details.

4.4 Kinematic splitting algorithm

In what follows we derive an efficient loosely-coupled fluid-structure interaction algorithm using an operator splitting technique applied on our fluid-structure interaction problem (4.1a)-(4.1b) and (4.2). Here we are inspired by the paper of Guidoboni et al. [50]. Similarly as in the recent work of Nobile and Vergara [81] our scheme is based on computing the fluid and structure equation just once per time step. In [81] the structure equation is embedded into the fluid equation as a generalized Robin boundary condition. On the other hand, in our kinematic splitting algorithm the coupled fluid-structure interaction problem is split following the underlying physics into the hydrodynamic (parabolic) and elastic (hyperbolic) part. It is just a part of the structure equation, the parabolic part with the viscoelastic term, that is used as the generalized Robin boundary condition in the fluid equation. The rest of the structure equation, the elastic part, is approximated by a suitable numerical scheme; we have used the second order Newmark method.

The kinematic splitting approach is based on the kinematic coupling condition (4.10). We define the operator A that includes the fluid solver and the viscoelastic part of structure equation by

$$\textbf{Operator A (hydrodynamic)} \begin{cases} \text{fluid solver } (\boldsymbol{u}, p), \\ \xi := u_2|_{\Gamma_{wall}}, \\ \dfrac{\partial \xi}{\partial t} = c\dfrac{\partial^2 \xi}{\partial {x_1}^2} + H(\boldsymbol{u}, p) \end{cases} \tag{4.22}$$

and the operator B for the purely elastic load of structure by

$$\textbf{Operator B (elastic)} \begin{cases} \dfrac{\partial \eta}{\partial t} = \xi, \\ \dfrac{\partial \xi}{\partial t} = a\dfrac{\partial^2 \eta}{\partial {x_1}^2} - b\eta + G(R_0), \end{cases} \tag{4.23}$$

where

$$H(\boldsymbol{u}, p) := -\frac{\Big((\mathbf{T} + P_{ext}\ \mathbf{I})\boldsymbol{n}\Big)\Big|_{\Gamma^0_{wall}} \cdot \boldsymbol{e}_r}{\rho_s h} \frac{R}{R_0} \frac{\sqrt{1 + (\partial_{x_1} R)^2}}{\sqrt{1 + (\partial_{x_1} R_0)^2}}, \quad G(R_0) := a\frac{\partial^2 R_0}{\partial x_1^2}\ . \tag{4.24}$$

Since the structure equation has been obtained under the assumption $\partial_{x_1}\eta(x_1, t) \ll 1$ (linear elasticity) we will approximate $\sqrt{1 + (\partial_{x_1} R)^2} \approx \sqrt{1 + (\partial_{x_1}(R_0))^2}$ in terms with P_{ext}.

4.5 Weak formulation for the kinematically splitted FSI problem

The weak formulation for the operator A can be easily obtained taking only those parts from the general weak formulation (4.15) which correspond to the operator A. Therefore assuming the test functions $\boldsymbol{v} \in V$ and $\tilde{q} \in Q$ we are looking for functions $\boldsymbol{u} \in V^F$ and $\eta \in V^S$ such that for almost all $t \in I$ it holds

$$
\begin{aligned}
&\int_{\Omega_t} \frac{\mathcal{D}^{\mathcal{A}}\boldsymbol{u}}{\mathcal{D}t}\cdot\boldsymbol{v}\ \mathrm{d}\omega + \frac{2}{\rho_f}\int_{\Omega_t}\mu(|\mathbf{D}(\boldsymbol{u})|)\ \mathbf{D}(\boldsymbol{u}):\mathbf{D}(\boldsymbol{v})\ \mathrm{d}\omega - \frac{1}{\rho_f}\int_{\Omega_t} p\ \bigtriangledown\cdot\boldsymbol{v}\ \mathrm{d}\omega \\
&+\int_{\Omega_t}\big[(\boldsymbol{u}-\boldsymbol{w})\cdot\bigtriangledown\boldsymbol{u}\big]\cdot\boldsymbol{v}\ \mathrm{d}\omega \quad = \quad \frac{1}{\rho_f}\int_{\Omega_t}\boldsymbol{f}\cdot\boldsymbol{v}\ \mathrm{d}\omega \\
&-\frac{\rho_s h_s}{\rho_f}\int_{\Gamma^0_{wall}}\left(\frac{\partial^2\eta}{\partial t^2}-c\frac{\partial^3\eta}{\partial t\partial x_1^2}\right)v_2|_{\Gamma^0_{wall}}\ \mathrm{d}l_0 - \frac{1}{\rho_f}\int_{\Gamma_{wall}}\frac{P_{ext}\ v_2}{\sqrt{1+(\partial_{x_1}R)^2}}\ \mathrm{d}l \\
&+\int_{\Gamma_{in}}\left(\frac{1}{\rho_f}P_{in}-\frac{1}{2}|\boldsymbol{u}|^2\right)v_1\ \mathrm{d}x_2 - \int_{\Gamma_{out}}\left(\frac{1}{\rho_f}P_{out}-\frac{1}{2}|\boldsymbol{u}|^2\right)v_1\ \mathrm{d}x_2, \quad \forall\boldsymbol{v}\in V, \qquad (4.25a)\\
&\int_{\Omega_t}\bigtriangledown\cdot\boldsymbol{u}\ \tilde{q}\ \mathrm{d}\omega \quad = \quad 0, \quad \forall\tilde{q}\in Q, \qquad (4.25b)
\end{aligned}
$$

The operator B can be written in the variational formulation as follows: find $\eta\in V^S$ such that for each $v\in H_0^1(\Gamma^0_{wall})$ a.e. $t\in I$ it holds

$$
\begin{aligned}
\int_{\Gamma^0_{wall}}\frac{\partial\eta}{\partial t}\ v\ \mathrm{d}x_2 &= \int_{\Gamma^0_{wall}}\xi\ v\ \mathrm{d}x_2, \qquad (4.26a)\\
\int_{\Gamma^0_{wall}}\frac{\partial\xi}{\partial t}\ v\ \mathrm{d}x_2 &= a\int_{\Gamma^0_{wall}}\frac{\partial^2\eta}{\partial x_1^2}\ v\ \mathrm{d}x_2 - b\int_{\Gamma^0_{wall}}\eta\ v\ \mathrm{d}x_2 + \int_{\Gamma^0_{wall}}G(R_0)\ v\ \mathrm{d}x_2. \qquad (4.26b)
\end{aligned}
$$

The formulations presented in this section will be a starting point for the theoretical analysis of stability and error estimates presented in the next chapters.

Chapter 5

Stability analysis

In this chapter we focus on theoretical analysis of stability of our kinematic splitting algorithm applied to the fluid-structure interaction problem (4.22)-(4.23). Firstly, we derive a priori estimate for the differential problem (4.22)-(4.23). The analysis is based on the weak formulation (4.25a)-(4.25b) and (4.26a)-(4.26b) introduced in the previous chapter. Then, we look more precisely on the semi-discretized problem (4.22)-(4.23) and we derive corresponding stability estimates. This will be done with respect to the energy norms.

5.1 A priori estimates for the continuous problem

In this section we will derive formally energy equation for the weak formulation of our kinematic splitting fluid-structure algorithm on the continuous level, which will give us hint for a suitable functional spaces setting we use in the stability analysis. Let us start with the weak formulation for the operator A and the operator B, separately. We will see that a priori estimates arising from both operators will give us altogether desired a priori estimates.

5.1.1 A priori estimate for the operator A

Let us start with the weak formulation as presented in (4.25a)-(4.25b). We can clearly take in (4.25a)-(4.25b) test functions that are space-time dependent. In particular, by choosing the test function to be equal to the fluid velocity, i.e. $\boldsymbol{v} = \boldsymbol{u}$, and assuming that $\bigtriangledown \cdot \boldsymbol{u} = 0$ we get

$$\begin{aligned}
&\int_{\Omega_t} \frac{\mathcal{D}^{\mathcal{A}}\boldsymbol{u}}{\mathcal{D}t} \cdot \boldsymbol{u} \, \mathrm{d}\omega + \frac{2}{\rho_f} \int_{\Omega_t} \mu(|\mathbf{D}(\boldsymbol{u})|) \, \mathbf{D}(\boldsymbol{u}) : \mathbf{D}(\boldsymbol{u}) \, \mathrm{d}\omega + \int_{\Omega_t} \left[(\boldsymbol{u} - \boldsymbol{w}) \cdot \bigtriangledown \boldsymbol{u} \right] \cdot \boldsymbol{u} \, \mathrm{d}\omega \\
&= \frac{1}{\rho_f} \int_{\Omega_t} \boldsymbol{f} \cdot \boldsymbol{u} \, \mathrm{d}\omega - \frac{\rho_s h_s}{\rho_f} \int_{\Gamma^0_{wall}} \left(\frac{\partial^2 \eta}{\partial t^2} - c \frac{\partial^3 \eta}{\partial t \partial x_1^2} \right) u_2|_{\Gamma^0_{wall}} \, \mathrm{d}l_0 - \frac{1}{\rho_f} \int_{\Gamma_{wall}} \frac{P_{ext} \; u_2}{\sqrt{1 + (\partial_{x_1} R_0)^2}} \, \mathrm{d}l \\
&+ \int_{\Gamma_{in}} \left(\frac{1}{\rho_f} P_{in} - \frac{1}{2} |\boldsymbol{u}|^2 \right) u_1 \, \mathrm{d}x_2 - \int_{\Gamma_{out}} \left(\frac{1}{\rho_f} P_{out} - \frac{1}{2} |\boldsymbol{u}|^2 \right) u_1 \, \mathrm{d}x_2. \qquad (5.1)
\end{aligned}$$

The non-conservative weak formulation (5.1) can be rewritten into the conservative form after some manipulations of the term with time derivative and the convective term. Using the Reynolds transport theorem in the ALE frame, cf. (2.12), we can easily shift the time-derivative from the first term on the left hand side of (5.1) in front of the integral. This yields

$$\int_{\Omega_t} \frac{\mathcal{D}^{\mathcal{A}}\boldsymbol{u}}{\mathcal{D}t} \cdot \boldsymbol{u} \, \mathrm{d}\omega = \frac{1}{2} \int_{\Omega_t} \frac{\mathcal{D}^{\mathcal{A}}|\boldsymbol{u}|^2}{\mathcal{D}t} \, \mathrm{d}\omega = \frac{1}{2} \frac{\mathrm{d}}{\mathrm{d}t} \int_{\Omega_t} |\boldsymbol{u}|^2 \, \mathrm{d}\omega - \frac{1}{2} \int_{\Omega_t} |\boldsymbol{u}|^2 \bigtriangledown \cdot \boldsymbol{w} \, \mathrm{d}\omega. \qquad (5.2)$$

Moreover, let us rewrite the convective term from (5.1) using the product rule for divergence operator, the Green theorem, cf. (1.21) and integration by parts, i.e.

$$\int_{\Omega_t}[(\boldsymbol{u}-\boldsymbol{w})\cdot\bigtriangledown\boldsymbol{u}]\cdot\boldsymbol{u}\ \mathrm{d}\omega \ = \ \int_{\Omega_t}\boldsymbol{u}\bigtriangledown\cdot\left[(\boldsymbol{u}-\boldsymbol{w})\ \boldsymbol{u}\right]\mathrm{d}\omega-\int_{\Omega_t}|\boldsymbol{u}|^2\bigtriangledown\cdot(\boldsymbol{u}-\boldsymbol{w})\ \mathrm{d}\omega, \quad (5.3)$$

where the first integral on the right hand side of (5.3) can be manipulated as follows

$$\begin{aligned}\int_{\Omega_t}\boldsymbol{u}\bigtriangledown\cdot\left[(\boldsymbol{u}-\boldsymbol{w})\ \boldsymbol{u}\right]\mathrm{d}\omega \ &= \ -\int_{\Omega_t}\bigtriangledown\boldsymbol{u}\cdot[(\boldsymbol{u}-\boldsymbol{w})\boldsymbol{u}]\ \mathrm{d}\omega+\int_{\partial\Omega_t}|\boldsymbol{u}|^2(\boldsymbol{u}-\boldsymbol{w})\cdot\boldsymbol{n}\ \mathrm{d}\gamma\\ &=-\frac{1}{2}\int_{\Omega_t}(\bigtriangledown\boldsymbol{u}^2)(\boldsymbol{u}-\boldsymbol{w})\ \mathrm{d}\omega+\int_{\partial\Omega_t}|\boldsymbol{u}|^2(\boldsymbol{u}-\boldsymbol{w})\cdot\boldsymbol{n}\ \mathrm{d}\gamma\\ &=\frac{1}{2}\int_{\Omega_t}|\boldsymbol{u}|^2\bigtriangledown\cdot(\boldsymbol{u}-\boldsymbol{w})\ \mathrm{d}\omega+\frac{1}{2}\int_{\partial\Omega_t}|\boldsymbol{u}|^2(\boldsymbol{u}-\boldsymbol{w})\cdot\boldsymbol{n}\ \mathrm{d}\gamma. \quad (5.4)\end{aligned}$$

Further, for the boundary term in (5.4) we apply the prescribed boundary conditions on Γ_{in},Γ_{out}, Γ_{sym} and Γ_{wall}. This yields

$$\frac{1}{2}\int_{\partial\Omega_t}|\boldsymbol{u}|^2(\boldsymbol{u}-\boldsymbol{w})\cdot\boldsymbol{n}\ \mathrm{d}\gamma \ = \ -\int_0^{R_0(0)}\left(\frac{1}{2}|\boldsymbol{u}|^2\right)u_1|_{x=0}\ \mathrm{d}x_2+\int_0^{R_0(L)}\left(\frac{1}{2}|\boldsymbol{u}|^2\right)u_1|_{x=L}\ \mathrm{d}x_2. \quad (5.5)$$

Inserting the manipulations (5.4)-(5.5) into (5.3) we can rewrite the convective term as follows

$$\begin{aligned}\int_{\Omega_t}[(\boldsymbol{u}-\boldsymbol{w})\cdot\bigtriangledown\boldsymbol{u}]\cdot\boldsymbol{u}\ \mathrm{d}\omega \ &= \ -\frac{1}{2}\int_{\Omega_t}|\boldsymbol{u}|^2\bigtriangledown\cdot(\boldsymbol{u}-\boldsymbol{w})\ \mathrm{d}\omega-\int_0^{R_0(0)}\left(\frac{1}{2}|\boldsymbol{u}|^2\right)u_1|_{x=0}\ \mathrm{d}x_2\\ &\quad+\int_0^{R_0(L)}\left(\frac{1}{2}|\boldsymbol{u}|^2\right)u_1|_{x=L}\ \mathrm{d}x_2. \quad (5.6)\end{aligned}$$

Now, using the equalities (5.2) and (5.6), assuming that the fluid velocity is divergence-free and that for the structure velocity it holds $\xi=\partial\eta/\partial t$ we can rewrite (5.1) in the following way

$$\begin{aligned}&\frac{1}{2}\frac{\mathrm{d}}{\mathrm{d}t}\int_{\Omega_t}|\boldsymbol{u}|^2\ \mathrm{d}\omega+\frac{2}{\rho_f}\int_{\Omega_t}\mu(|\mathbf{D}(\boldsymbol{u})|)\ \mathbf{D}(\boldsymbol{u}):\mathbf{D}(\boldsymbol{u})\ \mathrm{d}\omega\\ &=\frac{1}{\rho_f}\int_{\Omega_t}\boldsymbol{f}\cdot\boldsymbol{u}\ \mathrm{d}\omega-\frac{\rho_s h_s}{\rho_f}\int_{\Gamma^0_{wall}}\left(\frac{\partial\xi}{\partial t}-c\frac{\partial^2\xi}{\partial x_1^2}\right)\xi\ \mathrm{d}l_0\\ &-\frac{1}{\rho_f}\int_{\Gamma_{wall}}\frac{P_{ext}\ u_2}{\sqrt{1+(\partial_{x_1}R_0)^2}}\ \mathrm{d}l\ +\int_{\Gamma_{in}}\frac{1}{\rho_f}P_{in}\ u_1\ \mathrm{d}x_2-\int_{\Gamma_{out}}\frac{1}{\rho_f}P_{out}\ u_1\ \mathrm{d}x_2. \quad (5.7)\end{aligned}$$

In order to obtain a priori estimate for the operator A we proceed with finding suitable bounds for each individual term from (5.7). In what follows we will denote by C a generic time-independent constant arising from different inequalities. When it will be important to work with a particular constant C that comes from a specific inequality we will use, e.g. a subscript. Moreover, the positive constant ε will be a generic constant arising from the Young inequality except the cases when a specific choice of ε is needed.

It is easy to see that the first term from (5.7) gives us directly the time derivative of L^2-norm of velocity. Before estimating the viscous term, let us point out that for both shear-thinning viscosity function models, the Carreau and the Yeleswarapu, we have

$$\mu(|\mathbf{D}(\boldsymbol{u})|) \ \geq \ \mu_\infty. \tag{5.8}$$

This and the Poincaré inequality (1.16) yield the existence of a constant $C^* > 0$, such that

$$\frac{2}{\rho_f} \int\limits_{\Omega_t} \mu(|\mathbf{D}(\boldsymbol{u})|) \ \mathbf{D}(\boldsymbol{u}) : \mathbf{D}(\boldsymbol{u}) \ \mathrm{d}\omega \ \geq \ C^* ||\boldsymbol{u}||^2_{W^{1,2}(\Omega_t)}. \tag{5.9}$$

Moreover, we have for the Carreau model, cf. [59], [73], Lemma 5.1.19,

$$\frac{2}{\rho_f} \int\limits_{\Omega^n} \mu(|\mathbf{D}(\boldsymbol{u})|) \ \mathbf{D}(\boldsymbol{u}) : \mathbf{D}(\boldsymbol{u}) \ \mathrm{d}\omega \ \geq \ C^* ||\boldsymbol{u}||^q_{W^{1,q}(\Omega_t)} \ - \kappa C^*, \tag{5.10}$$

where $\kappa := 0$ for $q \geq 2$ and $\kappa = 1$ for $1 \leq q < 2$. For $q \geq 2$, see [73], we also have

$$\frac{2}{\rho_f} \int\limits_{\Omega^n} \mu(|\mathbf{D}(\boldsymbol{u})|) \ \mathbf{D}(\boldsymbol{u}) : \mathbf{D}(\boldsymbol{u}) \ \mathrm{d}\omega \ \geq \ C^* ||\boldsymbol{u}||^q_{W^{1,q}(\Omega_t)} + C^* ||\boldsymbol{u}||^2_{W^{1,2}(\Omega_t)}. \tag{5.11}$$

In what follows we will present the theoretical analysis for a polynomial growth model with the property (5.10). We use (5.10) instead of (5.11), because we are focused on shear thinning fluids. However, the analysis will be analogous for (5.9) and (5.11), too.

Using the Young inequality (1.10) we can find a small positive constant ε and positive constants C_1, C_2 such that the following inequality is fulfilled

$$\int\limits_{\Omega_t} \boldsymbol{u} \cdot \boldsymbol{f} \ \mathrm{d}\omega \ \leq \ C_1 \varepsilon ||\boldsymbol{u}||^q_{L^q(\Omega_t)} + \frac{C_2}{\varepsilon^{q'/q}} ||\boldsymbol{f}||^{q'}_{L^{q'}(\Omega_t)}, \tag{5.12}$$

where for q' it holds: $q' \geq 1$ and $1/q + 1/q' = 1$. Applying the trace inequality on (5.12) we obtain the estimate

$$\int\limits_{\Omega_t} \boldsymbol{u} \cdot \boldsymbol{f} \ \mathrm{d}\omega \ \leq \ C_1 C^{tr} \varepsilon ||\boldsymbol{u}||^q_{W^{1,q}(\Omega_t)} + \frac{C_2}{\varepsilon^{q'/q}} ||\boldsymbol{f}||^{q'}_{L^{q'}(\Omega_t)}, \tag{5.13}$$

Each term from (5.7) with a pressure contribution can be bounded from above using the Young and the trace inequality. Hence, we obtain

$$\frac{1}{\rho_f} \int_0^{R_0(0)} P_{in} \ u_1|_{x_1=0} \ \mathrm{d}x_2 \quad \leq \quad \frac{C_2}{\varepsilon_1^{q'/q}} ||P_{in}||^{q'}_{L^{q'}(\Gamma_{in})} + \varepsilon_1 C_1 C^{tr}(\Omega_t) ||\boldsymbol{u}||^q_{W^{1,q}(\Omega_t)}, \tag{5.14}$$

$$-\frac{1}{\rho_f} \int_0^{R_0(L)} P_{out} \ u_1|_{x_1=L} \ \mathrm{d}x_2 \quad \leq \quad \frac{C_2}{\varepsilon_2^{q'/q}} ||P_{out}||^{q'}_{L^{q'}(\Gamma_{out})} + \varepsilon_2 C_1 C^{tr}(\Omega_t) ||\boldsymbol{u}||^q_{W^{1,q}(\Omega_t)}, \tag{5.15}$$

$$-\frac{1}{\rho_f} \int\limits_{\Gamma_{wall}} \frac{P_{ext} \ u_2}{\sqrt{1 + (\partial_{x_1} R_0)^2}} \ \mathrm{d}l \quad \leq \quad \frac{K C_2}{\varepsilon_3^{q'/q}} ||P_{ext}||^{q'}_{L^{q'}(\Gamma_{wall})} + \varepsilon_3 C_1 C^{tr}(\Omega_t) ||\boldsymbol{u}||^q_{W^{1,q}(\Omega_t)}, \tag{5.16}$$

where $C^{tr}(\Omega_t)$ and $\varepsilon_i, i \in \{1, 2, 3\}$, are positive constants such that $\varepsilon_1 = \varepsilon_2 =: \varepsilon$, $\varepsilon_3 \geq K\varepsilon$ and

$$K := \left\| [1 + (\partial_{x_1} R_0)^2]^{-1/2} \right\|_{L^\infty(\Gamma_{wall})}.$$

Using the integration by parts and some manipulations, we can rewrite the integral over Γ^0_{wall} in the following way

$$-\int\limits_{\Gamma^0_{wall}} \left(\frac{\partial \xi}{\partial t} - c\frac{\partial^2 \xi}{\partial x_1^2}\right)\xi \ \mathrm{d}l_0 \ = \ -\frac{1}{2}\ \frac{\mathrm{d}}{\mathrm{d}t}\ ||\xi||^2_{L^2(\Gamma^0_{wall})} - c\ ||\xi_{x_1}||^2_{L^2(\Gamma^0_{wall})} \tag{5.17}$$

Finally, assuming ε is sufficiently small such that $\varepsilon \leq C^*/(8C_1C^{tr})$ and inserting the estimates from (5.10), (5.13)-(5.17) into (5.7) we obtain a priori estimate for the operator A

$$\begin{aligned}&\frac{\mathrm{d}}{\mathrm{d}t}||\boldsymbol{u}||^2_{L^2(\Omega_t)} + \frac{\rho_s h_s}{\rho_f}\frac{\mathrm{d}}{\mathrm{d}t}||\xi||^2_{L^2(\Gamma^0_{wall})} + C^*||\boldsymbol{u}||^q_{W^{1,q}(\Omega_t)} + 2c\ \frac{\rho_s h_s}{\rho_f}||\xi_{x_1}||^2_{L^2(\Gamma^0_{wall})} \\ &\quad\leq\ 2\kappa C^* + \frac{2C_2}{\varepsilon^{q'/q}}\left[||\boldsymbol{f}||^{q'}_{L^{q'}(\Omega_t)} + ||P_{in}||^{q'}_{L^{q'}(\Gamma_{in})} + ||P_{out}||^{q'}_{L^{q'}(\Gamma_{out})} + ||P_{ext}||^{q'}_{L^{q'}(\Gamma_{wall})}\right].\end{aligned} \tag{5.18}$$

5.1.2 A priori estimate for the operator B

Taking the test function $v = b\eta$ in (4.26a) and $v = \xi$ in (4.26b) and summing up both multiplied equations we obtain

$$b\int_{\Gamma^0_{wall}} \frac{\partial \eta}{\partial t}\ \eta\ \mathrm{d}x_2 + \int_{\Gamma^0_{wall}} \frac{\partial \xi}{\partial t}\ \xi\ \mathrm{d}x_2 = a\int_{\Gamma^0_{wall}} \frac{\partial^2 \eta}{\partial x_1^2}\ \xi\ \mathrm{d}x_2 + \int_{\Gamma^0_{wall}} G(R_0)\ \xi\ \mathrm{d}x_2. \tag{5.19}$$

The first term on the right hand side of (5.19) can be rewritten using integration by parts and the kinematic coupling condition $\xi = \partial\eta/\partial t$ as follows

$$a\int_{\Gamma^0_{wall}} \frac{\partial^2 \eta}{\partial x_1^2}\ \xi\ \mathrm{d}x_2 = a\int_{\Gamma^0_{wall}} \frac{\partial^2 \eta}{\partial x_1^2}\ \frac{\partial \eta}{\partial t}\ \mathrm{d}x_2 = -a\int_{\Gamma^0_{wall}} \frac{\partial \eta}{\partial x_1}\ \frac{\partial^2 \eta}{\partial t \partial x_1}\ \mathrm{d}x_2 = -\frac{a}{2}\int_{\Gamma^0_{wall}} \frac{\partial(\eta^2_{x_1})}{\partial t}\ \mathrm{d}x_2. \tag{5.20}$$

After some manipulations of integrals on the left hand side of (5.19) and using the formula (5.20) we get the energy equality of the form

$$\frac{1}{2}\frac{\mathrm{d}}{\mathrm{d}t}\left[b||\eta||^2_{L^2(\Gamma^0_{wall})} + ||\xi||^2_{L^2(\Gamma^0_{wall})} + a||\eta_{x_1}||^2_{L^2(\Gamma^0_{wall})}\right] = \int_{\Gamma^0_{wall}} G(R_0)\ \xi\ \mathrm{d}x_2, \tag{5.21}$$

where $G(R_0) := a\frac{\partial^2 R_0}{\partial x_1^2}$. From the equation (5.21) we see that the energy corresponding to the operator B remains constant considering only constant reference radius. However, in more general situations, when $R_0 \neq$ const, also the initial geometry comes into play. The integral on the right hand side of (5.21) can be estimated using the Young inequality as follows

$$a\int_{\Gamma^0_{wall}} \frac{\partial^2 R_0}{\partial x_1^2}\ \xi\ \mathrm{d}x_2 \ \leq\ \frac{a^2}{4\varepsilon}\left|\left|\frac{\partial^2 R_0}{\partial x_1^2}\right|\right|^2_{L^2(\Gamma^0_{wall})} + \varepsilon||\xi||^2_{L^2(\Gamma^0_{wall})}. \tag{5.22}$$

Hence, a priori estimate for the operator B reads as follows

$$\frac{1}{2}\frac{\mathrm{d}}{\mathrm{d}t}\left[b||\eta||^2_{L^2(\Gamma^0_{wall})} + ||\xi||^2_{L^2(\Gamma^0_{wall})} + a||\eta_{x_1}||^2_{L^2(\Gamma^0_{wall})}\right] \ \leq\ \frac{a^2}{4\varepsilon}\left|\left|\frac{\partial^2 R_0}{\partial x_1^2}\right|\right|^2_{L^2(\Gamma^0_{wall})} + \varepsilon||\xi||^2_{L^2(\Gamma^0_{wall})}. \tag{5.23}$$

5.1.3 A priori estimate of the coupled problem

In order to obtain a priori estimate for the kinematic splitting fluid-structure interaction scheme, cf. (4.22)-(4.23), we multiply a priori estimate for the operator B, cf. (5.23), by $(2\rho_s h_s/\rho_f)$ and sum it up to a priori estimate obtained for the operator A, cf. (5.18). It yields

$$\begin{aligned}
&\frac{\mathrm{d}}{\mathrm{d}t}||\boldsymbol{u}||^2_{L^2(\Omega_t)} + C^*||\boldsymbol{u}||^q_{W^{1,q}(\Omega_t)} + 2c\ \frac{\rho_s h_s}{\rho_f}||\xi_{x_1}||^2_{L^2(\Gamma^0_{wall})} \\
&+ \frac{\rho_s h_s}{\rho_f}\frac{\mathrm{d}}{\mathrm{d}t}\left[b||\eta||^2_{L^2(\Gamma^0_{wall})} + 2||\xi||^2_{L^2(\Gamma^0_{wall})} + a||\eta_{x_1}||^2_{L^2(\Gamma^0_{wall})}\right] \\
&\quad\leq\ 2\varepsilon\ \frac{\rho_s h_s}{\rho_f}||\xi||^2_{L^2(\Gamma^0_{wall})} + \ \frac{a^2}{2\varepsilon}\frac{\rho_s h_s}{\rho_f}\left|\left|\frac{\partial^2 R_0}{\partial x_1^2}\right|\right|^2_{L^2(\Gamma^0_{wall})} + 2\kappa C^* \\
&\quad+ \frac{2C_2}{\varepsilon^{q'/q}}\left[||\boldsymbol{f}||^{q'}_{L^{q'}(\Omega_t)} + ||P_{in}||^{q'}_{L^{q'}(\Gamma_{in})} + ||P_{out}||^{q'}_{L^{q'}(\Gamma_{out})} + ||P_{ext}||^{q'}_{L^{q'}(\Gamma_{wall})}\right]. \quad (5.24)
\end{aligned}$$

From the inequality (5.24) it is immediately visible that the derivative of fluid's kinetic energy is bounded with data arising from initial geometry, boundary conditions and the movement of structure, which is represented by the first term on the right hand side. In order to obtain the desired estimate in terms of the kinetic energy for both, the fluid and the structure, let us integrate the inequality (5.24) from t_0 to $t \in I$, where $I := (t_0, T]$. We get the inequality

$$\begin{aligned}
&||\boldsymbol{u}(t)||^2_{L^2(\Omega_t)} + \frac{\rho_s h_s}{\rho_f}\left[b||\eta(t)||^2_{L^2(\Gamma^0_{wall})} + 2||\xi(t)||^2_{L^2(\Gamma^0_{wall})} + a||\eta_{x_1}(t)||^2_{L^2(\Gamma^0_{wall})}\right] \\
&+ C^*\int_{t_0}^{t}||\boldsymbol{u}(\tau)||^q_{W^{1,q}(\Omega_\tau)}\,\mathrm{d}\tau + 2c\ \frac{\rho_s h_s}{\rho_f}\int_{t_0}^{t}||\xi_{x_1}(\tau)||^2_{L^2(\Gamma^0_{wall})}\,\mathrm{d}\tau \\
&\leq\ ||\boldsymbol{u}(t_0)||^2_{L^2(\Omega_0)} + \frac{\rho_s h_s}{\rho_f}\left[b||\eta(t_0)||^2_{L^2(\Gamma^0_{wall})} + 2||\xi(t_0)||^2_{L^2(\Gamma^0_{wall})} + a||\eta_{x_1}(t_0)||^2_{L^2(\Gamma^0_{wall})}\right] \\
&\quad+ 2\varepsilon\ \frac{\rho_s h_s}{\rho_f}\int_{t_0}^{t}||\xi(\tau)||^2_{L^2(\Gamma^0_{wall})}\,\mathrm{d}\tau + \frac{a^2(t-t_0)}{2\varepsilon}\frac{\rho_s h_s}{\rho_f}\left|\left|\frac{\partial^2 R_0}{\partial x_1^2}\right|\right|^2_{L^2(\Gamma^0_{wall})} + 2\kappa C^*(t-t_0) \\
&\quad+ \frac{2C_2}{\varepsilon^{q'/q}}\int_{t_0}^{t}\left[||\boldsymbol{f}||^{q'}_{L^{q'}(\Omega_\tau)} + ||P_{in}||^{q'}_{L^{q'}(\Gamma_{in})} + ||P_{out}||^{q'}_{L^{q'}(\Gamma_{out})} + ||P_{ext}||^{q'}_{L^{q'}(\Gamma_{wall})}\right]\mathrm{d}\tau. \quad (5.25)
\end{aligned}$$

Let us denote

$$E(t) := ||\boldsymbol{u}(t)||^2_{L^2(\Omega_t)} + \frac{\rho_s h_s}{\rho_f}\left[b||\eta(t)||^2_{L^2(\Gamma^0_{wall})} + 2||\xi(t)||^2_{L^2(\Gamma^0_{wall})} + a||\eta_{x_1}(t)||^2_{L^2(\Gamma^0_{wall})}\right], \quad (5.26a)$$

$$G(t) := C^*\int_{t_0}^{t}||\boldsymbol{u}(\tau)||^q_{W^{1,q}(\Omega_\tau)}\,\mathrm{d}\tau + 2c\ \frac{\rho_s h_s}{\rho_f}\int_{t_0}^{t}||\xi_{x_1}(\tau)||^2_{L^2(\Gamma^0_{wall})}\,\mathrm{d}\tau, \quad (5.26b)$$

$$Q(t) := \frac{a^2(t-t_0)}{2\varepsilon}\frac{\rho_s h_s}{\rho_f}\left|\left|\frac{\partial^2 R_0}{\partial x_1^2}\right|\right|^2_{L^2(\Gamma^0_{wall})} + 2\kappa C^*(t-t_0), \quad (5.26c)$$

$$P(t) := \frac{2C_2}{\varepsilon^{q'/q}}\int_{t_0}^{t}\left[||\boldsymbol{f}||^{q'}_{L^{q'}(\Omega_\tau)} + ||P_{in}||^{q'}_{L^{q'}(\Gamma_{in})} + ||P_{out}||^{q'}_{L^{q'}(\Gamma_{out})} + ||P_{ext}||^{q'}_{L^{q'}(\Gamma_{wall})}\right]\mathrm{d}\tau. \quad (5.26d)$$

Using the notation (5.26a) - (5.26d) we can write the inequality (5.25) as follows

$$E(t)+G(t) \;\leq\; E(t_0)+2\varepsilon\,\frac{\rho_s h_s}{\rho_f}\int\limits_{t_0}^{t}||\xi(\tau)||^2_{L^2(\Gamma^0_{wall})}\,\mathrm{d}\tau+P(t)+Q(t). \tag{5.27}$$

From (5.26a) it is easy to see that

$$2\varepsilon\,\frac{\rho_s h_s}{\rho_f}\,||\xi(t)||^2_{L^2(\Gamma^0_{wall})} \;\leq\; \varepsilon E(t) \;\leq\; \varepsilon\Big[E(t)+G(t)\Big]$$

and consecutively for $t\in I$ we have

$$2\varepsilon\,\frac{\rho_s h_s}{\rho_f}\int\limits_{t_0}^{t}||\xi(\tau)||^2_{L^2(\Gamma^0_{wall})}\,\mathrm{d}\tau \;\leq\; \varepsilon\int\limits_{t_0}^{t}\Big[E(\tau)+G(\tau)\Big]\,\mathrm{d}\tau. \tag{5.28}$$

Inserting (5.28) into (5.27) we obtain the inequality

$$E(t)+G(t) \;\leq\; E(t_0)+\varepsilon\int\limits_{t_0}^{t}\Big[E(\tau)+G(\tau)\Big]\,\mathrm{d}\tau+P(t)+Q(t),$$

which is ready for the use of the Gronwall lemma, cf. (1.26)-(1.28). It yields final a priori estimate for the fluid-structure interaction problem based on the kinematic splitting technique, i.e.

$$E(t)+G(t) \;\leq\; e^{\varepsilon(t-t_0)}\Big[E(t_0)+P(t)+Q(t)\Big] \tag{5.29}$$

or in terms of energy norms

$$\begin{aligned}
&||\boldsymbol{u}(t)||^2_{L^2(\Omega_t)}+\frac{\rho_s h_s}{\rho_f}\left[b||\eta(t)||^2_{L^2(\Gamma^0_{wall})}+2||\xi(t)||^2_{L^2(\Gamma^0_{wall})}+a||\eta_{x_1}(t)||^2_{L^2(\Gamma^0_{wall})}\right]\\
&+\,C^*\int\limits_{t_0}^{t}||\boldsymbol{u}(\tau)||^q_{W^{1,q}(\Omega_\tau)}\,\mathrm{d}\tau+2c\,\frac{\rho_s h_s}{\rho_f}\int\limits_{t_0}^{t}||\xi_{x_1}(\tau)||^2_{L^2(\Gamma^0_{wall})}\,\mathrm{d}\tau\\
&\leq\;\; e^{\varepsilon(t-t_0)}\Bigg\{||\boldsymbol{u}(t_0)||^2_{L^2(\Omega_0)}+\frac{\rho_s h_s}{\rho_f}\left[b||\eta(t_0)||^2_{L^2(\Gamma^0_{wall})}+2||\xi(t_0)||^2_{L^2(\Gamma^0_{wall})}\right.\\
&\quad\left.+\,a||\eta_{x_1}(t_0)||^2_{L^2(\Gamma^0_{wall})}\right]+\frac{2C_2}{\varepsilon^{q'/q}}\int\limits_{t_0}^{t}\left[||\boldsymbol{f}(\tau)||^{q'}_{L^{q'}(\Omega_\tau)}+||P_{in}(\tau)||^{q'}_{L^{q'}(\Gamma_{in})}\right.\\
&\quad\left.+\,||P_{out}(\tau)||^{q'}_{L^{q'}(\Gamma_{out})}+||P_{ext}(\tau)||^{q'}_{L^{q'}(\Gamma_{wall})}\right]\mathrm{d}\tau\\
&\quad+\,\frac{a^2(t-t_0)}{2\varepsilon}\frac{\rho_s h_s}{\rho_f}\left|\left|\frac{\partial^2 R_0}{\partial x_1^2}\right|\right|^2_{L^2(\Gamma^0_{wall})}+2\kappa C^*(t-t_0)\Bigg\}.
\end{aligned}\tag{5.30}$$

Assuming ε to be sufficiently small, then the constant $e^{\varepsilon(t-t_0)}$ arising from the Gronwall lemma acquires a small value. We see that a priori estimates for our kinematic splitting fluid-structure interaction problem (4.22)-(4.23) are bounded only with given data. No

restrictions due to the structure movement appear. In other words, it holds

$$
\begin{aligned}
&||\boldsymbol{u}||_{L^\infty(I;L^2(\Omega_t))} + ||\boldsymbol{u}||_{L^q(I;W^{1,q}(\Omega_t))} + ||\xi_{x_1}||_{L^2(I;L^2(\Gamma^0_{wall}))} \\
&+ ||\eta||_{L^\infty(I;L^2(\Gamma^0_{wall}))} + ||\xi||_{L^\infty(I;L^2(\Gamma^0_{wall}))} + ||\eta_{x_1}||_{L^\infty(I;L^2(\Gamma^0_{wall}))} \\
&\leq C\ \big(||\boldsymbol{u}(t_0)||_{L^2(\Omega_0)},\ ||\eta(t_0)||_{L^2(\Gamma^0_{wall})},\ ||\xi(t_0)||_{L^2(\Gamma^0_{wall})},\ ||\eta_{x_1}(t_0)||_{L^2(\Gamma^0_{wall})}, \\
&\qquad ||\boldsymbol{f}||_{L^\infty(I;L^{q'}(\Omega_t))},\ ||P_{in}||_{L^\infty(I;L^{q'}(\Gamma_{in}))},\ ||P_{out}||_{L^\infty(I;L^{q'}(\Gamma_{out}))}, \\
&\qquad ||P_{ext}||_{L^\infty(I;L^{q'}(\Gamma_{wall}))},\ ||R_0||_{H^2(0,L)}\big),
\end{aligned}
\tag{5.31}
$$

where C is a positive and nondecreasing function linear with respect to its arguments. From a priori estimate (5.31) we see that assuming

$$
\begin{aligned}
&\boldsymbol{u}(t_0) \in L^2(\Omega_0), \quad \eta(t_0) \in H^1(\Omega_0), \quad \boldsymbol{f} \in L^\infty(I;L^{q'}(\Omega_t)), \quad R_0 \in H^2(0,L), \\
&P_{in} \in L^\infty(I;L^{q'}(\Gamma_{in})), \quad P_{out} \in L^\infty(I;L^{q'}(\Gamma_{out})), \quad P_{ext} \in L^\infty(I;L^{q'}(\Gamma_{wall}))
\end{aligned}
$$

with $I = [t_0, T]$ we have the following regularity for the solution $\boldsymbol{u}$ and η

$$
\boldsymbol{u} \in L^q(I;V) \cap L^\infty(I;L^2(\Omega_t)), \tag{5.32}
$$

$$
\eta \in H^1(I;H^1(0,L)) \cap W^{1,\infty}(I;L^2(0,L)). \tag{5.33}
$$

Note that the functional spaces (5.32) and (5.33) obtained from a priori analysis coincide with the functional spaces V^F and V^S introduced in (4.13) and (4.14), respectively.

Moreover, let us point out that due to the use of the Reynold transport theorem, the same a priori estimate is obtained for both, the conservative as well as the non-conservative weak formulation. However, in the analysis of stability of the semi-discrete problem from non-conservative weak formulation a stability constrain can appear. This will be discussed in more detail in the following section.

5.2 Stability analysis of semi-discrete problem

We derive an energy estimate for the discretized problem (4.22)-(4.23). The coupling condition allows us to rewrite the hydrodynamic part of structure equation in terms of the wall velocity ξ. This is a suitable form for numerical simulations, cf. Chapter 7.

Let us consider the following uniform partition of the time interval $I = [0,T]$: $0 = t_0 < t^1 < \cdots < t^N = T$ with the time step size $\triangle t = t^{n+1} - t^n$ for $n = 0, \cdots, N-1$. Time discretization of our problem is done as follows: we start with the fluid equation in Ω^n (i.e. Ω_t for $t = t^n$). For $n \geq 0$, $\boldsymbol{u}^n$ and ξ^n being known, we compute new velocities $\tilde{\boldsymbol{u}}^{n+1}$, pressures $\tilde{p}^{n+1}$ and the wall velocity $\xi^{n+\frac{1}{2}}$. Herewith the computation of the operator A, cf. (4.22), is completed and we proceed with the operator B. From the elastic load of structure new wall displacement η^{n+1} and new wall velocity ξ^{n+1} are computed. Knowing η^{n+1} the geometry is updated from Ω^n to Ω^{n+1} and new values of fluid velocity $\boldsymbol{u}^{n+1}$ and pressure p^{n+1} are mapped onto Ω^{n+1}. It means $\tilde{\boldsymbol{u}}^{n+1} = \boldsymbol{u}^{n+1} \circ \mathcal{A}_{t^{n+1}} \circ \mathcal{A}^{-1}_{t^n}$ and $\tilde{p}^{n+1} = p^{n+1} \circ \mathcal{A}_{t^{n+1}} \circ \mathcal{A}^{-1}_{t^n}$, where $\mathcal{A}_{t^n}$ is the ALE mapping from a reference domain Ω^0 onto Ω^n. Moreover, we will use the notation $\mathcal{A}_{t^n,t^{n+1}} := \mathcal{A}_{t^{n+1}} \circ \mathcal{A}^{-1}_{t^n}$ for the ALE mapping between two time levels t^n and t^{n+1}. In order to update the domain Ω^n we need to define the grid velocity $\boldsymbol{w}$. First, we set $\boldsymbol{w}|_{\Gamma_{wall}} \cdot \boldsymbol{e}_r = \xi^{n+1}$. In order to define grid velocity also inside Ω^n we may solve an auxiliary problem, e.g. cf. [41]. For $\boldsymbol{x}^n \in \Omega^n$ and $\Theta^{n+1} := (0, \eta^{n+1})$

$$
\begin{aligned}
&\Delta_Y \boldsymbol{x} = 0 \quad \text{for} \quad Y \in \Omega^0, \\
&\boldsymbol{x} := \mathcal{A}_t(\boldsymbol{Y}) = \boldsymbol{x}^n + \Theta^{n+1} \quad \text{on} \quad \Gamma^{n+1}_{wall}, \\
&\boldsymbol{x} = \boldsymbol{x}^n \quad \text{on} \quad \partial\Omega^{n+1} \setminus \Gamma^{n+1}_{wall}.
\end{aligned}
$$

Consequently, we get $\boldsymbol{x}^{n+1} = \boldsymbol{x}$ and compute the grid velocity as $\boldsymbol{w}^{n+1} := \dfrac{\boldsymbol{x}^{n+1} - \boldsymbol{x}^n}{t^{n+1} - t^n}$. As in [41] the above auxiliary problem can be approximated with higher order finite elements, so that the (discrete) ALE mapping and correspondingly the grid velocity satisfy the required regularity; in particular $\boldsymbol{w}^n \in W^{1,\infty}(\Omega^n)$. In order to define $\boldsymbol{x}(t),\ t \in (t^n, t^{n+1}]$ we can use the linear interpolation in time

$$\boldsymbol{x}(t) = \mathcal{A}_t(\boldsymbol{Y}) := \frac{t - t^n}{t^{n+1} - t^n}\ \mathcal{A}_{t^{n+1}}(\boldsymbol{Y}) + \frac{t^{n+1} - t}{t^{n+1} - t^n}\ \mathcal{A}_{t^n}(\boldsymbol{Y}), \quad t \in (t^n, t^{n+1}]. \tag{5.34}$$

Now, we can define $\boldsymbol{w}(t)$ as

$$\boldsymbol{w}(\boldsymbol{x}(t), t) = \frac{\boldsymbol{x}(t) - \boldsymbol{x}^n}{t - t^n}. \tag{5.35}$$

In what follows our aim is to derive an energy estimate for the operator splitting scheme (4.22)-(4.23). To this end we derive firstly a suitable semi-discrete scheme for the operator A. Let us start with the discrete counterpart to the weak formulation (4.25a)-(4.25b), where the time derivative will be approximated by the backward Euler method. The first order Euler scheme has been chosen for convenience. Analysis for the second order schemes, e.g. the Crank-Nicolson scheme, would be analogous. Taking the test function $\tilde{\boldsymbol{u}}^{n+1}$ in the discrete form of (4.25a) and assuming that $\tilde{\boldsymbol{u}}^{n+1}$ is divergence-free we obtain

$$\begin{aligned}
&\int_{\Omega^n} \frac{\tilde{\boldsymbol{u}}^{n+1} - \boldsymbol{u}^n}{\Delta t} \cdot \tilde{\boldsymbol{u}}^{n+1}\ \mathrm{d}\omega + \frac{2}{\rho_f} \int_{\Omega^n} \mu(|\mathbf{D}(\tilde{\boldsymbol{u}}^{n+1})|)\ \mathbf{D}(\tilde{\boldsymbol{u}}^{n+1}) : \mathbf{D}(\tilde{\boldsymbol{u}}^{n+1})\ \mathrm{d}\omega \\
&+ \int_{\Omega^n} [(\tilde{\boldsymbol{u}}^{n+1} - \boldsymbol{w}^n) \cdot \tilde{\boldsymbol{u}}^{n+1}] \cdot \tilde{\boldsymbol{u}}^{n+1}\ \mathrm{d}\omega \quad = \quad \frac{1}{\rho_f} \int_{\Omega^n} \boldsymbol{f}^{n+1} \cdot \tilde{\boldsymbol{u}}^{n+1}\ \mathrm{d}\omega \\
&- \frac{\rho_s h_s}{\rho_f} \int_{\Gamma^0_{wall}} \left[\frac{\xi^{n+\frac{1}{2}} - \xi^n}{\Delta t}\right] \xi^{n+\frac{1}{2}}\ \mathrm{d}l_0 - \ c\ \frac{\rho_s h_s}{\rho_f} \int_{\Gamma^0_{wall}} \left[\frac{\partial \xi^{n+\frac{1}{2}}}{\partial x_1}\right]^2\ \mathrm{d}l_0 \\
&- \frac{1}{\rho_f} \int_{\Gamma^n_{wall}} \frac{P_{ext}(t^{n+1})\ \tilde{u}_2^{n+1}}{\sqrt{1 + (\partial_{x_1} R_0)^2}}\ \mathrm{d}l + \ \frac{1}{\rho_f} \int_0^{R_0(0)} \Big(P_{in}(t^{n+1}) - \frac{1}{2}\big|\tilde{\boldsymbol{u}}^{n+1}\big|^2\Big) \tilde{u}_1^{n+1}\big|_{x_1=0}\ \mathrm{d}x_2 \\
&- \frac{1}{\rho_f} \int_0^{R_0(L)} \Big(P_{out}(t^{n+1}) - \frac{1}{2}\big|\tilde{\boldsymbol{u}}^{n+1}\big|^2\Big) \tilde{u}_1^{n+1}\big|_{x_1=L}\ \mathrm{d}x_2.
\end{aligned} \tag{5.36}$$

We consider here only semi-discrete scheme having space continuous representation. To simplify the matter we assume that we have divergence-free velocities on Ω^n. In our numerical scheme this is realized through the artificial compressibility approach. More precisely, the solenoidal condition is replaced by

$$-\varepsilon \Delta \tilde{p}^{n+1} + \nabla \cdot \tilde{\boldsymbol{u}}^{n+1} = 0 \quad \text{on } \Omega^n.$$

Here ε is a small positive constant, $\varepsilon \approx \triangle h^2$, where $\triangle h$ denotes the grid size. See also recent theoretical work by Hundertmark, Lukáčová and Nečasová [59], where the artificial compressibility approach is used to show the existence of a weak solution and [93]. Another approach to deal with the divergence-free condition on moving domains has been used in the projection semi-implicit FSI scheme by Fernández, Gerbeau and Grandmont [37], where the pressure projection step (Chorin projection) is applied as an implicit coupling.

Rewriting the convective term from (5.36) analogously to (5.6), i.e.

$$\begin{aligned}
\int_{\Omega^n} [(\tilde{\boldsymbol{u}}^{n+1} - \boldsymbol{w}^n) \cdot \tilde{\boldsymbol{u}}^{n+1}] \cdot \tilde{\boldsymbol{u}}^{n+1}\ \mathrm{d}\omega \ &= \ -\frac{1}{2} \int_{\Omega^n} |\tilde{\boldsymbol{u}}^{n+1}|^2 \bigtriangledown \cdot (\tilde{\boldsymbol{u}}^{n+1} - \boldsymbol{w}^n)\ \mathrm{d}\omega \\
&- \frac{1}{2} \int_0^{R_0(0)} \big|\tilde{\boldsymbol{u}}^{n+1}\big|^2\ \tilde{u}_1^{n+1}\big|_{x=0}\ \mathrm{d}x_2 + \frac{1}{2} \int_0^{R_0(L)} \big|\tilde{\boldsymbol{u}}^{n+1}\big|^2\ \tilde{u}_1^{n+1}\big|_{x=L}\ \mathrm{d}x_2
\end{aligned} \tag{5.37}$$

and inserting (5.37) into (5.36) we obtain the following integral equation for the semi-discrete operator A

$$\begin{aligned}
&\int_{\Omega^n} \frac{\tilde{\boldsymbol{u}}^{n+1} - \boldsymbol{u}^n}{\Delta t} \cdot \tilde{\boldsymbol{u}}^{n+1} \, \mathrm{d}\omega + \frac{2}{\rho_f} \int_{\Omega^n} \mu(|\mathbf{D}(\tilde{\boldsymbol{u}}^{n+1})|) \, \mathbf{D}(\tilde{\boldsymbol{u}}^{n+1}) : \mathbf{D}(\tilde{\boldsymbol{u}}^{n+1}) \, \mathrm{d}\omega \\
&+ \frac{1}{2} \int_{\Omega^n} |\tilde{\boldsymbol{u}}^{n+1}|^2 \bigtriangledown \cdot \boldsymbol{w}^n \, \mathrm{d}\omega \quad = \quad \frac{1}{\rho_f} \int_{\Omega^n} \boldsymbol{f}^{n+1} \cdot \tilde{\boldsymbol{u}}^{n+1} \, \mathrm{d}\omega - \frac{1}{\rho_f} \int_{\Gamma^n_{wall}} \frac{P_{ext}(t^{n+1}) \, \tilde{u}_2^{n+1}}{\sqrt{1 + (\partial_{x_1} R_0)^2}} \, \mathrm{d}l \\
&- \frac{\rho_s h_s}{\rho_f} \int_{\Gamma^0_{wall}} \left[\frac{\xi^{n+\frac{1}{2}} - \xi^n}{\Delta t} \right] \xi^{n+\frac{1}{2}} \, \mathrm{d}l_0 - c \, \frac{\rho_s h_s}{\rho_f} \int_{\Gamma^0_{wall}} \left[\frac{\partial \xi^{n+\frac{1}{2}}}{\partial x_1} \right]^2 \mathrm{d}l_0 \\
&+ \frac{1}{\rho_f} \int_0^{R_0(0)} P_{in}(t^{n+1}) \tilde{u}_1^{n+1}|_{x_1=0} \, \mathrm{d}x_2 - \frac{1}{\rho_f} \int_0^{R_0(L)} P_{out}(t^{n+1}) \tilde{u}_1^{n+1}|_{x_1=L} \, \mathrm{d}x_2. \qquad (5.38)
\end{aligned}$$

The operator B will be discretized in time via the Crank-Nicolson scheme as follows i.e.

$$\frac{\eta^{n+1} - \eta^n}{\Delta t} = \frac{1}{2}\left(\xi^{n+1} + \xi^{n+\frac{1}{2}}\right), \qquad (5.39)$$

$$\frac{\xi^{n+1} - \xi^{n+\frac{1}{2}}}{\Delta t} = \frac{a}{2}\left(\eta^{n+1}_{x_1 x_1} + \eta^n_{x_1 x_1}\right) - \frac{b}{2}\left(\eta^{n+1} + \eta^n\right) + G(R_0). \qquad (5.40)$$

Recall that the parameters a, b and c from (5.38) and (5.40) are defined in (2.30). The discrete scheme (5.39)-(5.40) is also reported in literature as the Newmark scheme. Next, we derive energy estimates for the operator A and the operator B, respectively.

5.2.1 Energy estimate for the operator A

For each time step $t = t^{n+1}$ we look for an energy estimate of the non-conservative discrete weak formulation of the momentum equation (5.38). In order to control the energy of the operator A we firstly apply the Young inequality for the time-difference term

$$\int_{\Omega^n} \tilde{\boldsymbol{u}}^{n+1} \cdot \frac{\tilde{\boldsymbol{u}}^{n+1} - \boldsymbol{u}^n}{\Delta t} \, \mathrm{d}\omega \quad \geq \quad \frac{1}{2\Delta t} \, ||\tilde{\boldsymbol{u}}^{n+1}||^2_{L^2(\Omega^n)} - \frac{1}{2\Delta t} \, ||\boldsymbol{u}^n||^2_{L^2(\Omega^n)}. \qquad (5.41)$$

Applying the same arguments as in the Section 5.1.1, cf. (5.8)-(5.11), but on the semi-discrete problem, we can estimate the viscous term from (5.38) by

$$\frac{2}{\rho_f} \int_{\Omega^n} \mu(|\mathbf{D}(\tilde{\boldsymbol{u}}^{n+1})|) \, \mathbf{D}(\tilde{\boldsymbol{u}}^{n+1}) : \mathbf{D}(\tilde{\boldsymbol{u}}^{n+1}) \, \mathrm{d}\omega \quad \geq \quad C^* ||\tilde{\boldsymbol{u}}^{n+1}||^q_{W^{1,q}(\Omega^n)} - \kappa C^*, \quad (5.42)$$

where $\kappa := 0$ for $q \geq 2$ and $\kappa = 1$ for $1 \leq q < 2$.

Third term from (5.38) contains the domain velocity function. It can be bounded from above by

$$-\int_{\Omega^n} |\tilde{\boldsymbol{u}}^{n+1}|^2 \bigtriangledown \cdot \boldsymbol{w}^n \, \mathrm{d}\omega \quad \leq \quad \alpha^n \, ||\tilde{\boldsymbol{u}}^{n+1}||^2_{L^2(\Omega^n)}, \qquad (5.43)$$

where $\alpha^n := || \bigtriangledown \cdot \boldsymbol{w}^n||_{L^\infty(\Omega^n)}$.

Moreover, using the Young inequality we can estimate the source term by

$$\frac{1}{\rho_f} \int_{\Omega^n} \tilde{\boldsymbol{u}}^{n+1} \cdot \boldsymbol{f}^{n+1} \, \mathrm{d}\omega \quad \leq \quad C_1 \varepsilon \, ||\tilde{\boldsymbol{u}}^{n+1}||^q_{L^q(\Omega^n)} + \frac{C_2}{\varepsilon^{q'/q}} \, ||\boldsymbol{f}^{n+1}||^{q'}_{L^{q'}(\Omega^n)}, \qquad (5.44)$$

where $q' \geq 1$, such that $1/q + 1/q' = 1$ and C_1, C_2 are positive constants.

Applying the Young and the trace inequality on the boundary terms with a prescribed pressure contribution we obtain

$$\begin{aligned}
\frac{1}{\rho_f}\int_0^{R_0(0)} P_{in}(t^{n+1})\ \tilde{u_1}^{n+1}|_{x_1=0}\ \mathrm{d}x_2 &\leq \frac{C_2}{\varepsilon_1^{q'/q}}\ ||P_{in}(t^{n+1})||^{q'}_{L^{q'}(\Gamma_{in})} \\
&\quad + \varepsilon_1 C_1 C_1^{tr}(\Omega^n)\ ||\tilde{\boldsymbol{u}}^{n+1}||^q_{W^{1,q}(\Omega^n)}, \quad (5.45)\\
\frac{1}{\rho_f}\int_0^{R_0(L)} -P_{out}(t^{n+1})\ \tilde{u_1}^{n+1}|_{x_1=L}\ \mathrm{d}x_2 &\leq \frac{C_2}{\varepsilon_2^{q'/q}}\ ||P_{out}(t^{n+1})||^{q'}_{L^{q'}(\Gamma_{out})} \\
&\quad + \varepsilon_2 C_1 C_2^{tr}(\Omega^n)\ ||\tilde{\boldsymbol{u}}^{n+1}||^q_{W^{1,q}(\Omega^n)}, \quad (5.46)\\
-\frac{1}{\rho_f}\int_{\Gamma^n_{wall}} \frac{P_{ext}(t^{n+1})\ \tilde{u}_2^{n+1}}{\sqrt{1+(\partial_{x_1}R_0)^2}}\ \mathrm{d}l &\leq \frac{KC_2}{\varepsilon_3^{q'/q}}\ ||P_{ext}(t^{n+1})||^{q'}_{L^{q'}(\Gamma^n_{wall})} \\
&\quad + \varepsilon_3 C_1 C_3^{tr}(\Omega^n)\ ||\tilde{\boldsymbol{u}}^{n+1}||^q_{W^{1,q}(\Omega^n)}, \quad (5.47)
\end{aligned}$$

where ε_i and $C_i^{tr}(\Omega^{n+1}), i \in \{1,2,3\}$, are positive constants and

$$K := \left\| [1+(\partial_{x_1}R_0)^2]^{-1/2} \right\|_{L^\infty(\Gamma^n_{wall})}.$$

Further estimates on Γ^0_{wall} are obtained using the Young inequality

$$\begin{aligned}
-\int_{\Gamma^0_{wall}} \frac{\xi^{n+\frac{1}{2}}-\xi^n}{\Delta t}\ \xi^{n+\frac{1}{2}}\ \mathrm{d}l_0 &\leq -\frac{1}{2\Delta t}\ ||\xi^{n+\frac{1}{2}}||^2_{L^2(\Gamma^0_{wall})} + \frac{1}{2\Delta t}\ ||\xi^n||^2_{L^2(\Gamma^0_{wall})}, \quad (5.48)\\
-c\int_{\Gamma^0_{wall}} \left[\frac{\partial \xi^{n+\frac{1}{2}}}{\partial x_1}\right]^2 \mathrm{d}l_0 &= -c||\xi_{x_1}^{n+\frac{1}{2}}\ ||^2_{L^2(\Gamma^0_{wall})}. \quad (5.49)
\end{aligned}$$

Let $C^{tr} := C_1^{tr} = C_2^{tr} = C_3^{tr}$ and $\varepsilon := \varepsilon_1 = \varepsilon_2 = \varepsilon_3/K$. Inserting (5.41)-(5.49) into (5.38) we obtain

$$\begin{aligned}
&\frac{1}{2\Delta t}\left[||\tilde{\boldsymbol{u}}^{n+1}||^2_{L^2(\Omega^n)} - ||\boldsymbol{u}^n||^2_{L^2(\Omega^n)}\right] + C^*\left[||\tilde{\boldsymbol{u}}^{n+1}||^q_{W^{1,q}(\Omega^n)} - \kappa\right]\\
&+\frac{\rho_s h_s}{\rho_f}\left[\frac{1}{2\Delta t}\ ||\xi^{n+\frac{1}{2}}||^2_{L^2(\Gamma^0_{wall})} - \frac{1}{2\Delta t}\ ||\xi^n||^2_{L^2(\Gamma^0_{wall})} + c\ ||\xi_{x_1}^{n+\frac{1}{2}}||^2_{L^2(\Gamma^0_{wall})}\right]\\
&\leq \frac{\alpha^n}{2}\ ||\tilde{\boldsymbol{u}}^{n+1}||^2_{L^2(\Omega^n)} + \varepsilon C_1\ ||\tilde{\boldsymbol{u}}^{n+1}||^q_{L^q(\Omega^n)} + 3\varepsilon C_1 C^{tr}(\Omega^n)\ ||\tilde{\boldsymbol{u}}^{n+1}||^q_{W^{1,q}(\Omega^n)}\\
&\quad + \frac{C_2}{\varepsilon^{q'/q}}\ \mathrm{RHS}^{n+1}, \quad (5.50)
\end{aligned}$$

where

$$\begin{aligned}
\mathrm{RHS}^{n+1} &:= ||P_{in}(t^{n+1})||^{q'}_{L^{q'}(\Gamma_{in})} + ||P_{out}(t^{n+1})||^{q'}_{L^{q'}(\Gamma_{out})} + ||P_{ext}(t^{n+1})||^{q'}_{L^{q'}(\Gamma^n_{wall})}\\
&\quad + ||\boldsymbol{f}^{n+1}||^{q'}_{L^{q'}(\Omega^{n+1})}. \quad (5.51)
\end{aligned}$$

Moreover, let $\varepsilon > 0$ be sufficiently small, such that $\varepsilon < C^*/(2C_1(1+3C^{tr}))$. Then it holds

$$\begin{aligned}
&C^*||\tilde{\boldsymbol{u}}^{n+1}||^q_{W^{1,q}(\Omega^n)} - \varepsilon C_1||\tilde{\boldsymbol{u}}^{n+1}||^q_{L^q(\Omega^n)} - 3\varepsilon C_1 C^{tr}(\Omega_t)||\tilde{\boldsymbol{u}}^{n+1}||^q_{W^{1,q}(\Omega^n)}\\
&\qquad \geq \frac{C^*}{2}||\tilde{\boldsymbol{u}}^{n+1}||^q_{W^{1,q}(\Omega^n)}. \quad (5.52)
\end{aligned}$$

Multiplying (5.50) by $2\Delta t$ and using the estimate (5.52) we have

$$
\begin{aligned}
&||\tilde{\boldsymbol{u}}^{n+1}||^2_{L^2(\Omega^n)} + C^*\Delta t\ ||\tilde{\boldsymbol{u}}^{n+1}||^q_{W^{1,q}(\Omega^n)} \\
&+\frac{\rho_s h_s}{\rho_f}\ \left[||\xi^{n+\frac{1}{2}}||^2_{L^2(\Gamma^0_{wall})} - ||\xi^n||^2_{L^2(\Gamma^0_{wall})} + 2c\ \Delta t\ ||\xi^{n+\frac{1}{2}}_{x_1}||^2_{L^2(\Gamma^0_{wall})}\right] \\
&\leq ||\boldsymbol{u}^n||^2_{L^2(\Omega^n)} + \alpha^n\Delta t\ ||\tilde{\boldsymbol{u}}^{n+1}||^2_{L^2(\Omega^n)} + \frac{2\Delta t C_2}{\varepsilon^{q'/q}}\ \mathrm{RHS}^{\mathrm{n+1}} + 2C^*\kappa\ \Delta t. \qquad (5.53)
\end{aligned}
$$

The basic idea of implementation of time dependent domain requires that a numerical scheme should reproduce a constant solution, cf. [68, 80]. As a consequence we will assume that the so-called **Geometric Conservation Law** (GCL) holds true, i.e.

$$
\int_{\Omega^{n+1}} \mathrm{d}\omega - \int_{\Omega^n} \mathrm{d}\omega = \int_{t^n}^{t^{n+1}} \int_{\Omega_t} \bigtriangledown \cdot \boldsymbol{w}\ \mathrm{d}\omega\ \mathrm{d}t, \qquad (5.54)
$$

where $\boldsymbol{w}(\boldsymbol{x},t),\ t \in (t^n, t^{n+1}]$ is defined in (5.35). Analogously, from the Reynold transport theorem the following formula can be derived, see also [41, 81]

$$
||\boldsymbol{u}^{n+1}||^2_{L^2(\Omega^{n+1})} - ||\tilde{\boldsymbol{u}}^{n+1}||^2_{L^2(\Omega^n)} = \int\limits_{t^n}^{t^{n+1}} \int\limits_{\Omega_t} |\tilde{\boldsymbol{u}}|^2\ \bigtriangledown \cdot \boldsymbol{w}\ \mathrm{d}\omega\ \mathrm{d}t. \qquad (5.55)
$$

Here $\tilde{\boldsymbol{u}} := \boldsymbol{u}^{n+1} \circ \mathcal{A}_{t,t^{n+1}}$ and we used the fact that $\boldsymbol{u}^{n+1}(\boldsymbol{x}) = \sum\limits_{i=1}^{\infty} u_i^{n+1}\psi_i(\boldsymbol{x}),\ \boldsymbol{x} \in \Omega^{n+1}$, where $\psi_i(\boldsymbol{x}) = \psi_i(\mathcal{A}_t(\boldsymbol{Y}))$ and $\psi_i(\boldsymbol{Y}), i \in \mathbb{N}$ are the basis functions from $W^{1,q}(\Omega^0)$. Denoting $DJ_{\mathcal{A}}$ the determinant of the Jacobian matrix of the ALE mapping the right hand side of (5.55) can be further estimated in the following way

$$
\begin{aligned}
&\int\limits_{t^n}^{t^{n+1}} \int\limits_{\Omega_t} |\tilde{\boldsymbol{u}}|^2\ \bigtriangledown \cdot \boldsymbol{w}\ \mathrm{d}\omega\ \mathrm{d}t = \int\limits_{t^n}^{t^{n+1}} \int\limits_{\Omega^n} |\boldsymbol{u}^n|^2\ \bigtriangledown \cdot \boldsymbol{w}\ |DJ^{-1}_{\mathcal{A}_{t^n,t^{n+1}}}(t)|\ \mathrm{d}\omega\ \mathrm{d}t \\
&\leq \int\limits_{t^n}^{t^{n+1}} ||\bigtriangledown \cdot \boldsymbol{w}\ |DJ^{-1}_{\mathcal{A}_{t^n,t^{n+1}}}|\ ||_{L^\infty(\Omega^n)} \int\limits_{\Omega^n} |\boldsymbol{u}^n|^2\ \mathrm{d}\omega\ \mathrm{d}t \quad \leq \quad \beta^n\Delta t\ ||\boldsymbol{u}^n||^2_{L^2(\Omega^n)}, \qquad (5.56)
\end{aligned}
$$

where $\beta^n := \sup\limits_{t\in(t^n,t^{n+1})} \left\{||\bigtriangledown \cdot \boldsymbol{w}| DJ^{-1}_{\mathcal{A}_{t^n,t^{n+1}}}|\ ||_{L^\infty(\Omega^n)}\right\}$. Inserting (5.56) to (5.55) we obtain the estimate

$$
||\tilde{\boldsymbol{u}}^{n+1}||^2_{L^2(\Omega^n)} \geq ||\boldsymbol{u}^{n+1}||^2_{L^2(\Omega^{n+1})} - \beta^n\Delta t\ ||\boldsymbol{u}^n||^2_{L^2(\Omega^n)}. \qquad (5.57)
$$

Moreover, using the GCL condition (5.55) we can rewrite the second term on the right hand side of (5.53) in the following way

$$
\alpha^n\Delta t||\tilde{\boldsymbol{u}}^{n+1}||^2_{L^2(\Omega^n)} \leq \alpha^n\Delta t||\boldsymbol{u}^{n+1}||^2_{L^2(\Omega^{n+1})} + \alpha^n\beta^n(\Delta t)^2||\boldsymbol{u}^n||^2_{L^2(\Omega^n)}. \qquad (5.58)
$$

Finally, using the inequalities (5.57) and (5.58) we can rewrite (5.53) as follows

$$
\begin{aligned}
&||\boldsymbol{u}^{n+1}||^2_{L^2(\Omega^{n+1})} - ||\boldsymbol{u}^n||^2_{L^2(\Omega^n)} + C^*\Delta t\ ||\tilde{\boldsymbol{u}}^{n+1}||^q_{W^{1,q}(\Omega^n)} \\
&+\ \frac{\rho_s h_s}{\rho_f}\ \left[||\xi^{n+\frac{1}{2}}||^2_{L^2(\Gamma^0_{wall})} - ||\xi^n||^2_{L^2(\Gamma^0_{wall})} + 2c\ \Delta t\ ||\xi^{n+\frac{1}{2}}_{x_1}||^2_{L^2(\Gamma^0_{wall})}\right] \\
&\leq \beta^n\Delta t(1+\alpha^n\Delta t)||\boldsymbol{u}^n||^2_{L^2(\Omega^n)} + \alpha^n\Delta t||\boldsymbol{u}^{n+1}||^2_{L^2(\Omega^{n+1})} \\
&+\frac{2\Delta t C_2}{\varepsilon^{q'/q}}\ \mathrm{RHS}^{\mathrm{n+1}} + 2C^*\kappa\ \Delta t. \qquad (5.59)
\end{aligned}
$$

Summing (5.59) for the first $n+1$ time steps we obtain the following estimate for the operator A

$$
\begin{aligned}
&||\boldsymbol{u}^{n+1}||^2_{L^2(\Omega^{n+1})} + C^*\Delta t \ \sum_{i=0}^{n} ||\tilde{\boldsymbol{u}}^{i+1}||^q_{W^{1,q}(\Omega^i)} \\
&+\frac{\rho_s h_s}{\rho_f} \sum_{i=0}^{n} \left[||\xi^{i+\frac{1}{2}}||^2_{L^2(\Gamma^0_{wall})} - ||\xi^i||^2_{L^2(\Gamma^0_{wall})} + 2c\ \Delta t\ ||\xi^{i+\frac{1}{2}}_{x_1}||^2_{L^2(\Gamma^0_{wall})} \right] \\
&\leq \left[1 + \Delta t\beta^0 + (\Delta t)^2\alpha^0\beta^0 \right] ||\boldsymbol{u}^0||^2_{L^2(\Omega^0)} + \Delta t \sum_{i=1}^{n+1} \left[\beta^i(1+\alpha^i\Delta t) + \alpha^{i-1} \right] ||\boldsymbol{u}^i||^2_{L^2(\Omega^i)} \\
&+\frac{2\Delta t C_2}{\varepsilon^{q'/q}} \ \sum_{i=1}^{n+1} \mathrm{RHS}^{\mathrm{i}} + 2C^*\kappa\ T. \qquad (5.60)
\end{aligned}
$$

5.2.2 Energy estimate for the operator B

The goal of this section is to find an energy estimate for the semi-discrete scheme (5.39)-(5.40). Multiplying the equation (5.39) by $b(\eta^{n+1}+\eta^n)$ and the equation (5.40) by $(\xi^{n+1}+\xi^{n+\frac{1}{2}})$ we obtain

$$
\begin{aligned}
b\ \frac{(\eta^{n+1})^2-(\eta^n)^2}{\Delta t} &= \frac{b}{2}\big(\xi^{n+1}+\xi^{n+\frac{1}{2}}\big)\ (\eta^{n+1}+\eta^n), \qquad (5.61)\\
\frac{(\xi^{n+1})^2-(\xi^{n+\frac{1}{2}})^2}{\Delta t} &= \frac{a}{2}\big(\eta^{n+1}_{x_1x_1}+\eta^n_{x_1x_1}\big)\ (\xi^{n+1}+\xi^{n+\frac{1}{2}}) - \frac{b}{2}\big(\eta^{n+1}+\eta^n\big)\ (\xi^{n+1}+\xi^{n+\frac{1}{2}}) \\
&\quad + G(R_0)(\xi^{n+1}+\xi^{n+\frac{1}{2}}). \qquad (5.62)
\end{aligned}
$$

Summing (5.61) and (5.62), rewriting the left hand side and integrating over Γ^0_{wall} we obtain the following equation

$$
\begin{aligned}
&\int_{\Gamma^0_{wall}} \left(b\ \frac{(\eta^{n+1})^2-(\eta^n)^2}{\Delta t} + \frac{(\xi^{n+1})^2-(\xi^n)^2}{\Delta t} + \frac{(\xi^n)^2-(\xi^{n+\frac{1}{2}})^2}{\Delta t} \right) \mathrm{d}l_0 \\
&= \int_{\Gamma^0_{wall}} \frac{a}{2}\big(\eta^{n+1}_{x_1x_1}+\eta^n_{x_1x_1}\big)\ (\xi^{n+1}+\xi^{n+\frac{1}{2}})\ \mathrm{d}l_0 + \int_{\Gamma^0_{wall}} G(R_0)(\xi^{n+1}+\xi^{n+\frac{1}{2}})\ \mathrm{d}l_0. \qquad (5.63)
\end{aligned}
$$

For the sake of simplicity let us assume that we have zero boundary conditions for η, see (4.9). Then using (5.39) and integration by parts the right hand side of (5.63) reads as follows

$$
\begin{aligned}
\frac{a}{2}\int_{\Gamma^0_{wall}} \big(\eta^{n+1}_{x_1x_1}+\eta^n_{x_1x_1}\big)\ (\xi^{n+1}+\xi^{n+\frac{1}{2}})\ \mathrm{d}l_0 &= -a\int_{\Gamma^0_{wall}} \frac{(\eta^{n+1}_{x_1})^2-(\eta^n_{x_1})^2}{\Delta t}\ \mathrm{d}l_0, \qquad (5.64)\\
\int_{\Gamma^0_{wall}} G(R_0)(\xi^{n+1}+\xi^{n+\frac{1}{2}})\ \mathrm{d}l_0 &= \frac{2}{\Delta t}\int_{\Gamma^0_{wall}} G(R_0)(\eta^{n+1}-\eta^n)\ \mathrm{d}l_0. \qquad (5.65)
\end{aligned}
$$

Inserting (5.64) and (5.65) into (5.63) and summing from 0 to n we obtain

$$
\begin{aligned}
&a\ ||\eta^{n+1}_{x_1}||^2_{L^2(\Gamma^0_{wall})} + b\ ||\eta^{n+1}||^2_{L^2(\Gamma^0_{wall})} + ||\xi^{n+1}||^2_{L^2(\Gamma^0_{wall})} \\
&\leq a||\eta^0_{x_1}||^2_{L^2(\Gamma^0_{wall})} + b\ ||\eta^0||^2_{L^2(\Gamma^0_{wall})} + ||\xi^0||^2_{L^2(\Gamma^0_{wall})} \\
&\quad +\sum_{i=0}^{n} \Big(||\xi^{i+\frac{1}{2}}||^2_{L^2(\Gamma^0_{wall})} - ||\xi^i||^2_{L^2(\Gamma^0_{wall})} \Big) + \int_{\Gamma^0_{wall}} 2G(R_0)(\eta^{n+1}-\eta^0)\ \mathrm{d}l_0. \qquad (5.66)
\end{aligned}
$$

Recall that $G(R_0) := a\dfrac{\partial^2 R_0}{\partial x_1^2}$. Now, for small positive numbers $\delta_1,\ \delta_2$ the integral in (5.66) can be estimates as follows

$$\int_{\Gamma^0_{wall}} 2G(R_0)\ (\eta^{n+1}-\eta^0)\ \mathrm{d}l_0 \ \leq\ 2aL\Bigg[\frac{|\Gamma^0_{wall}|}{4\ \delta_1}+\frac{|\Gamma^0_{wall}|}{4\ \delta_2}+\delta_1||\eta^{n+1}||^2_{L^2(\Gamma^0_{wall})} + \delta_2||\eta^0||^2_{L^2(\Gamma^0_{wall})}\Bigg],$$

where $L := \left\|\dfrac{\partial^2 R_0}{\partial x_1^2}\right\|^2_{L^\infty(\Gamma^0_{wall})}$. Let $\delta_1=\delta_2=:\delta$ be sufficiently small such that $aL\delta \leq b/4$, then

$$\int_{\Gamma^0_{wall}} 2G(R_0)\ (\eta^{n+1}-\eta^0)\ \mathrm{d}l_0 \ \leq\ \frac{aL|\Gamma^0_{wall}|}{\delta}+\frac{b}{2}\Big[||\eta^{n+1}||^2_{L^2(\Gamma^0_{wall})}+||\eta^0||^2_{L^2(\Gamma^0_{wall})}\Big]. \quad (5.67)$$

Inserting (5.67) into (5.66) we obtain an estimate of the operator B

$$\begin{aligned}
&a||\eta^{n+1}_{x_1}||^2_{L^2(\Gamma^0_{wall})}+\frac{b}{2}\ ||\eta^{n+1}||^2_{L^2(\Gamma^0_{wall})}+||\xi^{n+1}||^2_{L^2(\Gamma^0_{wall})}\\
&\leq a||\eta^0_{x_1}||^2_{L^2(\Gamma^0_{wall})}+\frac{3b}{2}\ ||\eta^0||^2_{L^2(\Gamma^0_{wall})}+||\xi^0||^2_{L^2(\Gamma^0_{wall})}\\
&\quad+\sum_{i=0}^{n}\Big(||\xi^{i+\frac{1}{2}}||^2_{L^2(\Gamma^0_{wall})}-||\xi^i||^2_{L^2(\Gamma^0_{wall})}\Big)+\frac{aL|\Gamma^0_{wall}|}{\delta}. \qquad (5.68)
\end{aligned}$$

Note that in our model we have $\eta^0=0$ and $\xi^0=u_2^0|_{\Gamma_{wall}}$.

5.2.3 Energy estimate of the coupled problem

Combining the estimates for the operator A, cf. (5.60), with the operator B, cf. (5.68), we obtain

$$\begin{aligned}
&||\boldsymbol{u}^{n+1}||^2_{L^2(\Omega^{n+1})}+\frac{\rho_s h_s}{\rho_f}\Big[a||\eta^{n+1}_{x_1}||^2_{L^2(\Gamma^0_{wall})}+\frac{b}{2}\ ||\eta^{n+1}||^2_{L^2(\Gamma^0_{wall})}+||\xi^{n+1}||^2_{L^2(\Gamma^0_{wall})}\Big]\\
&+C^*\Delta t\ \sum_{i=0}^{n}||\tilde{\boldsymbol{u}}^{i+1}||^q_{W^{1,q}(\Omega^i)}+2c\ \frac{\rho_s h_s}{\rho_f}\ \Delta t\ \sum_{i=0}^{n}||\xi^{i+\frac{1}{2}}_{x_1}||^2_{L^2(\Gamma^0_{wall})}\\
&\leq ||\boldsymbol{u}^0||^2_{L^2(\Omega^0)}+\frac{\rho_s h_s}{\rho_f}\Big[a||\eta^0_{x_1}||^2_{L^2(\Gamma^0_{wall})}+\frac{b}{2}\ ||\eta^0||^2_{L^2(\Gamma^0_{wall})}+||\xi^0||^2_{L^2(\Gamma^0_{wall})}\Big]\\
&\quad+\Big[\Delta t\beta^0+(\Delta t)^2\alpha^0\beta^0\Big]||\boldsymbol{u}^0||^2_{L^2(\Omega^0)}+b\ \frac{\rho_s h_s}{\rho_f}\ ||\eta^0||^2_{L^2(\Gamma^0_{wall})}+2C^*\kappa\ T\\
&\quad+\Delta t\sum_{i=1}^{n+1}\Big[\beta^i(1+\alpha^i\Delta t)+\alpha^{i-1}\Big]||\boldsymbol{u}^i||^2_{L^2(\Omega^i)}+\frac{2\Delta t C_2}{\varepsilon^{q'/q}}\ \sum_{i=1}^{n+1}\mathrm{RHS}^{\mathrm{i}}+a\ \frac{\rho_s h_s}{\rho_f}\ \frac{L|\Gamma^0_{wall}|}{\delta}.
\end{aligned} \quad (5.69)$$

Let us denote

$$\begin{aligned}
E^i &:= ||\boldsymbol{u}^i||^2_{L^2(\Omega^i)}+\frac{\rho_s h_s}{\rho_f}\Big[a||\eta^i_{x_1}||^2_{L^2(\Gamma^0_{wall})}+\frac{b}{2}\ ||\eta^i||^2_{L^2(\Gamma^0_{wall})}+||\xi^i||^2_{L^2(\Gamma^0_{wall})}\Big],\\
G^i &:= C^*||\tilde{\boldsymbol{u}}^i||^q_{W^{1,q}(\Omega^{i-1})}+2c\ \frac{\rho_s h_s}{\rho_f}||\xi^{i-\frac{1}{2}}_{x_1}||^2_{L^2(\Gamma^0_{wall})},\\
Q^0 &:= \Big[\Delta t\beta^0+(\Delta t)^2\alpha^0\beta^0\Big]||\boldsymbol{u}^0||^2_{L^2(\Omega^0)}+b\ \frac{\rho_s h_s}{\rho_f}\ ||\eta^0||^2_{L^2(\Gamma^0_{wall})}+a\ \frac{\rho_s h_s}{\rho_f}\frac{L|\Gamma^0_{wall}|}{\delta}\ +2C^*\kappa T,\\
P^i &:= \frac{2C_2}{\varepsilon^{q'/q}}\ \mathrm{RHS}^{\mathrm{i}},
\end{aligned}$$

where $i = 0, \dots, n+1$. Clearly, $||\boldsymbol{u}^i||^2_{L^2(\Omega^i)} \leq E^i$ for all $i = 0, \dots, n+1$ and thus, we can rewrite (5.69) as follows

$$E^{n+1} + \Delta t \sum_{i=1}^{n+1} G^i \leq E^0 + Q^0 + \Delta t \sum_{i=1}^{n+1} P^i + \Delta t \sum_{i=1}^{n+1} \left[\beta^i (1 + \alpha^i \Delta t) + \alpha^{i-1} \right] E^i.$$

Finally, using the discrete Gronwall lemma, cf. (1.29)-(1.30), we obtain

$$E^{n+1} + \Delta t \sum_{i=1}^{n+1} G^i \leq \left[E^0 + Q^0 + \Delta t \sum_{i=1}^{n+1} P^i \right] \exp \left\{ \sum_{i=1}^{n+1} \frac{(\beta^i (1 + \alpha^i \Delta t) + \alpha^{i-1}) \Delta t}{1 - (\beta^i (1 + \alpha^i \Delta t) + \alpha^{i-1}) \Delta t} \right\}$$

with the following condition on the time step

$$\Delta t \leq \frac{1}{\beta^i (1 + \alpha^i \Delta t) + \alpha^{i-1}} \quad \text{for} \quad i = 0, \dots, n+1. \tag{5.70}$$

We remind that

$$\alpha^n := || \bigtriangledown \cdot \boldsymbol{w}^n ||_{L^\infty(\Omega^n)}, \quad \beta^n := \sup_{t \in (t^n, t^{n+1})} \left\{ || \bigtriangledown \cdot \boldsymbol{w} | D J^{-1}_{\mathcal{A}_{t^n, t}} | \; ||_{L^\infty(\Omega^n)} \right\}.$$

We would like to point out that assuming a smooth grid movement the coefficients α^i and β^i are sufficiently small and thus condition (5.70) is not very restrictive. Indeed, our estimate is more general than those obtained by Formaggia et al. [41]. Both estimates in fact show that $E^{n+1} + \Delta t \sum_{i=1}^{n+1} G^i$ is bounded by the initial and boundary data as well as by a small constant arising from smooth mesh movement.

Remark 5.1 (Energy estimate for the midpoint rule) *In what follows we will apply the midpoint rule in order to approximate convective term in the ALE formulation and show that we can derive corresponding energy estimate of the semi-discrete scheme without any dependence on the domain velocity $\boldsymbol{w}$, i.e. α^i, β^i from (5.69). Applying the midpoint rule for the ALE convective term the semi-discrete scheme reads*

$$\begin{aligned}
&\int_{\Omega^n} \frac{\tilde{\boldsymbol{u}}^{n+1} - \boldsymbol{u}^n}{\Delta t} \cdot \tilde{\boldsymbol{u}}^{n+1} \, \mathrm{d}\omega + \frac{2}{\rho_f} \int_{\Omega^n} \mu(|\mathbf{D}(\tilde{\boldsymbol{u}}^{n+1})|) \, \mathbf{D}(\tilde{\boldsymbol{u}}^{n+1}) : \mathbf{D}(\tilde{\boldsymbol{u}}^{n+1}) \, \mathrm{d}\omega \\
&+ \frac{1}{2} \int_{\Omega^{n+1/2}} |\hat{\boldsymbol{u}}^{n+1}|^2 \bigtriangledown \cdot \boldsymbol{w}^{n+1/2} \, \mathrm{d}\omega \quad = \quad - \frac{\rho_s h_s}{\rho_f} \int_{\Gamma^0_{wall}} \left[\frac{\xi^{n+\frac{1}{2}} - \xi^n}{\Delta t} \right] \xi^{n+\frac{1}{2}} \, \mathrm{d}l_0 \\
&- c \, \frac{\rho_s h_s}{\rho_f} \int_{\Gamma^0_{wall}} \left[\frac{\partial \xi^{n+\frac{1}{2}}}{\partial x_1} \right]^2 \mathrm{d}l_0 + \frac{1}{\rho_f} \int_{\Omega^n} \tilde{\boldsymbol{u}}^{n+1} \cdot \boldsymbol{f}^{n+1} \, \mathrm{d}\omega - \frac{1}{\rho_f} \int_{\Gamma^n_{wall}} \frac{P_{ext}(t^{n+1}) \; \tilde{u}_2^{n+1}}{\sqrt{1 + (\partial_{x_1} R_0)^2}} \, \mathrm{d}l \\
&+ \frac{1}{\rho_f} \int_0^{R_0(0)} P_{in}(t^{n+1}) \; \tilde{u}_1^{n+1}|_{x_1 = 0} \, \mathrm{d}x_2 - \frac{1}{\rho_f} \int_0^{R_0(L)} P_{out}(t^{n+1}) \; \tilde{u}_1^{n+1}|_{x_1 = L} \, \mathrm{d}x_2,
\end{aligned} \tag{5.71}$$

where $\hat{\boldsymbol{u}}^{n+1} = \boldsymbol{u}^{n+1} \circ A_{t^{n+1}} \circ A^{-1}_{t^{n+1/2}}$ is defined on $\Omega^{n+1/2}$. Analogously as before, using the estimates (5.41), (5.10), (5.43)-(5.49) and (5.52) we obtain

$$\begin{aligned}
&||\tilde{\boldsymbol{u}}^{n+1}||^2_{L^2(\Omega^n)} + \Delta t \int_{\Omega^{n+1/2}} |\hat{\boldsymbol{u}}^{n+1}|^2 \bigtriangledown \cdot \boldsymbol{w}^{n+1/2} \, \mathrm{d}\omega + C^* \Delta t \; ||\tilde{\boldsymbol{u}}^{n+1}||^q_{W^{1,q}(\Omega^n)} \\
&+ \frac{\rho_s h_s}{\rho_f} \left[||\xi^{n+\frac{1}{2}}||^2_{L^2(\Gamma^0_{wall})} - ||\xi^n||^2_{L^2(\Gamma^0_{wall})} + 2c \; \Delta t \; ||\xi^{n+\frac{1}{2}}_{x_1}||^2_{L^2(\Gamma^0_{wall})} \right] \\
&\leq ||\boldsymbol{u}^n||^2_{L^2(\Omega^n)} + \frac{2 \Delta t C_2}{\varepsilon^{q'/q}} \; \mathrm{RHS}^{n+1} + 2 C^* \kappa \Delta t,
\end{aligned} \tag{5.72}$$

where RHS^{n+1} *is defined in (5.51). Now, let us use the midpoint rule for time integration of the right hand side of the geometric conservation law condition (5.55), i.e.*

$$\int_{t^n}^{t^{n+1}} \int_{\Omega_t} |\tilde{\boldsymbol{u}}|^2 \ \bigtriangledown \cdot \boldsymbol{w} \ \mathrm{d}\omega \ \mathrm{d}t \ = \Delta t \int_{\Omega^{n+1/2}} |\hat{\boldsymbol{u}}^{n+1}|^2 \ \bigtriangledown \cdot \boldsymbol{w}^{n+1/2} \ \mathrm{d}\omega. \tag{5.73}$$

The main reason for this numerical integration arises from the analysis of flow problem with moving boundaries, where in two-dimensional case the integrand on the left hand side of (5.73) can be exactly computed using the midpoint integration rule, cf. [68, 80]. Moreover, we see that (5.73) balances out the term arising from the ALE derivative and we obtain the following estimate for the operator A

$$\begin{aligned}
&||\boldsymbol{u}^{n+1}||^2_{L^2(\Omega^{n+1})} + C^* \Delta t \ \sum_{i=0}^{n} ||\tilde{\boldsymbol{u}}^{i+1}||^q_{W^{1,q}(\Omega^i)} \\
&+ \frac{\rho_s h_s}{\rho_f} \sum_{i=0}^{n} \left[||\xi^{i+\frac{1}{2}}||^2_{L^2(\Gamma^0_{wall})} - ||\xi^i||^2_{L^2(\Gamma^0_{wall})} + 2c \ \Delta t ||\xi^{i+\frac{1}{2}}_{x_1}||^2_{L^2(\Gamma^0_{wall})} \right] \\
&\leq ||\boldsymbol{u}^0||^2_{L^2(\Omega^0)} + \frac{2\Delta t C_2}{\varepsilon^{q'/q}} \ \sum_{i=1}^{n+1} \mathrm{RHS}^{\mathrm{i}} + 2C^* \kappa T.
\end{aligned} \tag{5.74}$$

Analogously as before, the final energy estimate is obtained by summing the contributions from the operator A, cf. (5.74), and the operator B, cf. (5.68), i.e.

$$\begin{aligned}
&||\boldsymbol{u}^{n+1}||^2_{L^2(\Omega^{n+1})} + \frac{\rho_s h_s}{\rho_f} \left[a ||\eta^{n+1}_{x_1}||^2_{L^2(\Gamma^0_{wall})} + \frac{b}{2} \ ||\eta^{n+1}||^2_{L^2(\Gamma^0_{wall})} + ||\xi^{n+1}||^2_{L^2(\Gamma^0_{wall})} \right] \\
&+ C^* \Delta t \ \sum_{i=0}^{n} ||\tilde{\boldsymbol{u}}^{i+1}||^q_{W^{1,q}(\Omega^i)} + 2c \ \frac{\rho_s h_s}{\rho_f} \ \Delta t \ \sum_{i=0}^{n} ||\xi^{i+\frac{1}{2}}_{x_1}||^2_{L^2(\Gamma^0_{wall})} \\
&\leq ||\boldsymbol{u}^0||^2_{L^2(\Omega^0)} + \frac{\rho_s h_s}{\rho_f} \left[a ||\eta^0_{x_1}||^2_{L^2(\Gamma^0_{wall})} + \frac{3b}{2} \ ||\eta^0||^2_{L^2(\Gamma^0_{wall})} + ||\xi^0||^2_{L^2(\Gamma^0_{wall})} \right] \\
&+ \frac{2\Delta t C_2}{\varepsilon^{q'/q}} \ \sum_{i=1}^{n+1} \mathrm{RHS}^{\mathrm{i}} + a \ \frac{\rho_s h_s}{\rho_f} \frac{L|\Gamma^0_{wall}|}{\delta} + 2C^* \kappa T.
\end{aligned}$$

Thus, the total energy at the new time step t^{n+1} *is bounded with the initial energy and the boundary data.*

Chapter 6

Convergence analysis

In this chapter we deal with error analysis for kinematic splitting scheme applied to the semi-discrete fluid-structure interaction problem. The fluid equations are discretized using the finite element method. The mathematical model used in this chapter is simplified. Instead of non-linear generalized Navier-Stokes equations we consider a problem of Oseen type. The structure equation providing dynamic coupling on moving boundary is modelled by the generalized string equation (4.2).

6.1 Mathematical model

In order to point out clearly the main difficulties appearing in the coupling of the fluid and structure and to omit additional technical difficulties due to the divergence-free spaces we consider in what follows a simplified fluid model of the convection-diffusion equation. In fact, it is the generalized Oseen type equation instead of the full non-Newtonian fluid flow equation. In what follows, we analyse the following fluid-structure interaction problem

$$\frac{\mathcal{D}^{\mathcal{A}}\boldsymbol{u}}{\mathcal{D}t} + (\boldsymbol{\beta} - \boldsymbol{w}) \cdot \bigtriangledown \boldsymbol{u} + \bigtriangledown \cdot \Big[\mu(|\mathbf{D}(\boldsymbol{u})|)\mathbf{D}(\boldsymbol{u})\Big] = \boldsymbol{f} \quad \text{in} \quad \Omega_t,\ t \in I, \tag{6.1}$$

where $\boldsymbol{w}$ denotes the domain velocity as defined in (2.10) and $\boldsymbol{\beta}$ is a given function such that $\boldsymbol{\beta} \in L^\infty(I; W^{1,\infty}(\Omega_t))$ for a.e. $t \in I$. Moreover, we assume that $\bigtriangledown \cdot \boldsymbol{\beta} = 0$ in Ω_t, $\beta_2|_{\Gamma_{sym}} = 0$ and $\beta_2|_{\Gamma_{wall}} = \xi$. The equation (6.1) is equipped with the following initial conditions

$$\boldsymbol{u}(\cdot, t_0) = \boldsymbol{u}_0 \qquad \text{in} \quad \Omega_0, \tag{6.2}$$

$$\eta(\cdot, t_0) = 0, \quad \frac{\partial \eta}{\partial t}(\cdot, t_0) = \boldsymbol{u}_0|_{\Gamma^0_{wall}} \cdot \boldsymbol{e}_r \qquad \text{on} \quad \Gamma^0_{wall} \tag{6.3}$$

and boundary conditions

$$\boldsymbol{u} = \boldsymbol{u}_{in} \qquad \text{on} \quad \Gamma_{in},\ t \in I, \tag{6.4}$$

$$\boldsymbol{u} = \boldsymbol{u}_{out} \qquad \text{on} \quad \Gamma_{out},\ t \in I, \tag{6.5}$$

$$\frac{\partial u_1}{\partial x_2} = 0, \quad u_2 = 0, \qquad \text{on} \quad \Gamma_{sym},\ t \in I, \tag{6.6}$$

$$\eta(0, t) = \eta_1, \quad \eta(L, t) = \eta_2, \qquad \text{for} \quad t \in I. \tag{6.7}$$

The coupling is done through the kinematic and dynamic coupling conditions, see also (4.10) and (4.2), which read as follows

$$\boldsymbol{u} = \boldsymbol{w} := \left(0, \frac{\partial \eta}{\partial t}\right)^T \qquad \text{on} \quad \Gamma_{wall}(t), \tag{6.8}$$

$$\frac{\partial^2 \eta}{\partial t^2} - a\frac{\partial^2(\eta + R_0)}{\partial x_1^2} + b\eta - c\frac{\partial^3 \eta}{\partial t \partial x_1^2} = H(\boldsymbol{u}) \qquad \text{on} \quad \Gamma^0_{wall}. \tag{6.9}$$

Here $H(\boldsymbol{u})$ represents the fluid load, analogous to (2.35), i.e.

$$H(\boldsymbol{u}) := -\frac{\Big(\mu(|\mathbf{D}(\boldsymbol{u})|)\ \mathbf{D}(\boldsymbol{u})\boldsymbol{n}\Big)\Big|_{\Gamma^0_{wall}} \cdot \boldsymbol{e}_r}{\rho_s h_s} \frac{R}{R_0} \frac{\sqrt{1+(\partial_{x_1} R)^2}}{\sqrt{1+(\partial_{x_1} R_0)^2}}, \quad G(R_0) := a\frac{\partial^2 R_0}{\partial x_1^2} \tag{6.10}$$

and a, b, c are the structure parameters defined in (2.30).

6.2 Weak formulation

Let us now write down the weak formulation of the problem (6.1)-(6.9). It will have a form similar to (4.15). Set $I = [t_0, T]$. Let the test function $\boldsymbol{v}$ belong to the following space

$$U \ := \ \{\boldsymbol{v}|\ \boldsymbol{v} \in\ W^{1,q}(\Omega_t):\ \boldsymbol{v}|_{\Gamma_{in}} = 0,\ \boldsymbol{v}|_{\Gamma_{out}} = 0,\ v_1|_{\Gamma_{wall}} = 0,\ v_2|_{\Gamma_{sym}} = 0\}, \quad \text{a. e.} \quad t \in I. \tag{6.11}$$

Then we are looking for functions

$$\begin{aligned} \boldsymbol{u} \ &\in \ U^F \ := \ \Big\{\boldsymbol{v}|\ \boldsymbol{v} \in L^q(I; W^{1,q}(\Omega_t)) \cap L^\infty(I; L^2(\Omega_t)):\\ &\qquad \boldsymbol{v}|_{\Gamma_{in}} = \boldsymbol{u}_{in},\ \boldsymbol{v}|_{\Gamma_{in}} = \boldsymbol{u}_{out},\ v_1|_{\Gamma_{wall}} = 0,\ v_2|_{\Gamma_{sym}} = 0\Big\}, \qquad (6.12)\\ \eta \ &\in \ U^S \ := \ H^1(I; H^1_0(0,L)) \cap W^{1,\infty}(I; L^2(0,L)), \qquad (6.13) \end{aligned}$$

such that for a.e. $t \in I$

$$\begin{aligned} &\int_{\Omega_t} \frac{\mathcal{D}^{\mathcal{A}}\boldsymbol{u}}{\mathcal{D}t} \cdot \boldsymbol{v}\ \mathrm{d}\omega + \frac{2}{\rho_f}\int_{\Omega_t} \mu(|\mathbf{D}(\boldsymbol{u})|)\ \mathbf{D}(\boldsymbol{u}) : \mathbf{D}(\boldsymbol{v})\ \mathrm{d}\omega + \int_{\Omega_t} \big[(\boldsymbol{\beta} - \boldsymbol{w}) \cdot \bigtriangledown \boldsymbol{u}\big] \cdot \boldsymbol{v}\ \mathrm{d}\omega \\ &= \frac{1}{\rho_f}\int_{\Omega_t} \boldsymbol{f} \cdot \boldsymbol{v}\ \mathrm{d}\omega - \frac{\rho_s h_s}{\rho_f}\int_{\Gamma^0_{wall}} \left(\frac{\partial^2 \eta}{\partial t^2} - a\frac{\partial^2 \eta}{\partial x_1^2} + b\eta - c\frac{\partial^3 \eta}{\partial t \partial x_1^2}\right) v_2|_{\Gamma^0_{wall}}\ \mathrm{d}l_0 \\ &\quad + a\frac{\rho_s h_s}{\rho_f}\int_{\Gamma^0_{wall}} \frac{\partial^2 R_0}{\partial x_1^2}\ v_2|_{\Gamma^0_{wall}}\ \mathrm{d}l_0, \quad \forall\ \boldsymbol{v} \in U. \end{aligned} \tag{6.14}$$

6.3 Kinematic splitting of the continuous problem (6.1)-(6.9)

Now, we define the kinematic splitting scheme for the fluid structure-interaction problem (6.1)-(6.9) and write down the weak formulation corresponding to the operator A and the operator B. We proceed analogously as in Section 4.2. Thus, the operator A describes the hydrodynamic part of the problem composed from the fluid solver, i.e. (6.1), and the parabolic part of the structure equation. The operator B consists only from the elastic load of structure. Hence, we have

$$\textbf{Operator A} \begin{cases} \text{fluid solver for } \boldsymbol{u}, \\ \xi := u_2|_{\Gamma_{wall}}, \\ \dfrac{\partial \xi}{\partial t} = c\dfrac{\partial^2 \xi}{\partial {x_1}^2} + H(\boldsymbol{u}), \end{cases} \tag{6.15}$$

$$\textbf{Operator B} \begin{cases} \dfrac{\partial \eta}{\partial t} = \xi, \\ \dfrac{\partial \xi}{\partial t} = a\dfrac{\partial^2 \eta}{\partial {x_1}^2} - b\eta + G(R_0). \end{cases} \tag{6.16}$$

Here, we would like to emphasize that even if we use different fluid solver, see (6.1)-(6.9), the main idea of the kinematic splitting is governed in the theoretical analysis.

The operator A can be written in the weak formulation as follows: find $\boldsymbol{u} \in U^F$ and $\eta \in U^S$ such that for all $\boldsymbol{v} \in U$ a.e. $t \in I$ holds

$$\begin{aligned}\int\limits_{\Omega_t} \frac{\mathcal{D}^{\mathcal{A}}\boldsymbol{u}}{\mathcal{D}t} \cdot \boldsymbol{v} \ \mathrm{d}\omega + \frac{2}{\rho_f}\int\limits_{\Omega_t} \mu(|\mathbf{D}(\boldsymbol{u})|)\ \mathbf{D}(\boldsymbol{u}) : \mathbf{D}(\boldsymbol{v}) \ \mathrm{d}\omega + \int\limits_{\Omega_t} \left[(\boldsymbol{\beta} - \boldsymbol{w}) \cdot \bigtriangledown \boldsymbol{u}\right] \cdot \boldsymbol{v} \ \mathrm{d}\omega \\ = \quad \frac{1}{\rho_f}\int\limits_{\Omega_t} \boldsymbol{f} \cdot \boldsymbol{v} \ \mathrm{d}\omega - \frac{\rho_s h_s}{\rho_f}\int\limits_{\Gamma^0_{wall}} \left(\frac{\partial^2 \eta}{\partial t^2} - c\frac{\partial^3 \eta}{\partial t \partial x_1^2}\right) v_2 \ \mathrm{d}l_0, \end{aligned} \tag{6.17}$$

where $\eta_t = \xi$. The operator B will have the following weak formulation: find $\eta \in U^S$ such that for all $v \in H_0^1(\Gamma^0_{wall})$ a.e. $t \in I$ holds

$$\int_{\Gamma^0_{wall}} \frac{\partial \eta}{\partial t}\ v \ \mathrm{d}x_2 \ = \ \int_{\Gamma^0_{wall}} \xi \ v \ \mathrm{d}x_2, \tag{6.18a}$$

$$\int_{\Gamma^0_{wall}} \frac{\partial \xi}{\partial t}\ v \ \mathrm{d}x_2 \ = \ a\int_{\Gamma^0_{wall}} \frac{\partial^2 \eta}{\partial x_1^2}\ v \ \mathrm{d}x_2 - b\int_{\Gamma^0_{wall}} \eta \ v \ \mathrm{d}x_2 + \int_{\Gamma^0_{wall}} G(R_0)\ v \ \mathrm{d}x_2. \tag{6.18b}$$

Before presenting the convergence analysis for our semi-discrete fluid-structure interaction problem, let us collect necessary assumptions on the finite element discretization, the standard error estimates and the finite element operators.

6.4 Finite element discretization and approximation errors

Let $\mathcal{A}_{h,t}$, where h is a space-discretization parameter, denotes the discrete ALE mapping. From the definition of $\mathcal{A}_{h,t}$ it is clear that it depends on the discrete boundary displacement as well as on the definition of the grid velocity inside the domain of interest. Let us denote by $\Omega_{h,0}$ the discrete counterpart to the reference domain Ω_0. Let t be an arbitrary and fixed time instant such that $t \in I,\ I := [t_0, T]$. Using the discrete ALE mapping we define for each $t \in I$ the discrete actual domain by $\Omega_{h,t} = \mathcal{A}_{h,t}(\Omega_{h,0})$. We note that, in general, the continuous and discrete domain do not coincide, because Ω_0 and Ω_t may have curved boundaries. Therefore, one may introduce an auxiliary domain $\tilde{\Omega}_0$ consisting of both domains Ω_0 and $\Omega_{h,0}$ and analogously $\tilde{\Omega}_t$ consisting of Ω_t and $\Omega_{h,t}$. However, for simplicity, we will restrict ourselves on the situation, when $\Omega_t = \Omega_{h,t}$ and $\Omega_0 = \Omega_{h,0}$.

Let the boundary of $\Omega_{h,0}$, denoted by $\partial\Omega_{h,0}$, consists of finitely many simple, closed, piecewise linear curves. Analogously, let $\partial\Omega_{h,t}$ be the boundary of $\Omega_{h,t}$. The triangulation of $\Omega_{h,0}$, resp. $\Omega_{h,t}$, will be composed from finitely many closed triangles $\hat{K}$ and K denoted by $\mathcal{T}_{h,0}$ and $\mathcal{T}_{h,t}$, respectively. We assume that the triangulation $\mathcal{T}_{h,t}$ has standard properties, i.e. $\overline{\Omega}_{h,t} = \bigcup_{K \in \mathcal{T}_h} K$ and

$$K_i \cap K_j \ = \ \begin{cases} \text{vertex or side of } K_i, K_j \text{ or empty set} & \text{if} \quad i \neq j, \\ K_i = K_j & \text{if} \quad i = j \end{cases} \tag{6.19}$$

and similarly for $\mathcal{T}_{h,0}$.

The parameter h used in the discretization of Ω_t and its boundaries represents the length of maximum side of the triangles K from $\mathcal{T}_{h,t}$, i.e.

$$h := \max_{K \in \mathcal{T}_{h,t}} h_K, \quad \text{where} \quad h_K := \operatorname{diam} K. \tag{6.20}$$

The parameter h used in the discretization of Ω_0, let us call it $\hat{h}$ now, is in general different from h defined in (6.20). We can write

$$\hat{h} := \max_{\hat{K}\in\hat{\mathcal{T}}_{h,0}} \hat{h}_{\hat{K}}, \quad \text{where} \quad \hat{h}_{\hat{K}} := \text{diam } \hat{K}. \tag{6.21}$$

We assume that $\mathcal{T}_{h,0}$ is regular, i.e.

$$\exists c_1, c_2 > 0 \quad \text{s.t.} \quad \forall \hat{K} \in \mathcal{T}_{h,0} : \; c_1 h_{\hat{K}} \le \rho_{\hat{K}} \le c_2 h_{\hat{K}}, \tag{6.22}$$

where $\rho_{\hat{K}}$ is the radius of the ball of maximal size contained in $\hat{K}$. Moreover, we assume that there exist positive constants c_3, c_4, depending only on the domain evolution, such that it holds

$$c_3\hat{h} \;\le\; h \;\le\; c_4\hat{h}, \tag{6.23}$$

cf. [25]. From (6.22) and (6.23) it follows immediately that $\mathcal{T}_{h,t}$ remains also regular for each $t \in I$. Thanks to the assumption (6.23) we can simplify the notation in such a way that we will use the same discretization parameter h for both discrete domains $\Omega_{h,0}$ and $\Omega_{h,t}$. Moreover, the discrete counterparts for the domain boundaries $\Gamma_{in}, \Gamma_{out}, \Gamma_{sym}, \Gamma_{wall}, \Gamma^0_{wall}$ will be denoted by $\Gamma_{in,h}, \Gamma_{out,h}, \Gamma_{sym,h}, \Gamma_{wall,h}$, $\Gamma^0_{wall,h}$, respectively.

In order to approximate (6.17) and (6.18a)-(6.18b) we need to define approximation spaces for fluid and structure. Let us assume that $\mathcal{T}_{h,0}$ and $\mathcal{T}_{h,t}$ are geometrically conforming triangulations of the computational domain $\Omega_{h,0}$ and $\Omega_{h,t}$, respectively. Let $U^F_h(\Omega_{h,0})$ be the Lagrangian finite element space defined by

$$\begin{aligned} U^F_h(\Omega_{h,0}) \;:=\; & \{\hat{\boldsymbol{v}}_h |\; \hat{\boldsymbol{v}}_h \in C^0(\overline{\Omega}_{h,0}),\; \hat{\boldsymbol{v}}_h|_{\hat{K}} \in \mathbb{P}^1(\hat{K}), \forall\; \hat{K} \in \mathcal{T}_{h,0} : \\ & \hat{v}_{h,1}|_{\Gamma_{wall}} = 0,\; \hat{v}_{h,2}|_{\Gamma_{sym}} = 0\}, \end{aligned}$$

where $\mathbb{P}^1$ denotes the space of linear polynomials. Then, using the discrete ALE mapping we define the finite element space for velocities $U^F_h(\Omega_{h,t})$ by

$$\begin{aligned} U^F_h(\Omega_{h,t}) \;:=\; & \{\boldsymbol{v}_h |\; \boldsymbol{v}_h : \Omega_{h,t} \to \mathbb{R},\; \boldsymbol{v}_h := \hat{\boldsymbol{v}}_h \circ \mathcal{A}^{-1}_{h,t},\; \hat{\boldsymbol{v}}_h \in U^F_h(\Omega_{h,0}) : \\ & v_{h,1}|_{\Gamma_{wall}} = 0,\; v_{h,2}|_{\Gamma_{sym}} = 0\}, \quad \text{for a.e. } t \in I. \end{aligned} \tag{6.24}$$

Assuming that the discrete ALE mapping $\mathcal{A}_{h,t}$ is piecewise linear, we have $\mathcal{A}_{h,t} \in W^{1,\infty}(\Omega_{h,0})$ and we can rewrite (6.24) as

$$\begin{aligned} U^F_h(\Omega_{h,t}) \;:=\; & \{\boldsymbol{v}_h |\; \boldsymbol{v}_h \in C^0(\overline{\Omega}_{h,t}),\; \boldsymbol{v}_h|_K \in \mathbb{P}^1(K),\; \forall\; K \in \mathcal{T}_{h,t} : \\ & v_{h,1}|_{\Gamma_{wall}} = 0,\; v_{h,2}|_{\Gamma_{sym}} = 0\}, \quad \text{for a.e. } t \in I. \end{aligned}$$

The finite element approximation space for test functions for fluid equation $U^F_{h,0}(\Omega_{h,t})$ is defined by

$$U^F_{h,0}(\Omega_{h,t}) \;:=\; \{\boldsymbol{v}_h |\; \boldsymbol{v}_h \in U^F_h(\Omega_{h,t}) :\; \boldsymbol{v}_h|_{\Gamma_{in}} = 0,\; \boldsymbol{v}_h|_{\Gamma_{out}} = 0\}. \tag{6.25}$$

Let $\mathcal{N}_h := \dim(U^F_h(\Omega_{h,t}))$. We denote by $\boldsymbol{Y}_i$ the coordinate i-th node from the triangulation $\mathcal{T}_{h,0}$ and by $\boldsymbol{x}_{h,i}(t) := \mathcal{A}_{h,t}(\boldsymbol{Y}_i)$ the coordinates of i-th node from $\mathcal{T}_{h,t}$. Moreover, let $\{\hat{\varphi}_i, \hat{\varphi}_i \in \Omega_{h,0},\; i = 1, \ldots, \mathcal{N}_h\}$ and $\{\varphi_i(t) = \hat{\varphi}_i \circ \mathcal{A}^{-1}_{h,t},\; \varphi_i(t) \in \Omega_{h,t},\; i \in 1, \ldots, \mathcal{N}_h\}$ be the set of nodal basis functions of $U^F_h(\Omega_{h,0})$ and $U^F_h(\Omega_{h,t})$, respectively. Then a finite element approximation function $\hat{\boldsymbol{v}}_h \in U^F_h(\Omega_{h,0})$ and $\boldsymbol{v}_h \in U^F_h(\Omega_{h,t})$ can be expressed as

$$\begin{aligned} \hat{\boldsymbol{v}}_h(\boldsymbol{Y}) \;&=\; \sum_{i\in\mathcal{N}_h} \hat{\boldsymbol{v}}_h(\boldsymbol{Y}_i)\; \hat{\varphi}_i(\boldsymbol{Y}), \qquad \boldsymbol{Y} \in \Omega_{h,0}, \\ \boldsymbol{v}_h(\boldsymbol{x}, t) \;&=\; \sum_{i\in\mathcal{N}_h} \boldsymbol{v}_h(\boldsymbol{x}_{h,i}(t))\; \varphi_i(\boldsymbol{x}, t), \quad \boldsymbol{x} \in \Omega_{h,t} \quad \forall t \in I. \end{aligned}$$

Note that the coefficient $\hat{\boldsymbol{v}}_h(\boldsymbol{Y}_i)$ is obviously time independent, whereas $\boldsymbol{v}_h(\boldsymbol{x}_{h,i}(t))$ depends but on time through the discrete ALE mapping. Therefore let us write the coefficient $\boldsymbol{v}_h(\boldsymbol{x}_{h,i}(t))$ as $\boldsymbol{v}_i(t)$.

Concerning the discrete ALE mapping we can express for each $t \in I$ the relation between the functions $\hat{\boldsymbol{v}}_h \in U_h^F(\Omega_{h,0}) : \Omega_{h,0} \times I \to \mathbb{R}$ and $\boldsymbol{v}_h \in U_h^F(\Omega_{h,t}) : \Omega_{h,t} \to \mathbb{R}$, $\forall t \in I$ as follows

$$\begin{aligned}
\hat{\boldsymbol{v}}_h(\boldsymbol{Y},t) &= \boldsymbol{v}_h(\mathcal{A}_{h,t}(\boldsymbol{Y}),t) = \boldsymbol{v}_h(\boldsymbol{x}_h(\boldsymbol{Y},t),t),\\
\boldsymbol{v}_h(\boldsymbol{x},t) &= \hat{\boldsymbol{v}}_h(\mathcal{A}_{h,t}^{-1}(\boldsymbol{x}_h),t) = \hat{\boldsymbol{v}}_h(\boldsymbol{Y},t),\\
\left.\frac{\partial \boldsymbol{v}_h}{\partial t}\right|_Y(\boldsymbol{x},t) &= \frac{\partial \hat{\boldsymbol{v}}_h}{\partial t}(\boldsymbol{Y},t), \quad \boldsymbol{Y} = \mathcal{A}_{h,t}^{-1}(\boldsymbol{x}_h).
\end{aligned}$$

Finally, we denote by $I_h\boldsymbol{u}$ the **linear interpolation of** $\boldsymbol{u}$ in $U_h^F(\Omega_{h,t})$, i.e.

$$I_h : \ C^0(\Omega_{h,t}) \to U_h^F(\Omega_{h,t}), \tag{6.26a}$$

$$I_h\boldsymbol{u}(\boldsymbol{x},t) \ := \ \sum_{i\in\mathcal{N}_h} \boldsymbol{u}(\boldsymbol{x}_{h,i}(t)) \ \varphi_i(\boldsymbol{x},t), \quad \boldsymbol{x} \in \Omega_{h,t} \quad \forall t \in I. \tag{6.26b}$$

Lemma 6.1 (see [36, 80])
Let $\boldsymbol{u} \in H^3(\Omega_t)$, $\boldsymbol{u}_t \in H^2(\Omega_t)$ and $I_h\boldsymbol{u} \in U_h^F(\Omega_{h,t})$. Moreover, let $\boldsymbol{w}_h \in W^{2,\infty}(K)$, for all $K \in \mathcal{T}_{h,t}$, i.e. elementwise we have

$$||\boldsymbol{w}_h||_{W^{2,\infty}(K)} \ \leq \ \gamma, \quad \forall K \in \mathcal{T}_{h,t}. \tag{6.27}$$

Then it holds

$$\textbf{(a)} \quad ||\boldsymbol{u} - I_h\boldsymbol{u}||_{L^2(\Omega_{h,t})} + h \ ||\boldsymbol{u} - I_h\boldsymbol{u}||_{H^1(\Omega_{h,t})} \ \leq \ C \ h^2 \ ||\boldsymbol{u}||_{H^2(\Omega_{h,t})}, \tag{6.28a}$$

$$\begin{aligned}
\textbf{(b)} \quad \left|\left|\frac{\partial(\boldsymbol{u} - I_h\boldsymbol{u})}{\partial t}\right|\right|_{L^2(\Omega_{h,t})} &\leq C \ h^2 \ \left\{ \left|\left|\frac{\partial \boldsymbol{u}}{\partial t}\right|\right|_{H^2(\Omega_{h,t})} \right.\\
&\left. + \ \Big[||\boldsymbol{w}_h||_{L^\infty(\Omega_{h,t})} + \gamma\Big] ||\boldsymbol{u}||_{H^3(\Omega_{h,t})} \right\}.
\end{aligned} \tag{6.28b}$$

Proof. The estimate (a) is standard finite element error estimates for interpolation of a function as defined in (6.26a)-(6.26b), i.e.

$$||\boldsymbol{u} - I_h\boldsymbol{u}||_{H^m(\Omega_{h,t})} \ \leq \ Ch^{2-m}||\boldsymbol{u}||_{H^2(\Omega_{h,t})}, \quad m = 0, 1.$$

In order to prove (b) let us firstly show that the time derivative of an interpolated function with respect to the reference configuration equals the interpolation of time derivative of this function with respect of the reference frame. More precisely, we want to prove that

$$\left.\frac{\partial(I_h\boldsymbol{u})}{\partial t}\right|_{\boldsymbol{Y}}(\boldsymbol{x},t) \ = \ I_h \left.\frac{\partial \boldsymbol{u}}{\partial t}\right|_{\boldsymbol{Y}}(\boldsymbol{x},t). \tag{6.29}$$

Let us firstly express the interpolation of $\boldsymbol{u}$ with respect to the nodes from $\Omega_{h,t}$ and $\Omega_{h,0}$. Hence,

$$\begin{aligned}
I_h\boldsymbol{u}(\boldsymbol{x},t) \ &:= \ \sum_{i\in\mathcal{N}_h} \boldsymbol{u}(\boldsymbol{x}_{h,i}(t)) \ \varphi_i(\boldsymbol{x},t), \quad \boldsymbol{x} \in \Omega_{h,t} \quad \forall t \in I,\\
I_h\hat{\boldsymbol{u}}(\boldsymbol{Y},t) \ &:= \ \sum_{i\in\mathcal{N}_h} \hat{\boldsymbol{u}}(\boldsymbol{Y}_i,t) \ \hat{\varphi}_i(\boldsymbol{Y}), \quad \boldsymbol{Y} \in \Omega_{h,0} \quad \forall t \in I.
\end{aligned}$$

Then, it holds

$$\begin{aligned}\left.\frac{\partial(I_h\boldsymbol{u})}{\partial t}\right|_{\boldsymbol{Y}}(\boldsymbol{x},t) &= \frac{\partial(I_h\hat{\boldsymbol{u}})}{\partial t}\,(\boldsymbol{Y},t) = \frac{\partial}{\partial t}\Big[\sum_{i\in\mathcal{N}_h}\hat{\boldsymbol{u}}(\boldsymbol{Y}_i,t)\;\hat{\varphi}(\boldsymbol{Y})\Big]\\ &= \sum_{i\in\mathcal{N}_h}\frac{\partial\hat{\boldsymbol{u}}}{\partial t}(\boldsymbol{Y}_i,t)\;\hat{\varphi}(\boldsymbol{Y}) = I_h\frac{\partial\hat{\boldsymbol{u}}}{\partial t}(\boldsymbol{Y},t) \;= I_h\left.\frac{\partial\boldsymbol{u}}{\partial t}\right|_{\boldsymbol{Y}}(\boldsymbol{x},t). \quad (6.30)\end{aligned}$$

Now, using the equality (6.30) and the definition of ALE derivative we express the derivative of an interpolated function with respect to the actual configuration $\Omega_{h,t}$, i.e.

$$\begin{aligned}\frac{\partial(I_h\boldsymbol{u})}{\partial t}\,(\boldsymbol{x},t) &= \left.\frac{\partial(I_h\boldsymbol{u})}{\partial t}\right|_{\boldsymbol{Y}}(\boldsymbol{x},t) - \boldsymbol{w}_h\cdot\bigtriangledown(I_h\boldsymbol{u}) \;= I_h\left.\frac{\partial\boldsymbol{u}}{\partial t}\right|_{\boldsymbol{Y}}(\boldsymbol{x},t) - \boldsymbol{w}_h\cdot\bigtriangledown(I_h\boldsymbol{u})\\ &= I_h\left(\frac{\partial\boldsymbol{u}}{\partial t}\,(\boldsymbol{x},t) + \boldsymbol{w}_h\cdot\bigtriangledown\boldsymbol{u}\right) - \boldsymbol{w}_h\cdot\bigtriangledown(I_h\boldsymbol{u})\\ &= I_h\frac{\partial\boldsymbol{u}}{\partial t}\,(\boldsymbol{x},t) - [\boldsymbol{w}_h\cdot\bigtriangledown\boldsymbol{u} - I_h(\boldsymbol{w}_h\cdot\bigtriangledown\boldsymbol{u})] + \boldsymbol{w}_h\cdot\bigtriangledown(\boldsymbol{u}-I_h\boldsymbol{u}). \quad (6.31)\end{aligned}$$

From (6.31) we have

$$\begin{aligned}\left|\left|\frac{\partial\boldsymbol{u}}{\partial t} - \frac{\partial(I_h\boldsymbol{u})}{\partial t}\right|\right|_{L^2(\Omega_{h,t})} &\le \left|\left|\frac{\partial\boldsymbol{u}}{\partial t} - I_h\frac{\partial\boldsymbol{u}}{\partial t}\right|\right|_{L^2(\Omega_{h,t})} + ||\boldsymbol{w}_h\cdot\bigtriangledown\boldsymbol{u} - I_h(\boldsymbol{w}_h\cdot\bigtriangledown\boldsymbol{u})||_{L^2(\Omega_{h,t})}\\ &+ ||\boldsymbol{w}_h\cdot\bigtriangledown(\boldsymbol{u}-I_h\boldsymbol{u})||_{L^2(\Omega_{h,t})}. \quad (6.32)\end{aligned}$$

Now, we estimate each term from (6.32).

$$\left|\left|\frac{\partial\boldsymbol{u}}{\partial t} - I_h\frac{\partial\boldsymbol{u}}{\partial t}\right|\right|_{L^2(\Omega_{h,t})} \le Ch^2\left|\left|\frac{\partial\boldsymbol{u}}{\partial t}\right|\right|_{H^2(\Omega_{h,t})}, \quad (6.33)$$

In the next term we need to make estimates for triangles K from the configuration $\Omega_{h,t}$, since the domain velocity is at most $W^{1,\infty}(\Omega_{h,t})$ regular on the whole domain.

$$\begin{aligned}||\boldsymbol{w}_h\cdot\bigtriangledown\boldsymbol{u} - I_h(\boldsymbol{w}_h\cdot\bigtriangledown\boldsymbol{u})||_{L^2(\Omega_{h,t})} &= \sum_{K\in\mathcal{T}_{h,t}}||\boldsymbol{w}_h\cdot\bigtriangledown\boldsymbol{u} - I_h(\boldsymbol{w}_h\cdot\bigtriangledown\boldsymbol{u})||_{L^2(K)}\\ &\le \sum_{K\in\mathcal{T}_{h,t}} C\;h^2\;||\boldsymbol{w}_h\cdot\bigtriangledown\boldsymbol{u}||_{H^2(K)}\\ &\le \sum_{K\in\mathcal{T}_{h,t}} C\;h^2\;||\boldsymbol{w}_h||_{W^{2,\infty}(K)}\;||\bigtriangledown\boldsymbol{u}||_{H^2(K)}\\ &\le C\;h^2\;\gamma\;||\boldsymbol{u}||_{H^3(\Omega_{h,t})}. \quad (6.34)\end{aligned}$$

For the third term from (6.32) it holds

$$\begin{aligned}||\boldsymbol{w}_h\cdot\bigtriangledown(\boldsymbol{u}-I_h\boldsymbol{u})||_{L^2(\Omega_{h,t})} &\le ||\boldsymbol{w}_h||_{L^\infty(\Omega_{h,t})}||\bigtriangledown(\boldsymbol{u}-I_h\boldsymbol{u})||_{L^2(\Omega_{h,t})}\\ &\le C\;h^2\;||\boldsymbol{w}_h||_{L^\infty(\Omega_{h,t})}\;||\boldsymbol{u}||_{H^3(\Omega_{h,t})}, \quad (6.35)\end{aligned}$$

Finally, inserting estimates (6.33)-(6.35) we obtain the interpolation error (b). ■

Now, we proceed with the definition of the approximation space for structure. Let $U_h^S(\Gamma^0_{wall,h})$ be the finite element approximation space for structure defined by

$$\begin{aligned}U_h^S(\Gamma^0_{wall,h}) := \{&\hat{\psi}_h|\;\hat{\psi}_h\in H_0^1(\Gamma^0_{wall,h}):\;\hat{\psi}|_{[x_{1,i},x_{1,i+1}]}\in\mathbb{P}^1([x_{1,i},x_{1,i+1}]),\;x_{1,i}\in\Gamma^0_{wall,h},\\ &i=0,\ldots,N-1: x_{1,0}=0,\ldots,x_{1,n}=L\}.\end{aligned}$$

We would like to point out that the points x_i for $i = 0, \dots, N-1$ coincide with the mesh points of $\mathcal{T}_{h,0}$ on $\Gamma^0_{wall,h}$. Using the discrete ALE mapping we can define $U_h^S(\Gamma_{wall,h})$ as follows

$$U_h^S(\Gamma_{wall,h}) \ := \ \{\psi_h |\ \psi_h : \Gamma_{wall,h} \to \mathbb{R},\ \psi_h := \hat{\psi}_h \circ \mathcal{A}_{h,t}^{-1},\ \hat{\psi}_h \in U_h^S(\Gamma^0_{wall,h})\}$$

or alternatively we can write

$$\begin{aligned} U_h^S(\Gamma_{wall,h}) \ := \ & \{\hat{\psi}_h |\ \hat{\psi}_h \in H_0^1(\Gamma_{wall,h}) :\ \hat{\psi}|_{[x_{1,i},x_{1,i+1}]} \in \mathbb{P}^1([x_{1,i}, x_{1,i+1}]),\ x_{1,i} \in \Gamma_{wall,h}, \\ & i = 0, \dots, N-1 : x_{1,0} = 0, \dots, x_{1,n} = L\}. \end{aligned}$$

In order to simplify the matter, we make the following assumption:

$$\begin{aligned} \boldsymbol{u}_{h,2}|_{\Gamma_{wall,h}} &= \xi_h = \frac{\partial \eta_h}{\partial t} \quad \text{on} \quad \Gamma_{wall,h}, \quad \text{for a.e. } t \in I, \\ \boldsymbol{u}_{h,2}|_{\Gamma^0_{wall,h}} &= \xi_h = \frac{\partial \eta_h}{\partial t} \quad \text{on} \quad \Gamma^0_{wall,h}. \end{aligned}$$

In the energy estimates we will use for the test functions of the structure equation the second component of the test functions from $U_{h,0}^F$ restricted to the $\Gamma_{wall,h}$ or $\Gamma^0_{Wall,h}$, respectively. Hence, the space of test function for the structure equation is is defined by

$$U_{h,0}^S(\Gamma_{wall,h}) \ := \ \{\psi_h |\ \psi_h \in U_h^S(\Gamma_{wall,h}) :\ \psi_h(x_{1,0}) = \psi_h(x_{1,n}) = 0\} \quad \text{for a.e. } t \in I. \quad (6.36)$$

In general, however, this assumption is not automatically satisfied. Therefore, a suitable interface matching operator technique should be introduced, e.g. a pointwise matching, a Mortar matching [5].

Moreover, let $S_h\eta(x_1, t)$ and $S_h\xi(x_1, t)$ be the linear spline interpolations of $\eta(x_1, t)$ and $\xi(x_1, t)$ in $U_h^S(\Gamma^0_{wall,h})$, i.e. for $x_1 \in [x_{1,i}, x_{1,i+1}]$ and $i = 0, \dots, N-1$ it holds

$$S_h\eta(x_1, t) = \eta(x_{1,i+1}, t) + [\eta(x_{1,i+1}, t) - \eta(x_{1,i}, t)]\ \frac{x_1 - x_{1,i}}{x_{1,i+1} - x_{1,i}}, \quad (6.37)$$

$$S_h\xi(x_1, t) = \xi(x_{1,i+1}, t) + [\xi(x_{1,i+1}, t) - \xi(x_{1,i}, t)]\ \frac{x_1 - x_{1,i}}{x_{1,i+1} - x_{1,i}}. \quad (6.38)$$

From the definition of the interpolation $I_h\boldsymbol{u}$ it follows that on the boundary Γ_{wall} and Γ^0_{wall} we have

$$I_h u_2\Big(x_1, R_0(x_1) + \eta(x_1, t), t\Big) \ = \ S_h\xi(x_1, t) \quad \text{for} \quad x_1 \in (0, L). \quad (6.39)$$

The next lemma gives the approximation error estimates for structure.

Lemma 6.2 (see [36, 54, 80])
Let $\eta \in H^2(\Gamma^0_{wall})$, $\xi \in H^2(\Gamma^0_{wall})$ be the structure displacement and structure velocity and $S_h\eta$, $S_h\xi \in U_h^S(\Gamma^0_{wall,h})$ their linear spline interpolations, respectively. Moreover, let $\eta_t \in H^2(\Gamma^0_{wall})$, $\xi_t \in H^2(\Gamma^0_{wall})$. Then assuming (6.23) it holds

$$\textbf{(a)} \quad ||\eta - S_h\eta||_{L^2(\Gamma^0_{wall,h})} + h\ ||\eta - S_h\eta||_{H^1(\Gamma^0_{wall,h})} \le C\ h^2\ ||\eta||_{H^2(\Gamma^0_{wall,h})}, \quad (6.40a)$$

$$\textbf{(b)} \quad \left|\left|\frac{\partial(\xi - S_h\xi)}{\partial t}\right|\right|_{L^2(\Gamma^0_{wall,h})} + h\ \left|\left|\frac{\partial(\xi - S_h\xi)}{\partial t}\right|\right|_{H^1(\Gamma^0_{wall,h})} \le C\ h^2\ \left|\left|\frac{\partial \xi}{\partial t}\right|\right|_{H^2(\Gamma^0_{wall,h})}, \quad (6.40b)$$

$$\textbf{(c)} \quad ||\xi - S_h\xi||_{L^2(\Gamma^0_{wall,h})} + h\ ||\xi - S_h\xi||_{H^1(\Gamma^0_{wall,h})} \le C\ h^2\ ||\xi||_{H^2(\Gamma^0_{wall,h})}, \quad (6.40c)$$

$$\textbf{(d)} \quad \left|\left|\frac{\partial(\eta - S_h\eta)}{\partial t}\right|\right|_{L^2(\Gamma^0_{wall,h})} + h\ \left|\left|\frac{\partial(\eta - S_h\eta)}{\partial t}\right|\right|_{H^1(\Gamma^0_{wall,h})} \le C\ h^2\ \left|\left|\frac{\partial \eta}{\partial t}\right|\right|_{H^2(\Gamma^0_{wall,h})}. \quad (6.40d)$$

Proof. The estimates (a) and (c) are again standard finite element interpolation estimates for linear splines, i.e.

$$||\eta - S_h\eta||_{H^m(\Gamma^0_{wall,h})} \leq Ch^{2-m}||\eta||_{H^2(\Gamma^0_{wall,h})}, \quad m = 0, 1, \tag{6.41}$$

$$||\xi - S_h\xi||_{H^m(\Gamma^0_{wall,h})} \leq Ch^{2-m}||\xi||_{H^2(\Gamma^0_{wall,h})}, \quad m = 0, 1. \tag{6.42}$$

From the definitions (6.37)-(6.38) we see that it holds

$$\left.\frac{\partial(S_h\eta)}{\partial t}\right|_{\Gamma^0_{wall,h}} = S_h \left.\frac{\partial\eta}{\partial t}\right|_{\Gamma^0_{wall,h}} \quad \text{and} \quad \left.\frac{\partial(S_h\xi)}{\partial t}\right|_{\Gamma^0_{wall,h}} = S_h \left.\frac{\partial\xi}{\partial t}\right|_{\Gamma^0_{wall,h}}.$$

This yields directly the estimate (b) and (d). ∎

6.5 Finite element weak formulation

Let us now write down the finite element formulation of problem (6.1)-(6.9). Let $\boldsymbol{u}_h \in L^q(I; U_h^F(\Omega_{h,t}))$ and $\eta_h \in H^1(I; U_h^S(0, L))$ denote the numerical solution, i.e. finite element approximation of the fluid velocity $\boldsymbol{u} \in U^F$ and the structure displacement $\eta \in U^S$, respectively. Let us assume that the following initial, boundary and coupling conditions are prescribed

$$\boldsymbol{u}_h(\cdot, t_0) = I_h\boldsymbol{u}_0 \qquad \text{in} \quad \Omega_{h,0}, \tag{6.43}$$

$$\eta_h(\cdot, t_0) = 0, \quad \xi_h(\cdot, t_0) = \frac{\partial\eta_h(\cdot, t_0)}{\partial t} = I_h\boldsymbol{u}_0|_{\Gamma^0_{wall}} \cdot \boldsymbol{e}_r \qquad \text{on} \quad \Gamma^0_{wall,h} \tag{6.44}$$

$$\boldsymbol{u}_h = I_h\boldsymbol{u} \qquad \text{on} \quad \Gamma_{in,h},\ t \in I, \tag{6.45}$$

$$\boldsymbol{u}_h = I_h\boldsymbol{u} \qquad \text{on} \quad \Gamma_{out,h},\ t \in I, \tag{6.46}$$

$$\frac{\partial u_{h,1}}{\partial x_2} = 0, \quad u_{h,2} = 0 \qquad \text{on} \quad \Gamma_{sym,h},\ t \in I, \tag{6.47}$$

$$\eta_h(0, t) = I_h\eta(0, t), \quad \eta_h(L, t) = I_h\eta(L, t) \qquad \text{for} \quad t \in I, \tag{6.48}$$

$$\boldsymbol{u}_h = \boldsymbol{w}_h := \left(0, \frac{\partial\eta_h}{\partial t}\right)^T \qquad \text{on} \quad \Gamma_{wall,h} \tag{6.49}$$

$$\frac{\partial^2\eta_h}{\partial t^2} - a\frac{\partial^2(\eta_h + R_0)}{\partial x_1^2} + b\eta_h - c\frac{\partial^3\eta_h}{\partial t\partial x_1^2} = H(\boldsymbol{u}_h) \qquad \text{on} \quad \Gamma^0_{wall,h}. \tag{6.50}$$

Let $\boldsymbol{w}_h$ be the discrete domain velocity defined using the discrete ALE mapping $\mathcal{A}_{h,t}$. Moreover, we assume that for a given function $\boldsymbol{\beta} \in L^\infty(I; W^{1,\infty}(\Omega_t))$ it holds $\beta_2|_{\Gamma_{sym,h}} = 0$ and $\beta_2|_{\Gamma_{wall,h}} = \xi$. Then the weak formulation of the semi-discrete problem reads as follows: find $\boldsymbol{u}_h \in L^q(I; U_h^F(\Omega_{h,t}))$ and $\eta_h \in H^1(I; U_h^S(0, L))$ such that for all $\boldsymbol{v} \in U^F_{h,0}(\Omega_{h,t})$ and a.e. $t \in I$ it holds

$$\begin{aligned}
&\int_{\Omega_{h,t}} \frac{\mathcal{D}^{\mathcal{A}}\boldsymbol{u}_h}{\mathcal{D}t} \cdot \boldsymbol{v}\ \mathrm{d}\omega + \frac{2}{\rho_f}\int_{\Omega_{h,t}} \mu(|\mathbf{D}(\boldsymbol{u}_h)|)\ \mathbf{D}(\boldsymbol{u}_h) : \mathbf{D}(\boldsymbol{v})\ \mathrm{d}\omega + \int_{\Omega_{h,t}} \left[(\boldsymbol{\beta} - \boldsymbol{w}_h) \cdot \bigtriangledown\boldsymbol{u}_h\right] \cdot \boldsymbol{v}\ \mathrm{d}\omega \\
&= \frac{1}{\rho_f}\int_{\Omega_{h,t}} \boldsymbol{f} \cdot \boldsymbol{v}\ \mathrm{d}\omega - \frac{\rho_s h_s}{\rho_f}\int_{\Gamma^0_{wall,h}} \left(\frac{\partial^2\eta_h}{\partial t^2} - a\frac{\partial^2\eta_h}{\partial x_1^2} + b\eta_h - c\frac{\partial^3\eta_h}{\partial t\partial x_1^2}\right) v_2|_{\Gamma^0_{wall,h}}\ \mathrm{d}l_0 \\
&\quad + a\frac{\rho_s h_s}{\rho_f}\int_{\Gamma^0_{wall,h}} \frac{\partial^2 R_0}{\partial x_1^2}\ v_2|_{\Gamma^0_{wall,h}}\ \mathrm{d}l_0.
\end{aligned} \tag{6.51}$$

6.6 Kinematic splitting of the semi-discrete problem (6.43)-(6.51)

Applying the strategy of kinematic splitting as defined in (6.15)-(6.16) we can write the weak formulation for the operator A as follows: find $\boldsymbol{u}_h \in L^q(I; U_h^F(\Omega_{h,t}))$ and $\eta_h \in H^1(I; U_h^S(\Gamma^0_{wall}))$ such that for all $\boldsymbol{v} \in U_{h,0}^F(\Omega_{h,t})$ and a.e. $t \in I$ it holds

$$\int\limits_{\Omega_{h,t}} \frac{\mathcal{D}^{\mathcal{A}}\boldsymbol{u}_h}{\mathcal{D}t} \cdot \boldsymbol{v} \, \mathrm{d}\omega + \frac{2}{\rho_f} \int\limits_{\Omega_{h,t}} \mu(|\mathbf{D}(\boldsymbol{u}_h)|) \, \mathbf{D}(\boldsymbol{u}_h) : \mathbf{D}(\boldsymbol{v}) \, \mathrm{d}\omega + \int\limits_{\Omega_{h,t}} \left[(\boldsymbol{\beta} - \boldsymbol{w}_h) \cdot \bigtriangledown \boldsymbol{u}_h\right] \cdot \boldsymbol{v} \, \mathrm{d}\omega$$
$$= \frac{1}{\rho_f} \int\limits_{\Omega_{h,t}} \boldsymbol{f} \cdot \boldsymbol{v} \, \mathrm{d}\omega - \frac{\rho_s h_s}{\rho_f} \int\limits_{\Gamma^0_{wall,h}} \left(\frac{\partial^2 \eta_h}{\partial t^2} - c \frac{\partial^3 \eta_h}{\partial t \partial x_1^2} \right) v_2 \, \mathrm{d}l_0. \tag{6.52}$$

The weak formulation of the operator B reads: find $\eta_h \in H^1(I; U_h^S(\Gamma^0_{wall}))$ such that for all $v \in U_{h,0}^S(\Gamma^0_{wall})$ and a.e. $t \in I$ the following integral equation is valid

$$\int_{\Gamma^0_{wall,h}} \frac{\partial \eta_h}{\partial t} \, v \, \mathrm{d}x_2 = \int_{\Gamma^0_{wall,h}} \xi_h \, v \, \mathrm{d}x_2, \tag{6.53a}$$

$$\int_{\Gamma^0_{wall,h}} \frac{\partial \xi_h}{\partial t} \, v \, \mathrm{d}x_2 = a \int_{\Gamma^0_{wall,h}} \frac{\partial^2 \eta_h}{\partial x_1^2} \, v \, \mathrm{d}x_2 - b \int_{\Gamma^0_{wall,h}} \eta_h \, v \, \mathrm{d}x_2 + \int_{\Gamma^0_{wall,h}} G(R_0) \, v \, \mathrm{d}x_2. \tag{6.53b}$$

6.7 Error analysis

In this section we will derive the error equation in order to investigate the convergence order of our fluid-structure interaction problem defined in (6.1)-(6.9). We will proceed as follows: using the weak formulation of the continuous problem, see Section 6.3, and the finite element weak formulation for the semi-discrete problem, see Section 6.6, we derive the error equation for the difference between an approximated solution and its interpolation. This analysis will be done for the operator A and the operator B separately. Finally, with help of the Gronwall lemma we obtain an auxiliary estimate, which will be rewritten in terms of the difference between the approximated and exact solution of the fluid-structure interaction problem.

In this section we assume that the following regularity of the weak solution is given

$$\boldsymbol{u} \in L^2(I; H^3(\Omega_{h,t})) \cap L^\infty(I; H^2(\Omega_{h,t})), \tag{6.54}$$
$$\eta \in H^2(I; H_0^2(0, L)) \cap L^\infty(I; H^1(0, L)). \tag{6.55}$$

Moreover, we suppose that time derivatives of $\boldsymbol{u}$ and η are from the following functional spaces

$$\boldsymbol{u}_t \in L^2(I; H^2(\Omega_{h,t})) \cap L^\infty(I; H^2(\Omega_{h,t})), \tag{6.56}$$
$$\eta_t = \xi \in H^1(I; H_0^2(0, L)) \cap L^\infty(I; H^1(0, L)), \tag{6.57}$$
$$\xi_t \in L^2(I; H_0^2(0, L)) \cap L^\infty(I; H^1(0, L)). \tag{6.58}$$

In addition, denoting the initial conditions for the numerical solution by $\boldsymbol{u}_h(\cdot, t_0) := \boldsymbol{u}_h(t_0)$, $\eta_h(\cdot, t_0) := \eta_h(t_0)$, $\xi_h(\cdot, t_0) := \xi_h(t_0)$ we assume that it holds

$$||\boldsymbol{u}_h(t_0) - \boldsymbol{u}_0||_{L^2(\Omega_{h,0})} \leq Ch^2 \, ||\boldsymbol{u}_0||_{H^2(\Omega_{h,0})}, \tag{6.59a}$$
$$||\xi_h(t_0) - \xi_0||_{L^2(\Gamma^0_{wall,h})} \leq Ch^2 \, ||\xi_0||_{H^2(\Gamma^0_{wall,h})}, \tag{6.59b}$$
$$||\eta_h(t_0) - \eta_0||_{L^2(\Gamma^0_{wall,h})} \leq Ch^2 \, ||\eta_0||_{H^2(\Gamma^0_{wall,h})}, \tag{6.59c}$$
$$||\eta_h(t_0) - \eta_0||_{H^1(\Gamma^0_{wall,h})} \leq Ch \, ||\eta_0||_{H^2(\Gamma^0_{wall,h})}. \tag{6.59d}$$

6.7.1 Error analysis for the operator A

Before starting the error analysis of the operator A, let us assume that for a fixed time instant $t \in I$ we can replace the real computational domain Ω_t by its discrete counterpart $\Omega_{h,t}$. If this is not the case the additional sources of error, the so-called variational crimes errors, have to be taken into account. Moreover, we will adopt the discrete ALE mapping and consecutively also the discrete domain velocity $\boldsymbol{w}_h$ for both, the continuous and the semi-discrete weak formulations. Therefore the continuous weak formulation for the operator A, cf. (6.17), can be written for all $\boldsymbol{v} \in C(I; U^F_{h,0}(\Omega_{h,t}))$ by

$$\begin{aligned}
&\int\limits_{\Omega_{h,t}} \frac{\mathcal{D}^{\mathcal{A}}\boldsymbol{u}}{\mathcal{D}t} \cdot \boldsymbol{v} \ \mathrm{d}\omega + \frac{2}{\rho_f} \int\limits_{\Omega_{h,t}} \mu(|\mathbf{D}(\boldsymbol{u})|)\ \mathbf{D}(\boldsymbol{u}) : \mathbf{D}(\boldsymbol{v}) \ \mathrm{d}\omega + \int\limits_{\Omega_{h,t}} \left[(\boldsymbol{\beta} - \boldsymbol{w}_h) \cdot \bigtriangledown \boldsymbol{u}\right] \cdot \boldsymbol{v} \ \mathrm{d}\omega \\
&= \quad \frac{1}{\rho_f} \int\limits_{\Omega_{h,t}} \boldsymbol{f} \cdot \boldsymbol{v} \ \mathrm{d}\omega - \frac{\rho_s h_s}{\rho_f} \int\limits_{\Gamma^0_{wall,h}} \left(\frac{\partial^2 \eta}{\partial t^2} - c \frac{\partial^3 \eta}{\partial t \partial x_1^2} \right) v_2 \ \mathrm{d}l_0. \qquad (6.60)
\end{aligned}$$

Assuming that $\xi = \partial\eta/\partial t$, $\xi_h = \partial\eta_h/\partial t$ we subtract the semi-discrete problem for the operator A, cf. (6.52), from the differential problem for the operator A, cf. (6.60). We obtain

$$\begin{aligned}
&\int\limits_{\Omega_{h,t}} \frac{\mathcal{D}^{\mathcal{A}}(\boldsymbol{u}_h - \boldsymbol{u})}{\mathcal{D}t} \cdot \boldsymbol{v} \ \mathrm{d}\omega + \frac{2}{\rho_f} \int\limits_{\Omega_{h,t}} \Big[\mu(|\mathbf{D}(\boldsymbol{u}_h)|)\ \mathbf{D}(\boldsymbol{u}_h) : \mathbf{D}(\boldsymbol{v}) - \mu(|\mathbf{D}(\boldsymbol{u})|)\ \mathbf{D}(\boldsymbol{u}) : \mathbf{D}(\boldsymbol{v})\Big] \ \mathrm{d}\omega \\
&+ \int\limits_{\Omega_{h,t}} \Big[(\boldsymbol{\beta} - \boldsymbol{w}_h) \cdot \bigtriangledown (\boldsymbol{u}_h - \boldsymbol{u})\Big] \cdot \boldsymbol{v} \ \mathrm{d}\omega = -\frac{\rho_s h_s}{\rho_f} \int\limits_{\Gamma^0_{wall,h}} \left(\frac{\partial(\xi_h - \xi)}{\partial t} - c \frac{\partial^2 (\xi_h - \xi)}{\partial x_1^2} \right) v_2 \ \mathrm{d}l_0.
\end{aligned} \qquad (6.61)$$

After some manipulations and applying the Reynolds transport theorem in the ALE frame, see (2.2), we can rewrite the first term from (6.61) as follows

$$\begin{aligned}
\int\limits_{\Omega_{h,t}} \frac{\mathcal{D}^{\mathcal{A}}(\boldsymbol{u}_h - \boldsymbol{u})}{\mathcal{D}t} \cdot \boldsymbol{v} \ \mathrm{d}\omega \quad &= \quad \int\limits_{\Omega_{h,t}} \frac{\mathcal{D}^{\mathcal{A}}[(\boldsymbol{u}_h - \boldsymbol{u}) \cdot \boldsymbol{v}]}{\mathcal{D}t} \ \mathrm{d}\omega - \int\limits_{\Omega_{h,t}} (\boldsymbol{u}_h - \boldsymbol{u}) \cdot \frac{\mathcal{D}^{\mathcal{A}}\boldsymbol{v}}{\mathcal{D}t} \ \mathrm{d}\omega \\
&= \int\limits_{\Omega_{h,t}} \frac{\partial[(\boldsymbol{u}_h - \boldsymbol{u}) \cdot \boldsymbol{v}]}{\partial t} \ \mathrm{d}\omega + \int\limits_{\Omega_{h,t}} \bigtriangledown \ [(\boldsymbol{u}_h - \boldsymbol{u}) \cdot \boldsymbol{v}] \cdot \boldsymbol{w}_h \ \mathrm{d}\omega - \int\limits_{\Omega_{h,t}} (\boldsymbol{u}_h - \boldsymbol{u}) \frac{\mathcal{D}^{\mathcal{A}}\boldsymbol{v}}{\mathcal{D}t} \ \mathrm{d}\omega \\
&= \frac{\mathrm{d}}{\mathrm{d}t} \int\limits_{\Omega_{h,t}} (\boldsymbol{u}_h - \boldsymbol{u}) \cdot \boldsymbol{v} \ \mathrm{d}\omega - \int\limits_{\Omega_{h,t}} (\boldsymbol{u}_h - \boldsymbol{u}) \cdot \boldsymbol{v} \bigtriangledown \cdot \boldsymbol{w}_h \ \mathrm{d}\omega \ - \int\limits_{\Omega_{h,t}} (\boldsymbol{u}_h - \boldsymbol{u}) \cdot \frac{\mathcal{D}^{\mathcal{A}}\boldsymbol{v}}{\mathcal{D}t} \ \mathrm{d}\omega.
\end{aligned} \qquad (6.62)$$

Moreover, noting that $\bigtriangledown \cdot \boldsymbol{\beta} = 0$ it holds

$$(\boldsymbol{\beta} - \boldsymbol{w}_h) \cdot \bigtriangledown (\boldsymbol{u}_h - \boldsymbol{u}) \quad = \quad \bigtriangledown \cdot \Big[(\boldsymbol{\beta} - \boldsymbol{w}_h)\ (\boldsymbol{u}_h - \boldsymbol{u})\Big] + (\boldsymbol{u}_h - \boldsymbol{u}) \bigtriangledown \cdot \boldsymbol{w}_h. \qquad (6.63)$$

The equation (6.61) can be rewritten using the equalities (6.62) and (6.63) as follows

$$\begin{aligned}
&\frac{\mathrm{d}}{\mathrm{d}t}\int\limits_{\Omega_{h,t}}(\boldsymbol{u}_h-\boldsymbol{u})\cdot\boldsymbol{v}\ \mathrm{d}\omega-\int\limits_{\Omega_{h,t}}(\boldsymbol{u}_h-\boldsymbol{u})\cdot\frac{\mathcal{D}^{\mathcal{A}}\boldsymbol{v}}{\mathcal{D}t}\ \mathrm{d}\omega+\int\limits_{\Omega_{h,t}}\bigtriangledown\cdot\Big[(\boldsymbol{\beta}-\boldsymbol{w}_h)\ (\boldsymbol{u}_h-\boldsymbol{u})\Big]\ \boldsymbol{v}\ \mathrm{d}\omega\\
&+\frac{2}{\rho_f}\int\limits_{\Omega_{h,t}}\Big[\mu(|\mathbf{D}(\boldsymbol{u}_h)|)\ \mathbf{D}(\boldsymbol{u}_h):\mathbf{D}(\boldsymbol{v})-\mu(|\mathbf{D}(\boldsymbol{u})|)\ \mathbf{D}(\boldsymbol{u}):\mathbf{D}(\boldsymbol{v})\Big]\ \mathrm{d}\omega\\
&\quad=-\frac{\rho_s h_s}{\rho_f}\int\limits_{\Gamma^0_{wall,h}}\frac{\partial(\xi_h-\xi)}{\partial t}\ v_2\ \mathrm{d}l_0+\frac{\rho_s h_s c}{\rho_f}\int\limits_{\Gamma^0_{wall,h}}\frac{\partial^2(\xi_h-\xi)}{\partial x_1^2}\ v_2\ \mathrm{d}l_0.
\end{aligned}\tag{6.64}$$

Let us take the following test function $\boldsymbol{v}:=\boldsymbol{u}_h-I_h\boldsymbol{u}$. Then, we can write

$$\begin{aligned}
&\frac{\mathrm{d}}{\mathrm{d}t}\int\limits_{\Omega_{h,t}}(\boldsymbol{u}_h-\boldsymbol{u})\cdot(\boldsymbol{u}_h-I_h\boldsymbol{u})\ \mathrm{d}\omega-\int\limits_{\Omega_{h,t}}(\boldsymbol{u}_h-\boldsymbol{u})\cdot\frac{\mathcal{D}^{\mathcal{A}}(\boldsymbol{u}_h-I_h\boldsymbol{u})}{\mathcal{D}t}\ \mathrm{d}\omega\\
&+\int\limits_{\Omega_{h,t}}\bigtriangledown\cdot\Big[(\boldsymbol{\beta}-\boldsymbol{w}_h)\ (\boldsymbol{u}_h-\boldsymbol{u})\Big]\cdot(\boldsymbol{u}_h-I_h\boldsymbol{u})\ \mathrm{d}\omega\\
&+\frac{2}{\rho_f}\int\limits_{\Omega_{h,t}}\Big[\mu(|\mathbf{D}(\boldsymbol{u}_h)|)\ \mathbf{D}(\boldsymbol{u}_h):\mathbf{D}(\boldsymbol{u}_h-I_h\boldsymbol{u})-\mu(|\mathbf{D}(\boldsymbol{u})|)\ \mathbf{D}(\boldsymbol{u}):\mathbf{D}(\boldsymbol{u}_h-I_h\boldsymbol{u})\Big]\ \mathrm{d}\omega\\
&=-\frac{\rho_s h_s}{\rho_f}\int\limits_{\Gamma^0_{wall,h}}\frac{\partial(\xi_h-\xi)}{\partial t}\ (\xi_h-S_h\xi)\ \mathrm{d}l_0+\frac{\rho_s h_s c}{\rho_f}\int\limits_{\Gamma^0_{wall,h}}\frac{\partial^2(\xi_h-\xi)}{\partial x_1^2}\ (\xi_h-S_h\xi)\ \mathrm{d}l_0.
\end{aligned}\tag{6.65}$$

In order to rewrite the first two terms from (6.65) in more suitable forms, we use the Reynolds transport theorem, definition of the ALE derivative as well as suitable properties of the divergence operator. Hence, the time derivative reads as follows

$$\frac{\mathrm{d}}{\mathrm{d}t}\int\limits_{\Omega_{h,t}}(\boldsymbol{u}_h-\boldsymbol{u})\cdot(\boldsymbol{u}_h-I_h\boldsymbol{u})\ \mathrm{d}\omega\quad=\quad\frac{\mathrm{d}}{\mathrm{d}t}||\boldsymbol{u}_h-I_h\boldsymbol{u}||^2_{L^2(\Omega_{h,t})}-\frac{\mathrm{d}}{\mathrm{d}t}\int_{\Omega_t}(\boldsymbol{u}-I_h\boldsymbol{u})\cdot(\boldsymbol{u}_h-I_h\boldsymbol{u})\ \mathrm{d}\omega,\tag{6.66}$$

where

$$\begin{aligned}
&\frac{\mathrm{d}}{\mathrm{d}t}\int\limits_{\Omega_{h,t}}(\boldsymbol{u}-I_h\boldsymbol{u})\cdot(\boldsymbol{u}_h-I_h\boldsymbol{u})\ \mathrm{d}\omega\\
&\quad=\int_{\Omega_{h,t}}\frac{\partial(\boldsymbol{u}-I_h\boldsymbol{u})\ (\boldsymbol{u}_h-I_h\boldsymbol{u})}{\partial t}\ \mathrm{d}\omega+\int_{\Omega_{h,t}}\bigtriangledown\cdot\Big[(\boldsymbol{u}-I_h\boldsymbol{u})\ (\boldsymbol{u}_h-I_h\boldsymbol{u})\ \boldsymbol{w}_h\Big]\mathrm{d}\omega\\
&\quad=\int\limits_{\Omega_{h,t}}(\boldsymbol{u}_h-I_h\boldsymbol{u})\ \frac{\partial(\boldsymbol{u}-I_h\boldsymbol{u})}{\partial t}\ \mathrm{d}\omega+\int\limits_{\Omega_{h,t}}(\boldsymbol{u}-I_h\boldsymbol{u})\Big[\frac{\mathcal{D}^{\mathcal{A}}(\boldsymbol{u}_h-I_h\boldsymbol{u})}{\mathcal{D}t}-\bigtriangledown(\boldsymbol{u}_h-I_h\boldsymbol{u})\cdot\boldsymbol{w}_h\Big]\mathrm{d}\omega\\
&\qquad+\int_{\Omega_{h,t}}\bigtriangledown\cdot\Big[(\boldsymbol{u}-I_h\boldsymbol{u})(\boldsymbol{u}_h-I_h\boldsymbol{u})\ \boldsymbol{w}_h\Big]\mathrm{d}\omega\\
&\quad=\int\limits_{\Omega_{h,t}}(\boldsymbol{u}_h-I_h\boldsymbol{u})\ \frac{\partial(\boldsymbol{u}-I_h\boldsymbol{u})}{\partial t}\ \mathrm{d}\omega+\int\limits_{\Omega_{h,t}}(\boldsymbol{u}-I_h\boldsymbol{u})\ \frac{\mathcal{D}^{\mathcal{A}}(\boldsymbol{u}_h-I_h\boldsymbol{u})}{\mathcal{D}t}\ \mathrm{d}\omega\\
&\qquad-\int\limits_{\Omega_{h,t}}(\boldsymbol{u}-I_h\boldsymbol{u})\ \bigtriangledown(\boldsymbol{u}_h-I_h\boldsymbol{u})\cdot\boldsymbol{w}_h\ \mathrm{d}\omega+\int_{\Omega_{h,t}}\bigtriangledown\cdot\Big[(\boldsymbol{u}-I_h\boldsymbol{u})(\boldsymbol{u}_h-I_h\boldsymbol{u})\ \boldsymbol{w}_h\Big]\mathrm{d}\omega
\end{aligned}$$

$$= \int\limits_{\Omega_{h,t}} (\boldsymbol{u}_h - I_h\boldsymbol{u}) \ \frac{\partial(\boldsymbol{u} - I_h\boldsymbol{u})}{\partial t} \ \mathrm{d}\omega + \int\limits_{\Omega_{h,t}} (\boldsymbol{u} - I_h\boldsymbol{u}) \ \frac{\mathcal{D}^{\mathcal{A}}(\boldsymbol{u}_h - I_h\boldsymbol{u})}{\mathcal{D}t} \ \mathrm{d}\omega$$
$$+ \int\limits_{\Omega_{h,t}} (\boldsymbol{u}_h - I_h\boldsymbol{u})(\boldsymbol{u} - I_h\boldsymbol{u}) \bigtriangledown \cdot \boldsymbol{w}_h \ \mathrm{d}\omega + \int\limits_{\Omega_{h,t}} (\boldsymbol{u}_h - I_h\boldsymbol{u}) \bigtriangledown (\boldsymbol{u} - I_h\boldsymbol{u}) \cdot \boldsymbol{w}_h \ \mathrm{d}\omega. \qquad (6.67)$$

Inserting (6.67) in (6.66) we have

$$\frac{\mathrm{d}}{\mathrm{d}t} \int\limits_{\Omega_{h,t}} (\boldsymbol{u}_h - \boldsymbol{u}) \ (\boldsymbol{u}_h - I_h\boldsymbol{u}) \ \mathrm{d}\omega \quad = \quad \frac{\mathrm{d}}{\mathrm{d}t} ||\boldsymbol{u}_h - I_h\boldsymbol{u}||^2_{L^2(\Omega_{h,t})} - \int\limits_{\Omega_{h,t}} (\boldsymbol{u}_h - I_h\boldsymbol{u}) \ \frac{\partial(\boldsymbol{u} - I_h\boldsymbol{u})}{\partial t} \ \mathrm{d}\omega$$
$$- \int\limits_{\Omega_{h,t}} (\boldsymbol{u} - I_h\boldsymbol{u}) \ \frac{\mathcal{D}^{\mathcal{A}}(\boldsymbol{u}_h - I_h\boldsymbol{u})}{\mathcal{D}t} \ \mathrm{d}\omega - \int\limits_{\Omega_{h,t}} (\boldsymbol{u}_h - I_h\boldsymbol{u})(\boldsymbol{u} - I_h\boldsymbol{u}) \bigtriangledown \cdot \boldsymbol{w}_h \ \mathrm{d}\omega$$
$$- \int\limits_{\Omega_{h,t}} (\boldsymbol{u}_h - I_h\boldsymbol{u}) \bigtriangledown (\boldsymbol{u} - I_h\boldsymbol{u}) \cdot \boldsymbol{w}_h \ \mathrm{d}\omega. \qquad (6.68)$$

The second term from (6.65) can be rewritten as

$$- \int\limits_{\Omega_{h,t}} (\boldsymbol{u}_h - \boldsymbol{u}) \ \frac{\mathcal{D}^{\mathcal{A}}(\boldsymbol{u}_h - I_h\boldsymbol{u})}{\mathcal{D}t} \ \mathrm{d}\omega$$
$$= - \int\limits_{\Omega_{h,t}} (\boldsymbol{u}_h - I_h\boldsymbol{u}) \left[\frac{\partial(\boldsymbol{u}_h - I_h\boldsymbol{u})}{\partial t} + \bigtriangledown(\boldsymbol{u}_h - I_h\boldsymbol{u}) \cdot \boldsymbol{w}_h \right] \mathrm{d}\omega + \int\limits_{\Omega_{h,t}} (\boldsymbol{u} - I_h\boldsymbol{u}) \ \frac{\mathcal{D}^{\mathcal{A}}(\boldsymbol{u}_h - I_h\boldsymbol{u})}{\mathcal{D}t} \ \mathrm{d}\omega$$
$$= -\frac{1}{2} \int\limits_{\Omega_{h,t}} \frac{\partial(\boldsymbol{u}_h - I_h\boldsymbol{u})^2}{\partial t} - \int\limits_{\Omega_{h,t}} (\boldsymbol{u}_h - I_h\boldsymbol{u}) \bigtriangledown (\boldsymbol{u}_h - I_h\boldsymbol{u}) \cdot \boldsymbol{w}_h \mathrm{d}\omega$$
$$+ \int\limits_{\Omega_{h,t}} (\boldsymbol{u} - I_h\boldsymbol{u}) \ \frac{\mathcal{D}^{\mathcal{A}}(\boldsymbol{u}_h - I_h\boldsymbol{u})}{\mathcal{D}t} \ \mathrm{d}\omega$$
$$= -\frac{1}{2} \frac{\mathrm{d}}{\mathrm{d}t} ||\boldsymbol{u}_h - I_h\boldsymbol{u}||^2_{L^2(\Omega_{h,t})} + \frac{1}{2} \int\limits_{\Omega_{h,t}} \bigtriangledown \cdot \left[|\boldsymbol{u}_h - I_h\boldsymbol{u}|^2 \boldsymbol{w}_h \right] \mathrm{d}\omega$$
$$- \frac{1}{2} \int\limits_{\Omega_{h,t}} \bigtriangledown (\boldsymbol{u}_h - I_h\boldsymbol{u})^2 \cdot \boldsymbol{w}_h \ \mathrm{d}\omega + \int\limits_{\Omega_{h,t}} (\boldsymbol{u} - I_h\boldsymbol{u}) \ \frac{\mathcal{D}^{\mathcal{A}}(\boldsymbol{u}_h - I_h\boldsymbol{u})}{\mathcal{D}t} \ \mathrm{d}\omega$$
$$= -\frac{1}{2} \frac{\mathrm{d}}{\mathrm{d}t} ||\boldsymbol{u}_h - I_h\boldsymbol{u}||^2_{L^2(\Omega_{h,t})} + \frac{1}{2} \int\limits_{\Omega_{h,t}} |\boldsymbol{u}_h - I_h\boldsymbol{u}|^2 \bigtriangledown \cdot \boldsymbol{w}_h \mathrm{d}\omega + \frac{1}{2} \int\limits_{\Omega_{h,t}} \bigtriangledown (\boldsymbol{u}_h - I_h\boldsymbol{u})^2 \cdot \boldsymbol{w}_h \mathrm{d}\omega$$
$$- \frac{1}{2} \int\limits_{\Omega_{h,t}} \bigtriangledown (\boldsymbol{u}_h - I_h\boldsymbol{u})^2 \cdot \boldsymbol{w}_h \ \mathrm{d}\omega + \int\limits_{\Omega_{h,t}} (\boldsymbol{u} - I_h\boldsymbol{u}) \ \frac{\mathcal{D}^{\mathcal{A}}(\boldsymbol{u}_h - I_h\boldsymbol{u})}{\mathcal{D}t} \ \mathrm{d}\omega$$
$$= -\frac{1}{2} \frac{\mathrm{d}}{\mathrm{d}t} ||\boldsymbol{u}_h - I_h\boldsymbol{u}||^2_{L^2(\Omega_{h,t})} + \frac{1}{2} \int\limits_{\Omega_{h,t}} |\boldsymbol{u}_h - I_h\boldsymbol{u}|^2 \bigtriangledown \cdot \boldsymbol{w}_h \ \mathrm{d}\omega$$
$$+ \int\limits_{\Omega_{h,t}} (\boldsymbol{u} - I_h\boldsymbol{u}) \ \frac{\mathcal{D}^{\mathcal{A}}(\boldsymbol{u}_h - I_h\boldsymbol{u})}{\mathcal{D}t} \ \mathrm{d}\omega. \qquad (6.69)$$

Observing that for two functions $\boldsymbol{g}$ and $\boldsymbol{h}$ it holds

$$\begin{aligned}
\int_{\Omega_{h,t}} \bigtriangledown \cdot (\boldsymbol{g}\boldsymbol{h})\ \boldsymbol{h}\ \mathrm{d}\omega &= -\int_{\Omega_{h,t}} \boldsymbol{g}\boldsymbol{h} \bigtriangledown \boldsymbol{h}\ \mathrm{d}\omega + \int_{\partial\Omega_{h,t}} (\boldsymbol{h})^2 \boldsymbol{g}\cdot\boldsymbol{n}\ \mathrm{d}\gamma \\
&= -\frac{1}{2}\int_{\Omega_{h,t}} \boldsymbol{g} \bigtriangledown (\boldsymbol{h})^2\ \mathrm{d}\omega + \int_{\partial\Omega_{h,t}} (\boldsymbol{h})^2 \boldsymbol{g}\cdot\boldsymbol{n}\ \mathrm{d}\gamma \\
&= \frac{1}{2}\int_{\Omega_{h,t}} (\boldsymbol{h})^2 \bigtriangledown \cdot \boldsymbol{g}\ \mathrm{d}\omega - \frac{1}{2}\int_{\partial\Omega_{h,t}} (\boldsymbol{h})^2 \boldsymbol{g}\cdot\boldsymbol{n}\ \mathrm{d}\gamma + \int_{\partial\Omega_{h,t}} (\boldsymbol{h})^2 \boldsymbol{g}\cdot\boldsymbol{n}\ \mathrm{d}\gamma \\
&= \frac{1}{2}\int_{\Omega_{h,t}} (\boldsymbol{h})^2 \bigtriangledown \cdot \boldsymbol{g}\ \mathrm{d}\omega + \frac{1}{2}\int_{\partial\Omega_{h,t}} (\boldsymbol{h})^2 \boldsymbol{g}\cdot\boldsymbol{n}\ \mathrm{d}\gamma,
\end{aligned}$$

we can manipulate the convective term appearing in (6.65) in the following way

$$\begin{aligned}
&\int_{\Omega_{h,t}} \bigtriangledown \cdot \Big[(\boldsymbol{\beta}-\boldsymbol{w}_h)\ (\boldsymbol{u}_h-\boldsymbol{u})\Big]\ (\boldsymbol{u}_h - I_h\boldsymbol{u})\ \mathrm{d}\omega \\
&\quad= \int_{\Omega_{h,t}} \bigtriangledown \cdot \Big[(\boldsymbol{\beta}-\boldsymbol{w}_h)\ (\boldsymbol{u}_h-I_h\boldsymbol{u})\Big]\ (\boldsymbol{u}_h - I_h\boldsymbol{u})\ \mathrm{d}\omega \\
&\qquad- \int_{\Omega_{h,t}} \bigtriangledown \cdot \Big[(\boldsymbol{\beta}-\boldsymbol{w}_h)\ (\boldsymbol{u}-I_h\boldsymbol{u})\Big]\ (\boldsymbol{u}_h - I_h\boldsymbol{u})\ \mathrm{d}\omega \\
&\quad= \frac{1}{2}\int_{\Omega_{h,t}} (\boldsymbol{u}_h - I_h\boldsymbol{u})^2 \bigtriangledown \cdot\ (\boldsymbol{\beta}-\boldsymbol{w}_h)\ \mathrm{d}\omega + \frac{1}{2}\int_{\partial\Omega_{h,t}} (\boldsymbol{u}_h - I_h\boldsymbol{u})^2(\boldsymbol{\beta}-\boldsymbol{w}_h)\cdot\boldsymbol{n}\ \mathrm{d}l \\
&\qquad- \int_{\Omega_{h,t}} (\boldsymbol{u}_h - I_h\boldsymbol{u})\ \bigtriangledown (\boldsymbol{u}-I_h\boldsymbol{u})\cdot(\boldsymbol{\beta}-\boldsymbol{w}_h)\ \mathrm{d}\omega \\
&\qquad- \int_{\Omega_{h,t}} (\boldsymbol{u}_h - I_h\boldsymbol{u})(\boldsymbol{u}-I_h\boldsymbol{u}) \bigtriangledown \cdot\ (\boldsymbol{\beta}-\boldsymbol{w}_h)\ \mathrm{d}\omega \\
&\quad= -\frac{1}{2}\int_{\Omega_{h,t}} (\boldsymbol{u}_h - I_h\boldsymbol{u})^2 \bigtriangledown \cdot\ \boldsymbol{w}_h\ \mathrm{d}\omega + \frac{1}{2}\int_{\partial\Omega_{h,t}} (\boldsymbol{u}_h - I_h\boldsymbol{u})^2(\boldsymbol{\beta}-\boldsymbol{w}_h)\cdot\boldsymbol{n}\ \mathrm{d}l \\
&\qquad- \int_{\Omega_{h,t}} (\boldsymbol{u}_h - I_h\boldsymbol{u})\ \bigtriangledown (\boldsymbol{u}-I_h\boldsymbol{u})\cdot\boldsymbol{\beta}\ \mathrm{d}\omega + \int_{\Omega_{h,t}} (\boldsymbol{u}_h - I_h\boldsymbol{u})\ \bigtriangledown (\boldsymbol{u}-I_h\boldsymbol{u})\cdot\boldsymbol{w}_h\ \mathrm{d}\omega \\
&\qquad+ \int_{\Omega_{h,t}} (\boldsymbol{u}_h - I_h\boldsymbol{u})(\boldsymbol{u}-I_h\boldsymbol{u}) \bigtriangledown \cdot\ \boldsymbol{w}_h\ \mathrm{d}\omega. \qquad (6.70)
\end{aligned}$$

Here the boundary term can be written as

$$\frac{1}{2}\int_{\partial\Omega_{h,t}} (\boldsymbol{u}_h - I_h\boldsymbol{u})^2(\boldsymbol{\beta}-\boldsymbol{w}_h)\cdot\boldsymbol{n}\ \mathrm{d}l \quad = \quad \frac{1}{2}\int_{\Gamma_{wall,h}} \frac{1}{\sqrt{1+(\partial_{x_1}R)^2}}\,(\boldsymbol{u}_h - I_h\boldsymbol{u})^2(\xi-\xi_h)\ \mathrm{d}l. \quad (6.71)$$

Note that integrals over $\Gamma_{in}, \Gamma_{out}$ and Γ_{sym} disappear due to the definition of velocity and $\boldsymbol{\beta}$ on these boundaries, i.e. it holds $\boldsymbol{u}_h|_{\Gamma_{in,h}} = I_h\boldsymbol{u}_h|_{\Gamma_{in,h}}$, $\boldsymbol{u}_h|_{\Gamma_{out,h}} = I_h\boldsymbol{u}_h|_{\Gamma_{out,h}}$, $\beta_2|_{\Gamma_{sym,h}} = 0$ and $\beta_2|_{\Gamma_{wall,h}} = \xi$. The factor $1/\sqrt{1+(\partial_{x_1}R)^2}$ arises from the definition of the outward unit

normal vector on Γ_{wall}, see (2.24). Inserting (6.68)-(6.71) into (6.65) we obtain

$$\begin{aligned}
&\frac{1}{2}\frac{\mathrm{d}}{\mathrm{d}t}||\boldsymbol{u}_h - I_h\boldsymbol{u}||^2_{L^2(\Omega_{h,t})} \\
&+ \frac{2}{\rho_f}\int\limits_{\Omega_{h,t}} \left[\mu(|\mathbf{D}(\boldsymbol{u}_h)|)\ \mathbf{D}(\boldsymbol{u}_h) : \mathbf{D}(\boldsymbol{u}_h - I_h\boldsymbol{u}) - \mu(|\mathbf{D}(\boldsymbol{u})|)\ \mathbf{D}(\boldsymbol{u}) : \mathbf{D}(\boldsymbol{u}_h - I_h\boldsymbol{u})\right]\mathrm{d}\omega \\
&\quad = \int\limits_{\Omega_{h,t}} (\boldsymbol{u}_h - I_h\boldsymbol{u})\ \frac{\partial(\boldsymbol{u} - I_h\boldsymbol{u})}{\partial t}\ \mathrm{d}\omega + \int\limits_{\Omega_{h,t}} (\boldsymbol{u}_h - I_h\boldsymbol{u})\ \bigtriangledown(\boldsymbol{u} - I_h\boldsymbol{u})\cdot\boldsymbol{\beta}\ \mathrm{d}\omega \\
&\qquad - \frac{\rho_s h_s}{\rho_f}\int\limits_{\Gamma^0_{wall,h}} \frac{\partial(\xi_h - \xi)}{\partial t}\ (\xi_h - S_h\xi)\ \mathrm{d}l_0 + c\ \frac{\rho_s h_s}{\rho_f}\int\limits_{\Gamma^0_{wall,h}} \frac{\partial^2(\xi_h - \xi)}{\partial x_1^2}\ (\xi_h - S_h\xi)\ \mathrm{d}l_0 \\
&\qquad - \frac{1}{2}\int\limits_{\Gamma_{wall,h}} \frac{1}{\sqrt{1 + (\partial_{x_1}R)^2}}\ (\boldsymbol{u}_h - I_h\boldsymbol{u})^2(\xi - \xi_h)\ \mathrm{d}l. \qquad (6.72)
\end{aligned}$$

Let us proceed with estimating the integrals from (6.72). Firstly, let us denote the integral on the left hand side by P_1 and the integrals on the right hand side by P_i, $i = 2, \ldots, 6$.

In order to simplify the matter, we estimate firstly the viscosity function appearing in the viscous term P_1. Considering shear thinning viscosity models, as it is the case for blood, we can bound the viscosity function from bellow with the asymptotic value μ_∞. Hence, we obtain

$$P_1 \geq \frac{2\mu_\infty}{\rho_f}\left(\int\limits_{\Omega_{h,t}} \mathbf{D}(\boldsymbol{u}_h - I_h\boldsymbol{u}) : \mathbf{D}(\boldsymbol{u}_h - I_h\boldsymbol{u})\ \mathrm{d}\omega - \int\limits_{\Omega_{h,t}} \mathbf{D}(\boldsymbol{u} - I_h\boldsymbol{u}) : \mathbf{D}(\boldsymbol{u}_h - I_h\boldsymbol{u})\ \mathrm{d}\omega\right). \quad (6.73)$$

The first integral from (6.73) can be estimated using the Poincaré inequality (1.16) as follows

$$\int\limits_{\Omega_{h,t}} \mathbf{D}(\boldsymbol{u}_h - I_h\boldsymbol{u}) : \mathbf{D}(\boldsymbol{u}_h - I_h\boldsymbol{u})\ \mathrm{d}\omega \quad \geq \quad C^*||\boldsymbol{u}_h - I_h\boldsymbol{u}||^2_{H^1(\Omega_{h,t})}. \qquad (6.74)$$

Applying the Young inequality for the second integral we get

$$\int\limits_{\Omega_{h,t}} \mathbf{D}(\boldsymbol{u} - I_h\boldsymbol{u}) : \mathbf{D}(\boldsymbol{u}_h - I_h\boldsymbol{u})\ \mathrm{d}\omega \quad \leq \quad \frac{C}{\varepsilon}\ ||\boldsymbol{u} - I_h\boldsymbol{u}||^2_{H^1(\Omega_{h,t})} + C\ \varepsilon\ ||\boldsymbol{u}_h - I_h\boldsymbol{u}||^2_{H^1(\Omega_{h,t})}. \qquad (6.75)$$

Here C^* and C are positive constants. Inserting (6.74) and (6.75) into (6.73) we can bound the term P_1 as follows

$$P_1 \quad \geq \quad \frac{2\mu_\infty}{\rho_f}\ (C^* - C\varepsilon)\ ||\boldsymbol{u}_h - I_h\boldsymbol{u}||^2_{H^1(\Omega_{h,t})} - \frac{2\mu_\infty}{\rho_f}\ \frac{1}{\varepsilon}\ ||\boldsymbol{u} - I_h\boldsymbol{u}||^2_{H^1(\Omega_{h,t})}. \qquad (6.76)$$

Using the Young and the trace inequality for the term with time-derivative P_2 we obtain

$$\begin{aligned}
P_2 \quad &\leq \quad \varepsilon\ ||\boldsymbol{u}_h - I_h\boldsymbol{u}||^2_{L^2(\Omega_{h,t})} + \frac{1}{4\varepsilon}\left|\left|\frac{\partial(\boldsymbol{u} - I_h\boldsymbol{u})}{\partial t}\right|\right|^2_{L^2(\Omega_{h,t})} \\
&\leq \quad C\varepsilon\ ||\boldsymbol{u}_h - I_h\boldsymbol{u}||^2_{H^1(\Omega_{h,t})} + \frac{1}{4\varepsilon}\left|\left|\frac{\partial(\boldsymbol{u} - I_h\boldsymbol{u})}{\partial t}\right|\right|^2_{L^2(\Omega_{h,t})}. \qquad (6.77)
\end{aligned}$$

Assuming that $\boldsymbol{\beta} \in L^\infty(I; W^{1,\infty}(\Omega_{h,t}))$ and using the Young inequality we obtain the estimate for the convective term, i.e.

$$\begin{aligned} P_3 &\leq ||\boldsymbol{\beta}||_{L^\infty(\Omega_{h,t})}||\boldsymbol{u}_h - I_h\boldsymbol{u}||_{L^2(\Omega_{h,t})} \; ||\bigtriangledown(\boldsymbol{u} - I_h\boldsymbol{u})||_{L^2(\Omega_{h,t})} \\ &\leq C \; ||\boldsymbol{\beta}||_{L^\infty(\Omega_{h,t})}||\boldsymbol{u}_h - I_h\boldsymbol{u}||_{H^1(\Omega_{h,t})} \; ||\boldsymbol{u} - I_h\boldsymbol{u}||_{H^1(\Omega_{h,t})} \\ &\leq \left(\frac{C^2}{4\varepsilon} \; ||\boldsymbol{\beta}||^2_{L^\infty(\Omega_{h,t})}\right)||\boldsymbol{u} - I_h\boldsymbol{u}||^2_{H^1(\Omega_{h,t})} + \varepsilon \; ||\boldsymbol{u}_h - I_h\boldsymbol{u}||^2_{H^1(\Omega_{h,t})}. \end{aligned} \tag{6.78}$$

Let us use the notation $d_1 := C^2/2$.

Now we will estimate the boundary terms P_4, P_5, P_6.

$$\begin{aligned} P_4 &= \frac{\rho_s h_s}{\rho_f}\left(-\int\limits_{\Gamma^0_{wall,h}} \frac{\partial(\xi_h - S_h\xi)}{\partial t}(\xi_h - S_h\xi) \; \mathrm{d}l_0 + \int\limits_{\Gamma^0_{wall,h}} \frac{\partial(\xi - S_h\xi)}{\partial t}(\xi_h - S_h\xi) \; \mathrm{d}l_0\right) \\ &\leq \frac{\rho_s h_s}{\rho_f}\left(-\frac{1}{2}\frac{\mathrm{d}}{\mathrm{d}t}||\xi_h - S_h\xi||^2_{L^2(\Gamma^0_{wall,h})} + \frac{1}{4\varepsilon}\left|\left|\frac{\partial(\xi - S_h\xi)}{\partial t}\right|\right|^2_{L^2(\Gamma^0_{wall,h})}\right. \\ &\qquad \left. + \varepsilon \; ||\xi_h - S_h\xi||^2_{L^2(\Gamma^0_{wall,h})}\right). \end{aligned} \tag{6.79}$$

Applying integration by parts we can estimate the term P_5 as follows

$$\begin{aligned} P_5 &= c\,\frac{\rho_s h_s}{\rho_f}\left(-\int\limits_{\Gamma^0_{wall,h}} \frac{\partial(\xi_h - S_h\xi)}{\partial x_1}\frac{\partial(\xi_h - S_h\xi)}{\partial x_1} \; \mathrm{d}l_0 + \int\limits_{\Gamma^0_{wall,h}} \frac{\partial(\xi - S_h\xi)}{\partial x_1}\frac{\partial(\xi_h - S_h\xi)}{\partial x_1} \; \mathrm{d}l_0\right) \\ &\leq c\,\frac{\rho_s h_s}{\rho_f}\left(-||(\xi_h - S_h\xi)_{x_1}||^2_{L^2(\Gamma^0_{wall,h})} + \frac{1}{4\tilde{\varepsilon}} \; ||(\xi - S_h\xi)_{x_1}||^2_{L^2(\Gamma^0_{wall,h})}\right. \\ &\qquad \left. + \tilde{\varepsilon} \; ||(\xi_h - S_h\xi)_{x_1}||^2_{L^2(\Gamma^0_{wall,h})}\right). \end{aligned}$$

Let $\tilde{\varepsilon}$ be a sufficiently small positive constant such that $\tilde{\varepsilon} < 1/2$. Then we can bound the term P_5 as follows

$$P_5 \leq c\,\frac{\rho_s h_s}{\rho_f}\left(-\frac{1}{2} \; ||(\xi_h - S_h\xi)_{x_1}||^2_{L^2(\Gamma^0_{wall,h})} + \frac{1}{4\tilde{\varepsilon}} \; ||(\xi - S_h\xi)_{x_1}||^2_{L^2(\Gamma^0_{wall,h})}\right). \tag{6.80}$$

Before estimating the term P_6, let us firstly transform the integral over $\Gamma_{wall,h}$ to the integral over $\Gamma^0_{wall,h}$. The coefficient of transformation $\tilde{g}$ is defined in (2.32). Hence, we have

$$\begin{aligned} P_6 &= -\frac{1}{2}\int\limits_{\Gamma^0_{wall,h}} \frac{\tilde{g}}{\sqrt{1 + (\partial_{x_1}R)^2}} \; (\boldsymbol{u}_h - I_h\boldsymbol{u})^2(\xi - \xi_h) \; \mathrm{d}x_2 \\ &= -\frac{1}{2}\frac{1}{\sqrt{1 + (\partial_{x_1}R_0)^2}}\int\limits_{\Gamma^0_{wall,h}} (\boldsymbol{u}_h - I_h\boldsymbol{u})^2(\xi - \xi_h) \; \mathrm{d}x_2. \end{aligned} \tag{6.81}$$

Rewriting $(\xi - \xi_h)$, using the formulas (6.39) and (6.49) and nothing that for $R_0 \in H^2(0, L)$ there exist a positive constant C^T such that

$$\frac{1}{\sqrt{1 + (\partial_{x_1}R_0)^2}} \leq \left|\left|\frac{1}{\sqrt{1 + (\partial_{x_1}R_0)^2}}\right|\right|_{L^\infty(\Gamma^0_{wall,h})} \leq C^T \tag{6.82}$$

we can rewrite (6.81) as

$$P_6 \;\leq\; \frac{C^T}{2}\int\limits_{\Gamma^0_{wall,h}} (\xi_h - S_h\xi)^2|\xi - S_h\xi|\ \mathrm{d}x_2 + \frac{C^T}{2}\int\limits_{\Gamma^0_{wall,h}} (\xi_h - S_h\xi)^2|\xi_h - S_h\xi|\ \mathrm{d}x_2. \tag{6.83}$$

Using the stability arguments analogous to those from the continuous problem, see Section 5.1, the inequality (5.31), we would get for our fluid-structure interaction problem (6.1)-(6.9) the following a priori estimate

$$\begin{aligned} ||\xi_h||_{L^\infty(I;H^1(\Gamma^0_{wall,h}))} \;\leq\; \tilde{C}\big(&||\boldsymbol{u}(t_0)||_{L^2(\Omega_{h,0})},\ |\eta(t_0)||_{H^1(\Gamma^0_{wall,h})},\ ||\xi(t_0)||_{L^2(\Gamma^0_{wall,h})},\\ &||\boldsymbol{f}||_{L^\infty(I;L^2(\Omega_{h,t}))},\ ||R_0||_{H^2(0,L)}\big), \end{aligned} \tag{6.84}$$

where $\tilde{C}$ denotes a linear function with respect to its arguments and it depends only on the prescribed data. Note that it holds: $H^1(\Gamma^0_{wall,h}) \hookrightarrow C(\Gamma^0_{wall,h})$. Moreover, let us assume that

$$\begin{gathered} \xi \in L^\infty(I; H^1(\Gamma^0_{wall,h})),\\ \exists\ \overline{C} > 0 \quad \text{s.t.} \quad ||\mathcal{S}_h\xi||_{H^1(\Gamma^0_{wall,h})} \;\leq\; \overline{C}\ ||\xi||_{H^1(\Gamma^0_{wall,h})}, \quad \forall \xi \in H^1(\Gamma^0_{wall,h}), \end{gathered}$$

see (5.31) and [36]. Then we can bound the integrals from (6.83) in the following way

$$\begin{aligned} &\frac{C^T}{2}\int\limits_{\Gamma^0_{wall,h}} (\xi_h - S_h\xi)^2|\xi - S_h\xi|\ \mathrm{d}x_2\\ &\qquad\leq \frac{C^T}{2}\Big(||\xi_h||^2_{C(\Gamma^0_{wall,h})} + ||S_h\xi||^2_{C(\Gamma^0_{wall,h})}\Big)\ ||\xi - S_h\xi||^2_{L^2(\Gamma^0_{wall,h})}\\ &\qquad\leq C^T C\ \Big(||\xi_h||^2_{H^1(\Gamma^0_{wall,h})} + ||S_h\xi_h||^2_{H^1(\Gamma^0_{wall,h})}\Big)||\xi - S_h\xi||^2_{L^2(\Gamma^0_{wall,h})}\\ &\qquad\leq C^T C\ \Big(||\xi_h||^2_{H^1(\Gamma^0_{wall,h})} + ||\xi||^2_{H^1(\Gamma^0_{wall,h})}\Big)||\xi - S_h\xi||^2_{L^2(\Gamma^0_{wall,h})}\\ &\qquad\leq C^T\ C\ (\tilde{C} + \overline{C})\ ||\xi - S_h\xi||^2_{L^2(\Gamma^0_{wall,h})}, \end{aligned} \tag{6.85}$$

$$\begin{aligned} &\frac{C^T}{2}\int\limits_{\Gamma^0_{wall,h}} (\xi_h - S_h\xi)^2|\xi_h - S_h\xi|\ \mathrm{d}x_2\\ &\qquad\leq C^T\ C\ (\tilde{C} + \overline{C})\ ||\xi_h - S_h\xi||^2_{L^2(\Gamma^0_{wall,h})}. \end{aligned} \tag{6.86}$$

Using (6.85) and (6.86) we can estimate the P_6 term with

$$P_6\ \leq C^\triangle\Big(||\xi - S_h\xi||^2_{L^2(\Gamma^0_{wall,h})} + ||\xi_h - S_h\xi||^2_{L^2(\Gamma^0_{wall,h})}\Big) \quad \text{with} \quad C^\triangle := C^T C\ (\tilde{C} + \overline{C}). \tag{6.87}$$

Let us assume $\varepsilon > 0$ sufficiently small such that $C\varepsilon + \rho_f\varepsilon(1 + C)/(2\mu_\infty) \leq C^*$. Then using the estimates for $P_i, i \in \{1, \ldots, 6\}$, cf. (6.76)-(6.80) and (6.87), we obtain the final estimate

for the operator A, which reads as follows

$$\begin{aligned}
&\frac{\mathrm{d}}{\mathrm{d}t}\,||\boldsymbol{u}_h - I_h\boldsymbol{u}||^2_{L^2(\Omega_{h,t})} + \frac{\rho_s h_s}{\rho_f}\frac{\mathrm{d}}{\mathrm{d}t}\,||\xi_h - S_h\xi||^2_{L^2(\Gamma^0_{wall,h})} \\
&+\frac{\mu_\infty C^*}{\rho_f}\,||\boldsymbol{u}_h - I_h\boldsymbol{u}||^2_{H^1(\Omega_{h,t})} + c\,\frac{\rho_s h_s}{\rho_f}\,||(\xi_h - S_h\xi)_{x_1}||^2_{L^2(\Gamma^0_{wall,h})} \\
&\quad\le \left[2\varepsilon\,\frac{\rho_s h_s}{\rho_f} + 2C^{\triangle}\right]||\xi_h - S_h\xi||^2_{L^2(\Gamma^0_{wall,h})} \\
&\qquad + \left[\frac{d_1}{\varepsilon}\,||\boldsymbol{\beta}||^2_{L^\infty(\Omega_{h,t})} + \frac{4\mu_\infty}{\varepsilon\rho_f}\right]||\boldsymbol{u} - I_h\boldsymbol{u}||^2_{H^1(\Omega_{h,t})} \\
&\qquad + 2C^{\triangle}||\xi - S_h\xi||^2_{L^2(\Gamma^0_{wall,h})} + \frac{c}{2\tilde{\varepsilon}}\,\frac{\rho_s h_s}{\rho_f}\,||(\xi - S_h\xi)_{x_1}||^2_{L^2(\Gamma^0_{wall,h})} \\
&\qquad + \frac{1}{2\varepsilon}\left|\left|\frac{\partial(\boldsymbol{u} - I_h\boldsymbol{u})}{\partial t}\right|\right|^2_{L^2(\Omega_{h,t})} + \frac{1}{2\varepsilon}\frac{\rho_s h_s}{\rho_f}\left|\left|\frac{\partial(\xi - S_h\xi)}{\partial t}\right|\right|^2_{L^2(\Gamma^0_{wall,h})}.
\end{aligned} \tag{6.88}$$

6.7.2 Error analysis for the operator B

In order to find the error estimate for the operator B let us start with subtracting the weak formulation for the semi-discrete problem from the weak formulation for the continuous problem, i.e. we subtract (6.53a) from (6.18a) and (6.53b) from (6.18b) and obtain

$$\int_{\Gamma^0_{wall,h}} \frac{\partial(\eta_h - \eta)}{\partial t}\,v\,\mathrm{d}x_2 = \int_{\Gamma^0_{wall,h}} (\xi_h - \xi)\,v\,\mathrm{d}x_2, \tag{6.89a}$$

$$\int_{\Gamma^0_{wall,h}} \frac{\partial(\xi_h - \xi)}{\partial t}\,v\,\mathrm{d}x_2 = a\int_{\Gamma^0_{wall,h}} \frac{\partial^2(\eta_h - \eta)}{\partial x_1^2}\,v\,\mathrm{d}x_2 - b\int_{\Gamma^0_{wall,h}} (\eta_h - \eta)\,v\,\mathrm{d}x_2, \tag{6.89b}$$

where $v \in C(I; U^S_{h,0}(\Gamma^0_{wall,h}))$. Then choosing the test function $v = b(\eta_h - S_h\eta)$ for the equation (6.89a) and $v = (\xi_h - S_h\xi)$ for the equation (6.89b) we can write

$$b\int_{\Gamma^0_{wall,h}} \frac{\partial(\eta_h - \eta)}{\partial t}\,(\eta_h - S_h\eta)\,\mathrm{d}x_2 = b\int_{\Gamma^0_{wall,h}} (\xi_h - \xi)\,(\eta_h - S_h\eta)\,\mathrm{d}x_2, \tag{6.90a}$$

$$\begin{aligned}
\int_{\Gamma^0_{wall,h}} \frac{\partial(\xi_h - \xi)}{\partial t}\,(\xi_h - S_h\xi)\,\mathrm{d}x_2 &= a\int_{\Gamma^0_{wall,h}} \frac{\partial^2(\eta_h - \eta)}{\partial x_1^2}\,(\xi_h - S_h\xi)\,\mathrm{d}x_2 \\
&\quad - b\int_{\Gamma^0_{wall,h}} (\eta_h - \eta)\,(\xi_h - S_h\xi)\,\mathrm{d}x_2.
\end{aligned} \tag{6.90b}$$

Now, noting that

$$(\eta_h - \eta) = (\eta_h - S_h\eta) - (\eta - S_h\eta), \quad (\xi_h - \xi) = (\xi_h - S_h\xi) - (\xi - S_h\xi)$$

and summing up equations (6.90a) and (6.90b) we obtain the following integral equation

$$\begin{aligned}
&b\int_{\Gamma^0_{wall,h}} \frac{\partial(\eta_h - S_h\eta)}{\partial t}\,(\eta_h - S_h\eta) - b\int_{\Gamma^0_{wall,h}} \frac{\partial(\eta - S_h\eta)}{\partial t}\,(\eta_h - S_h\eta)\,\mathrm{d}l_0 \\
&+\int_{\Gamma^0_{wall,h}} \frac{\partial(\xi_h - S_h\xi)}{\partial t}\,(\xi_h - S_h\xi) - \int_{\Gamma^0_{wall,h}} \frac{\partial(\xi - S_h\xi)}{\partial t}\,(\xi_h - S_h\xi)\,\mathrm{d}l_0 \\
&\quad = -b\int_{\Gamma^0_{wall,h}} (\xi - S_h\xi)(\eta_h - S_h\eta)\,\mathrm{d}l_0 + a\int_{\Gamma^0_{wall,h}} \frac{\partial^2(\eta_h - S_h\eta)}{\partial x_1^2}\,(\xi_h - S_h\xi)\,\mathrm{d}l_0 \\
&\qquad -a\int_{\Gamma^0_{wall,h}} \frac{\partial^2(\eta - S_h\eta)}{\partial x_1^2}\,(\xi_h - S_h\xi)\,\mathrm{d}l_0 + b\int_{\Gamma^0_{wall,h}} (\eta - S_h\eta)(\xi_h - S_h\xi)\,\mathrm{d}l_0,
\end{aligned}$$

which yields

$$\begin{aligned}
&\frac{b}{2}\,\frac{\mathrm{d}}{\mathrm{d}t}\,||\eta_h - S_h\eta||^2_{L^2(\Gamma^0_{wall,h})} - b\int_{\Gamma^0_{wall,h}} \frac{\partial(\eta - S_h\eta)}{\partial t}\,(\eta_h - S_h\eta)\,\mathrm{d}l_0 \\
&+\frac{1}{2}\,\frac{\mathrm{d}}{\mathrm{d}t}\,||\xi_h - S_h\xi||^2_{L^2(\Gamma^0_{wall,h})} - \int_{\Gamma^0_{wall,h}} \frac{\partial(\xi - S_h\xi)}{\partial t}\,(\xi_h - S_h\xi)\,\mathrm{d}l_0 \\
&\quad = -b\int_{\Gamma^0_{wall,h}} (\xi - S_h\xi)(\eta_h - S_h\eta)\,\mathrm{d}l_0 + a\int_{\Gamma^0_{wall,h}} \frac{\partial^2(\eta_h - S_h\eta)}{\partial x_1^2}\,(\xi_h - S_h\xi)\,\mathrm{d}l_0 \\
&\qquad -a\int_{\Gamma^0_{wall,h}} \frac{\partial^2(\eta - S_h\eta)}{\partial x_1^2}\,(\xi_h - S_h\xi)\,\mathrm{d}l_0 + b\int_{\Gamma^0_{wall,h}} (\eta - S_h\eta)(\xi_h - S_h\xi)\,\mathrm{d}l_0.
\end{aligned} \tag{6.91}$$

Using the definitions of structure velocity in the continuous as well as the semi-discrete case, i.e. $\xi = \partial\eta/\partial t$ and $\xi_h = \partial\eta_h/\partial t$, we have

$$(\xi_h - S_h\xi) = \frac{\partial(\eta_h - S_h\eta)}{\partial t} - \frac{\partial(\eta - S_h\eta)}{\partial t} + (\xi - S_h\xi). \tag{6.92}$$

The equality (6.92) and integration by parts helps us to rewrite the following integral

$$\begin{aligned}
&a\int_{\Gamma^0_{wall,h}} \frac{\partial^2(\eta_h - S_h\eta)}{\partial x_1^2}\,(\xi_h - S_h\xi)\,\mathrm{d}l_0 \\
&\quad = -a\int_{\Gamma^0_{wall,h}} \frac{\partial(\eta_h - S_h\eta)}{\partial x_1}\frac{\partial(\xi_h - S_h\xi)}{\partial x_1}\,\mathrm{d}l_0 \\
&\quad = -\frac{a}{2}\,\frac{\mathrm{d}}{\mathrm{d}t}\,||(\eta_h - S_h\eta)_{x_1}||^2_{L^2(\Gamma^0_{wall,h})} + a\int_{\Gamma^0_{wall,h}} \frac{\partial(\eta_h - S_h\eta)}{\partial x_1}\frac{\partial^2(\eta - S_h\eta)}{\partial t\partial x_1}\,\mathrm{d}l_0 \\
&\qquad -a\int_{\Gamma^0_{wall,h}} \frac{\partial(\eta_h - S_h\eta)}{\partial x_1}\frac{\partial(\xi - S_h\xi)}{\partial x_1}\,\mathrm{d}l_0.
\end{aligned} \tag{6.93}$$

Moreover, integration by parts yields

$$-a\int_{\Gamma^0_{wall,h}} \frac{\partial^2(\eta - S_h\eta)}{\partial x_1^2}(\xi_h - S_h\xi)\,\mathrm{d}l_0 \quad = \quad a\int_{\Gamma^0_{wall,h}} \frac{\partial(\eta - S_h\eta)}{\partial x_1}\frac{\partial(\xi_h - S_h\xi)}{\partial x_1}\,\mathrm{d}l_0. \tag{6.94}$$

Inserting (6.93)-(6.94) into (6.91) we have

$$\begin{aligned}
&\frac{1}{2}\,\frac{\mathrm{d}}{\mathrm{d}t}||\xi_h - S_h\xi||^2_{L^2(\Gamma^0_{wall,h})} + \frac{b}{2}\,\frac{\mathrm{d}}{\mathrm{d}t}||\eta_h - S_h\eta||^2_{L^2(\Gamma^0_{wall,h})} + \frac{a}{2}\,\frac{\mathrm{d}}{\mathrm{d}t}||(\eta_h - S_h\eta)_{x_1}||^2_{L^2(\Gamma^0_{wall,h})} \\
&\quad = b\int_{\Gamma^0_{wall,h}} \frac{\partial(\eta - S_h\eta)}{\partial t}(\eta_h - S_h\eta)\,\mathrm{d}l_0 + \int_{\Gamma^0_{wall,h}} \frac{\partial(\xi - S_h\xi)}{\partial t}(\xi_h - S_h\xi)\,\mathrm{d}l_0 \\
&\qquad - b\int_{\Gamma^0_{wall,h}} (\xi - S_h\xi)(\eta_h - S_h\eta)\,\mathrm{d}l_0 + a\int_{\Gamma^0_{wall,h}} \frac{\partial(\eta_h - S_h\eta)}{\partial x_1}\frac{\partial^2(\eta - S_h\eta)}{\partial t\partial x_1}\,\mathrm{d}l_0 \\
&\qquad - a\int_{\Gamma^0_{wall,h}} \frac{\partial(\eta_h - S_h\eta)}{\partial x_1}\frac{\partial(\xi - S_h\xi)}{\partial x_1}\,\mathrm{d}l_0 + a\int_{\Gamma^0_{wall,h}} \frac{\partial(\eta - S_h\eta)}{\partial x_1}\frac{\partial(\xi_h - S_h\xi)}{\partial x_1}\,\mathrm{d}l_0 \\
&\qquad + b\int_{\Gamma^0_{wall,h}} (\eta - S_h\eta)(\xi_h - S_h\xi)\,\mathrm{d}l_0.
\end{aligned} \tag{6.95}$$

Finally, applying the Young inequality on each term on the right hand side of (6.95), we

obtain the error estimate of the operator B, i.e.

$$\begin{aligned}
&\frac{1}{2}\,\frac{\mathrm{d}}{\mathrm{d}t}\,||\xi_h - S_h\xi||^2_{L^2(\Gamma^0_{wall,h})} + \frac{b}{2}\,\frac{\mathrm{d}}{\mathrm{d}t}\,||\eta_h - S_h\eta||^2_{L^2(\Gamma^0_{wall,h})} + \frac{a}{2}\,\frac{\mathrm{d}}{\mathrm{d}t}\,||(\eta_h - S_h\eta)_{x_1}||^2_{L^2(\Gamma^0_{wall,h})} \\
&\qquad \leq\ \bar{\varepsilon}(1+b)\,||\xi_h - S_h\xi||^2_{L^2(\Gamma^0_{wall,h})} + 2b\bar{\varepsilon}\,||\eta_h - S_h\eta||^2_{L^2(\Gamma^0_{wall,h})} \\
&\qquad\quad +2a\bar{\varepsilon}\,||(\eta_h - S_h\eta)_{x_1}||^2_{L^2(\Gamma^0_{wall,h})} + a\bar{\varepsilon}\,||(\xi_h - S_h\xi)_{x_1}||^2_{L^2(\Gamma^0_{wall,h})} \\
&\qquad\quad +\frac{b}{4\bar{\varepsilon}}\,||\xi - S_h\xi||^2_{L^2(\Gamma^0_{wall,h})} + \frac{b}{4\bar{\varepsilon}}\,||\eta - S_h\eta||^2_{L^2(\Gamma^0_{wall,h})} \\
&\qquad\quad +\frac{a}{4\bar{\varepsilon}}\,||(\xi - S_h\xi)_{x_1}||^2_{L^2(\Gamma^0_{wall,h})} + \frac{a}{4\bar{\varepsilon}}\,||(\eta - S_h\eta)_{x_1}||^2_{L^2(\Gamma^0_{wall,h})} \\
&\qquad\quad +\frac{1}{4\bar{\varepsilon}}\left|\left|\frac{\partial(\xi - S_h\xi)}{\partial t}\right|\right|^2_{L^2(\Gamma^0_{wall,h})} + \frac{b}{4\bar{\varepsilon}}\left|\left|\frac{\partial(\eta - S_h\eta)}{\partial t}\right|\right|^2_{L^2(\Gamma^0_{wall,h})} \\
&\qquad\quad +\frac{a}{4\bar{\varepsilon}}\left|\left|\frac{\partial(\eta - S_h\eta)_{x_1}}{\partial t}\right|\right|^2_{L^2(\Gamma^0_{wall,h})},
\end{aligned} \tag{6.96}$$

where $\bar{\varepsilon}$ is a small positive constant.

6.7.3 Error estimate of the coupled problem

Let $\bar{\varepsilon} < c/(4a)$. Multiplying the error estimate of the operator B (6.96) by $(2\rho_s h_s)/\rho_f$ and adding to the error estimate of the operator A, i.e. (6.88), we obtain

$$\begin{aligned}
&\frac{\mathrm{d}}{\mathrm{d}t}||\boldsymbol{u}_h - I_h\boldsymbol{u}||^2_{L^2(\Omega_{h,t})} + \frac{\mu_\infty C^*}{\rho_f}\,||\boldsymbol{u}_h - I_h\boldsymbol{u}||^2_{H^1(\Omega_{h,t})} + c\,\frac{\rho_s h_s}{2\rho_f}\,||(\xi_h - S_h\xi)_{x_1}||^2_{L^2(\Gamma^0_{wall,h})} \\
&+\ \frac{\rho_s h_s}{\rho_f}\,\frac{\mathrm{d}}{\mathrm{d}t}\left[2\,||\xi_h - S_h\xi||^2_{L^2(\Gamma^0_{wall,h})} + b\,||\eta_h - S_h\eta||^2_{L^2(\Gamma^0_{wall,h})} + a\,||(\eta_h - S_h\eta)_{x_1}||^2_{L^2(\Gamma^0_{wall,h})}\right] \\
&\qquad \leq \left(\frac{d_1}{\varepsilon}\,||\boldsymbol{\beta}||^2_{L^\infty(\Omega_{h,t})} + \frac{4\mu_\infty}{\varepsilon\rho_f}\right)||\boldsymbol{u} - I_h\boldsymbol{u}||^2_{H^1(\Omega_{h,t})} \\
&\qquad\quad + \frac{\rho_s h_s}{\rho_f}\left(2\varepsilon + 2\bar{\varepsilon}(1+b) + \frac{\rho_f 2C^\triangle}{\rho_s h_s}\right)||\xi_h - S_h\xi||^2_{L^2(\Gamma^0_{wall,h})} \\
&\qquad\quad + \frac{\rho_s h_s}{\rho_f}\,4b\bar{\varepsilon}\,||\eta_h - S_h\eta||^2_{L^2(\Gamma^0_{wall,h})} + \frac{\rho_s h_s}{\rho_f}\,4a\bar{\varepsilon}\,||(\eta_h - S_h\eta)_{x_1}||^2_{L^2(\Gamma^0_{wall,h})} \\
&\qquad\quad + \frac{\rho_s h_s}{\rho_f}\left(\frac{b}{2\bar{\varepsilon}} + \frac{\rho_f 2C^\triangle}{\rho_s h_s}\right)||\xi - S_h\xi||^2_{L^2(\Gamma^0_{wall,h})} + \frac{\rho_s h_s}{\rho_f}\,\frac{b}{2\bar{\varepsilon}}\,||\eta - S_h\eta||^2_{L^2(\Gamma^0_{wall,h})} \\
&\qquad\quad + \frac{\rho_s h_s}{\rho_f}\left(\frac{a}{2\bar{\varepsilon}} + \frac{c}{2\bar{\varepsilon}}\right)||(\xi - S_h\xi)_{x_1}||^2_{L^2(\Gamma^0_{wall,h})} + \frac{\rho_s h_s}{\rho_f}\frac{a}{2\bar{\varepsilon}}\,||(\eta - S_h\eta)_{x_1}||^2_{L^2(\Gamma^0_{wall,h})} \\
&\qquad\quad + \frac{\rho_s h_s}{\rho_f}\left(\frac{1}{2\bar{\varepsilon}} + \frac{1}{2\varepsilon}\right)\left|\left|\frac{\partial(\xi - S_h\xi)}{\partial t}\right|\right|^2_{L^2(\Gamma^0_{wall,h})} + \frac{\rho_s h_s}{\rho_f}\,\frac{b}{2\bar{\varepsilon}}\left|\left|\frac{\partial(\eta - S_h\eta)}{\partial t}\right|\right|^2_{L^2(\Gamma^0_{wall,h})} \\
&\qquad\quad + \frac{\rho_s h_s}{\rho_f}\,\frac{a}{2\bar{\varepsilon}}\left|\left|\frac{\partial(\eta - S_h\eta)_{x_1}}{\partial t}\right|\right|^2_{L^2(\Gamma^0_{wall,h})} + \frac{1}{2\varepsilon}\left|\left|\frac{\partial(\boldsymbol{u} - I_h\boldsymbol{u})}{\partial t}\right|\right|^2_{L^2(\Omega_{h,t})}.
\end{aligned} \tag{6.97}$$

Using the notation

$$\delta_1 := \max\left\{2\left(\varepsilon+\bar{\varepsilon}(1+b)+\frac{\rho_f C^{\triangle}}{\rho_s h_s}\right);\ 4\bar{\varepsilon}\right\}, \tag{6.98a}$$

$$\delta_2 := \max\left\{\left(\frac{b}{2\bar{\varepsilon}}+\frac{\rho_f 2C^{\triangle}}{\rho_s h_s}\right);\ \left(\frac{a}{2\bar{\varepsilon}}+\frac{c}{2\tilde{\varepsilon}}\right);\ \left(\frac{1}{2\bar{\varepsilon}}+\frac{1}{2\varepsilon}\right)\right\}, \tag{6.98b}$$

$$\delta_3 := \left(\frac{d_1}{\varepsilon}\ ||\boldsymbol{\beta}||^2_{L^\infty(\Omega_{h,t})}+\frac{4\mu_\infty}{\varepsilon\rho_f}\right) \tag{6.98c}$$

and

$$\begin{aligned} E_h^I(t) &:= ||\boldsymbol{u}_h(t)-I_h\boldsymbol{u}(t)||^2_{L^2(\Omega_{h,t})}+\frac{2\rho_s h_s}{\rho_f}\ ||\xi_h(t)-S_h\xi(t)||^2_{L^2(\Gamma^0_{wall,h})} \\ &\quad+\frac{\rho_s h_s b}{\rho_f}\ ||\eta_h(t)-S_h\eta(t)||^2_{L^2(\Gamma^0_{wall,h})}+\frac{\rho_s h_s a}{\rho_f}\ ||(\eta_h(t)-S_h\eta(t))_{x_1}||^2_{L^2(\Gamma^0_{wall,h})} \end{aligned} \tag{6.99}$$

we can rewrite (6.97) as follows

$$\begin{aligned} &\frac{\mathrm{d}}{\mathrm{d}t}\ E_h^I(t)+\frac{\mu_\infty C^*}{\rho_f}\ ||\boldsymbol{u}_h-I_h\boldsymbol{u}||^2_{H^1(\Omega_{h,t})}+\frac{c}{2}\ \frac{\rho_s h_s}{\rho_f}\ ||(\xi_h-S_h\xi)_{x_1}||^2_{L^2(\Gamma^0_{wall,h})} \\ &\quad\le\ \delta_1\ E_h^I(t)+\delta_3||\boldsymbol{u}-I_h\boldsymbol{u}||^2_{H^1(\Omega_{h,t})}+\frac{1}{2\varepsilon}\left|\left|\frac{\partial(\boldsymbol{u}-I_h\boldsymbol{u})}{\partial t}\right|\right|^2_{L^2(\Omega_{h,t})} \\ &\quad+\frac{\rho_s h_s}{\rho_f}\ \delta_2\left\{||\xi-S_h\xi||^2_{L^2(\Gamma^0_{wall,h})}+\ ||\eta-S_h\eta||^2_{L^2(\Gamma^0_{wall,h})}+\ ||(\xi-S_h\xi)_{x_1}||^2_{L^2(\Gamma^0_{wall,h})}\right. \\ &\qquad+||(\eta-S_h\eta)_{x_1}||^2_{L^2(\Gamma^0_{wall,h})}+\left|\left|\frac{\partial(\xi-S_h\xi)}{\partial t}\right|\right|^2_{L^2(\Gamma^0_{wall,h})} \\ &\qquad\left.+\left|\left|\frac{\partial(\eta-S_h\eta)}{\partial t}\right|\right|^2_{L^2(\Gamma^0_{wall,h})}+\left|\left|\frac{\partial(\eta-S_h\eta)_{x_1}}{\partial t}\right|\right|^2_{L^2(\Gamma^0_{wall,h})}\right\}. \end{aligned} \tag{6.100}$$

Integrating (6.100) from t_0 to t, where $t\in(t_0,T]$, we obtain

$$\begin{aligned} &E_h^I(t)+\frac{\mu_\infty C^*}{\rho_f}\int_{t_0}^{t}||\boldsymbol{u}_h(\tau)-I_h\boldsymbol{u}(\tau)||^2_{H^1(\Omega_{h,\tau})}\,\mathrm{d}\tau \\ &+\frac{c}{2}\ \frac{\rho_s h_s}{\rho_f}\int_{t_0}^{t}||(\xi_h(\tau)-S_h\xi(\tau))_{x_1}||^2_{L^2(\Gamma^0_{wall,h})}\,\mathrm{d}\tau \\ &\quad\le\ E_h^I(t_0)+\int_{t_0}^{t}\delta_1\ E_h^I(\tau)\,\mathrm{d}\tau+\int_{t_0}^{t}\delta_3\ ||\boldsymbol{u}(\tau)-I_h\boldsymbol{u}(\tau)||^2_{H^1(\Omega_{h,\tau})}\,\mathrm{d}\tau \\ &\quad+\frac{1}{2\varepsilon}\int_{t_0}^{t}\left|\left|\frac{\partial(\boldsymbol{u}(\tau)-I_h\boldsymbol{u}(\tau))}{\partial\tau}\right|\right|^2_{L^2(\Omega_{h,\tau})}\mathrm{d}\tau+\frac{\rho_s h_s}{\rho_f}\int_{t_0}^{t}\delta_2\left\{||\xi(\tau)-S_h\xi(\tau)||^2_{L^2(\Gamma^0_{wall,h})}\right. \\ &\quad+||\eta(\tau)-S_h\eta(\tau)||^2_{L^2(\Gamma^0_{wall,h})}+||(\xi(\tau)-S_h\xi(\tau))_{x_1}||^2_{L^2(\Gamma^0_{wall,h})} \\ &\quad\left.+||(\eta(\tau)-S_h\eta(\tau))_{x_1}||^2_{L^2(\Gamma^0_{wall,h})}+\left|\left|\frac{\partial(\xi(\tau)-S_h\xi(\tau))}{\partial\tau}\right|\right|^2_{L^2(\Gamma^0_{wall,h})}\right. \end{aligned}$$

$$+ \left|\left| \frac{\partial(\eta(\tau) - S_h\eta(\tau))}{\partial\tau} \right|\right|^2_{L^2(\Gamma^0_{wall,h})} + \left|\left| \frac{\partial(\eta(\tau) - S_h\eta(\tau))_{x_1}}{\partial\tau} \right|\right|^2_{L^2(\Gamma^0_{wall,h})} \Bigg\} \, \mathrm{d}\tau. \quad (6.101)$$

Let us denote the left hand side of (6.101) by $F(t)$, i.e.

$$\begin{aligned} F(t) \;&:=\; E_h^I(t) + \frac{\mu_\infty C^*}{\rho_f} \int_{t_0}^{t} ||\boldsymbol{u}_h(\tau) - I_h\boldsymbol{u}(\tau)||^2_{W^{1,2}(\Omega_\tau)} \, \mathrm{d}\tau \\ &\quad + \frac{c}{2}\frac{\rho_s h_s}{\rho_f} \int_{t_0}^{t} ||(\xi_h(\tau) - S_h\xi(\tau))_{x_1}||^2_{L^2(\Gamma^0_{wall})} \, \mathrm{d}\tau. \end{aligned} \quad (6.102)$$

Then it holds

$$E_h^I(t) \;\le\; F(t) \quad \text{and} \quad \int_{t_0}^{t} E_h^I(\tau) \, \mathrm{d}\tau \;\le\; \int_{t_0}^{t} F(\tau) \, \mathrm{d}\tau. \quad (6.103)$$

Inserting (6.103) into (6.101) we have

$$\begin{aligned} F(t) \;&\le\; E_h^I(t_0) + \int_{t_0}^{t} \delta_1 \; F(t) \, \mathrm{d}\tau + \int_{t_0}^{t} \delta_3 \; ||\boldsymbol{u}(\tau) - I_h\boldsymbol{u}(\tau)||^2_{H^1(\Omega_{h,\tau})} \, \mathrm{d}\tau \\ &\quad + \frac{1}{2\varepsilon} \int_{t_0}^{t} \left|\left| \frac{\partial(\boldsymbol{u}(\tau) - I_h\boldsymbol{u}(\tau))}{\partial\tau} \right|\right|^2_{L^2(\Omega_{h,\tau})} \mathrm{d}\tau + \frac{\rho_s h_s}{\rho_f} \int_{t_0}^{t} \delta_2 \Bigg\{ ||\xi(\tau) - S_h\xi(\tau)||^2_{L^2(\Gamma^0_{wall,h})} \\ &\quad + ||\eta(\tau) - S_h\eta(\tau)||^2_{L^2(\Gamma^0_{wall,h})} + ||(\xi(\tau) - S_h\xi(\tau))_{x_1}||^2_{L^2(\Gamma^0_{wall,h})} \\ &\quad + ||(\eta(\tau) - S_h\eta(\tau))_{x_1}||^2_{L^2(\Gamma^0_{wall,h})} + \left|\left| \frac{\partial(\xi(\tau) - S_h\xi(\tau))}{\partial\tau} \right|\right|^2_{L^2(\Gamma^0_{wall,h})} \\ &\quad + \left|\left| \frac{\partial(\eta(\tau) - S_h\eta(\tau))}{\partial\tau} \right|\right|^2_{L^2(\Gamma^0_{wall,h})} + \left|\left| \frac{\partial(\eta(\tau) - S_h\eta(\tau))_{x_1}}{\partial\tau} \right|\right|^2_{L^2(\Gamma^0_{wall,h})} \Bigg\} \, \mathrm{d}\tau. \end{aligned} \quad (6.104)$$

Applying the Gronwall lemma (1.26)-(1.28) on (6.104) we obtain

$$\begin{aligned} F(t) \;&\le\; gE_h^I(t_0) + g \int_{t_0}^{t} \delta_3 \; ||\boldsymbol{u}(\tau) - I_h\boldsymbol{u}(\tau)||^2_{H^1(\Omega_{h,\tau})} \, \mathrm{d}\tau \\ &\quad + \frac{g}{2\varepsilon} \int_{t_0}^{t} \left|\left| \frac{\partial(\boldsymbol{u}(\tau) - I_h\boldsymbol{u}(\tau))}{\partial\tau} \right|\right|^2_{L^2(\Omega_{h,\tau})} \mathrm{d}\tau \\ &\quad + g \; \frac{\rho_s h_s}{\rho_f} \int_{t_0}^{t} \delta_2 \Bigg\{ ||\xi(\tau) - S_h\xi(\tau)||^2_{L^2(\Gamma^0_{wall,h})} + ||\eta(\tau) - S_h\eta(\tau)||^2_{L^2(\Gamma^0_{wall,h})} \\ &\quad + ||(\xi(\tau) - S_h\xi(\tau))_{x_1}||^2_{L^2(\Gamma^0_{wall,h})} + \; ||(\eta(\tau) - S_h\eta(\tau))_{x_1}||^2_{L^2(\Gamma^0_{wall,h})} \\ &\quad + \left|\left| \frac{\partial(\xi(\tau) - S_h\xi(\tau))}{\partial\tau} \right|\right|^2_{L^2(\Gamma^0_{wall,h})} + \; \left|\left| \frac{\partial(\eta(\tau) - S_h\eta(\tau))}{\partial\tau} \right|\right|^2_{L^2(\Gamma^0_{wall,h})} \\ &\quad + \left|\left| \frac{\partial(\eta(\tau) - S_h\eta(\tau))_{x_1}}{\partial\tau} \right|\right|^2_{L^2(\Gamma^0_{wall,h})} \Bigg\} \, \mathrm{d}\tau, \end{aligned} \quad (6.105)$$

where $g := e^{\,\delta_1(t-t_0)}$. From the definition of $F(t)$, cf. (6.102), we see that it combines several positive norms. Therefore, it can be seen like an operator $F\Big(||s_h(t)-P_hs(t)||^2_\Upsilon\Big)$ that acts on the norms expressing the difference between an approximated function and its interpolation, where $P_h := I_h$ or $P_h := S_h$, respectively. Here s denotes the vector consisting from the following functions $s := (\boldsymbol{u}, \xi, \eta, \eta_{x_1}, \boldsymbol{u}, \xi_{x_1})$ and Υ denotes the corresponding spaces, i.e.

$$\begin{aligned}\Upsilon \;:=\; \Big(&L^\infty(t_0,t;L^2(\Omega_{h,t})),\; L^\infty(t_0,t;L^2(\Gamma^0_{wall,h})),\; L^\infty(t_0,t;L^2(\Gamma^0_{wall,h})),\\ &L^\infty(t_0,t;L^2(\Gamma^0_{wall,h})),\; L^2(t_0,t;W^{1,2}(\Omega_{h,t})),\; L^2(t_0,t;L^2(\Gamma^0_{wall,h}))\Big).\end{aligned}$$

Since it holds

$$\frac{1}{2}\;||s_h(t)-s(t)||^2_\Upsilon \quad\leq\quad ||s_h(t)-P_hs(t)||^2_\Upsilon \;+\; ||s(t)-P_hs(t)||^2_\Upsilon$$

for each function s and Υ as defined before and the operator F is linear, we can also write

$$\frac{1}{2}\;F\Big(||s_h(t)-s(t)||^2_\Upsilon\Big) \quad\leq\quad F\Big(||s_h(t)-P_hs(t)||^2_\Upsilon\Big) \;+\; F\Big(||s(t)-P_hs(t)||^2_\Upsilon\Big). \tag{6.106}$$

Let us now define the following energy norms

$$\begin{aligned}E_h(t) \;:=\;& ||\boldsymbol{u}_h(t)-\boldsymbol{u}(t)||^2_{L^2(\Omega_{h,t})} + \frac{2\rho_s h_s}{\rho_f}\;||\xi_h(t)-\xi(t)||^2_{L^2(\Gamma^0_{wall,h})}\\ &+\frac{\rho_s h_s b}{\rho_f}\;||\eta_h(t)-\eta(t)||^2_{L^2(\Gamma^0_{wall,h})} + \frac{\rho_s h_s a}{\rho_f}\;||(\eta_h(t)-\eta(t))_{x_1}||^2_{L^2(\Gamma^0_{wall,h})},\end{aligned} \tag{6.107}$$

$$\begin{aligned}E^I(t) \;:=\;& ||\boldsymbol{u}(t)-I_h\boldsymbol{u}(t)||^2_{L^2(\Omega_{h,t})} + \frac{2\rho_s h_s}{\rho_f}\;||\xi(t)-S_h\xi(t)||^2_{L^2(\Gamma^0_{wall,h})}\\ &+\frac{\rho_s h_s b}{\rho_f}\;||\eta(t)-S_h\eta(t)||^2_{L^2(\Gamma^0_{wall,h})} + \frac{\rho_s h_s a}{\rho_f}\;||(\eta(t)-S_h\eta(t))_{x_1}||^2_{L^2(\Gamma^0_{wall,h})}.\end{aligned} \tag{6.108}$$

Then the inequality (6.106) can be rewritten as

$$\begin{aligned}&\frac{1}{2}\;E_h(t) + \frac{\mu_\infty C^*}{2\rho_f}\int_{t_0}^{t}||\boldsymbol{u}_h(\tau)-\boldsymbol{u}(\tau)||^2_{H^1(\Omega_{h,\tau})}\,\mathrm{d}\tau + \frac{\rho_s h_s c}{4\rho_f}\int_{t_0}^{t}||(\xi_h(\tau)-\xi(\tau))_{x_1}||^2_{L^2(\Gamma^0_{wall,h})}\,\mathrm{d}\tau\\ &\leq E^I(t) + \frac{\mu_\infty C^*}{\rho_f}\int_{t_0}^{t}||\boldsymbol{u}(\tau)-I_h\boldsymbol{u}(\tau)||^2_{H^1(\Omega_{h,\tau})}\,\mathrm{d}\tau + \frac{\rho_s h_s c}{2\rho_f}\int_{t_0}^{t}||(\xi(\tau)-S_h\xi(\tau))_{x_1}||^2_{L^2(\Gamma^0_{wall,h})}\,\mathrm{d}\tau\\ &+\; E^I_h(t) + \frac{\mu_\infty C^*}{\rho_f}\int_{t_0}^{t}||\boldsymbol{u}_h(\tau)-I_h\boldsymbol{u}(\tau)||^2_{H^1(\Omega_{h,\tau})}\,\mathrm{d}\tau + \frac{\rho_s h_s c}{2\rho_f}\int_{t_0}^{t}||(\xi_h(\tau)-S_h\xi(\tau))_{x_1}||^2_{L^2(\Gamma^0_{wall,h})}\,\mathrm{d}\tau.\end{aligned} \tag{6.109}$$

Finally, noting that it holds

$$E^I_h(t_0) \quad\leq\quad E_h(t_0) \;+\; E^I(t_0)$$

and inserting the energy estimate (6.105) in (6.109) we obtain the error equation for fluid-structure interaction problem (6.1)-(6.9)

$$\begin{aligned}
&\frac{1}{2}\ E_h(t) + \frac{\mu_\infty C^*}{2\rho_f}\ \int_{t_0}^{t} ||\boldsymbol{u}_h(\tau) - \boldsymbol{u}(\tau)||^2_{H^1(\Omega_{h,\tau})}\ \mathrm{d}\tau + \frac{\rho_s h_s c}{4\rho_f} \int_{t_0}^{t} ||(\xi_h(\tau) - \xi(\tau))_{x_1}||^2_{L^2(\Gamma^0_{wall,h})}\ \mathrm{d}\tau \\
&\leq \quad g\ E_h(t_0)\ + g\ E^I(t_0) + ||\boldsymbol{u}(t) - I_h\boldsymbol{u}(t)||^2_{L^2(\Omega_{h,t})} + \frac{2\rho_s h_s}{\rho_f}\ ||\xi(t) - S_h\xi(t)||^2_{L^2(\Gamma^0_{wall,h})} \\
&\quad + \frac{\rho_s h_s b}{\rho_f}\ ||\eta(t) - S_h\eta(t)||^2_{L^2(\Gamma^0_{wall,h})} + \frac{\rho_s h_s a}{\rho_f}\ ||\eta(t) - S_h\eta(t)||^2_{H^1(\Gamma^0_{wall,h})} \\
&\quad + \frac{\mu_\infty C^*}{\rho_f}\ \int_{t_0}^{t} ||\boldsymbol{u}(\tau) - I_h\boldsymbol{u}(\tau)||^2_{H^1(\Omega_{h,\tau})}\ \mathrm{d}\tau + \frac{\rho_s h_s c}{2\rho_f}\ \int_{t_0}^{t} ||\xi(\tau) - S_h\xi(\tau)||^2_{H^1(\Gamma^0_{wall,h})}\ \mathrm{d}\tau \\
&\quad + g \int_{t_0}^{t} \delta_3\ ||\boldsymbol{u}(\tau) - I_h\boldsymbol{u}(\tau)||^2_{H^1(\Omega_{h,\tau})}\ \mathrm{d}\tau + \frac{g}{2\varepsilon} \int_{t_0}^{t} \left|\left| \frac{\partial(\boldsymbol{u}(\tau) - I_h\boldsymbol{u}(\tau))}{\partial\tau} \right|\right|^2_{L^2(\Omega_{h,\tau})} \mathrm{d}\tau \\
&\quad + g\ \frac{\rho_s h_s}{\rho_f}\ \int_{t_0}^{t} \delta_2 \left\{ ||\xi(\tau) - S_h\xi(\tau)||^2_{L^2(\Gamma^0_{wall,h})} + ||\eta(\tau) - S_h\eta(\tau)||^2_{L^2(\Gamma^0_{wall,h})} \right. \\
&\quad + ||\eta(\tau) - S_h\eta(\tau)||^2_{H^1(\Gamma^0_{wall,h})} + \left|\left| \frac{\partial(\xi(\tau) - S_h\xi(\tau))}{\partial\tau} \right|\right|^2_{L^2(\Gamma^0_{wall,h})} \\
&\quad \left. + \left|\left| \frac{\partial(\eta(\tau) - S_h\eta(\tau))}{\partial\tau} \right|\right|^2_{L^2(\Gamma^0_{wall,h})} + \left|\left| \frac{\partial\eta(\tau) - S_h\eta(\tau)}{\partial\tau} \right|\right|^2_{H^1(\Gamma^0_{wall,h})} \right\} \mathrm{d}\tau. \qquad (6.110)
\end{aligned}$$

Using the estimates (6.59a)-(6.59d) we can bound the energy term $E_h(t_0)$ as follows

$$E_h(t_0) \leq Ch^4\ ||\boldsymbol{u}_0||^2_{H^2(\Omega_{h,0})} + Ch^2\ \frac{\rho_s h_s}{\rho_f}\ \left[2h^2\ ||\xi_0||^2_{H^2(\Gamma^0_{wall,h})} + (ah^2 + b)\ ||\eta_0||^2_{H^2(\Gamma^0_{wall,h})} \right]. \qquad (6.111)$$

Moreover, from interpolation error estimates, see Lemma 6.1 and Lemma 6.2, we have

$$E^I(t_0) \leq Ch^4\ ||\boldsymbol{u}_0||^2_{H^2(\Omega_{h,0})} + Ch^2\ \frac{\rho_s h_s}{\rho_f}\ \left[2h^2\ ||\xi_0||^2_{H^2(\Gamma^0_{wall,h})} + (ah^2 + b)\ ||\eta_0||^2_{H^2(\Gamma^0_{wall,h})} \right]. \qquad (6.112)$$

Inserting (6.111) and (6.112) into (6.110) and applying the Lemmas 6.1 and 6.2 on the left hand side term from (6.110) we finally obtain the error estimate

$$\begin{aligned}
&\frac{1}{2}\ ||\boldsymbol{u}_h(t) - \boldsymbol{u}(t)||^2_{L^2(\Omega_{h,t})} + \ \frac{\mu_\infty C^*}{2\rho_f}\ \int_{t_0}^{t} ||\boldsymbol{u}_h(\tau) - \boldsymbol{u}(\tau)||^2_{H^1(\Omega_{h,\tau})}\ \mathrm{d}\tau \\
&+ \frac{c}{4}\ \frac{\rho_s h_s}{\rho_f} \int_{t_0}^{t} ||(\xi_h(\tau) - \xi(\tau))_{x_1}||^2_{L^2(\Gamma^0_{wall,h})}\ \mathrm{d}\tau + \frac{\rho_s h_s}{\rho_f} ||\xi_h(t) - \xi(t)||^2_{L^2(\Gamma^0_{wall,h})} \\
&+ \frac{\rho_s h_s}{2\rho_f} \left[b\ ||\eta_h(t) - \eta(t)||^2_{L^2(\Gamma^0_{wall,h})} + \ a\ ||(\eta_h(t) - \eta(t))_{x_1}||^2_{L^2(\Gamma^0_{wall,h})} \right] \\
&\leq \quad Ch^4 2g\ ||\boldsymbol{u}_0||^2_{H^2(\Omega_{h,0})} + Ch^2 2g\ \frac{\rho_s h_s}{\rho_f}\ \left[2h^2\ ||\xi_0||^2_{H^2(\Gamma^0_{wall,h})} + (ah^2 + b)\ ||\eta_0||^2_{H^2(\Gamma^0_{wall,h})} \right]
\end{aligned}$$

$$
\begin{aligned}
&+ Ch^4 \ ||\boldsymbol{u}(t)||^2_{H^2(\Omega_{h,t})} + Ch^2 \ \frac{\rho_s h_s}{\rho_f} \ \left[2h^2 ||\xi(t)||^2_{H^2(\Gamma^0_{wall,h})} + (ah^2 + b) \ ||\eta(t)||^2_{H^2(\Gamma^0_{wall,h})} \right] \\
&+ Ch^4 \int\limits_{t_0}^{t} \left(\frac{\mu_\infty C^*}{\rho_f} + g\delta_3 \right) \ ||\boldsymbol{u}(\tau)||^2_{H^2(\Omega_{h,\tau})} \ \mathrm{d}\tau \\
&+ Ch^2 \ \frac{g}{2\varepsilon} \int\limits_{t_0}^{t} \left(\left|\left| \frac{\partial \boldsymbol{u}(\tau)}{\partial \tau} \right|\right|_{H^2(\Omega_{h,\tau})} + \left[||\boldsymbol{w}_h(\tau)||_{L^\infty(\Omega_{h,\tau})} + \gamma \right] ||\boldsymbol{u}(\tau)||_{H^3(\Omega_{h,\tau})} \right)^2 \mathrm{d}\tau \\
&+ Ch^2 \ \frac{\rho_s h_s}{\rho_f} \int\limits_{t_0}^{t} \left(\left(\frac{c}{2} + g\delta_2 \ h^2 \right) \ ||\xi(\tau)||^2_{H^2(\Gamma^0_{wall,h})} + \ g\delta_2 \ (1 + h^2) \ ||\eta(\tau)||^2_{H^2(\Gamma^0_{wall,h})} \right. \\
&\left. + \ g\delta_2 h^2 \left|\left| \frac{\partial \xi(\tau)}{\partial \tau} \right|\right|^2_{H^2(\Gamma^0_{wall,h})} + \ g\delta_2 (1 + h^2) \ \left|\left| \frac{\partial \eta(\tau)}{\partial \tau} \right|\right|^2_{H^2(\Gamma^0_{wall,h})} \right) \mathrm{d}\tau. \qquad (6.113)
\end{aligned}
$$

Hence, we compared the solution of the continuous problem, cf. (6.14), with the solution of its semi-discrete counterpart, cf. (6.51), assuming that the fluid-structure interaction algorithm is based on the kinematic splitting technique (6.15)-(6.16). We showed the convergence of the first order in space.

Remark 6.3 *In the analysis of convergence for the fluid-structure interaction problem (6.1)-(6.9) we restricted our attention on a simplified situation, when* $\Omega_t = \Omega_{h,t}$ *and* $\Omega_0 = \Omega_{h,0}$. *However, in general, the continuous and discrete domains do not coincide, because* Ω_0 *and* Ω_t *may have curved boundaries. Therefore, one may introduce an auxiliary domain* $\tilde{\Omega}_0$ *consisting of both domains* Ω_0 *and* $\Omega_{h,0}$ *and analogously* $\tilde{\Omega}_t$ *consisting of* Ω_t *and* $\Omega_{h,t}$. *The analysis of convergence will be performed on the domains* $\tilde{\Omega}_0$ *and* $\tilde{\Omega}_t$, *where extensions for fluid and structure variables are assumed. It has been shown, see [46], that in the case of linear advection-diffusion problem with a given evolution of the moving boundary, the extension of velocities and given source function can be designed in such a way that the convergence will be in general preserved, i.e. it will be of the same type as for the simplified case* $\Omega_t = \Omega_{h,t}$ *and* $\Omega_0 = \Omega_{h,0}$.

Remark 6.4 (Definition of the function $\boldsymbol{\beta}$) *We would like to point out that the assumption* $\beta_2|_{\Gamma_{wall}} = \xi$ *might look quite artificial at the first sight. However, it reflects the intrinsic nonlinear coupling which is the core of the fluid-structure interaction problem. In practical algorithm it would be necessary to require* $\boldsymbol{\beta} = (0, \xi_h^{(old)})^T$, *where* $\xi_h^{(old)}$ *is the known structure velocity from the old iteration. Following the steps done in the estimate (6.85) the boundary integral* P_6 *would yield*

$$
\begin{aligned}
P_6 \ &:= \ -\frac{1}{2} \int\limits_{\Gamma_{wall,h}} (\boldsymbol{u}_h - I_h\boldsymbol{u})^2 (\boldsymbol{\beta} - \boldsymbol{w}_h) \cdot \boldsymbol{n} \ \mathrm{d}x_2 = -\frac{1}{2} \int\limits_{\Gamma_{wall,h}} (\boldsymbol{u}_h - I_h\boldsymbol{u})^2 (\xi_h^{(old)} - \xi_h) \ n_2 \ \mathrm{d}x_2 \\
&\leq \ C^\triangle \ ||\xi_h^{(old)} - \xi_h||^2_{L^\infty(\Gamma^0_{wall})} \qquad (6.114)
\end{aligned}
$$

Now, if the iterative process is converging (e.g. the underlying nonlinear operator is contractive), then

$$
||\xi_h^{(old)} - \xi_h||^2_{L^\infty(\Gamma^0_{wall,h})} \leq \varepsilon \ \to \ 0 \quad \text{and} \quad P_6 \ \leq \ C^\triangle \varepsilon \ \to \ 0.
$$

Remark 6.5 (Extension for the Navier-Stokes equations) *For the Navier-Stokes equations we need to take care that the approximation spaces for velocity U_h^F (and U_h^S) and for pressure $\mathcal{Q}_h$ satisfy inf-sup condition, which is needed for stabilization and to get error estimate for pressure. This can be done, e.g. by working with the test functions whose interpolation is divergence-free. Similarly as proposed by Prohl and Růžička, see, e.g. [30, 87], we will postulate for the approximation spaces $(U_h^F, \mathcal{Q}_h)$ that they fulfil the following assumptions:*

(A1) (Definition of approximation spaces) Let U_h^F be the approximation space for velocity defined by

$$U_h^F := \{\boldsymbol{v}_h|\ \boldsymbol{v}_h \in L^2(\Omega_{h,t}) :\ \boldsymbol{v}_h|_K \in \mathbb{P}^3(K),\ \forall\ K \in \mathcal{T}_{h,t}\}$$

equipped with the norm

$$||\boldsymbol{v}_h||_{U_h^F} := \left(\sum_{K\in\mathcal{T}_{h,t}} ||\boldsymbol{v}_h||^2_{L^2(K)} + ||\bigtriangledown \boldsymbol{v}_h||^2_{L^2(K)} \right)^{1/2}.$$

Let $\mathcal{Q}_h$ be the approximation space for pressure defined by

$$\mathcal{Q}_h := \{q_h|\ q_h \in L^2(\Omega_{h,t}) :\ q_h|_K \in \mathbb{Q}(K),\ \forall\ K \in \mathcal{T}_{h,t}\}$$

equipped with the norm

$$||q_h||_{\mathcal{Q}_h} := \left(\sum_{K\in\mathcal{T}_{h,t}} ||q_h||^2_{L^2(K)} \right)^{1/2}.$$

Let us note that the use of third order polynomials to approximate velocity is motivated by our futher application to generalized Navier-Stokes equations, as it was done in [30, 87].

(A2) (Weak continuity) Let $\Gamma = K_i \cap K_j$ denotes interelement face between two arbitrary chosen but neighbouring triangles K_i and K_j from $\mathcal{T}_{h,t}$. Then it holds

$$\int_\Gamma \Big(\boldsymbol{v}_h|_{K_i} - \boldsymbol{v}_h|_{K_j} \Big) \mathrm{d}\boldsymbol{x} = 0, \quad \forall \boldsymbol{v}_h \in U_h^F.$$

(A3) (Inverse inequality) Let m, ℓ are two real numbers such that $0 \le \ell \le m$. Let $\boldsymbol{v}_h \in M_h^F$, where M_h^F be the following space

$$M_h^F := \{\boldsymbol{v}_h|\boldsymbol{v}_h \in L^2(\Omega_{h,t}),\ \boldsymbol{v}_h|_K \in \mathbb{P}^3(K),\ \forall\ K \in \mathcal{T}_{h,t}\}$$

equipped with the norm $||\boldsymbol{v}_h||_{M_h^F} := \left(\sum_{K\in\mathcal{T}_{h,t}} ||\boldsymbol{v}_h||^2_{L^2(K)} \right)^{1/2}$. Then there exist a positive constant $C \neq C(h)$, $C = C(m, \ell, \mathcal{T}_{h,t})$ such that

$$\left(\sum_{K\in\mathcal{T}_{h,t}} |\boldsymbol{v}_h|^2_{W^{m,2}(K)} \right)^{1/2} \le Ch^{\ell-m\}} \left(\sum_{K\in\mathcal{T}_{h,t}} |\boldsymbol{v}_h|^2_{W^{\ell,2}(K)} \right)^{1/2},$$

where $|\cdot|_{W^{m,2}(K)}$ denotes the sum of the L^2 norms of the highest order derivatives on K.

(A4) *(Discrete Korn's inequality)* *There exists a positive constant $C \neq C(h)$ such that*

$$||\boldsymbol{v}_h||_{U_h^F} \leq C \, ||\mathbf{D}(\boldsymbol{v}_h)||_{M_h^F}, \quad \forall \, \boldsymbol{v}_h \in U_h^F.$$

(A5) *(Interpolation error)* *We assume that there exists interpolation operators*

$$I_h : \boldsymbol{v} \in H^2(\Omega_t) \to I_h \boldsymbol{v} \in M_h^F,$$
$$J_h : p \in H^1(\Omega_t) \to J_h p \in \mathcal{Q}_h,$$

such that it holds

$$\begin{aligned} ||\boldsymbol{v} - I_h \boldsymbol{v}||_{M_h^F} + h \, || \bigtriangledown (\boldsymbol{v} - I_h \boldsymbol{v})||_{M_h^F} &\leq Ch^2 \, ||\boldsymbol{v}||_{H^2(\Omega_t)} \\ ||p - J_h p||_{\mathcal{Q}_h} &\leq Ch \, ||p||_{H^1(\Omega_t)}, \end{aligned}$$

where $C \neq C(h)$, $C = C(\mathcal{T}_{h,t})$ is a positive constant.

(A6) *(Discrete inf-sup condition) For each $q_h \in Q_h$ there exists a nontrivial function $\phi_h \in U_h^F$ such that*

$$\Big| \sum_{K \in \mathcal{T}_{h,t}} \int_K q_h \bigtriangledown \cdot \, \phi_h \, \mathrm{d}x \Big| \quad \geq \quad C_0 \, || \bigtriangledown \phi_h||_{M_h^F} ||q_h||_{Q_h},$$

where C_0 is a positive constant $C_0 \neq C_0(h)$.

The postulates (A1)-(A6) represents conditions on abstract finite element spaces for velocity and pressure that can be used for analysis of convergence of Newtonian fluids, for which the flow is described by the Navier-Stokes equations. Assumption on weak continuity includes also non-conforming linear elements for velocities. Note that this approach would yield additional terms for jumps along the cell interfaces in the error equation that need to be treated. The extension to the case of generalized Navier-Stokes equations for shear-dependent fluids can be done assuming analogous assumptions as for the Newtonian fluids with an additional parameter [87]. More precisely, the functional spaces will depend in addition on the power-law exponent q (see, e.g. Carreau viscosity function model (3.19)). Since we are interested in analysis of convergence of fluid-structure interaction problem based on the idea of kinematic splitting, several assumption on the finite element spaces for structure should be done. As it was already mentioned in the derivation of error equation, we need to pay attention to the matching operators on the interface of fluid and structure boundary. This is closely linked to the fact that the discretization parameter h appearing in the triangulation $\mathcal{T}_{h,t}$ is in general different from the discretization parameter corresponding to the discrete moving boundary, see, e.g. [5, 80]. For stability issues it is important to impose the continuity of displacement and velocity for both, the fluid and the structure, on the moving boundary. This can be done using, e.g. an interpolation based operator or an projection operator for the moving interface.

We would like to note that the above facts present only technical difficulties, which appear due to non-Newtonian rheology and compliance of the domain of interest. However, the main strategy for proving the error estimates for our kinematic splitting scheme is analogous to those presented for the Oseen-type equation (6.1). The generalization of the above problem for the non-Newtonian fluids is a topic of our further research.

Chapter 7

Numerical experiments

This chapter is divided in two main parts: in the first part we will explain discretization methods and parameter setting and in the second part we will present results obtained from numerical experiments.

We will start with the description of discretization methods that have been used for the approximation of the generalized Navier-Stokes equations in moving domains (4.1a)-(4.1b) and the generalized string equation (4.2) with focus on the kinematic splitting technique as defined in (4.22)-(4.23). Our numerical scheme has been implemented in the UG toolbox, see e.g. [7, 8, 17, 76], which is the partial differential equations solver based on the finite volume method. The implementation of the Navier-Stokes equations with moving boundaries has been done by Broser [17] and the extensions for non-Newtonian viscosity function, Neumann boundary conditions and structure solver has been done by Hundertmark-Zaušková [107]. We have implemented the structure solver based on the kinematic splitting strategy, which divides our problem in two parts, one corresponding to the operator A and the second one corresponding to the operator B.

In the second part we present results of numerical experiments. Firstly, an experiment with a simple rectangular geometry with the prescribed sinus pulsatile inflow and the model data for viscosity function will be shown. Afterwards several experiments performed for a stenotic and a bifurcation geometry, physiological pulses and physiologically relevant viscosity will be presented. We will focus in particular on the evolution of wall deformation along the moving boundary with respect to the reference geometry. The results will be compared with the so-called global iterative scheme developed by Hundertmark and Lukáčová [58].

In order to analyse the accuracy of our fluid-structure interaction problem, we compute the experimental order of convergence for both, space and time. This study will be done for a non-stenosed geometry and sinus pulsatile inflow as well as for the model viscosity parameters. We will present a comparison between the Newtonian and non-Newtonian rheology, explicit and implicit kinematic splitting scheme, as well as the Marchuk-Yanenko and the Strang splitting scheme.

The last series of experiments will be devoted to the analysis of hemodynamic wall indices such as the wall shear stress and the oscillatory shear index. These indices belong to the group of parameters that can help the medical doctors to localize and identify many diseases of the cardiovascular system, e.g. atherosclerosis and thrombosis. We will compare several geometries and several constitutive models in terms of the wall shear stress distribution along the reference boundary Γ^0_{wall} and its evolution during one heart cycle. Moreover, we will describe the influence of geometry and rheology on the fluid flow.

7.1 Discretization methods

Our numerical scheme for fluid equations (4.1a)-(4.1b) is based on the finite volume method with use of the artificial compressibility stabilization, cf. [76, 77] UG-toolbox. The Euler implicit method, the Crank-Nicolson method or the second order backward differentiation formula can be applied for time discretization. For simplicity we present in what follows the numerical scheme using the Euler implicit method. The nonlinear problem is solved via the Newton method. Structure equation (2.34) is discretized using the splitting approach (4.22)-(4.23) in time and finite differences in space.

The operator A, cf. (5.38), is discretized as follows, see also Section 7.2 for more details,

$$\begin{aligned}
&\int_{\Omega_k^n} \begin{pmatrix} (\tilde{\boldsymbol{u}}_{\ell+1}^{n+1} - \boldsymbol{u}^n) \\ 0 \end{pmatrix} \, \mathrm{d}\omega + \Delta t \int_{\Omega_k^n} \begin{pmatrix} (\bigtriangledown \cdot \boldsymbol{w}^n)\tilde{\boldsymbol{u}}_{\ell+1}^{n+1} \\ 0 \end{pmatrix} \, \mathrm{d}\omega \\
&+\Delta t \int_{\partial\Omega_k^n} \begin{pmatrix} [(\tilde{\boldsymbol{u}}_{\ell}^{n+1} - \boldsymbol{w}^n)\cdot\boldsymbol{n}]\tilde{\boldsymbol{u}}_{\ell+1}^{n+1} + [(\tilde{\boldsymbol{u}}_{\ell+1}^{n+1} - \tilde{\boldsymbol{u}}_{\ell}^{n+1})\cdot\boldsymbol{n}]\tilde{\boldsymbol{u}}_{\ell}^{n+1} \\ 0 \end{pmatrix} \, \mathrm{d}l \\
&+\Delta t \int_{\partial\Omega_k^n} \begin{pmatrix} -(1/\rho_f)\mu(|\mathbf{D}(\tilde{\boldsymbol{u}}_{\ell}^{n+1})|)(\bigtriangledown\tilde{\boldsymbol{u}}_{\ell+1}^{n+1}\cdot\boldsymbol{n}) + (1/\rho_f)\tilde{p}_{\ell+1}^{n+1}\ (\mathbf{I}\cdot\boldsymbol{n}) \\ \tilde{\boldsymbol{u}}_{\ell+1}^{n+1}\cdot\boldsymbol{n} - (\triangle h)^2 \bigtriangledown(\tilde{p}_{\ell+1}^{n+1} - \tilde{p}_{\ell}^{n+1})\cdot\boldsymbol{n} \end{pmatrix} \, \mathrm{d}l = 0, \quad (7.1a) \\
&\frac{\xi^{n+1/2} - \xi^n}{\Delta t} = c\alpha\ \xi_{x_1x_1}^{n+1/2} + c(1-\alpha)\ \xi_{x_1x_1}^{n} + H(\tilde{p}_{\ell+1}^{n+1}, \tilde{\boldsymbol{u}}_{\ell+1}^{n+1}), \quad \alpha\in\{0.5;1\}. \quad (7.1b)
\end{aligned}$$

Here k is the index of control volume Ω_k, n denotes the time step, ℓ is the index of iteration in the Newton method and $\triangle h$ denotes the grid size. Moreover, for simplicity we assumed $\boldsymbol{f} = 0$. The Newmark scheme parameter α is chosen to be either 0.5 or 1. A new solution obtained from (7.1a) -(7.1b) is the velocity $\tilde{\boldsymbol{u}}^{n+1}$ and the pressure $\tilde{p}^{n+1}$ on Ω^n as well as the wall velocity function $\xi^{n+1/2}$ on Γ_{wall}^n. In the second step of the operator splitting approach the operator B is approximated. It combines the purely elastic part of structure equation and the kinematic splitting condition. The latter defines time derivative of the wall displacement η, which is the velocity ξ. An explicit scheme reads as follows

$$\begin{aligned}
\frac{\eta^{n+1} - \eta^n}{\Delta t} &= \alpha_1\ \xi^{n+1/2} + (1-\alpha_1)\ \xi^n, &(7.2a)\\
\frac{\xi^{n+1} - \xi^{n+1/2}}{\Delta t} &= a\alpha_2\ \eta_{x_1x_1}^{n+1} + a(1-\alpha_2)\ \eta_{x_1x_1}^{n} - b\alpha_2\ \eta^{n+1} - b(1-\alpha_2)\ \eta^n + G(R_0) &(7.2b)
\end{aligned}$$

for $\alpha_1 = 0.5,\ \alpha_2\in\{0.5;1\}$. An implicit scheme has the following form

$$\begin{aligned}
\frac{\eta^{n+1} - \eta^n}{\Delta t} &= \alpha_1\ \xi^{n+1} + (1-\alpha_1)\ \xi^{n+1/2} &(7.3a)\\
\frac{\xi^{n+1} - \xi^{n+1/2}}{\Delta t} &= a\alpha_2\ \eta_{x_1x_1}^{n+1} + a(1-\alpha_2)\ \eta_{x_1x_1}^{n} - b\alpha_2\ \eta^{n+1} - b(1-\alpha_2)\ \eta^n + G(R_0) &(7.3b)
\end{aligned}$$

for $\alpha_1 = 0.5,\ \alpha_2 = 0.5$. Note that $\xi^{n+1/2}$ used in (7.2a)-(7.3b) is obtained in (7.1a)-(7.1b). In our experiments we have used both the explicit as well as the implicit method, cf. (7.2a)-(7.2b), (7.3a)-(7.3b). The implicit coupling was typically more stable. We note that once new values for the wall displacement η^{n+1} and the velocity ξ^{n+1} are known, we update the fluid velocity on the moving boundary to $\boldsymbol{u}^{n+1}$ as well as the geometry. Let us point out that the operator $H(\boldsymbol{u}, p)$, cf. (4.24), has a term $R/R_0 = (R_0+\eta)/R_0$. For technical reasons in our numerical experiment we insert a part having the factor η/R_0 in the operator B. As a consequence b-term in the code has the following form

$$\tilde{b} := b + \frac{(P_{ext}\mathbf{I} + \mathbf{T})\ \boldsymbol{n}\cdot\boldsymbol{e}_r}{\rho_s h R_0} \frac{\sqrt{1+(\partial_{x_1}R)^2}}{\sqrt{1+(\partial_{x_1}R_0)^2}}\ .$$

This is motivated by the fact that we want to separate η from the equation $(4.22)_3$, which results in a parabolic equation only for ξ.

Remark 7.1 (On time discretization by operator splitting methods) *Fluid-structure interaction problem (7.1a)-(7.1b), (7.2a)-(7.2b) or (7.1a)-(7.1b), (7.3a)-(7.3b) can be rewritten in the following way*

$$\mathcal{U}^{n+1} = B_{\triangle t} A_{\triangle t}\, \mathcal{U}^n, \tag{7.4}$$

where $\mathcal{U}^n$ is the approximate solution of coupled problem at the time level t^n and $A_{\triangle t}$ and $B_{\triangle t}$ denote the operator A, cf. (4.22), and the operator B, cf. (4.23), acting on interval $(t^n, t^{n+1}]$, $\triangle t = t^{n+1} - t^n$, respectively. The scheme (7.4) is known as the Marchuk-Yanenko splitting scheme, which is of the first order. The accuracy of our time-splitting scheme can be improved using the second order Strang splitting scheme, i.e.

$$\mathcal{U}^{n+1} = B_{\triangle t/2} A_{\triangle t} B_{\triangle t/2}\, \mathcal{U}^n. \tag{7.5}$$

Here $B_{\triangle t/2}$ denotes the operator B acting on interval of length $\triangle t/2$. Both schemes (7.4)-(7.5) belong to the class of operator splitting methods commonly used for time discretization of initial valued problems, see [48] for more detail. In our numerical experiments, see Section 7.6, both time-splitting schemes have been used successfully and (7.5) increases the convergence rate in time.

7.2 Finite volume approximation of the fluid equations in the ALE frame

In this section we present the finite volume method used for approximation of the generalized Navier-Stokes equations. In contrast to the finite difference method, the governing equations in the finite volume method are discretized in the integral form. The main idea consists in partitioning the domain of interest Ω_t into sub-domains, also called control volumes, on which the unknown field variables, e.g. velocity and pressure, are approximated by a constant value, see e.g. [69].

Let $t = t^{n+1}$ be a fixed time instant from $(0, T]$ denoting the $(n+1)$-th time step. For simplicity, in the following we omit the subscript t denoting explicit dependence of the domain Ω on time. Let Ω_h be a polygonal approximation of the domain Ω and $\mathcal{T}_h$ be a triangulation corresponding to Ω_h composed from n_{gp} nodes (also called grid points). Let $\mathcal{P}_h = \{P_i,\ i = 1, \ldots, n_{gp}\}$ be the set of all vertices of triangles from $\mathcal{T}_h$. The triangulation $\mathcal{T}_h$ is called the *basic mesh* having the following properties

$$\overline{\Omega}_h = \bigcup_{T \in \mathcal{T}_h} T \quad \text{and} \quad P_i \in \overline{\Omega}_h \quad \text{for} \quad i \in n_{gp},$$

$$T_i \cap T_j \;=\; \begin{cases} \text{boundary or empty set} & \text{if} \quad i \neq j, \\ T_i = T_j & \text{if} \quad i = j. \end{cases} \tag{7.6}$$

Then, we denote by $\mathcal{D}_h = \{\Omega_i, i = 1, \ldots, n_{gp}\}$ the polygonal finite volume *dual mesh* corresponding to the basic mesh $\mathcal{T}_h$ consisting from closed polygonals. Hence the dual mesh $\mathcal{D}_h$ divides the computational domain Ω into control volumes Ω_i with the following properties

$$\overline{\Omega}_h = \bigcup_{i=1}^{n_{gp}} \Omega_i,$$

$$\Omega_i \cap \Omega_j = \begin{cases} \text{boundary or empty set} & \text{if} \quad i \neq j, \\ \Omega_i = \Omega_j & \text{if} \quad i = j. \end{cases} \tag{7.7}$$

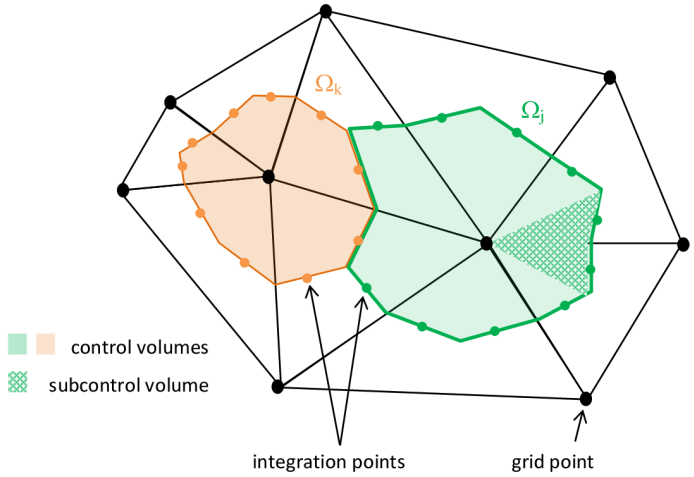

Figure 7.1: A possible grid arrangement for the FVM. Each control volume is represented by a grid point (gp) and a set of integration points (ip).

Note that each control volume is represented by a grid point (gp) situated at the centre of the control volume, see Fig. 7.1. Therefore the number of control volumes equals to the number of grid points. The grid points are used for interpolation of field variables. Let $N_{gp} := \{i : i = 1, \dots, n_{gp}\}$ is the set of all grid points. From the construction of dual mesh for arbitrary two control volumes Ω_k and Ω_j such that $k, j \in N_{gp},\ k \neq j$, it holds

$$\Omega_k \cap \Omega_j = \begin{cases} \text{either empty set} \\ \text{or one common edge } a_{kj} \\ \text{or two common edges } a_{kj} \cup b_{kj}. \end{cases}$$

If Ω_k is not a boundary control volume, i.e. $\partial\Omega_k \cap \partial\Omega_h = \emptyset$, we denote by $s(k)$ the set of all neighbouring control volumes to Ω_k, defined by

$$s(k) := \{j \in N_{gp},\ \partial\Omega_k \cap \partial\Omega_j \text{ is one or two straight segments}\}.$$

If Ω_k is a boundary element, i.e. $\partial\Omega_k \cap \partial\Omega_h \neq \emptyset$, then we define $\partial\Omega_{k,-1} := \partial\Omega_k \cap \partial\Omega_h$ and the corresponding set of neighbours to Ω_k is

$$s(k) := \{j = -1 \text{ and } j \in N_{gp},\ \partial\Omega_k \cap \partial\Omega_j \text{ is one or two straight segments}\}.$$

Hence, it holds

$$\partial\Omega_k = \bigcup_{j \in s(k)} \partial\Omega_{kj} \quad \text{and} \quad \partial\Omega = \bigcup_{k=1}^{n_{gp}} \bigcup_{j \in s(k)} \partial\Omega_{kj}.$$

Now we denote by Ω_{kj}, $j \in s(k)$ a subcontrol volume associated with the control volume Ω_k, for which it holds

$$\Omega_k = \bigcup_{j \in s(k)} \Omega_{kj}, \quad \text{where} \quad \Omega_{kj} \text{ is a triangle,}$$

$$\Omega_{ki} \cap \Omega_{kj} = \begin{cases} \text{boundary or empty set} & \text{if} \quad i \neq j, \\ \Omega_{ki} = \Omega_{kj} & \text{if} \quad i = j. \end{cases} \tag{7.8}$$

Finally, in the middle of each straight segment corresponding to the subcontrol volume boundary $\partial\Omega_{kj}$ we define the so-called integration point (ip), see Fig. 7.1.

In the following we apply the method of finite volumes on the fluid equations to discretize them in space and backward Euler implicit method for time discretization. Firstly, we rewrite the generalized fluid equations (4.1a)-(4.1b) as follows

$$\frac{\mathcal{D}^{\mathcal{A}} G(\boldsymbol{y})}{\mathcal{D}t} + F(\boldsymbol{y}) = 0 \quad \text{on} \quad \Omega, \tag{7.9}$$

where

$$\boldsymbol{y} := \begin{pmatrix} \boldsymbol{u} \\ p \end{pmatrix}, \quad G(\boldsymbol{y}) := \begin{pmatrix} \boldsymbol{u} \\ 0 \end{pmatrix},$$
$$F(\boldsymbol{y}) := \begin{pmatrix} (\boldsymbol{u}-\boldsymbol{w}) \cdot \bigtriangledown \boldsymbol{u} - (2/\rho_f) \bigtriangledown \cdot [\mu(|\mathbf{D}(\boldsymbol{u})|)\ \mathbf{D}(\boldsymbol{u})] + (1/\rho_f) \bigtriangledown \cdot (p\mathbf{I}) - (1/\rho_f)\boldsymbol{f} \\ \bigtriangledown \cdot \boldsymbol{u} \end{pmatrix}.$$

Let $0 = t_0 < t_1 < \cdots < t_n = T$ be a partition of the time interval $I = [0, T]$. For a fixed time instant $t = t^n$ let us denote by $\triangle t := t^{n+1} - t^n$. We perform our discretization on the domain corresponding to the time instant t^n, i.e. $\Omega^n := \Omega(t^n)$. Note, that discretization with respect to the computational domain Ω^{n+1} would look similarly. Then the backward Euler implicit method applied on time derivative term from (7.9) yields

$$\frac{G(\tilde{\boldsymbol{y}}^{n+1}) - G(\boldsymbol{y}^n)}{\triangle t} \ = \ -F(\tilde{\boldsymbol{y}}^{n+1}) \quad \text{on} \quad \Omega(t^n), \tag{7.10}$$

where $\tilde{\boldsymbol{y}}^{n+1} := \boldsymbol{y}^{n+1} \circ \mathcal{A}_{t^{n+1}} \circ \mathcal{A}_{t^n}^{-1}$. Using the test function $\phi \in H_0^1(\Omega^n)$ the problem (7.10) can be rewritten as

$$\int_{\Omega^n} \frac{G(\tilde{\boldsymbol{y}}^{n+1}) - G(\boldsymbol{y}^n)}{\triangle t}\ \phi\ \mathrm{d}\omega = -\int_{\Omega^n} F(\tilde{\boldsymbol{y}}^{n+1})\ \phi\ \mathrm{d}\omega, \quad \forall \phi \in H_0^1(\Omega^n). \tag{7.11}$$

In our discretization we assume ϕ is a characteristic function for control volumes, i.e. for $k \in N_{gp}$ it holds

$$Q = I_k(\boldsymbol{x}) = \begin{cases} 1 & \text{if} \quad \boldsymbol{x} \in \Omega_k^n, \\ 0 & \text{if} \quad \text{elsewhere.} \end{cases}$$

In order to linearize the problem (7.11) we use the Newton method. To this end let us define an operator

$$D(\tilde{\boldsymbol{y}}^{n+1}) := G(\tilde{\boldsymbol{y}}^{n+1}) - G(\boldsymbol{y}^n) + \triangle t\ F(\tilde{\boldsymbol{y}}^{n+1})$$

and solve the following problem

$$\tilde{\boldsymbol{y}}_{\ell+1}^{n+1} = \tilde{\boldsymbol{y}}_{\ell}^{n+1} + JD(\tilde{\boldsymbol{y}}_{\ell}^{n+1})^{-1} D(\tilde{\boldsymbol{y}}_{\ell}^{n+1}),$$

where JD denotes the Jacobian of the operator D and ℓ is the index of iteration in the Newton method. Thus, we solve the integral equation

$$\int_{\Omega^n} JD(\tilde{\boldsymbol{y}}_{\ell}^{n+1})(\tilde{\boldsymbol{y}}_{\ell+1}^{n+1} - \tilde{\boldsymbol{y}}_{\ell}^{n+1})\phi\ \mathrm{d}\omega \ = \ -\int_{\Omega^n} D(\tilde{\boldsymbol{y}}_{\ell}^{n+1})\ \phi\ \mathrm{d}\omega, \quad \forall \phi \in H_0^1, \tag{7.12}$$

where $(\tilde{\boldsymbol{y}}_{\ell+1}^{n+1} - \tilde{\boldsymbol{y}}_{\ell}^{n+1})$ represents the nonlinear correction. From (7.12) it follows that we have to solve altogether n_{gp} equations of the type

$$\int_{\Omega_k^n} JD(\boldsymbol{y}_{\ell}^{n+1})(\tilde{\boldsymbol{y}}_{\ell+1}^{n+1} - \tilde{\boldsymbol{y}}_{\ell}^{n+1})\ \mathrm{d}\omega \ = \ -\int_{\Omega_k^n} D(\tilde{\boldsymbol{y}}_{\ell}^{n+1})\ \mathrm{d}\omega, \quad \text{for} \quad k = 1, \ldots, n_{gp}. \tag{7.13}$$

The operator $D(\tilde{\boldsymbol{y}}_\ell^{n+1})$ on the right hand side of (7.13) has the following form

$$\begin{aligned} D(\tilde{\boldsymbol{y}}_\ell^{n+1}) &= \begin{pmatrix} \tilde{\boldsymbol{u}}_\ell^{n+1} - \boldsymbol{u}_\ell^n \\ 0 \end{pmatrix} + \Delta t \begin{pmatrix} (\bigtriangledown \cdot \boldsymbol{w}^n)\ \tilde{\boldsymbol{u}}_\ell^{n+1} \\ 0 \end{pmatrix} - \Delta t \begin{pmatrix} (1/\rho_f)\tilde{\boldsymbol{f}}^{n+1} \\ 0 \end{pmatrix} \\ &+\Delta t \begin{pmatrix} \bigtriangledown \cdot \left[\tilde{\boldsymbol{u}}_\ell^{n+1}\ (\tilde{\boldsymbol{u}}_\ell^{n+1} - \boldsymbol{w}^n) - (2/\rho_f)\ \mu(|\mathbf{D}(\tilde{\boldsymbol{u}}_\ell^{n+1})|)\mathbf{D}(\tilde{\boldsymbol{u}}_\ell^{n+1}) + (1/\rho_f)\ \tilde{p}_\ell^{n+1}\ \mathbf{I}\right] \\ \bigtriangledown \cdot \tilde{\boldsymbol{u}}_\ell^{n+1} \end{pmatrix}. \end{aligned} \tag{7.14}$$

Computing the Jacobian of the operator $D(\tilde{\boldsymbol{y}}_\ell^{n+1})$ and inserting it together with (7.14) into (7.12) we obtain the following system of integral equations

$$\begin{aligned} &\int\limits_{\Omega_k^n} \begin{pmatrix} (\tilde{\boldsymbol{u}}_{\ell+1}^{n+1} - \boldsymbol{u}_\ell^n) \\ 0 \end{pmatrix}\ \mathrm{d}\omega + \Delta t \int\limits_{\Omega_{k^n}} \begin{pmatrix} (\bigtriangledown \cdot \boldsymbol{w}^n)\ \boldsymbol{u}_{\ell+1}^{n+1} \\ 0 \end{pmatrix}\ \mathrm{d}\omega \\ &+\Delta t \int\limits_{\Omega_k^n} \begin{pmatrix} \bigtriangledown \cdot \left[(\tilde{\boldsymbol{u}}_\ell^{n+1} - \boldsymbol{w}^n)\ \tilde{\boldsymbol{u}}_{\ell+1}^{n+1} + (\tilde{\boldsymbol{u}}_{\ell+1}^{n+1} - \tilde{\boldsymbol{u}}_\ell^{n+1})\tilde{\boldsymbol{u}}_\ell^{n+1}\right] \\ 0 \end{pmatrix}\ \mathrm{d}\omega \\ &+\Delta t \int\limits_{\Omega_k^n} \begin{pmatrix} \bigtriangledown \cdot \Big[-(1/\rho_f)\ \mu(|\mathbf{D}(\tilde{\boldsymbol{u}}_{\ell+1}^{n+1})|) \bigtriangledown \tilde{\boldsymbol{u}}_{\ell+1}^{n+1} + (1/\rho_f)\ \tilde{p}_{\ell+1}^{n+1}\ \mathbf{I}\Big] \\ \bigtriangledown \cdot \Big[\tilde{\boldsymbol{u}}_{\ell+1}^{n+1} - \varepsilon \bigtriangledown \Big((\tilde{p}_{\ell+1}^{n+1} - \tilde{p}_\ell^{n+1})\ \mathbf{I}\Big)\Big] \end{pmatrix}\ \mathrm{d}\omega \\ &= \Delta t \int\limits_{\Omega_k^n} \begin{pmatrix} (1/\rho_f)\ \boldsymbol{f}^{n+1} \\ 0 \end{pmatrix}\ \mathrm{d}\omega. \end{aligned} \tag{7.15}$$

We note that the continuity equation has been stabilized using the pseudo-compressibility approach that yields in solving of the equation

$$\bigtriangledown \cdot \tilde{\boldsymbol{u}}_{\ell+1}^{n+1} + \varepsilon \bigtriangleup (\tilde{p}_\ell^{n+1} - \tilde{p}_{\ell+1}^{n+1}) = 0, \quad \varepsilon \approx (\bigtriangleup h)^2, \tag{7.16}$$

where $\bigtriangleup h$ denotes the grid size. The velocities in (7.16) are computed at integrations points by local approximation of the momentum equation via the finite element method at each control volume. By doing this the velocity at integration points remains coupled with the values of velocity and pressure at the grid points. This stabilization is based on the idea of Raw [92] and Karimian [62]. Description of implementation can be found in [17, 76].
Applying the Gauss theorem on (7.15) we obtain

$$\begin{aligned} &\int\limits_{\Omega_k^n} \begin{pmatrix} (\tilde{\boldsymbol{u}}_{\ell+1}^{n+1} - \boldsymbol{u}_\ell^n) \\ 0 \end{pmatrix}\ \mathrm{d}\omega + \Delta t \int\limits_{\Omega_k^n} \begin{pmatrix} (\bigtriangledown \cdot \boldsymbol{w}^n)\ \boldsymbol{u}_{\ell+1}^{n+1} \\ 0 \end{pmatrix}\ \mathrm{d}\omega \\ &+\Delta t \int\limits_{\partial\Omega_k^n} \begin{pmatrix} \tilde{\boldsymbol{u}}_{\ell+1}^{n+1}\Big[(\tilde{\boldsymbol{u}}_\ell^{n+1} - \boldsymbol{w}^n)\cdot \boldsymbol{n}_k\Big] + \tilde{\boldsymbol{u}}_\ell^{n+1}\Big[(\tilde{\boldsymbol{u}}_{\ell+1}^{n+1} - \tilde{\boldsymbol{u}}_\ell^{n+1})\cdot \boldsymbol{n}_k\Big] \\ 0 \end{pmatrix}\ \mathrm{d}\gamma \\ &+\Delta t \int\limits_{\partial\Omega_k^n} \begin{pmatrix} -(1/\rho_f)\ \mu(|\mathbf{D}(\tilde{\boldsymbol{u}}_{\ell+1}^{n+1})|) \bigtriangledown \tilde{\boldsymbol{u}}_{\ell+1}^{n+1}\cdot \boldsymbol{n}_k + (1/\rho_f)\ \tilde{p}_{\ell+1}^{n+1}\ \mathbf{I}\cdot \boldsymbol{n}_k \\ \tilde{\boldsymbol{u}}_{\ell+1}^{n+1}\cdot \boldsymbol{n}_k - \varepsilon \bigtriangledown \Big[(\tilde{p}_{\ell+1}^{n+1} - \tilde{p}_\ell^{n+1})\mathbf{I}\Big]\cdot \boldsymbol{n}_k \end{pmatrix}\ \mathrm{d}\gamma \\ &= \Delta t \int\limits_{\Omega_k^n} \begin{pmatrix} (1/\rho_f)\ \boldsymbol{f}^{n+1} \\ 0 \end{pmatrix}\ \mathrm{d}\omega, \end{aligned} \tag{7.17}$$

where $\boldsymbol{n}_k$ is the outward normal vector corresponding to the control volume boundary $\partial\Omega_k$. Note, that the Newton method linearizes the nonlinear convective term, see Remark 7.2. Moreover, we can linearize the viscous term, cf. Remark 7.3, by the fixed point method, i.e.

$$\mu(|\mathbf{D}(\tilde{\boldsymbol{u}}_{\ell+1}^{n+1})|)\mathbf{D}(\tilde{\boldsymbol{u}}_{\ell+1}^{n+1}) \approx \mu(|\mathbf{D}(\tilde{\boldsymbol{u}}_\ell^{n+1})|)\ \mathbf{D}(\tilde{\boldsymbol{u}}_{\ell+1}^{n+1}). \tag{7.18}$$

Remark 7.2 (Linearization of the convective term $\mathcal{N}(\boldsymbol{u}) := (\boldsymbol{u}\cdot\boldsymbol{n})\boldsymbol{u}$)
Let $\boldsymbol{u} := \tilde{\boldsymbol{u}}_{\ell+1}(\boldsymbol{x}, t^{n+1})$ and $\boldsymbol{u}^{old} := \tilde{\boldsymbol{u}}_{\ell}(\boldsymbol{x}, t^{n+1})$. Then we get from the Taylor expansion for $\mathcal{N}(\boldsymbol{u})$ around $\boldsymbol{u}^{old}$ the following approximation of the convective term

$$\begin{aligned}\mathcal{N}(\boldsymbol{u}) &\approx \mathcal{N}(\boldsymbol{u}^{old}) + \frac{\partial \mathcal{N}(\boldsymbol{u}^{old})}{\partial \boldsymbol{u}} \cdot (\boldsymbol{u}-\boldsymbol{u}^{old}) + \mathcal{O}(|\boldsymbol{u}-\boldsymbol{u}^{old}|^2)\\ &= (\boldsymbol{u}^{old}\cdot\boldsymbol{n})\ \boldsymbol{u}^{old} + (\boldsymbol{u}-\boldsymbol{u}^{old})\boldsymbol{u}^{old}\cdot\boldsymbol{n} + \boldsymbol{u}^{old}\big[(\boldsymbol{u}-\boldsymbol{u}^{old})\cdot\boldsymbol{n}\big] + \mathcal{O}(|\boldsymbol{u}-\boldsymbol{u}^{old}|^2).\end{aligned}$$

Moreover the fixed point method gives

$$\mathcal{N}(\boldsymbol{u}) \approx (\boldsymbol{u}^{old}\cdot\boldsymbol{n})\ \boldsymbol{u}^{old} + (\boldsymbol{u}-\boldsymbol{u}^{old})\boldsymbol{u}^{old}\cdot\boldsymbol{n} = (\boldsymbol{u}^{old}\cdot\boldsymbol{n})\ \boldsymbol{u}.$$

Remark 7.3 (Linearization of the viscous term $\mathcal{V}(\bigtriangledown\boldsymbol{u}) := \mu(|\mathbf{D}(\boldsymbol{u})|)\mathbf{D}(\boldsymbol{u})$)
Let us simplify the notation by defining

$$\begin{aligned}&\boldsymbol{u} := \tilde{\boldsymbol{u}}_{\ell+1}(\boldsymbol{x}, t^{n+1}), \quad \boldsymbol{u}^{old} := \tilde{\boldsymbol{u}}_{\ell}(\boldsymbol{x}, t^{n+1}),\\ &z_1 := \frac{\partial u_1}{\partial x_1}, \quad z_2 := \frac{\partial u_1}{\partial x_2}, \quad z_3 := \frac{\partial u_2}{\partial x_1}, \quad z_4 := \frac{\partial u_2}{\partial x_2}.\end{aligned}$$

Then the Taylor expansion of $\mathcal{V}(\bigtriangledown\boldsymbol{u})$ around the point $\bigtriangledown\boldsymbol{u}^{old}$ reads as follows

$$\begin{aligned}\mathcal{V}(\bigtriangledown\boldsymbol{u}) &\approx \mathcal{V}(\bigtriangledown\boldsymbol{u}^{old}) + \sum_{i=1}^{4} \frac{\partial \mathcal{V}(\bigtriangledown\boldsymbol{u}^{old})}{\partial z_i}\ (z_i - z_i^{old}) + \mathcal{O}(|\bigtriangledown\boldsymbol{u} - \bigtriangledown\boldsymbol{u}^{old}|^2)\\ &= \mu(|\mathbf{D}(\boldsymbol{u}^{old})|)\ \mathbf{D}(\boldsymbol{u}^{old}) + \mathbf{D}(\boldsymbol{u}^{old}) \sum_{i=1}^{4} \frac{\partial \mu(|\mathbf{D}(\boldsymbol{u}^{old})|)}{\partial z_i}\ (z_i - z_i^{old})\\ &\quad + \mu(|\mathbf{D}(\boldsymbol{u}^{old})|)\ [\mathbf{D}(\boldsymbol{u}) - \mathbf{D}(\boldsymbol{u}^{old})] + \mathcal{O}(|\bigtriangledown\boldsymbol{u} - \bigtriangledown\boldsymbol{u}^{old}|^2).\end{aligned}$$

Hence, the full Newton approximation yields

$$\begin{aligned}\mu(|\mathbf{D}(\boldsymbol{u})|)\ \mathbf{D}(\boldsymbol{u}) &\approx \mu(|\mathbf{D}(\boldsymbol{u}^{old})|)\ \mathbf{D}(\ \boldsymbol{u}^{old}) + \mathbf{D}(\boldsymbol{u}^{old})\ \sum_{i=1}^{4} \frac{\partial \mu(|\mathbf{D}(\bigtriangledown\boldsymbol{u}^{old})|)}{\partial z_i}\ (z_i - z_i^{old})\\ &\quad + \mu(|\mathbf{D}(\boldsymbol{u}^{old})|)\ [\mathbf{D}(\boldsymbol{u}) - \mathbf{D}(\boldsymbol{u}^{old})].\end{aligned}$$

Moreover, the fixed point method approximates the viscous term as follows

$$\begin{aligned}\mu(|\mathbf{D}(\boldsymbol{u})|)\mathbf{D}(\boldsymbol{u}) &\approx \mu(|\mathbf{D}(\boldsymbol{u}^{old})|)\ \mathbf{D}(\boldsymbol{u}^{old}) + \mu(|\mathbf{D}(\boldsymbol{u}^{old})|)\ [\mathbf{D}(\boldsymbol{u}) - \mathbf{D}(\boldsymbol{u}^{old})]\\ &= \mu(|\mathbf{D}(\boldsymbol{u}^{old})|)\ \mathbf{D}(\boldsymbol{u}).\end{aligned}$$

Finally, inserting (7.18) in (7.17) we obtain the following equations to solve

$$\begin{aligned}&\int_{\Omega_k^n} \begin{pmatrix} (\tilde{\boldsymbol{u}}_{\ell+1}^{n+1} - \boldsymbol{u}_{\ell}^{n}) \\ 0 \end{pmatrix}\ \mathrm{d}\omega + \Delta t \int_{\Omega_k^n} \begin{pmatrix} (\bigtriangledown\cdot\boldsymbol{w}^n)\ \boldsymbol{u}_{\ell+1}^{n+1} \\ 0 \end{pmatrix}\ \mathrm{d}\omega\\ &+\Delta t \int_{\partial\Omega_k^n} \begin{pmatrix} \tilde{\boldsymbol{u}}_{\ell+1}^{n+1}\Big[(\tilde{\boldsymbol{u}}_{\ell}^{n+1} - \boldsymbol{w}^n)\cdot\boldsymbol{n}_k\Big] + \tilde{\boldsymbol{u}}_{\ell}^{n+1}\Big[(\tilde{\boldsymbol{u}}_{\ell+1}^{n+1} - \tilde{\boldsymbol{u}}_{\ell}^{n+1})\cdot\boldsymbol{n}_k\Big] \\ 0 \end{pmatrix}\ \mathrm{d}\gamma\\ &+\Delta t \int_{\partial\Omega_k^n} \begin{pmatrix} -(1/\rho_f)\ \mu(|\mathbf{D}(\tilde{\boldsymbol{u}}_{\ell}^{n+1})|) \bigtriangledown \tilde{\boldsymbol{u}}_{\ell+1}^{n+1}\cdot\boldsymbol{n}_k + (1/\rho_f)\ \tilde{p}_{\ell+1}^{n+1}\ \mathbf{I}\cdot\boldsymbol{n}_k \\ \tilde{\boldsymbol{u}}_{\ell+1}^{n+1}\cdot\boldsymbol{n}_k - \varepsilon \bigtriangledown \Big[(\tilde{p}_{\ell+1}^{n+1} - \tilde{p}_{\ell}^{n+1})\mathbf{I}\Big]\cdot\boldsymbol{n}_k \end{pmatrix}\ \mathrm{d}\gamma\\ &= \Delta t \int_{\Omega_k^n} \begin{pmatrix} (1/\rho_f)\ \boldsymbol{f}^{n+1} \\ 0 \end{pmatrix}\ \mathrm{d}\omega \quad \text{for} \quad k = 1, \ldots, n_{gp}. \end{aligned} \tag{7.19}$$

Note that for each volume and surface integral from (7.19) it holds

$$\int\limits_{\Omega_k^n}(\cdot)\ \mathrm{d}\omega = \sum_{j\in s(k)}\int\limits_{\Omega_{kj}^n}(\cdot)\ \mathrm{d}\omega \quad \text{and} \quad \int\limits_{\partial\Omega_k^n}(\cdot)\ \mathrm{d}\gamma = \sum_{j\in s(k)}\int\limits_{\partial\Omega_{kj}^n}(\cdot)\ \mathrm{d}\gamma.$$

Now, we proceed with defining the nodal basis N_k consisting from piecewise linear functions with the value 1 at the grid point k and 0 in the neighbouring grid points, i.e.

$$N_k(gp_m) = \begin{cases} 1 & \text{if} \quad k = m \\ 0 & \text{if} \quad k \neq m \end{cases} \qquad k, m = 1, \ldots, n_{gp},$$

where gp_m denotes the grid point corresponding to the control volume Ω_m. With respect to this basis we can write the value of a function v (constant on each control volume) at the point $\boldsymbol{x} \in \Omega^n$ as follows

$$v(\boldsymbol{x}) = \sum_{k=1}^{n_{gp}} N_k(\boldsymbol{x})\ v(gp_k), \quad \bigtriangledown v(\boldsymbol{x}) = \sum_{k=1}^{n_{gp}} \bigtriangledown N_k(\boldsymbol{x})\ v(gp_k).$$

To approximate the integrals over control volumes and over control volume boundaries for a function defined at grid points the midpoint rule is used. Thus, we obtain for $\boldsymbol{x} \in \Omega_k^n$

$$\int\limits_{\Omega_k^n} v(\boldsymbol{x})\ \mathrm{d}\omega \ \approx\ |\Omega_k|\ v(gp_k), \quad \int\limits_{\partial\Omega_k^n} v(\boldsymbol{x})\ \mathrm{d}\gamma \approx \sum_{j\in s(k)} |\partial\Omega_{kj}|\ N_k(ip_{kj})\ v(gp_k),$$

where $|\Omega_k|$ and $|\partial\Omega_{kj}|$ denotes the area of the volume Ω_k and the boundary $\partial\Omega_{kj}$, respectively, and ip_{kj} is the integration point corresponding to the control volume boundary $\partial\Omega_{kj}$. Note that there are one or two integration points corresponding to the boundary $\partial\Omega_{kj}$ depending on the number of straight segments in $\partial\Omega_{kj}$. For simplicity and in order to avoid another subscript for the integration points we will associate the subcontrol volume boundary Ω_{kj} with only one integration point ip_{kj}. Let us now approximate each term appearing in the integral equations (7.19).

- **Approximation of the time-dependent term:**

$$\int\limits_{\Omega_k^n} (\tilde{\boldsymbol{u}}_{\ell+1}^{n+1} - \boldsymbol{u}_\ell^n)\ \mathrm{d}\omega \ \approx\ |\Omega_k|\ \Big[\tilde{\boldsymbol{u}}_{\ell+1}^{n+1}(gp_k) - \boldsymbol{u}_\ell^n(gp_k)\Big].$$

- **Approximation of the $\bigtriangledown \cdot \boldsymbol{w}$ term:**

$$\begin{aligned}
\int\limits_{\Omega_k^n} \tilde{\boldsymbol{u}}_{\ell+1}^{n+1} \bigtriangledown \cdot \boldsymbol{w}^n\ \mathrm{d}\omega \ &\approx\ \tilde{\boldsymbol{u}}_{\ell+1}^{n+1}(gp_k) \sum_{j\in s(k)} \int\limits_{\partial\Omega_{kj}^n} \boldsymbol{w}^n \cdot \boldsymbol{n}_{kj}\ \mathrm{d}\gamma \\
&\approx\ \tilde{\boldsymbol{u}}_{\ell+1}^{n+1}(gp_k) \sum_{j\in s(k)} |\partial\Omega_{kj}^n|\ N_k(ip_{kj}) \boldsymbol{w}^n(gp_k) \cdot \boldsymbol{n}(ip_{kj}) \\
&=\ \tilde{\boldsymbol{u}}_{\ell+1}^{n+1}(gp_k) \sum_{j\in s(k)} N_k(ip_{kj}) \boldsymbol{w}^n(gp_k) \cdot \overline{\boldsymbol{n}}(ip_{kj}), \\
&\text{where} \quad \overline{\boldsymbol{n}}(ip_{kj}) := \boldsymbol{n}(ip_{kj})\ |\partial\Omega_{kj}^n|.
\end{aligned}$$

Here $\boldsymbol{n}(ip_{kj})$ denotes the outward normal vector corresponding to the integration point ip_{kj}.

- **Approximation of the convective term:**

$$\int\limits_{\partial\Omega_k^n} \left(\tilde{\boldsymbol{u}}_{\ell+1}^{n+1} \Big[(\tilde{\boldsymbol{u}}_{\ell}^{n+1} - \boldsymbol{w}^n) \cdot \boldsymbol{n}_k \Big] + \tilde{\boldsymbol{u}}_{\ell}^{n+1} \Big[(\tilde{\boldsymbol{u}}_{\ell+1}^{n+1} - \tilde{\boldsymbol{u}}_{\ell}^{n+1}) \cdot \boldsymbol{n}_k \Big] \right) \mathrm{d}\gamma$$

$$\approx \sum_{j \in s(k)} \Bigg(\tilde{\boldsymbol{u}}_{\ell+1}^{up,n+1}(ip_{kj}) \Big[N_k(ip_{kj})\ \tilde{\boldsymbol{u}}_{\ell}^{n+1}(gp_k) \cdot \overline{\boldsymbol{n}}(ip_{kj}) - N_k(ip_{kj}) \boldsymbol{w}^n(gp_k) \cdot \overline{\boldsymbol{n}}(ip_{kj}) \Big] + N_k(ip_{kj})\ \tilde{\boldsymbol{u}}_{\ell}^{n+1}(gp_k) \Big[\tilde{\boldsymbol{u}}_{\ell+1}^{up,n+1}(ip_{kj}) \cdot \overline{\boldsymbol{n}}(ip_{kj}) - N_k(ip_{kj})\ \tilde{\boldsymbol{u}}_{\ell}^{n+1}(gp_k) \cdot \overline{\boldsymbol{n}}(ip_{kj}) \Big] \Bigg),$$

where $\tilde{\boldsymbol{u}}_{\ell+1}^{up,n+1}(ip_{kj})$ is the upwind velocity at the integration point ip_{kj}. For another ways how to treat the convective term, see [76].

- **Approximation of the viscous term:**

$$\int\limits_{\partial\Omega_k^n} \mu(|\mathbf{D}(\tilde{\boldsymbol{u}}_{\ell}^{n+1})|)\ \bigtriangledown \tilde{\boldsymbol{u}}_{\ell+1}^{n+1} \cdot \boldsymbol{n}_k\ \mathrm{d}\gamma$$

$$\approx \sum_{j \in s(k)} \int\limits_{\partial\Omega_{kj}^n} \mu(|\mathbf{D}(\tilde{\boldsymbol{u}}_{\ell}^{n+1})|)\ \bigtriangledown \tilde{\boldsymbol{u}}_{\ell+1}^{n+1} \cdot \boldsymbol{n}_{kj}\ \mathrm{d}\gamma$$

$$\approx \sum_{j \in s(k)} \mu\Big(\Big| \mathbf{D}(N_k(ip_{kj})\ \tilde{\boldsymbol{u}}_{\ell}^{n+1}(gp_k)) \Big| \Big)\ \bigtriangledown N_k(ip_{kj})\ \tilde{\boldsymbol{u}}_{\ell+1}^{n+1}(gp_k) \cdot \overline{\boldsymbol{n}}(ip_{kj}).$$

- **Approximation of the pressure term:**

$$\int\limits_{\partial\Omega_k^n} \tilde{p}_{\ell+1}^{n+1}\ \mathbf{I} \cdot \boldsymbol{n}_k\ \mathrm{d}\gamma\ \approx \sum_{j \in s(k)} N_k(ip_{kj})\ p(gp_k) \mathbf{I} \cdot \overline{\boldsymbol{n}}(ip_{kj}).$$

- **Approximation of the source term:**

$$\int\limits_{\Omega_k} \tilde{\boldsymbol{f}}^{n+1}\ \mathrm{d}\omega\ \approx\ |\Omega_{kj}|\ \tilde{\boldsymbol{f}}(gp_k).$$

- **Approximation of the continuity equation:**

$$\int\limits_{\partial\Omega_k^n} \left(\tilde{\boldsymbol{u}}_{\ell+1}^{n+1} \cdot \boldsymbol{n}_k - \varepsilon \bigtriangledown \Big[(\tilde{p}_{\ell+1}^{n+1} - \tilde{p}_{\ell}^{n+1}) \mathbf{I} \Big] \cdot \boldsymbol{n}_k \right) \mathrm{d}\gamma$$

$$\approx \sum_{j \in s(k)} \left(\check{\boldsymbol{u}}_{\ell+1}^{n+1}(ip_{kj}) \cdot \overline{\boldsymbol{n}}(ip_{kj}) - \varepsilon \bigtriangledown \Big[(\tilde{p}_{\ell+1}^{n+1}(ip_{kj}) - \tilde{p}_{\ell}^{n+1})(ip_{kj}) \mathbf{I} \Big] \cdot \overline{\boldsymbol{n}}(ip_{kj}) \right) \mathrm{d}\gamma,$$

where $\check{\boldsymbol{u}}(ip_{kj})$ is the velocity at the integration point received by solving locally the momentum equation on each control volume.

7.3 Finite difference approximation of the structure equation

In what follows we approximate the structure equation in space via central differences. First, let us discretize the space derivatives from (7.1b), i.e.

$$\frac{\partial \xi^{n+1/2}}{\partial x_1^2} = \frac{\xi_{i-1}^{n+1/2} - 2\ \xi_i^{n+1/2} + \xi_{i+1}^{n+1/2}}{(\triangle x)^2}, \tag{7.20a}$$

$$\frac{\partial \xi^{n}}{\partial x_1^2} = \frac{\xi_{i-1}^{n} - 2\ \xi_i^{n} + \xi_{i+1}^{n}}{(\triangle x)^2}, \quad i = 1, \ldots, N_{wall}, \tag{7.20b}$$

where N_{wall} denotes number of points arising from the discretization of moving boundary Γ_{wall} and $\triangle x$ is the distance between to neighbouring points on Γ_{wall}. The values for $i = 0$ and $i = N + 1$ correspond to the points $(x_1, x_2) = (x, R_0(0))$ and $(x_1, x_2) = (x, R_0(L))$, respectively, and are prescribed by the boundary conditions. Inserting (7.20a)-(7.20b) into (7.1b) yields the following algebraic system

$$K_1 \xi_{i-1}^{n+1/2} + K_2 \xi_i^{n+1/2} + K_1 \xi_{i+1}^{n+1/2} = P_i, \quad i = 1, \ldots, N_{wall}, \tag{7.21}$$

where

$$K_1 := -\frac{c\ \alpha\ \triangle t}{(\triangle x)^2}, \quad K_2 := 1 + \frac{2c\ \alpha\ \triangle t}{(\triangle x)^2},$$

$$P_i := \xi_i^n + \left[\frac{c\ (1-\alpha)\ \triangle t}{(\triangle x)^2}\right] (\xi_{i-1}^n - 2\ \xi_i^n + \xi_{i+1}^n) + \triangle t H(\tilde{p}^{n+1}, \tilde{\boldsymbol{u}}^{n+1}).$$

The system of equations (7.21) represents a trilinear algebraic system, for which we used the Gauss elimination method to solve.

The explicit scheme for the operator B, part (7.2a), yields directly the new wall displacement values computed by

$$\eta_i^{n+1} = \eta_i^n + \alpha_1 \Delta t\ \xi_i^{n+1/2} + (1-\alpha_1)\Delta t\ \xi_i^n, \quad i = 1, \ldots, N_{wall}. \tag{7.22}$$

Discretizing (7.2b) using the central difference scheme, i.e.

$$\frac{\partial \eta^{n+1}}{\partial x_1^2} = \frac{\eta_{i-1}^{n+1} - 2\ \eta_i^{n+1} + \eta_{i+1}^{n+1}}{(\triangle x)^2}, \tag{7.23a}$$

$$\frac{\partial \eta^{n}}{\partial x_1^2} = \frac{\eta_{i-1}^{n} - 2\ \eta_i^{n} + \eta_{i+1}^{n}}{(\triangle x)^2}, \quad i = 1, \ldots, N_{wall}, \tag{7.23b}$$

and inserting (7.23a)-(7.23b) into (7.2b) we obtain the formula for computing new values for wall displacement

$$\begin{aligned} \xi_i^{n+1} = \xi_i^{n+1/2} &+ \left[\frac{a\ \alpha_2\ \triangle t}{(\triangle x)^2}\right] (\eta_{i-1}^{n+1} - 2\eta_i^{n+1} + \eta_{i+1}^{n+1}) \\ &+ \left[\frac{a\ (1-\alpha_2)\ \triangle t}{(\triangle x)^2}\right] (\eta_{i-1}^{n} - 2\eta_i^{n} + \eta_{i+1}^{n}) \\ &- b\alpha_2 \Delta t \eta_i^{n+1} - b(1-\alpha_2)\ \Delta t \eta_i^n + \Delta t\ G(R_0). \end{aligned}$$

The implicit scheme for the operator B, as defined in (7.3a)-(7.3b), is solved as follows: firstly express the new wall displacement η_i^{n+1} from (7.3a), secondly insert η_i^{n+1} into (7.3b), then use the approximations as in (7.23a)-(7.23b) and finally express the new wall velocities ξ_i^{n+1}.

This yields the following system of equations

$$L_1\xi_{i-1}^{n+1/2} + L_2\xi_i^{n+1/2} + L_1\xi_{i+1}^{n+1/2} \;=\; Q_i, \quad i = 1, \ldots, N_{wall}, \tag{7.24}$$

where

$$\begin{aligned}
L_1 &:= -\frac{a\ \alpha_1\alpha_2\ (\triangle t)^2}{(\triangle x)^2},\\
L_2 &:= 1 + b\ \alpha_1\alpha_2\ (\triangle t)^2 + \frac{2a\ \alpha_1\alpha_2\ (\triangle t)^2}{(\triangle x)^2},\\
Q_i &:= \xi_i^{n+1/2} - b\Delta t\ \eta_i^n - b(1-\alpha_1)\ \alpha_2(\Delta t)^2\ \xi_i^{n+1/2} + \frac{a\Delta t}{(\Delta x)^2}\ (\eta_{i-1}^n - 2\eta_i^n + \eta_i^{n+1})\\
&\quad + \left[\frac{a\ (1-\alpha_1)\alpha_2(\Delta t)^2}{(\Delta x)^2}\right]\ (\xi_{i-1}^{n+1/2} - 2\ \xi_i^{n+1/2} + \xi_{i+1}^{n+1/2}) + \triangle t\ G(R_0).
\end{aligned}$$

Again, for solving of the algebraic system (7.24) the Gauss elimination method is used.

7.4 Computational geometry and parameter setting

Numerical experiments have been done for different reference geometries with both constant as well as non-constant reference radius R_0. The geometry shown in Fig. 7.2 is used for analysis of the experimental order of convergence. Fig. 7.3 illustrates a stenotic vessel and Fig. 7.4 represents a bifurcation geometry. In the case of stenotic reference geometry, the reference radius is prescribed in the following way

$$R_0(x_1) = \begin{cases} R_0(0)\left[1 - 0.15\left(1 + \cos\left(\dfrac{5\ \pi\ (x_1 - L/2)}{L}\right)\right)\right] & \text{if} \quad x_1 \in [0.3L; 0.7L], \\ R_0(0) \qquad\qquad \text{if} \quad x_1 \in [0; 0.3L) \cup (0.7L; L]\ , \end{cases} \tag{7.25}$$

where L denotes the length of vessel. In the experiments with prescribed sinus pulses on the inflow boundary, we set $R_0(0) = 1\,\text{cm}$ and $L = 10\,\text{cm}$. Taking into account physiological pulses prescribed by the iliac inflow rate (Fig. 7.5, left), the radius $R_0(0) = 0.6\,\text{cm}$ and the length $L = 6\,\text{cm}$ were chosen. This radius represents the physiological radius of an iliac artery, i.e. a daughter artery of the abdominal aorta bifurcation, cf. [101].

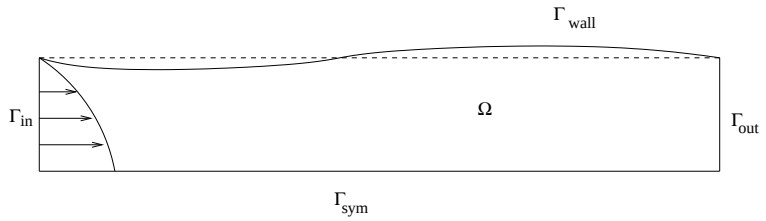

Figure 7.2: Symmetric non-stenosed computational geometry.

The bifurcation geometry shown in Fig. 7.4 represents a more complex geometry with asymmetric daughter vessels and the so-called sinus bulb area. It is a simplified example of a realistic carotid artery bifurcation, see [85]. The radii of the mother vessel (i.e. common carotid artery), daughter vessels (i.e. external and internal carotid artery) and the maximal

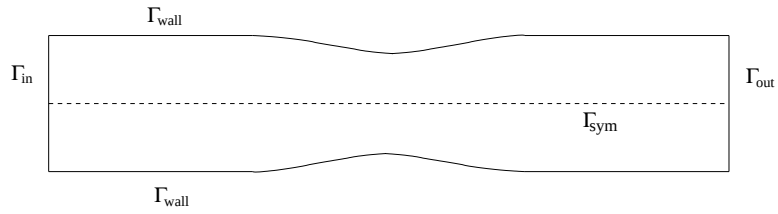

Figure 7.3: Stenotic reference geometry.

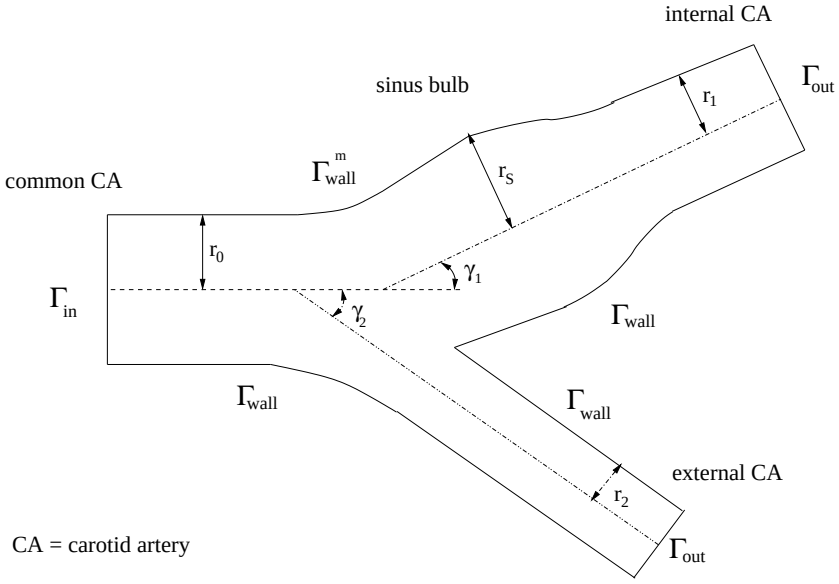

Figure 7.4: Bifurcation reference geometry, see [85].

radius of the sinus bulb area are $r_0 = 0.31\,\text{cm}$, $r_1 = 0.22\,\text{cm}$, $r_2 = 0.18\,\text{cm}$ and $r_S = 0.33\,\text{cm}$, respectively. The branching angles for the bifurcation in Fig. 7.4 are $\gamma_1 = \gamma_2 = 25°$.

We note that since the generalized string model has been derived for radially symmetric domains we need to preserve the radial symmetry for each single vessel of the carotid bifurcation. For this purpose we need to follow the axis of symmetry in order to define and compute the wall deformation η. In the situation depicted in Fig. 7.4 it would mean to rotate the original coordinate system with respect to the bifurcation angle γ_1 (for the internal carotid artery) and the bifurcation angle γ_2 (for the external carotid artery). In our simulations for simplicity we assume that only one part of boundary Γ_{wall} (this corresponds to the boundary Γ^m_{wall} in Fig. 7.4) is allowed to move. This is motivated by the fact that atherogenesis occurs preferably at the outer wall of daughter vessel, especially in the carotid sinus, see [72]. Therefore this area is of special interest. Note that we use two different reference frames. The first one corresponds to the mother vessel and in the second one the x_1-axis coincides with the axis of symmetry of the internal daughter vessel. To be more precise, it means that we introduce a new coordinate system $(\bar{x}_1, \bar{x}_2) \in \mathbb{R}^2$, i.e.

$$\bar{x}_1 = (x_1 - 0.9)\cos\gamma_1 + (x_2 + 0.05)\sin\gamma_1, \tag{7.26}$$

$$\bar{x}_2 = (0.9 - x_1)\sin\gamma_1 + (x_2 + 0.05)\cos\gamma_1. \tag{7.27}$$

Note that also the fluid load in the dynamic coupling condition (2.34), represented by the Cauchy stress applied to the walls, will be transformed into the coordinate system (7.26)-(7.27).

In what follows a parabolic inflow profile is prescribed on the inflow boundary, i.e.

$$\boldsymbol{u}_{in}((0,x_2),t) = \frac{R(0,t)^2 - x_2^2}{R(0,t)^2}\ f(t)\ \boldsymbol{e}_r\ ,$$

where $R(0,t) = R_0(0) + \eta(0,t)$ and $f(t)$ denotes a temporal function. In our experiments we have used a function that describes sinus pulses of heart, i.e

$$f(t) = U_0 \sin^2(\pi\ t/\omega), \quad t \in I \quad \text{with} \quad \omega = 1\ \text{s} \quad \text{or} \quad \omega = 0.9\ \text{s}\ , \tag{7.28}$$

where U_0 is the maximal inflow u_1-velocity and ω represents the period of one heart beat. Moreover, considering physiological pulses of heart, the temporal function depending on the flow rate $Q(t)$ in artery was prescribed, see Fig. 7.5. From the definition of the flow rate, i.e. $Q(t) = \int_{\Gamma_{in}} u_{in,1}\ \mathrm{d}S$, we obtain

$$f(t) = \frac{2Q(t)}{\pi R(0,t)^2}, \quad t \in I. \tag{7.29}$$

Here we note that the mean inflow velocity and the maximal inflow velocity are defined by

$$\bar{U} = \frac{Q(t)}{\pi R(0,t)^2}, \quad U_0 = \frac{2Q(t)}{\pi R(0,t)^2},$$

respectively.

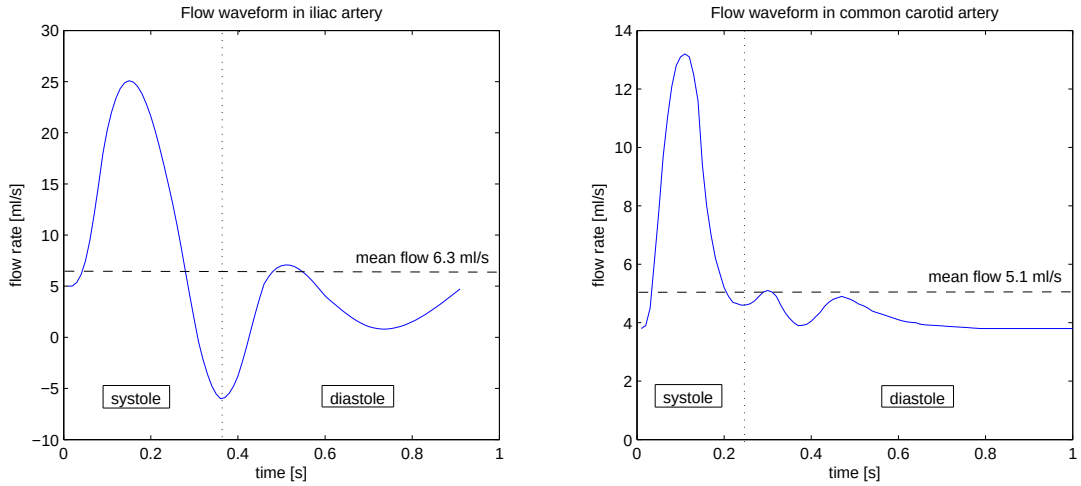

Figure 7.5: Inflow rate $Q(t)$ in iliac artery (left) and in common carotid artery (right), see [85, 101].

In the Tab. 7.1 the fluid and the structure model parameters are specified. Suitable parameters for the non-Newtonian viscosity models (3.19) and (3.20) are prescribed in the Tab. 7.2, see also [105].

In the Section 7.6 the model data for the Newtonian and the non-Newtonian viscosity function from Tab. 7.2 were used for the analysis of the experimental order of convergence. On the other hand the hemodynamic wall parameters were computed for stenotic as well as bifurcation geometry using the physiological parameters from Tab. 7.2.

Table 7.1: Fluid and structure model parameters.

Fluid parameters			
Newt. viscosity (in physiol. exp.)	μ	0.0345	P
Newt. viscosity (in model exp.)	μ	0.63	P
fluid density	ρ_f	1	g.cm^{-3}
Structure parameters			
wall density	ρ_s	1.1	g.cm^{-3}
wall thickness	h	0.1	cm
Young's modulus	E	0.75×10^5	dyn.cm^{-2}
Poisson's ratio	$\tilde{\xi}$	0.5	[1]
Timoshenko's factor	κ	1	[1]
viscoelasticity constant	γ	2×10^4	P.s.cm^{-1}

Table 7.2: Non-Newtonian model parameters.

Carreau model		Yeleswarapu model	
model data	physiological data	model data	physiological data
$\mu_0 = 1.26$ P	$\mu_0 = 0.56$ P	$\mu_0 = 1.26$ P	$\mu_0 = 0.736$ P
$\mu_\infty = 0.63$ P	$\mu_\infty = 0.0345$ P	$\mu_\infty = 0.63$ P	$\mu_\infty = 0.05$ P
$q = 1.6$	$q = 1.356$	$\Lambda = 14.81$	$\Lambda = 14.81$
$\lambda = 1$	$\lambda = 3.313$		
$U_0 = 38$ cm.s^{-1}	$U_0 = 17$ cm.s^{-1}	$U_0 = 38$ cm.s^{-1}	$U_0 = 22.3$ cm.s^{-1}

In the human circulatory system, the Reynolds number varies quite significantly. Over one cycle it reaches the values from 10^{-3} up to 6000. A typical critical number for a normal artery is around 2300, for bifurcation it is around 600. However, the recirculation zones start to be created already at the Reynolds number around 170. This explains the fact that small recirculation zones appear even in healthy bifurcations. The part of a bifurcation that is the most sensitive to the local change of flow is the so-called sinus bulb area. This is a part of a daughter vessel, where an atherosclerosis is usually formed, see Fig. 7.4. Indeed, our analysis of the local hemodynamic parameters (Section 7.7) confirms this fact.

In the following we give the overview of the Reynolds numbers Re_0 and Re_∞ defined by

$$\mathrm{Re}_0 := \frac{\rho_f \, |\bar{U}| \, 2R_0(0)}{\mu_0}, \quad \mathrm{Re}_\infty := \frac{\rho_f \, |\bar{U}| \, 2R_0(0)}{\mu_\infty} \, , \tag{7.30}$$

respectively, for the experiments presented in the next sections. Note that in the Newtonian case we have $\mathrm{Re} = \mathrm{Re}_\infty$. Concerning cylindrical geometry with $R_0 = 1cm$, non-Newtonian model parameters (both the Carreau and the Yeleswarapu) and model data, see Tab. 7.2, we have on Γ_{in} the following Reynold numbers: $\mathrm{Re} \in [30; 60]$. In the case of physiological data for the Carreau model and the Yeleswarapu model, see Tab. 7.2, the corresponding Reynolds numbers on Γ_{in} are from the ranges $\mathrm{Re} \in [30; 493]$ and $\mathrm{Re} \in [30; 446]$, respectively. In the Tab. 7.3 and Tab. 7.4 the Reynolds numbers for the experiments with physiological pulses corresponding to the carotid artery flow rate (Fig. 7.5, right) and the iliac artery flow rate (Fig. 7.5, left), respectively, are computed. We denote by Q_{mean}, Q_{max} and Q_{min} the mean, the maximal and the minimal flow rate, respectively. We can observe that in the case of carotid artery the Reynolds numbers corresponding to the mean flow are higher than the ones corresponding to the iliac artery. Consequently, larger recirculation zones can appear in the iliac arteries. We note here that the Newtonian viscosity corresponds to μ_∞ in the Carreau model and therefore the Reynolds numbers for these two cases coincide.

Table 7.3: Reynolds numbers for physiological data and physiological pulses for the common carotid artery.

	Newtonian model	Carreau model	Yeleswarapu model
	$R_0(0) = 0.31$ cm	$R_0(0) = 0.31$ cm	$R_0(0) = 0.31$ cm
$Q_{mean} = 5.1$ ml.s^{-1} $\bar{U} = 16.9$ cm.s^{-1}	$\mathrm{Re} \approx 304$	$\mathrm{Re}_0 \approx 19$ $\mathrm{Re}_{i\infty} \approx 304$	$\mathrm{Re}_0 \approx 14$ $\mathrm{Re}_\infty \approx 210$
$Q_{max} = 13.2$ ml.s^{-1} $\bar{U} = 43.7$ cm.s^{-1}	$\mathrm{Re} \approx 785$	$\mathrm{Re}_0 \approx 48$ $\mathrm{Re}_\infty \approx 785$	$\mathrm{Re}_0 \approx 37$ $\mathrm{Re}_\infty \approx 542$
$Q_{min} = 3.9$ ml.s^{-1} $\bar{U} = 12.9$ cm.s^{-1}	$\mathrm{Re} \approx 232$	$\mathrm{Re}_0 \approx 14$ $\mathrm{Re}_\infty \approx 232$	$\mathrm{Re}_0 \approx 11$ $\mathrm{Re}_\infty \approx 160$

Table 7.4: Reynolds numbers for physiological data and physiological pulses for the iliac artery.

	Newtonian model	Carreau model	Yeleswarapu model
	$R_0(0) = 0.6$ cm	$R_0(0) = 0.6$ cm	$R_0(0) = 0.6$ cm
$Q_{mean} = 6.3$ ml.s^{-1} $\bar{U} = 5.6$ cm.s^{-1}	$\mathrm{Re} \approx 195$	$\mathrm{Re}_0 \approx 12$ $\mathrm{Re}_\infty \approx 195$	$\mathrm{Re}_0 \approx 9$ $\mathrm{Re}_\infty \approx 134$
$Q_{max} = 25.1$ ml.s^{-1} $\bar{U} = 22.2$ cm.s^{-1}	$\mathrm{Re} \approx 772$	$\mathrm{Re}_0 \approx 48$ $\mathrm{Re}_\infty \approx 772$	$\mathrm{Re}_0 \approx 36$ $\mathrm{Re}_\infty \approx 533$
$Q_{min} = -6.0$ ml.s^{-1} $\bar{U} = -5.3$ cm.s^{-1}	$\mathrm{Re} \approx 185$	$\mathrm{Re}_0 \approx 14$ $\mathrm{Re}_\infty \approx 185$	$\mathrm{Re}_0 \approx 10$ $\mathrm{Re}_\infty \approx 114$

7.5 Experiments

In this section several numerical experiments will be presented. First, we would like to point out that in modelling the physically and biologically relevant situations, in particular concerning geometry and hemodynamics, we have used the data from measurements that are usually averaged and not person-specific. However, we were able to localize several significant flow characteristics, e.g. flow separation or recirculation zones, that are usually observed in the realistic blood flow in the cardiovascular system. Moreover, as it will be presented in the Section 7.7, the experiments help to compare Newtonian and non-Newtonian rheology and using the hemodynamic wall indices also to predict areas with possible plaque occurrence.

First experiment will be performed for the non-stenosed geometry, cf. Fig. 7.2, sinus pulses (7.28) and model data for Carreau viscosity function, cf. Tab. 7.2. Then we will focus on flow through the bifurcation geometry as shown in Fig. 7.4. This will be done for physiological non-Newtonian viscosity, see Tab. 7.2, and physiological pulses, cf. Fig. 7.5 (right), with the Reynolds numbers on the inflow boundary from the range $\mathrm{Re} \in [232; 785]$ and mean Reynolds number $\mathrm{Re} \approx 304$, cf. Tab.7.3. Concerning the bifurcation geometry an additional experiment for $\mathrm{Re} \in [116; 393]$ and the mean Reynolds number $\mathrm{Re} \approx 152$ will be presented. Aim is to show the changes in flow patterns as well as other characteristics due to local changes of Reynolds number. Finally, we will show the results from numerical modelling for a geometry corresponding to the stenosed iliac artery, see Fig. 7.3. Also here we focus on the physiological pulses, cf. Tab. 7.5 (left) and physiological non-Newtonian rheology, i.e. $\mathrm{Re} \in [185; 772]$ and mean Reynolds number $\mathrm{Re} \approx 195$. Moreover, we change the local hemodynamics by prescribing twice smaller Reynolds numbers on the inflow boundary, i.e. $\mathrm{Re} \in [93; 386]$ and mean Reynolds number $\mathrm{Re} \approx 98$.

In our numerical experiments the computational domain Ω_0 is covered by a mesh consisting of quadrilateral finite volumes. Each mesh element is characterized by a space step $\triangle h := \min\{\triangle x_1, \triangle x_2\}$, where $\triangle x_1$ and $\triangle x_2$ denotes the space step in x_1-direction and x_2-direction, respectively. Considering the simplified non-stenosed geometry the domain was discretized into 512 elements, for the stenotic geometry we used 2048 elements and in the case of bifurcation geometry 3072 elements built the grid. The corresponding time step for simulations was $\triangle t = 0.002\,\mathrm{s}$ (non-stenosed geometry), $\triangle t = 0.001\,\mathrm{s}$ (stenotic geometry) and $\triangle t = 0.0005\,\mathrm{s}$ (bifurcation geometry). Let us point out that before starting to compute the fluid-structure interaction problem (7.1a)-(7.1b) and (7.3a)-(7.3b) with moving boundaries a precomputation for a corresponding rigid domain has been done. This preprocessing takes one period of heart beat and yields a well-developed flow.

In what follows we present the results of numerical experiments using the kinematic coupling fluid-structure interaction algorithm (7.1a)-(7.1b) and (7.3a)-(7.3b). First, in Fig. 7.7, a simple model experiment showing the flow of shear-thinning fluid (Carreau model) through a non-stenosed computational domain (i.e. the reference radius is constant along Γ_{wall}) is presented. The pulses are modelled by the sinus temporal function, cf. (7.28). The corresponding wall displacement for several chosen time instants from two cycles is plotted in Fig. 7.6. Velocity streamlines and pressure isolines at four time instants are depicted in Fig. 7.7.

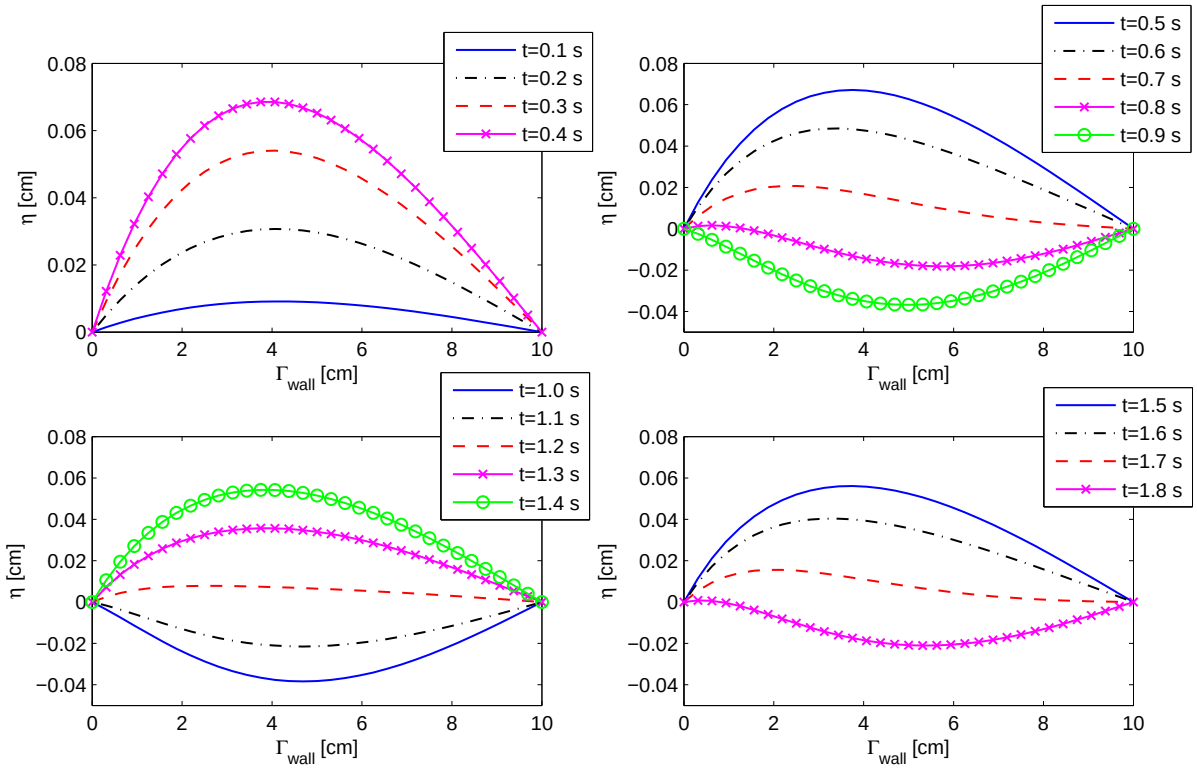

Figure 7.6: Evolution of domain deformation η along Γ^0_{wall} at several time instants; Carreau viscosity function; non-stenosed geometry, see Fig. 7.2.

In Figs. 7.8-7.11 streamlines (up left), velocity vector field (up right), pressure isolines (down left) and u_1-velocity isolines (down right) for bifurcation geometry are displayed.

(a) $t = 0.2\,\mathrm{s}$

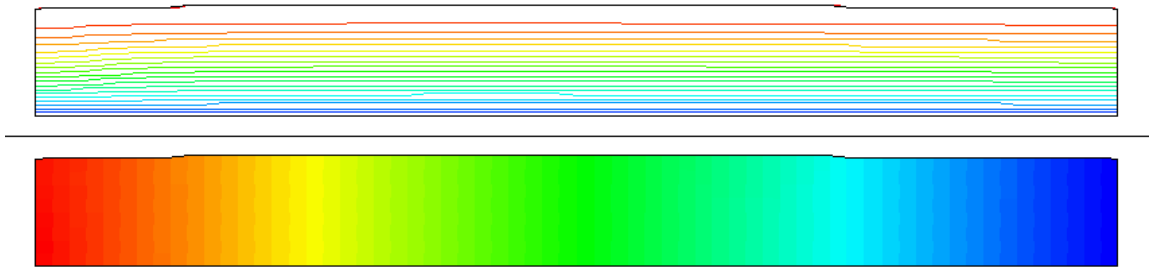

(b) $t = 0.4\,\mathrm{s}$

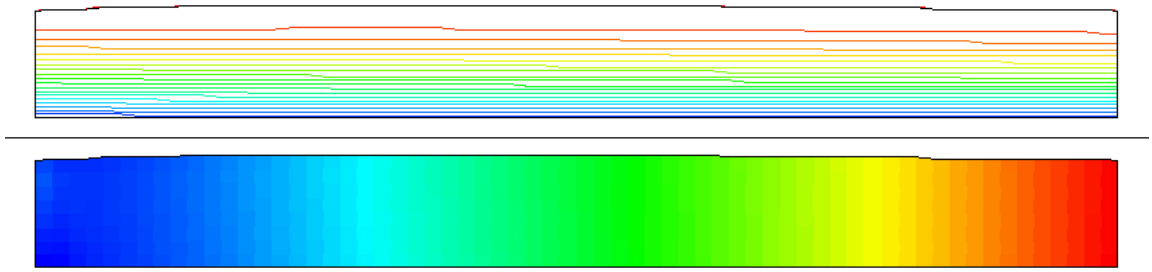

(c) $t = 0.6\,\mathrm{s}$

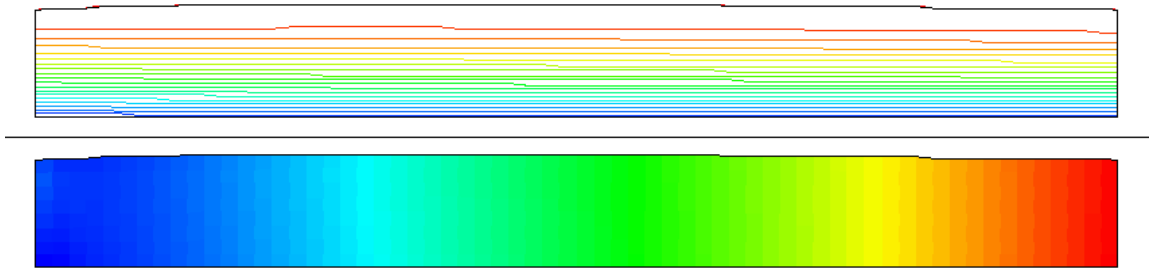

(d) $t = 0.8\,\mathrm{s}$

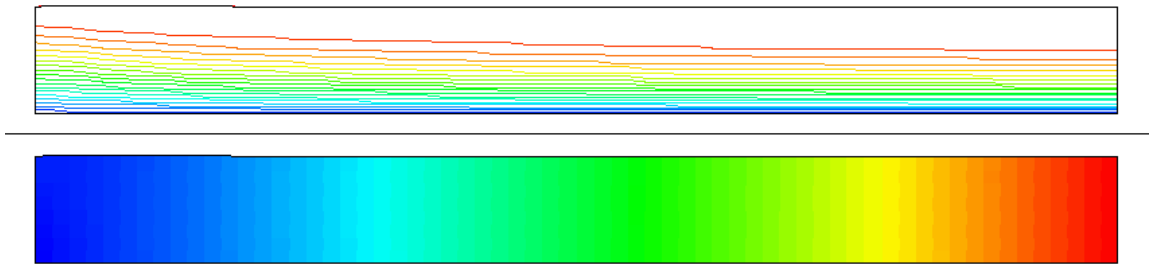

Figure 7.7: Velocity streamlines and pressure isolines for non-stenosed geometry at several time instants.

The plot in Fig. 7.8a corresponds to the systolic peak flow. Pressures and velocities are from the range $[-46.4, 291]\,\mathrm{Pa}$ and $[0, 87.7]\,\mathrm{cm.s^{-1}}$, respectively. Since we use the Carreau viscosity function (3.19) the parabolic inflow velocity profile changes its shape to a typi-

(a) $t = 0.10\,\mathrm{s}$

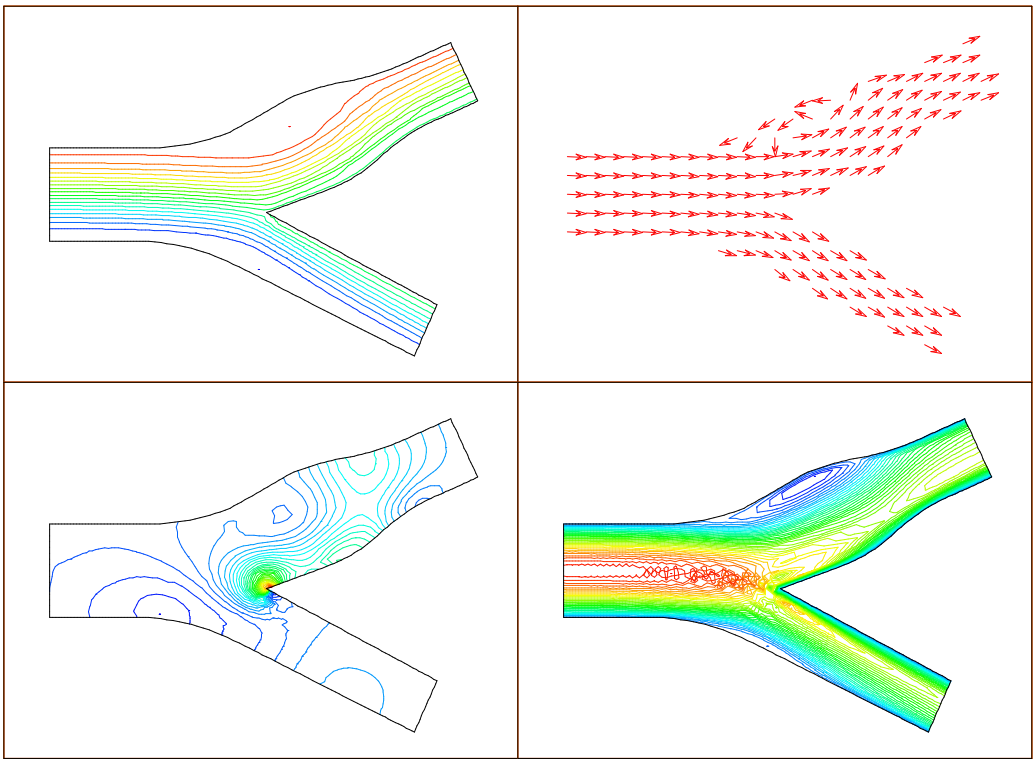

(b) $t = 0.23\,\mathrm{s}$

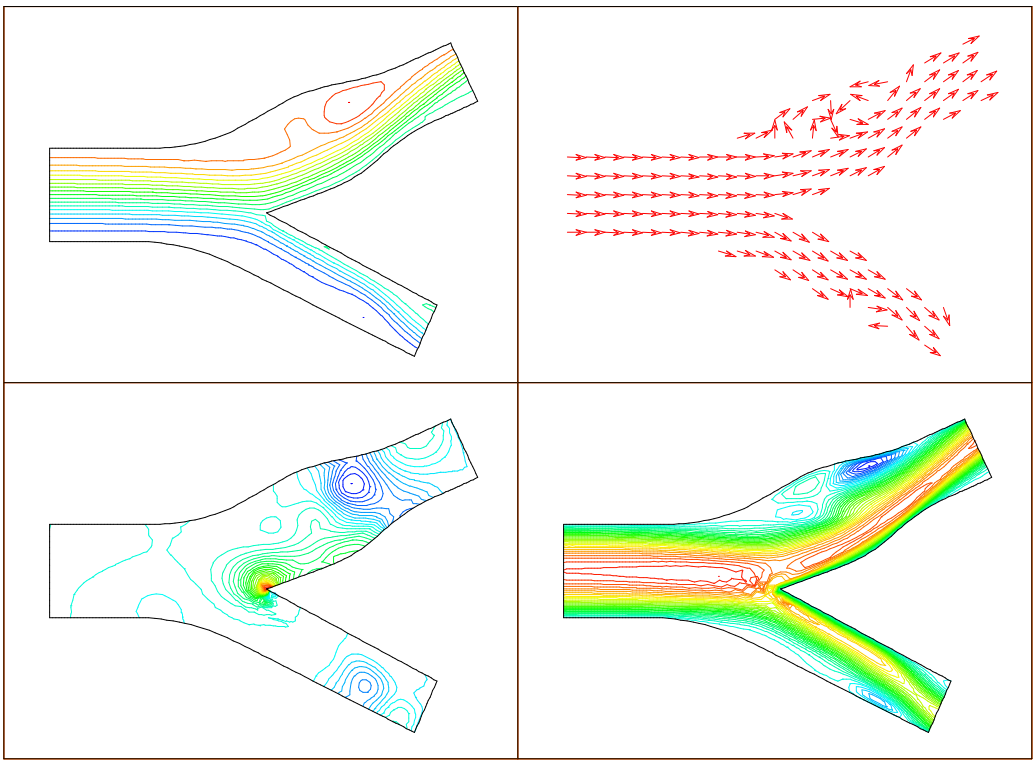

Figure 7.8: Streamlines, velocity vector field, pressure isolines and u_1-velocity isolines for bifurcation from Fig. 7.4 at two time instants; mean Reynolds number Re ≈ 304.

(a) $t = 0.36\,\mathrm{s}$

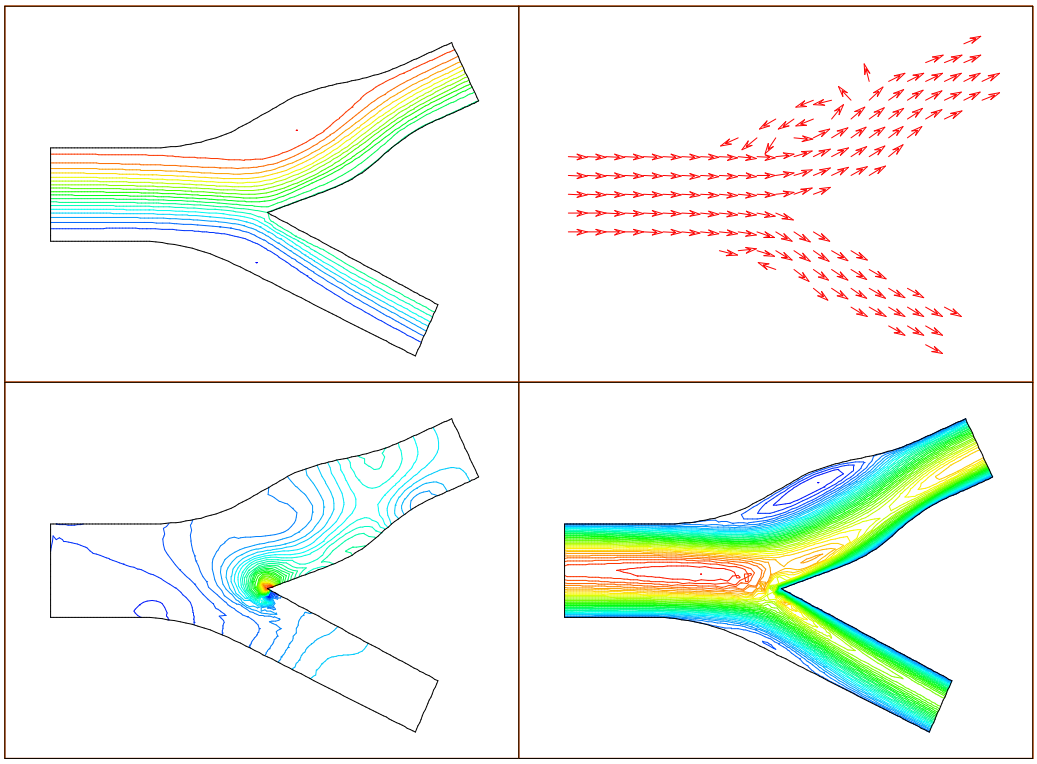

(b) $t = 0.96\,\mathrm{s}$

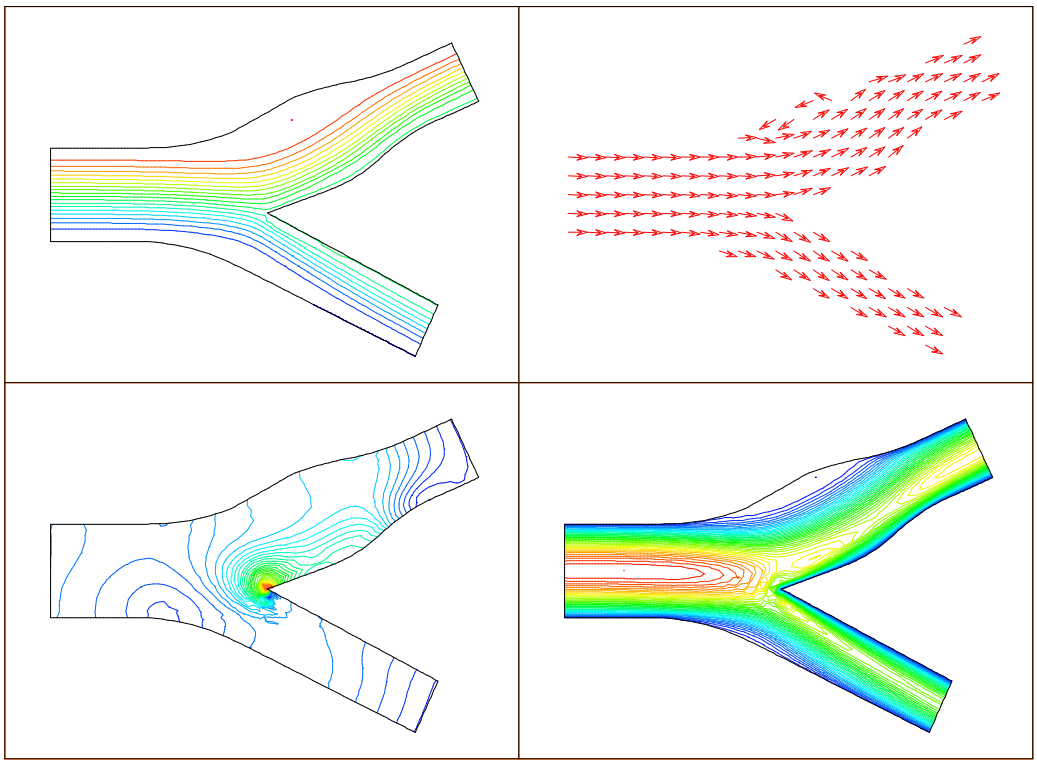

Figure 7.9: Streamlines, velocity vector field, pressure isolines and u_1-velocity isolines for bifurcation from Fig. 7.4 at two time instants; mean Reynolds number $\mathrm{Re} \approx 304$.

(a) $t = 0.10\,\mathrm{s}$

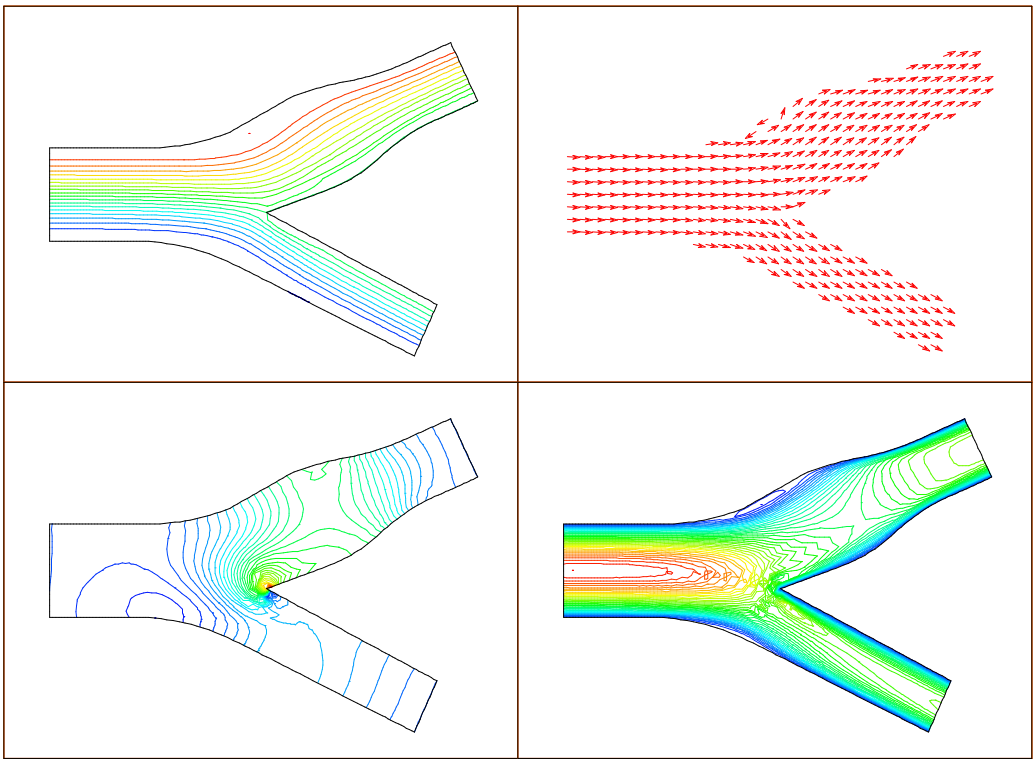

(b) $t = 0.23\,\mathrm{s}$

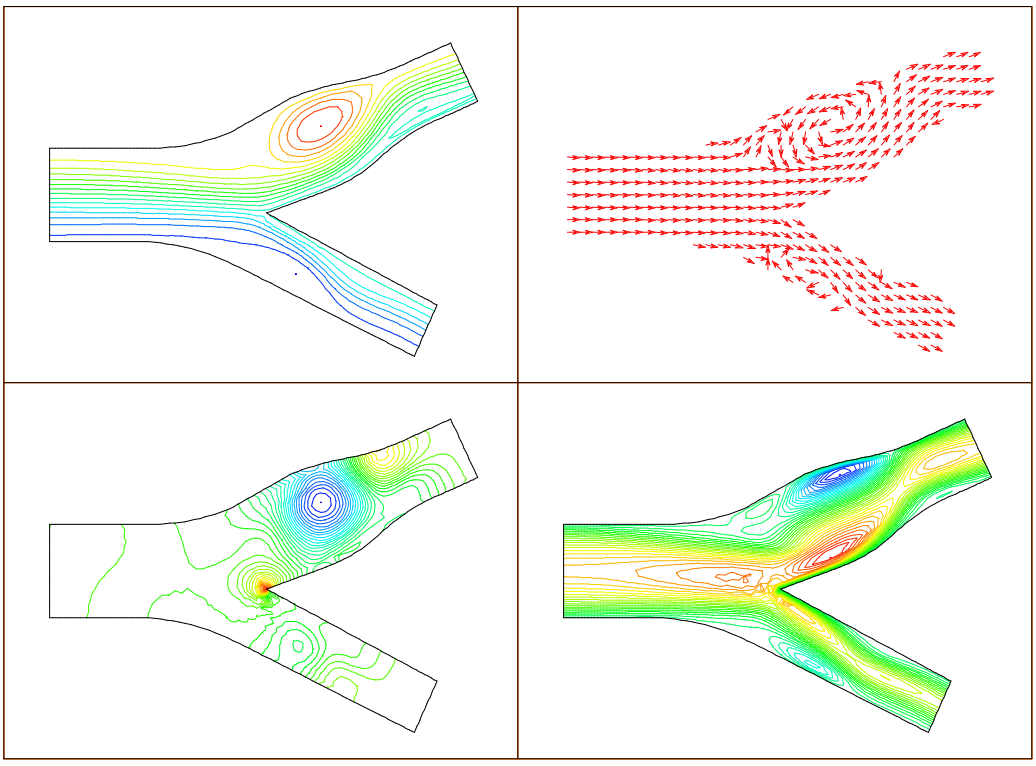

Figure 7.10: Streamlines, velocity vector field, pressure isolines and u_1-velocity isolines for bifurcation from Fig. 7.4 at two time instants; mean Reynolds number Re ≈ 152.

(a) $t = 0.36\,\mathrm{s}$

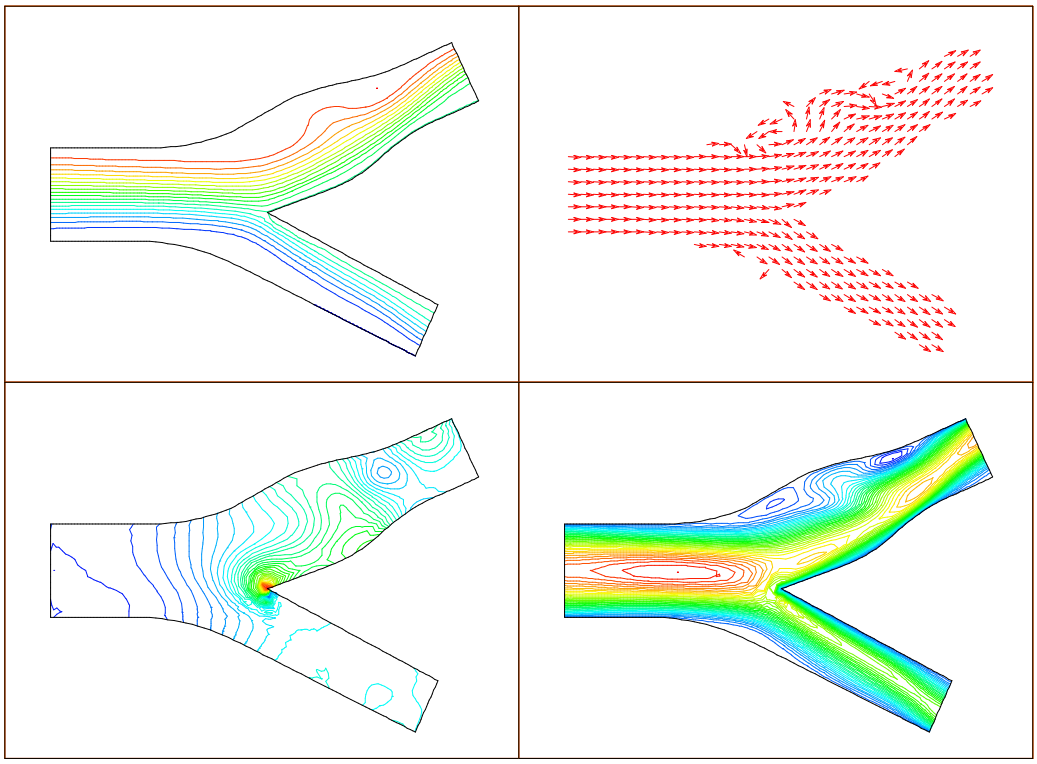

(b) $t = 0.96\,\mathrm{s}$

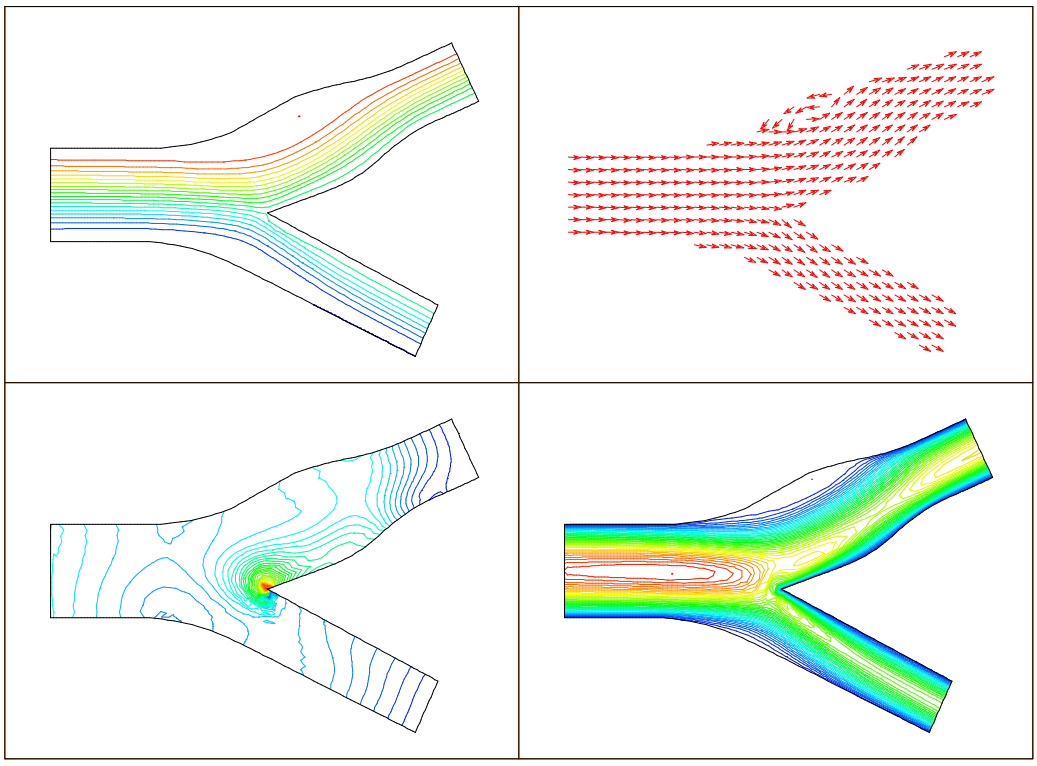

Figure 7.11: Streamlines, velocity vector field, pressure isolines and u_1-velocity isolines for bifurcation from Fig. 7.4 at two time instants; mean Reynolds number $\mathrm{Re} \approx 152$.

cal non-Newtonian profile before reaching the bifurcation apex. This can be seen in the plot of u_1-velocity isolines. In the systolic deceleration phase, see Fig. 7.8b, reversed flow appears. This can be visibly seen in the daughter vessels, especially in the carotid sinus bulb. Recirculation zones are also visible in the plots of streamlines and pressure isolines. After reaching the diastolic maximum, see Fig. 7.9a, reversed flow in the sinus bulb further develops. Similarly as in the previous plot, the streamlines and velocities have changed due to the diastolic deceleration phase of the cycle. However, the scales for velocity and pressure values are different in comparison to Fig. 7.8a. In particular, pressure is from the interval $[-7.6, 28.2]$ Pa and the velocities belong to $[0, 26.9]$ cm.s^{-1}. Finally, in Fig. 7.9b, velocities and pressures for diastolic flow are displayed. The plot represents the situation at the end of one cardiac cycle. We note that due to the bifurcation geometry the axial velocity profiles in daughter vessels are asymmetric. In both the internal and the external carotid artery the maximal u_1-velocity is shifted from the symmetry axis closer to the inner wall.

Next, we show results from an experiment for the same bifurcation geometry as described before, but for smaller Reynolds numbers, i.e. the mean Reynolds number is Re $\approx$ 152. Due to the change in local hemodynamics, flow patterns observed in Figs. 7.10-7.11 are more complex. See for example Fig. 7.11a, where two areas of reversed flow develop. We can observe larger areas, where recirculation occurs. Moreover, periods of stagnated and recirculated flow last longer.

In Figs. 7.12-7.13 we can see more precisely the evolution of the wall deformation function η in time along the moving boundary. Figs. 7.12-7.13 correspond to the mean Reynolds number Re $\approx$ 304 and Re $\approx$ 152, respectively. The curves in Figs. 7.12(left)-7.13(left) correspond to the significant time instants of the physiological flow for common carotid artery. In particular, we have at $t = 0.1$ s the systolic maximum, at $t = 0.23$ s the systolic minimum, at $t = 0.36$ s the diastolic minimum and $t = 0.96$ s corresponds to the final phase of one heart beat. We observe that the deformation is larger in the area of sinus bulb. This is caused by decreasing stresses, which directly influence the wall deformation. We point out that considering several constitutive models for viscosity function only slight differences in the deformation appear, see Figs. 7.12 (right)-7.13(right). Therefore we can conclude that the non-Newtonian rheology does not significantly influence the wall displacement.

In order to demonstrate the dependence of the wall movement on the reference geometry of vessel, we compare the results for bifurcation geometry from Figs. 7.12-7.13 with the ones for stenotic geometry plotted in Figs. 7.16-7.17. We see again that, as it is expected, the presence of a stenosed region has influence on the compliance of vessel wall. Moreover, decreasing the Reynolds number for both, the bifurcation and the stenosed vessel, see Figs. 7.13 and 7.17, quantitative differences in wall deformation can be observed.

In Figs. 7.14-7.15 velocities and pressures at several time instants for the stenosed iliac artery are shown. In each picture, from the top to the bottom, the streamlines, pressure isolines, velocity vector field and u_1-velocity isolines are plotted. The time instant $t = 0.15$ s corresponds to the flow rate maximum, i.e. the systolic peak flow, with velocities and pressures from the range $[0, 45.4]$ cm.s^{-1} and $[-38.4, 26.2]$ Pa, respectively. Passing the systolic deceleration phase, a reversed flow develops (Fig. 7.14b) and spreads in almost the whole domain (Fig. 7.15a). Indeed, at $t = 0.27$ s we observe in the plot of streamlines and the velocity field isolines the recirculation zones after and before the stenosed part of vessel. At the systolic minimum $t = 0.36$ s the negative flow with pressures from $[-51.6, 0]$ Pa and u_1-velocities from $[-21.5, 7.8]$ cm.s^{-1} develops. This is furthermore visible in the early diastolic phase. Finally, passing through the diastolic maximum a secondary reversed flow appears. As it is expected, it starts to develop around the stenosed parts. This can be observed in Fig. 7.15b.

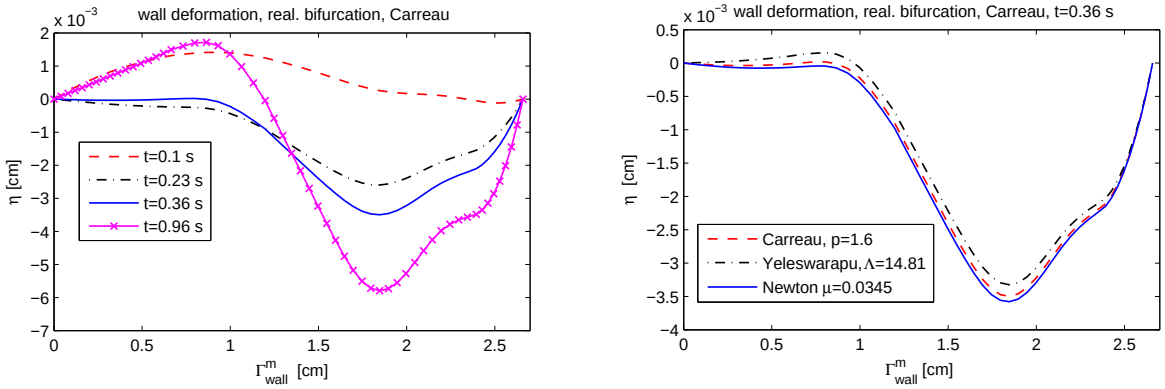

Figure 7.12: The evolution of η along the moving boundary Γ^m_{wall} for bifurcation geometry. Mean prescribed Reynolds number Re $\approx$ 304. Left: comparison at different time instants, right: comparison of constitutive models at $t = 0.36$ s.

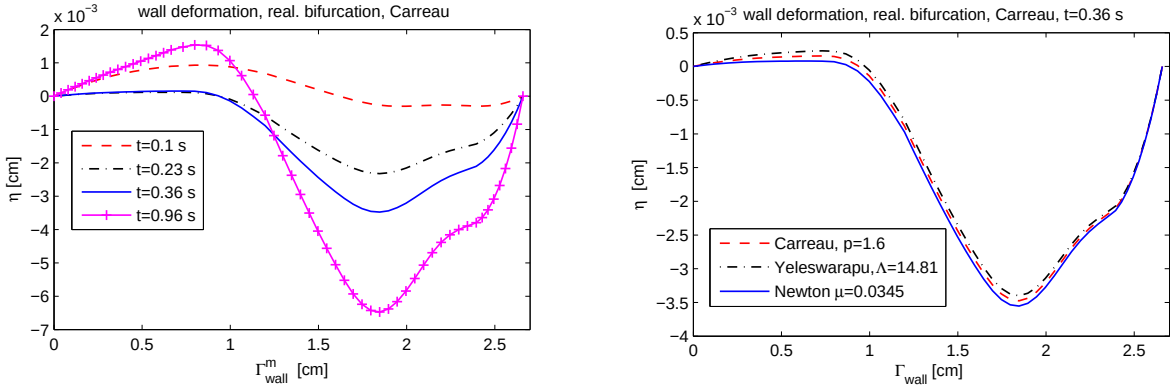

Figure 7.13: The evolution of η along the moving boundary Γ^m_{wall} for bifurcation geometry. Mean prescribed Reynolds number Re $\approx$ 152. Left: comparison at different time instants, right: comparison of constitutive models at $t = 0.36$ s.

Finally, in Fig. 7.18, let us compare our new kinematic splitting scheme with the so-called global iterative method developed by Hundertmark and Lukáčová [58]. The global iterative method is a strong coupling method based on the decoupling of fluid-structure interaction using global iterations with respect to the domain geometry. The results obtained by both methods are comparable. Note, moreover, that our new loosely coupled kinematic scheme does not require additional iterations as it is the case of the global iterative scheme. Therefore the new method is more efficient, while yielding comparable results, cf. also Tabs. 7.7 and 7.8 in Section 7.6.

(a) $t = 0.15\,\mathrm{s}$

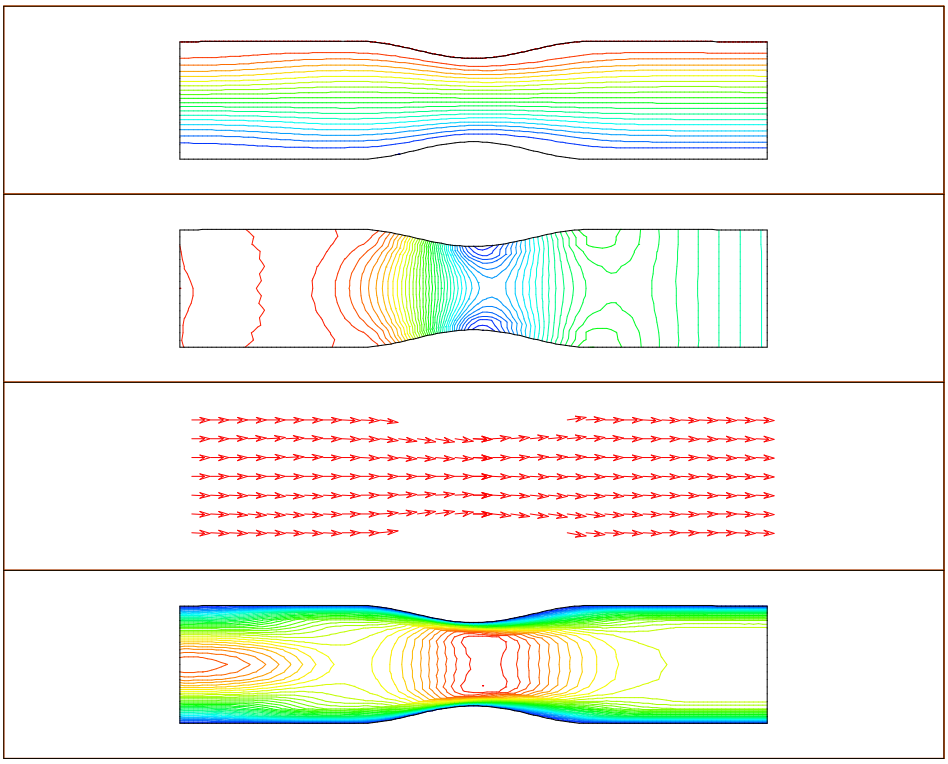

(b) $t = 0.27\,\mathrm{s}$

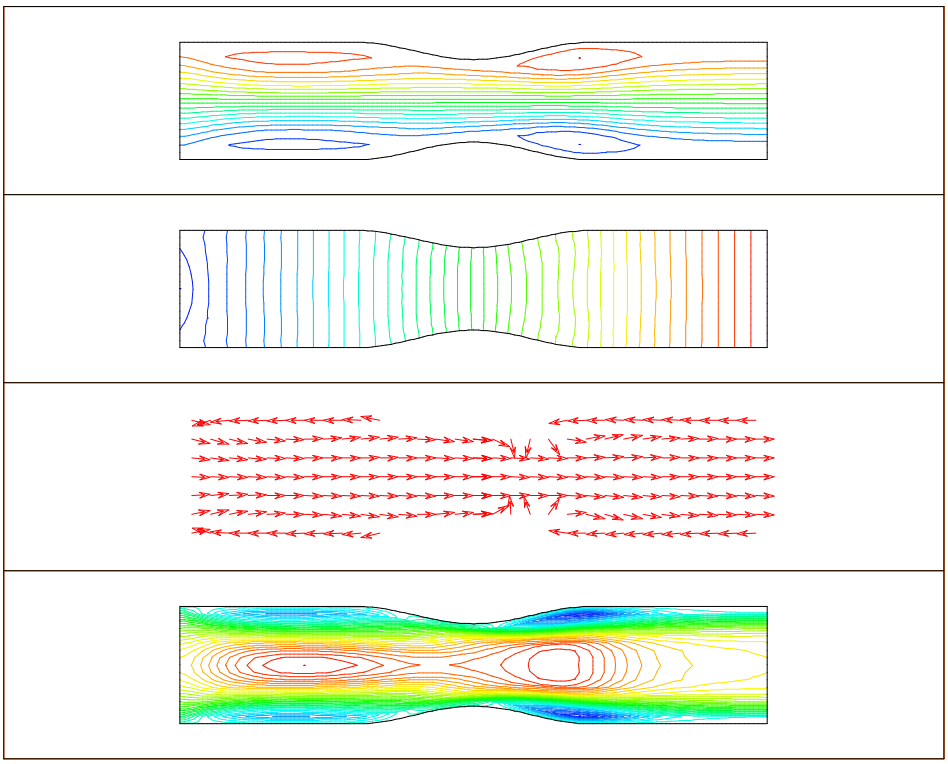

Figure 7.14: Streamlines, pressure isolines, velocity vector field and u_1-velocity isolines for stenosed vessel at two time instants.

(a) $t = 0.36\,\mathrm{s}$

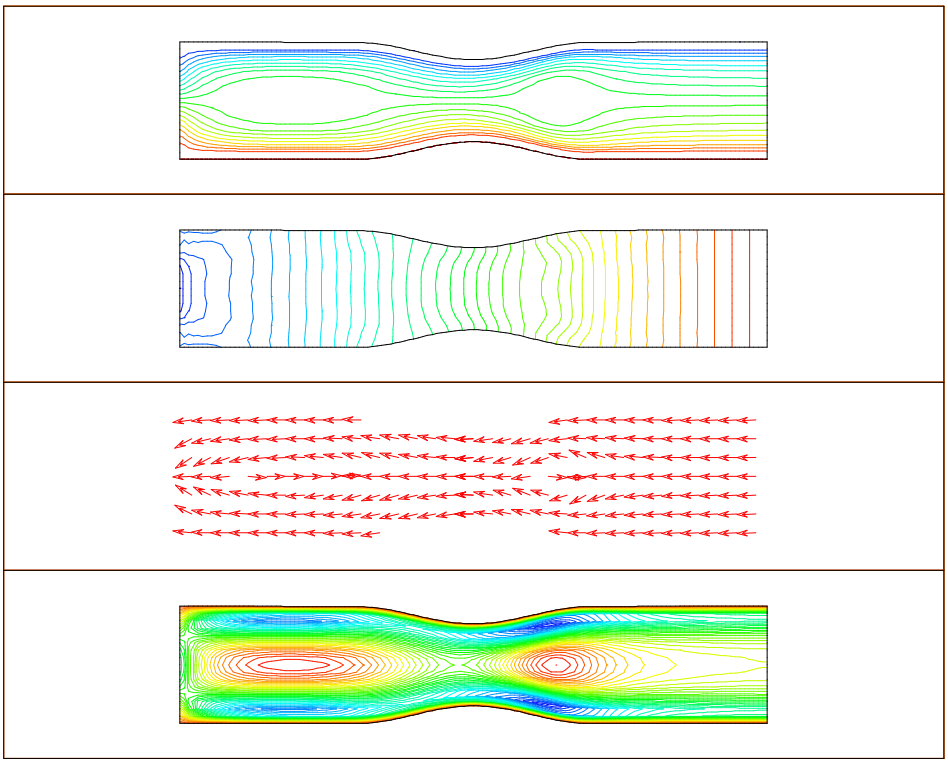

(b) $t = 0.8\,\mathrm{s}$

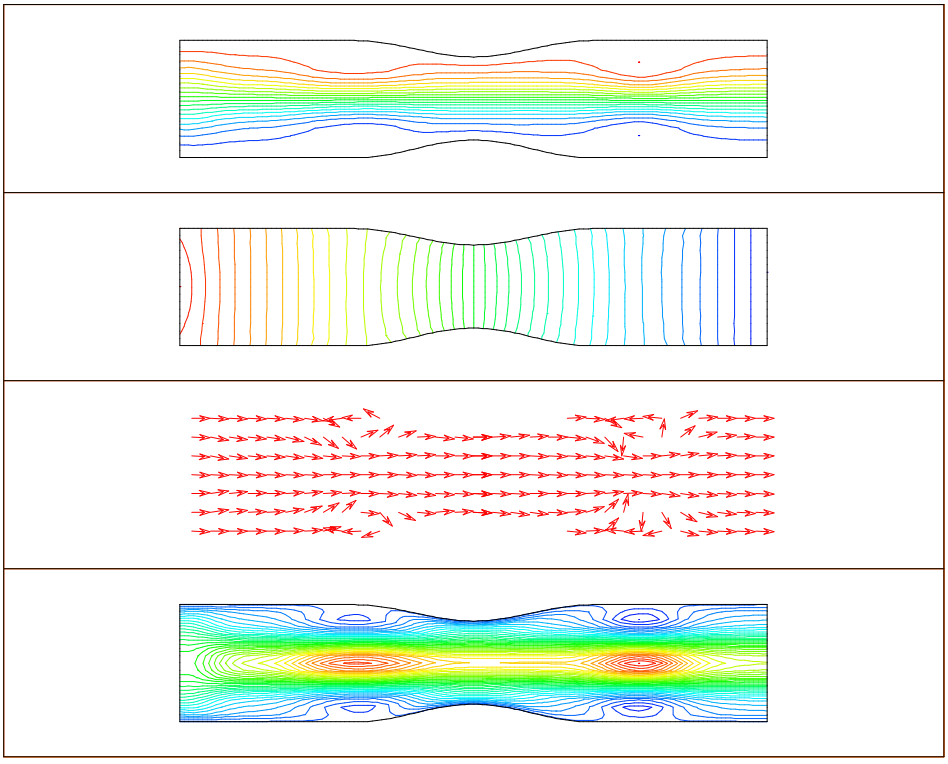

Figure 7.15: Streamlines, pressure isolines, velocity vector field and u_1-velocity isolines for stenosed vessel at two time instants.

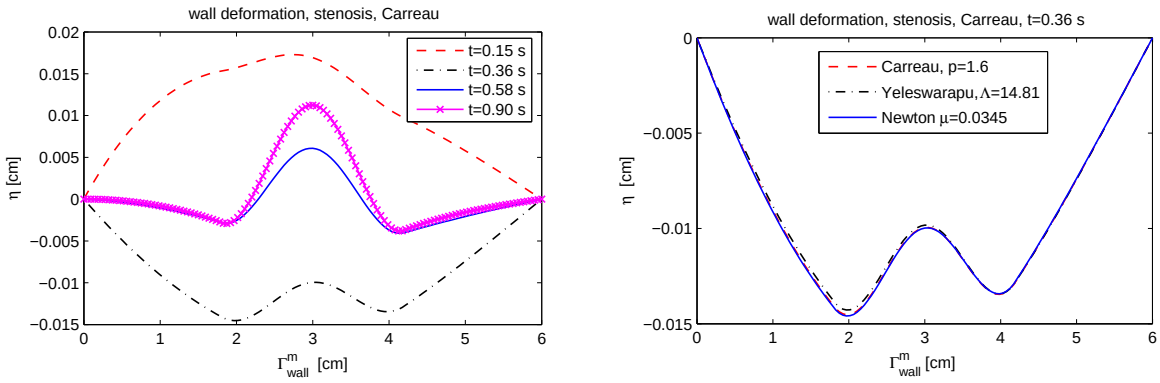

Figure 7.16: The evolution of η along the line $x_2 = R_0$ for stenosed vessel. Mean prescribed Reynolds number Re ≈ 195. Left: comparison at several time instants, right: comparison of constitutive models at $t = 0.36\,\mathrm{s}$.

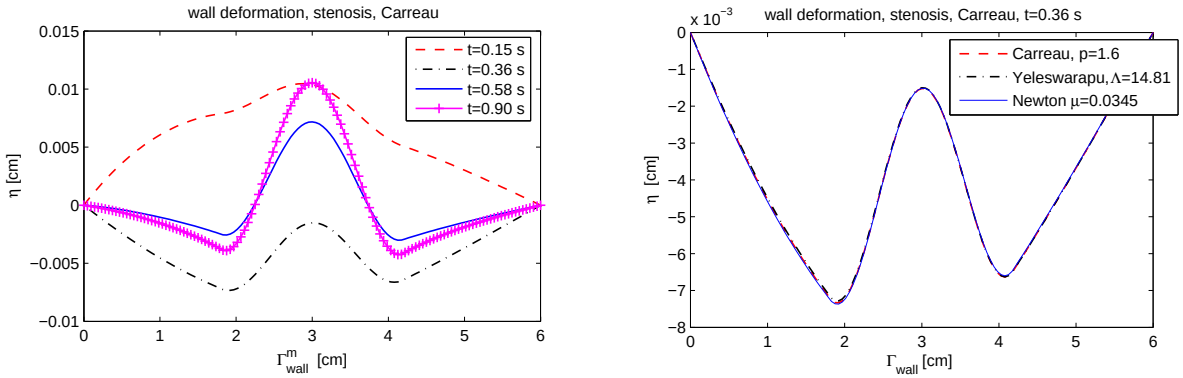

Figure 7.17: The evolution of η along the line $x_2 = R_0$ for stenosed vessel. Mean prescribed Reynolds number Re ≈ 98. Left: comparison at several time instants, right: comparison of constitutive models at $t = 0.36\,\mathrm{s}$.

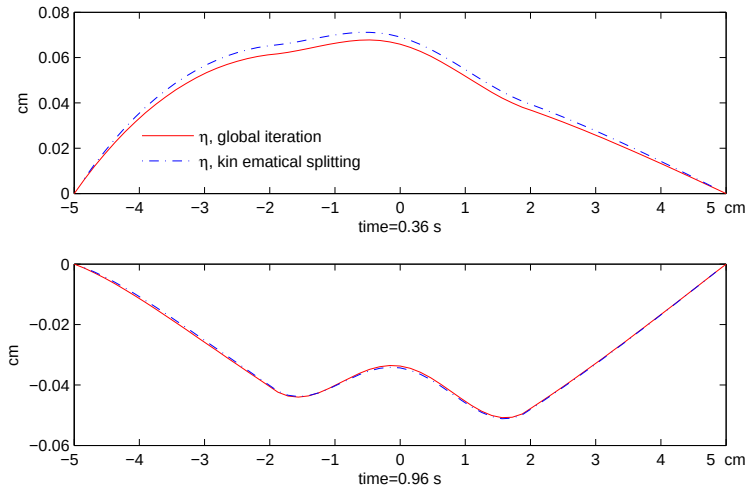

Figure 7.18: Comparison of the wall deformation η in stenosed vessel for the global iterative method and the explicit kinematic splitting; Carreau model: $\mu_0 = 1.26\mathrm{P}$, $\mu_\infty = 2.53\mathrm{P}$, $\Lambda = 1$, $q = 1.356$.

7.6 Experimental order of convergence

In order to study the accuracy of the coupled fluid-structure interaction problem the so-called *experimental order of convergence* (EOC) in space and time will be computed.

7.6.1 Experimental order of convergence in space

The EOC in space is defined in the following way

$$EOC(\boldsymbol{u}) = \log_2 \frac{||\boldsymbol{u}_{\triangle h,\triangle t} - \boldsymbol{u}_{\triangle h/2,\triangle t}||_{L^q}/|\Omega_{\triangle h}|^{1/q}}{||\boldsymbol{u}_{\triangle h/2,\triangle t} - \boldsymbol{u}_{\triangle h/4,\triangle t}||_{L^q}/|\Omega_{\triangle h/2}|^{1/q}} \ . \tag{7.31}$$

Moreover, let us define a normalized L^q error by

$$Err(\boldsymbol{u}) = \frac{||\boldsymbol{u}_{\triangle h,\triangle t} - \boldsymbol{u}_{\triangle h/2,\triangle t}||_{L^q}}{|\Omega_{\triangle h}|^{1/q}}. \tag{7.32}$$

Here $\boldsymbol{u}_{\triangle h,\triangle t}$ is the approximate velocity and $\Omega_{\triangle h}$ is the computational domain corresponding to the grid size $\triangle h$. We denote by $|\Omega_{\triangle h}|$ the area of the computational domain $\Omega_{\triangle h}$ and $||\boldsymbol{u}||^q_{L^q} := \sum_{i=1}^{n_{gp}} |A_i|\Big(|u_{1,i}|^q + |u_{2,i}|^q\Big)$ represents a discrete norm. Here $|A_i|$ denotes the area of the control volume corresponding to the grip point gp_i. We note that (7.31) and (7.32) are computed for the fixed space step $\triangle t$. The index q denotes a corresponding exponent in the power-law type model used for the non-Newtonian viscosity function (3.19). In our case the crucial value of q is 1.6. In the case of Newtonian flow L^2 norms (or H^1_0 norms) in space are used that corresponds to the space regularity of the weak solution, cf. [59], where the existence of weak solution of shear-dependent non-Newtonian fluids was analysed.

The computational geometry used in the experiments is shown in Fig. 7.2. Only the upper boundary Γ_{wall} is allowed to move. Note that the EOC in space (7.31) was computed for the time instant $T = 0.8$ s. The fixed time step $\triangle t$ was set to 0.002 s. The initial space step was $\triangle h = 0.625$ cm. We have used model data for the Newtonian as well as the non-Newtonian Carreau viscosity function, see Tabs. 7.1, 7.2.

In what follows we will present the convergence results in space in terms of the EOC values for velocity, gradient of velocity, pressure and domain displacement. The grid was consecutively divided having 32, 128, 512, 2048 elements for different grid levels.

First, we compare Newtonian and non-Newtonian rheology for the case of a non-stenosed rigid tube, i.e. no movement of boundaries is assumed, We use the model data, cf. Tab. 7.1-7.2, and the geometry from Fig. 7.2. We can observe that in the case of Newtonian rheology, see Tab. 7.5, the order of convergence for velocity is slightly better and the order of convergence for pressure slightly worse that in the non-Newtonian case, see Tab. 7.6.

Table 7.5: Convergence rates in space; rigid tube, Newtonian viscosity.

# refin ($\triangle h$)	$Err(\boldsymbol{u})$	$EOC(\boldsymbol{u})$	$Err(\bigtriangledown \boldsymbol{u})$	$EOC(\bigtriangledown \boldsymbol{u})$	$Err(p)$	$EOC(p)$
L^2-norm						
2/1	1.0785		0.0860		3.5200	
3/2	0.2757	1.97	0.0319	1.43	0.7522	2.23
4/3	0.0833	1.73	0.0040	3.00	0.3204	1.23

In the next experiment we present a comparison of the kinematic splitting algorithm, see Tab. 7.8, with the global iterative scheme of Hundertmark and Lukáčová, cf. [58], see Tab. 7.7. This experiment was performed for the non-Newtonian rheology and domain with movable boundary Γ_{wall}. We can clearly see the similar convergence rates in velocities, pressures and displacements that are of more than first order for velocities and the second

Table 7.6: Convergence rates in space; rigid tube, Carreau viscosity.

# refin ($\triangle h$)	$Err(\boldsymbol{u})$	$EOC(\boldsymbol{u})$	$Err(\bigtriangledown \boldsymbol{u})$	$EOC(\bigtriangledown \boldsymbol{u})$	$Err(p)$	$EOC(p)$
	L^q-norm				L^2-norm	
2/1	0.9083		0.0631		3.7209	
3/2	0.2494	1.86	0.0177	1.83	0.7703	2.27
4/3	0.1091	1.19	0.0024	2.92	0.1577	2.29

order for pressures and wall displacements. Note that our approach is more efficient, since it does not use additional iterations with respect to the domain as it is in the case for the strong coupling, cf. [58]. Moreover, we see that the kinematic splitting yields 10 times smaller relative errors in the wall displacement than the strong coupling scheme.

Table 7.7: Convergence rates in space; strong coupling scheme, Carreau viscosity.

# refin ($\triangle h$)	$Err(\boldsymbol{u})$	$EOC(\boldsymbol{u})$	$Err(\eta)$	$EOC(\eta)$	$Err(p)$	$EOC(p)$
	L^q-norm		L^2-norm			
2/1	0.9512		2.81 e-3		3.3925	
3/2	0.2563	1.89	8.88 e-4	1.69	0.7113	2.25
4/3	0.1074	1.26	1.85 e-4	2.23	0.1577	2.17

Now, we proceed with comparison of results obtained by using the kinematic splitting approach for both, the Newtonian (Tab. 7.9) and the non-Newtonian Carreau model (Tab. 7.8). Considering the non-Newtonian rheology the convergence rate in pressure is of the second order. It is typically better than in the Newtonian case. Since the convergence of η depends on the convergence rates of $\boldsymbol{u}$ and p, we see, in the case of non-Newtonian rheology, the improvement of convergence order for the wall displacement too.

Table 7.8: Convergence rates in space; kinematic splitting scheme, Carreau viscosity.

# refin ($\triangle h$)	$Err(\boldsymbol{u})$	$EOC(\boldsymbol{u})$	$Err(\bigtriangledown \boldsymbol{u})$	$EOC(\bigtriangledown \boldsymbol{u})$	$Err(\eta)$	$EOC(\eta)$	$Err(p)$	$EOC(p)$
	L^q-norm				L^2-norm			
2/1	0.8971		0.9682		2.62 e-4		3.1338	
3/2	0.2466	1.86	0.1408	2.78	1.84 e-5	0.51	0.7026	2.16
4/3	0.1051	1.23	0.0435	1.69	0.38 e-5	2.26	0.1461	2.27

Table 7.9: Convergence rates in space; kinematic splitting scheme, Newtonian viscosity.

# refin ($\triangle h$)	$Err(\boldsymbol{u})$	$EOC(\boldsymbol{u})$	$Err(\bigtriangledown \boldsymbol{u})$	$EOC(\bigtriangledown \boldsymbol{u})$	$Err(\eta)$	$EOC(\eta)$	$Err(p)$	$EOC(p)$
	L^2-norm							
2/1	1.0566		1.2723		1.56e-4		3.0076	
3/2	0.2780	1.93	0.2171	2.55	1.94e-4	-0.32	0.7081	2.09
4/3	0.0872	1.67	0.0483	2.17	1.12e-4	0.79	0.0313	1.18

In the following we compare results for the convergence in space obtained from four different schemes, namely, the explicit kinematic splitting approach (Tab. 7.10), implicit kinematic splitting approach (Tab. 7.11), explicit Strang splitting approach (Tab. 7.12) and implicit Strang splitting approach (Tab. 7.13). Since we used approximations of second order in space for the operator A as well as the operator B, also second order convergence rate is expected. Moreover, we note that in this case the choice of operator splitting type, i.e. either the Marchuk-Yanenko splitting (7.4) or the Strang splitting (7.5), has obviously

no visible influence on the accuracy results in space, since the Strang splitting scheme improves convergence rates only in time. What we can observe from the Tabs. 7.10-7.13 is the improvement of the convergence rate for implicit schemes. This results from the fact that the Crank-Nicolson time discretization has been used for the operator B.

Table 7.10: Convergence rates in space; explicit kinematic splitting scheme, Carreau viscosity.

# refin ($\triangle h$)	$Err(\boldsymbol{u})$	$EOC(\boldsymbol{u})$	$Err(\bigtriangledown \boldsymbol{u})$	$EOC(\bigtriangledown \boldsymbol{u})$	$Err(\eta)$	$EOC(\eta)$	$Err(p)$	$EOC(p)$
	L^q-norm				L^2-norm			
2/1	0.8667		0.9292		1.01 e-4		3.0097	
3/2	0.2338	1.89	0.1283	2.86	0.66 e-5	0.61	0.6451	2.22
4/3	0.1032	1.18	0.0437	1.55	0.25 e-5	1.37	0.1791	1.85

Table 7.11: Convergence rates in space; implicit kinematic splitting scheme, Carreau viscosity.

# refin ($\triangle h$)	$Err(\boldsymbol{u})$	$EOC(\boldsymbol{u})$	$Err(\bigtriangledown \boldsymbol{u})$	$EOC(\bigtriangledown \boldsymbol{u})$	$Err(\eta)$	$EOC(\eta)$	$Err(p)$	$EOC(p)$
	L^q-norm				L^2-norm			
2/1	1.0866		0.9470		1.04e-4		3.4332	
3/2	0.3300	1.72	0.1626	2.54	4.26e-5	1.29	0.8190	2.07
4/3	0.1034	1.67	0.0442	1.88	2.51e-5	0.76	0.1960	2.06

Table 7.12: Convergence rates in space; explicit Strang splitting scheme, Carreau viscosity.

# refin ($\triangle h$)	$Err(\boldsymbol{u})$	$EOC(\boldsymbol{u})$	$Err(\bigtriangledown \boldsymbol{u})$	$EOC(\bigtriangledown \boldsymbol{u})$	$Err(\eta)$	$EOC(\eta)$	$Err(p)$	$EOC(p)$
	L^q-norm				L^2-norm			
2/1	0.8015		0.8274		9.14e-4		3.0562	
3/2	0.2144	1.90	0.1170	2.82	9.77e-5	3.23	0.5403	2.50
4/3	0.1000	1.10	0.0447	1.39	8.34e-5	0.22	0.1580	1.77

Table 7.13: Convergence rates in space; implicit Strang splitting scheme, Carreau viscosity.

# refin ($\triangle h$)	$Err(\boldsymbol{u})$	$EOC(\boldsymbol{u})$	$Err(\bigtriangledown \boldsymbol{u})$	$EOC(\bigtriangledown \boldsymbol{u})$	$Err(\eta)$	$EOC(\eta)$	$Err(p)$	$EOC(p)$
	L^q-norm				L^2-norm			
2/1	0.8646		0.9260		1.23e-4		3.0057	
3/2	0.2332	1.89	0.1280	2.86	6.11e-5	1.01	0.6420	2.23
4/3	0.1032	1.18	0.0444	1.53	2.77e-5	1.14	0.1933	1.73

7.6.2 Experimental order of convergence in time

The EOC in time will be defined as

$$EOC(\boldsymbol{u}) = \log_2 \frac{\left(\sum_{j=1}^{N} ||\boldsymbol{u}^j_{\triangle h, \triangle t} - \boldsymbol{u}^j_{\triangle h, \triangle t/2}||^q_{L^q} / |\Omega^j_{\triangle h, \triangle t}|^q \right)^{1/q}}{\left(1/2 \sum_{j=1}^{2N} ||\boldsymbol{u}^j_{\triangle h, \triangle t/2} - \boldsymbol{u}^j_{\triangle h, \triangle t/4}||^q_{L^q} / |\Omega^j_{\triangle h, \triangle t/2}|^q \right)^{1/q}}, \tag{7.33}$$

where $T = \sum_{j=1}^{N} \triangle t = \triangle t\, N$. Moreover, we compute also the normalized relative $L^q(0,T;L^q(\Omega))$ error in time. This is defined by

$$Err(\boldsymbol{u}) = \frac{1}{T} \left(\sum_{j=1}^{N} \triangle t \left(\frac{||\boldsymbol{u}^j_{\triangle h, \triangle t} - \boldsymbol{u}^j_{\triangle h, \triangle t/2}||_{L^q}}{|\Omega^j_{\triangle h, \triangle t}|} \right)^q \right)^{1/q}, \tag{7.34}$$

where $\boldsymbol{u}^j_{\triangle h,\triangle t}$ and $\Omega^j_{\triangle h,\triangle t}$ denotes the velocity and the computational domain associated with the time instant $j \triangle t$, respectively. Note that (7.33)-(7.34) are computed for a grid size $\triangle h$.

The EOC in time (7.33) was computed on a computational mesh consisting of 585 elements. Going from one time refinement to the finer one, the time step was halved. The time period for the computation was $t \in [0.2; 0.8]\,\mathrm{s}$ and the initial time step was $\triangle t = 0.025\,\mathrm{s}$. Analogously as in the case of the EOC in space the initial computational domain is a rectangle, see Fig. 4.1, and the parameters for the Newtonian and the Carreau viscosity function are given in Tabs. 7.1, 7.2.

We start the analysis of convergence in time with presenting the results for constant reference radius and rigid geometry for both, the Newtonian as well as non-Newtonian rheology, see Tab. 7.14 and 7.15, respectively. We observe a very similar convergence rates. No visible differences due to the non-Newtonian rheology appear.

Table 7.14: Convergence rates in time; rigid domain, Newtonian viscosity.

# refin ($\triangle t$)	$Err(\boldsymbol{u})$	$EOC(\boldsymbol{u})$	$Err(\bigtriangledown \boldsymbol{u})$	$EOC(\bigtriangledown \boldsymbol{u})$	$Err(p)$	$EOC(p)$
	$L^2(L^2)$-norm					
2/1	0.0197		0.0284		0.3672	
3/2	0.0109	0.86	0.0151	0.91	0.1804	1.03
4/3	0.0059	0.91	0.0078	0.95	0.0892	1.02
5/4	0.0036	0.68	0.0048	0.69	0.0437	1.03

Table 7.15: Convergence rates in time; rigid domain, Carreau viscosity.

# refin ($\triangle t$)	$Err(\boldsymbol{u})$	$EOC(\boldsymbol{u})$	$Err(\bigtriangledown \boldsymbol{u})$	$EOC(\bigtriangledown \boldsymbol{u})$	$Err(p)$	$EOC(p)$
	$L^q(L^q)$-norm				$L^2(L^2)$-norm	
2/1	0.0185		0.0260		0.3745	
3/2	0.0101	0.88	0.0137	0.92	0.1846	1.02
4/3	0.0053	0.92	0.0070	0.96	0.0913	1.02
5/4	0.0033	0.69	0.0043	0.71	0.0450	1.02

For completeness of presentation, we compare also the convergence results for the Newtonian fluid flow, see Tab 7.16, with the results for the Carreau fluid flow, see Tab. 7.17, through deforming non-stenosed tube. Also here, the results are qualitatively as well as quantitatively very similar.

Table 7.16: Convergence rates in time; explicit kinematic splitting, Newtonian viscosity.

# refin ($\triangle t$)	$Err(\boldsymbol{u})$	$EOC(\boldsymbol{u})$	$Err(\bigtriangledown \boldsymbol{u})$	$EOC(\bigtriangledown \boldsymbol{u})$	$Err(\eta)$	$EOC(\eta)$	$Err(p)$	$EOC(p)$
	$L^2(L^2)$-norm							
2/1	0.2319		0.0208		0.0085		0.2873	
3/2	0.0126	0.88	0.0117	0.83	0.0057	0.56	0.1405	1.03
4/3	0.0067	0.91	0.0063	0.90	0.0040	0.54	0.0689	1.03
5/4	0.0040	0.74	0.0042	0.59	0.0016	1.41	0.0331	1.06

Similarly as for the convergence in space, we compare explicit and implicit kinematic splitting scheme (Tabs. 7.17, 7.18) and explicit and implicit Strang splitting scheme (Tabs. 7.19, 7.20). We see that for the explicit kinematic splitting scheme the EOC is around first order. Considering the second order explicit Strang splitting technique, the convergence orders are improved. Working with the implicit kinematic splitting scheme, we obtained better convergence than in the explicit kinematic splitting scheme. Finally, in Tab. 7.20, we see that

the EOC is significantly improved. Therefore we can note that the Strang splitting strategy gives better convergence results for both, the explicit and the implicit schemes.

Table 7.17: Convergence rates in time; explicit kinematic splitting, Carreau viscosity.

# refin ($\triangle t$)	$Err(\boldsymbol{u})$	$EOC(\boldsymbol{u})$	$Err(\bigtriangledown \boldsymbol{u})$	$EOC(\bigtriangledown \boldsymbol{u})$	$Err(\eta)$	$EOC(\eta)$	$Err(p)$	$EOC(p)$
	$L^q(L^q)$-norm				$L^2(L^2)$-norm			
2/1	0.0246		0.0159		0.0088		0.2905	
3/2	0.0132	0.89	0.0088	0.86	0.0060	0.56	0.1422	1.03
4/3	0.0070	0.92	0.0046	0.93	0.0041	0.53	0.0697	1.03
5/4	0.0042	0.74	0.0030	0.61	0.0016	1.40	0.0336	1.05

Table 7.18: Convergence rates in time; implicit kinematic splitting, Carreau viscosity.

# refin ($\triangle t$)	$Err(\boldsymbol{u})$	$EOC(\boldsymbol{u})$	$Err(\bigtriangledown \boldsymbol{u})$	$EOC(\bigtriangledown \boldsymbol{u})$	$Err(\eta)$	$EOC(\eta)$	$Err(p)$	$EOC(p)$
	$L^q(L^q)$-norm				$L^2(L^2)$-norm			
2/1	0.1491		0.1633		0.1640		0.5616	
3/2	0.1532	-0.03	0.1600	0.03	0.2706	-0.72	0.4332	0.37
4/3	0.0705	1.12	0.0747	1.10	0.2000	0.44	0.2286	0.92
5/4	0.0218	1.69	0.0234	1.67	0.0915	1.13	0.0683	1.74

Table 7.19: Convergence rates in time; explicit Strang splitting, Carreau viscosity.

# refin ($\triangle t$)	$Err(\boldsymbol{u})$	$EOC(\boldsymbol{u})$	$Err(\bigtriangledown \boldsymbol{u})$	$EOC(\bigtriangledown \boldsymbol{u})$	$Err(\eta)$	$EOC(\eta)$	$Err(p)$	$EOC(p)$
	$L^q(L^q)$-norm				$L^2(L^2)$-norm			
2/1	0.0564		0.0252		0.0583		0.3363	
3/2	0.0195	1.53	0.0081	1.65	0.0234	1.32	0.1539	1.13
4/3	0.0077	1.34	0.0024	1.75	0.0089	1.40	0.0712	1.11
5/4	0.0044	0.83	0.0013	0.90	0.0054	0.72	0.0315	1.18

Table 7.20: Convergence rates in time; implicit Strang splitting, Carreau viscosity.

# refin ($\triangle t$)	$Err(\boldsymbol{u})$	$EOC(\boldsymbol{u})$	$Err(\bigtriangledown \boldsymbol{u})$	$EOC(\bigtriangledown \boldsymbol{u})$	$Err(\eta)$	$EOC(\eta)$	$Err(p)$	$EOC(p)$
	$L^q(L^q)$-norm				$L^2(L^2)$-norm			
2/1	0.1826		0.1936		0.2211		0.5969	
3/2	0.0578	1.66	0.0609	1.67	0.1140	0.96	0.2411	1.31
4/3	0.0241	1.26	0.0243	1.32	0.0441	1.37	0.0896	1.43
5/4	0.0088	1.44	0.0078	1.64	0.0173	1.35	0.0297	1.60

7.7 Hemodynamic wall indices

Studying blood flow of patients with a cardiovascular disease, the choice of appropriate hemodynamic factors plays an important role. A significant index is the so-called shear rate. High shear rate in arteries plays a key role for the development of thrombosis. Also considering blood flow through a stenosed region, high shear areas appear, even if only for a short time. In these cases a plaque rupture can occur already after 7ms of high shear flow [53]. An important hemodynamic indicator of atherosclerosis is the so-called wall shear stress. It is well-known that high wall shear stress tends to a mechanical damage of inner parts of vessel walls. Moreover, even too low wall shear stress is not desirable since it can promote the accumulation of plaque. In addition, a mechanical sign of atherosclerotic diseases is formation of vortex structures and even turbulence. The latter increases the kinetic energy and also creates a stagnant blood flow. Stagnation regions occur usually in the areas with sharp curvatures such as those present at vessel bifurcation branchings or in severe stenosed vessels. Blood coagulation in these complex geometries can lead to formation of blood clots and induce ischemia, heart attack or an other pathological situations. In addition, devices implanted in the cardiovascular system, such as stents or prosthetic heart valves, can interrupt normal biochemical conditions too. Recently, there is an active mathematical research focused on blood coagulation, modelling of the equilibrium and of its stability, see, e.g. [2, 95] and the references therein. Since we are interested in modelling of blood flow in stenosed regions, we will consider preferably non-Newtonian constitutive models.

In this subsection we will compare several important hemodynamic wall parameters for different constitutive models as well as different reference geometries. Hemodynamic indices that help to predict areas sensitive to the stenotic plaque danger are the wall shear stress function (WSS) and the oscillatory shear index (OSI). The WSS is a local hemodynamic factor that is closely related to the occurrence of atherosclerosis. It is defined by

$$\mathrm{WSS} := \tau_w = -(\mathbf{T}\boldsymbol{n}) \cdot \boldsymbol{n}^{\perp}, \tag{7.35}$$

where $\boldsymbol{n}$ is the unit outward normal vector and $\boldsymbol{n}^{\perp}$ denotes the unit tangential vector. The OSI measures pointwisely the temporal oscillations of WSS and is computed by the formula

$$\mathrm{OSI} := \frac{1}{2}\left(1 - \frac{\int_0^T \tau_w \, \mathrm{d}t}{\int_0^T |\tau_w| \, \mathrm{d}t}\right). \tag{7.36}$$

It is known that the range of WSS in a normal artery is from $[1.0, 7.0]$ Pa and in the venous system it is from $[0.1, 0.6]$ Pa, see [72]. The regions of artery that are athero-prone, i.e. stimulates an atherogenic phenotype, are in the range of ± 0.4 Pa. On the other hand, WSS greater than 1.5 Pa induces an anti-proliferative and anti-thrombotic phenotype and therefore is found to be athero-protective. However, in the range of $[7, 10]$ Pa high-shear thrombosis is likely to be found.

In the experiments shown in Figs. 7.19-7.27, the physiological flow rates (Fig. 7.5) as well as physiological values for viscosity parameters (Tab. 7.2) were prescribed.

In Figs. 7.19-7.20 we see the distribution of WSS for different time instants during the cardiac cycle along the moving boundary of stenosed vessel. Fig. 7.19 corresponds to the mean $\mathrm{Re} \approx 195$ and Fig. 7.20 represents the WSS distribution for the lower prescribed mean Reynolds number $\mathrm{Re} \approx 98$.

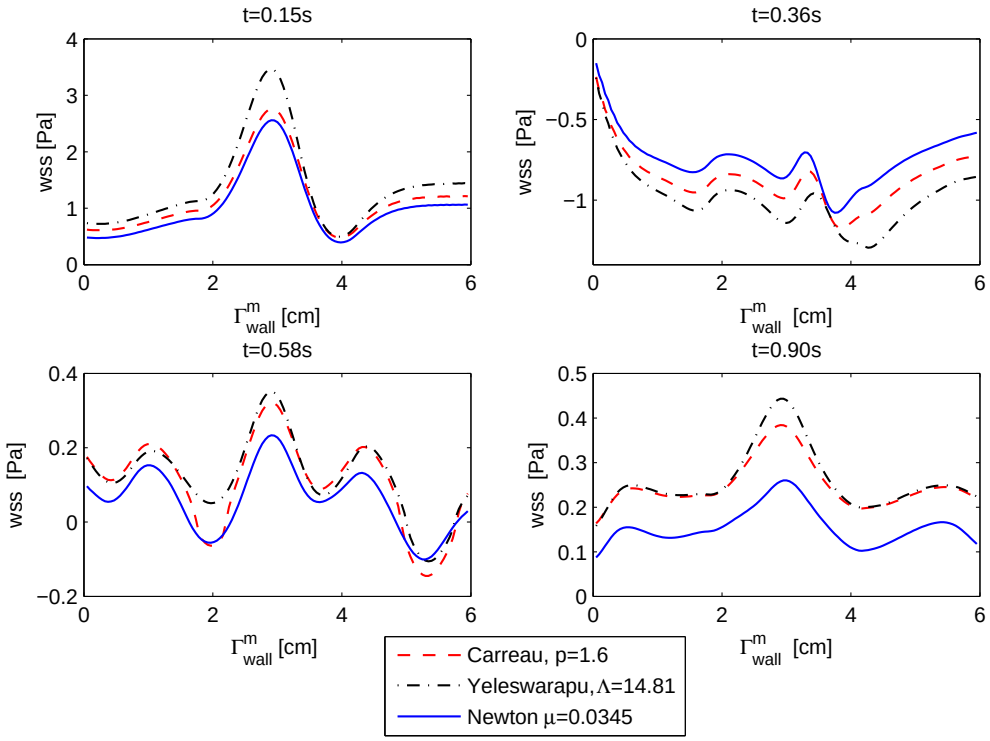

Figure 7.19: WSS along Γ_{wall} for stenotic vessel geometry at several time instants; mean Reynolds number Re $\approx$ 195.

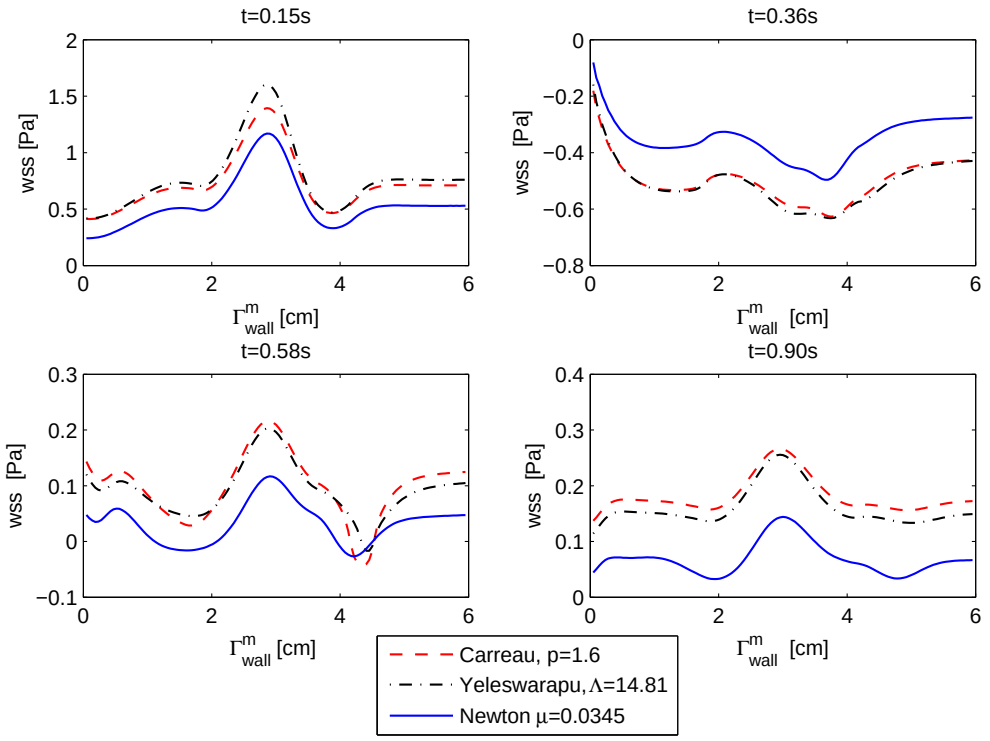

Figure 7.20: WSS along Γ_{wall} for stenotic vessel geometry at several time instants; mean Reynolds number Re $\approx$ 98.

Let us firstly describe the situation depicted in Fig. 7.19. The peak values of WSS (with exception of the time instant $t = 0.36$ s) correspond to the narrowed area of stenosed vessel. We see that the magnitude of the WSS differs with respect to time in the cardiac pulse cycle. In the systolic acceleration phase maximum ($t = 0.15$ s) the lower WSS area is at the beginning of vessel and behind the stenosis. In this period no reversed flow occurs and the WSS belongs to the athero-protective range. Different situation happens in the systolic minimum, i.e. at the end of systolic deceleration phase ($t = 0.36$ s). Negative values of WSS along the moving boundary are visible. In both cases we observe that the WSS corresponding to the non-Newtonian model gives higher extremal values. Passing the diastolic maximum a more complex behaviour can be seen. At $t = 0.58$ s two reversed flows develop. In the remaining phase, see $t = 0.90$ s, the magnitude of WSS is low, but not negative. Again, the non-Newtonian viscosities seem to elevate the values of WSS approaching the athero-protective range. Now, we briefly describe the plots corresponding to the lower Reynolds number shown in Fig. 7.20. The first thing to observe is that the values of WSS are approximately twice as low than the values corresponding to the higher Reynolds number flow. The situation in Fig. 7.20 is qualitatively similar to the one described before. Again, non-Newtonian rheology increases extremal values of WSS compared to the Newtonian one. Since the non-Newtonian rheology is considered to be more relevant for the modelling of blood flow, this can be interpreted in such a way, that the Newtonian rheology detects athero-prone zones too early. These results indicate that it is more accurate to use non-Newtonian viscosity models while modelling of blood flow.

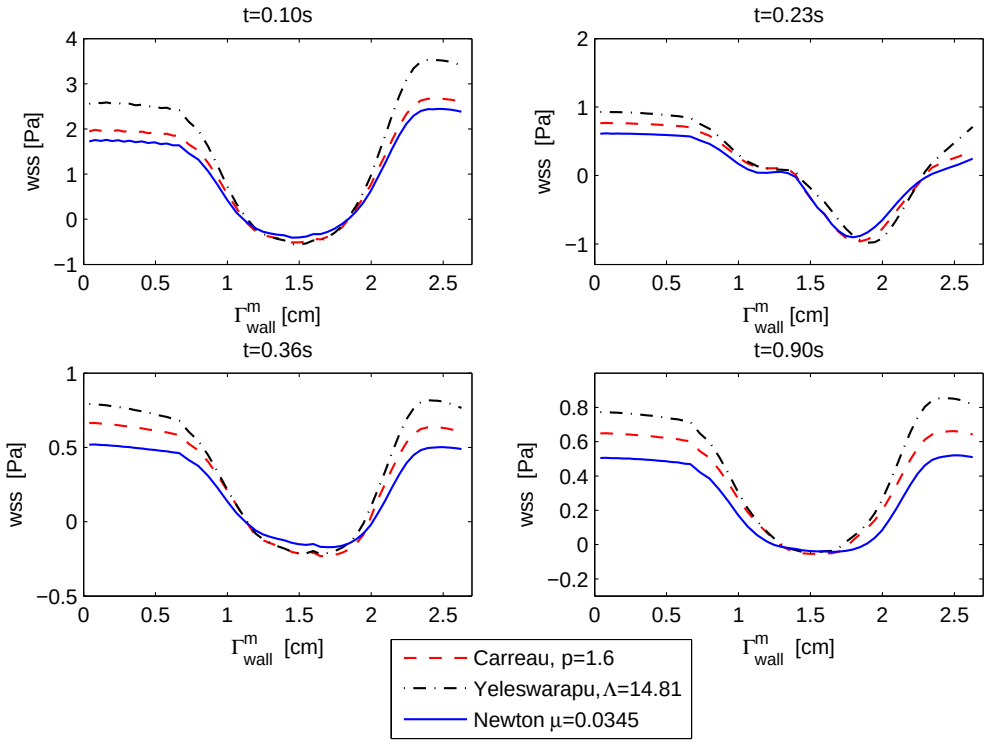

Figure 7.21: WSS along Γ^m_{wall} for bifurcation geometry at several time instants; mean Reynolds number Re ≈ 304.

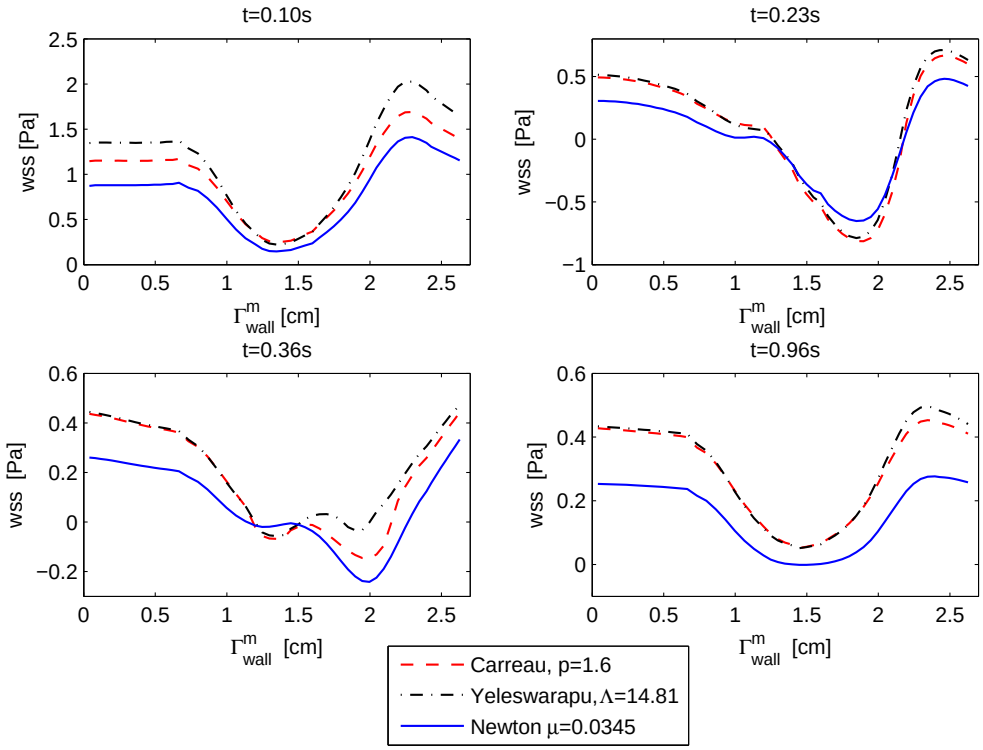

Figure 7.22: WSS along Γ^m_{wall} for bifurcation geometry at several time instants; mean Reynolds number Re $\approx$ 152.

In Figs. 7.21-7.22 the WSS evolution for bifurcation reference geometry (Fig. 7.4) is presented. At each time instant a period of negative flow around the sinus bulb is visible. In the area of bifurcation divider and carotid sinus we observe that the non-Newtonian rheology elevates the extremal values of WSS. Moreover,the magnitude of WSS falls into the atherosclerotic range around the sinus bulb area. This confirms the observations from clinical praxis, see [72].

The WSS distribution at several points on the moving boundary for bifurcation geometry and stenosed geometry is demonstrated in Figs. 7.23-7.24, 7.25-7.26, respectively. For the bifurcation geometry, see Fig. 7.4, points of measurement correspond to: $x \approx 0.6\,\text{cm}$ for the common carotid artery, $x \approx 1.2\,\text{cm}$ for the proximal to the internal carotid artery, $x \approx 1.6\,\text{cm}$ for the mid-carotid sinus bulb, $x \approx 2.0\,\text{cm}$ for the end of carotid sinus bulb and $x \approx 2.5\,\text{cm}$ for the internal carotid artery. In the case of stenosed vessel, see Fig. 7.3, the WSS was measured in front of the stenosis $x \approx 1.8\,\text{cm}$, in the maximal stenosed point $x \approx 3.0\,\text{cm}$ and after the stenosis $x \approx 4.0\,\text{cm}$.

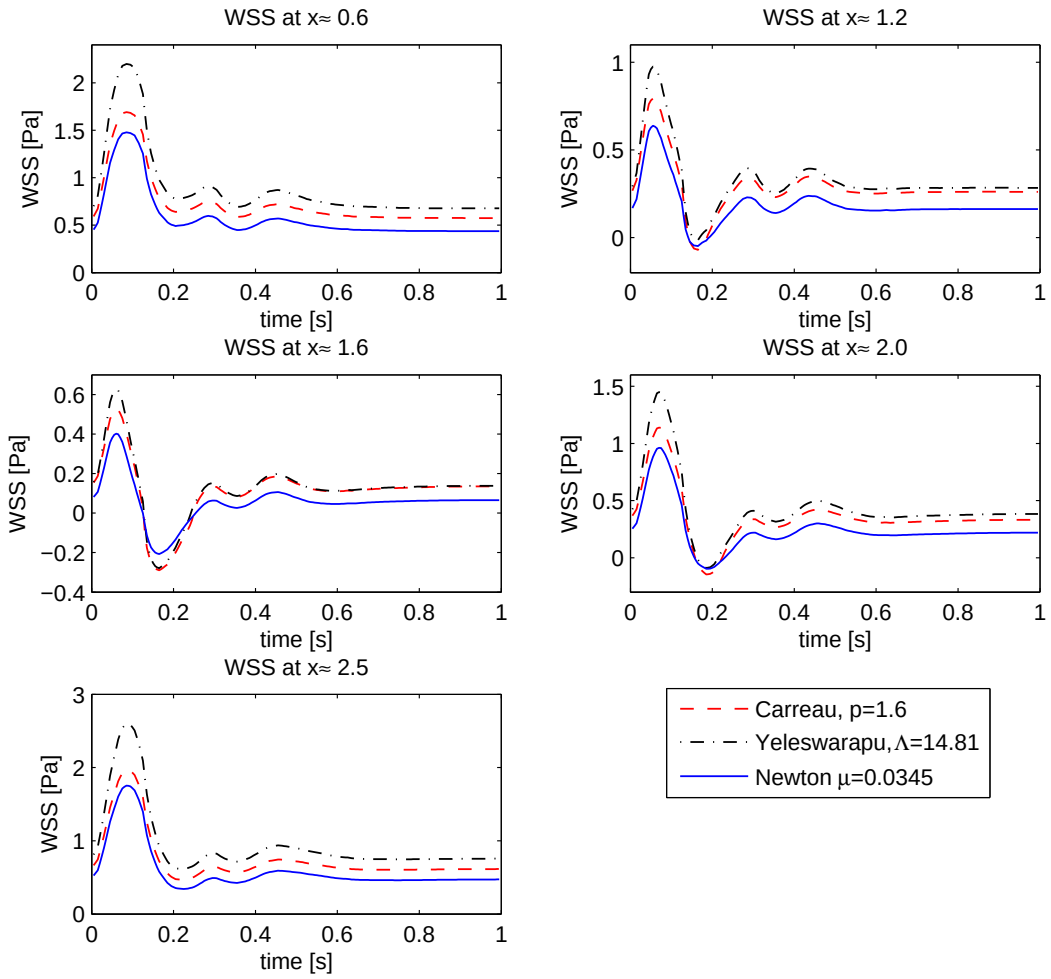

Figure 7.23: WSS at five different positions along Γ^m_{wall} for the period of one heart beat; bifurcation geometry; mean Reynolds number Re $\approx$ 304.

The evolution curves of the WSS, see Fig. 7.23, at the common carotid artery ($x \approx 0.6\,\text{cm}$) and the external carotid artery ($x \approx 2.5\,\text{cm}$) have similar shape as the prescribed flow rate, see Fig. 7.5 left. They belong to the athero-protective range (i.e. WSS is typically larger than 0.4 Pa in these parts of artery). Approaching the bifurcation divider (at points $x \approx 1.2\,\text{cm}$, $x \approx 1.6\,\text{cm}$ and $x \approx 2.0\,\text{cm}$) we observe a reversed flow period with negative values of WSS, which is mostly athero-prone. Moreover, analyzing the curves in Fig. 7.23, we observe that the non-Newtonian rheology seems to be more athero-protective than the Newtonian one. The non-Newtonian rheology yields larger extremal values of WSS and shortens the periods of reversed flow. The WSS evolution for the same bifurcation geometry, but different Reynolds number range, see Fig. 7.24, shows analogous characteristics as the ones observed in Fig. 7.23. In addition, we see development of stagnation flow before the sinus bulb area at point $x = 1.2\,\text{cm}$.

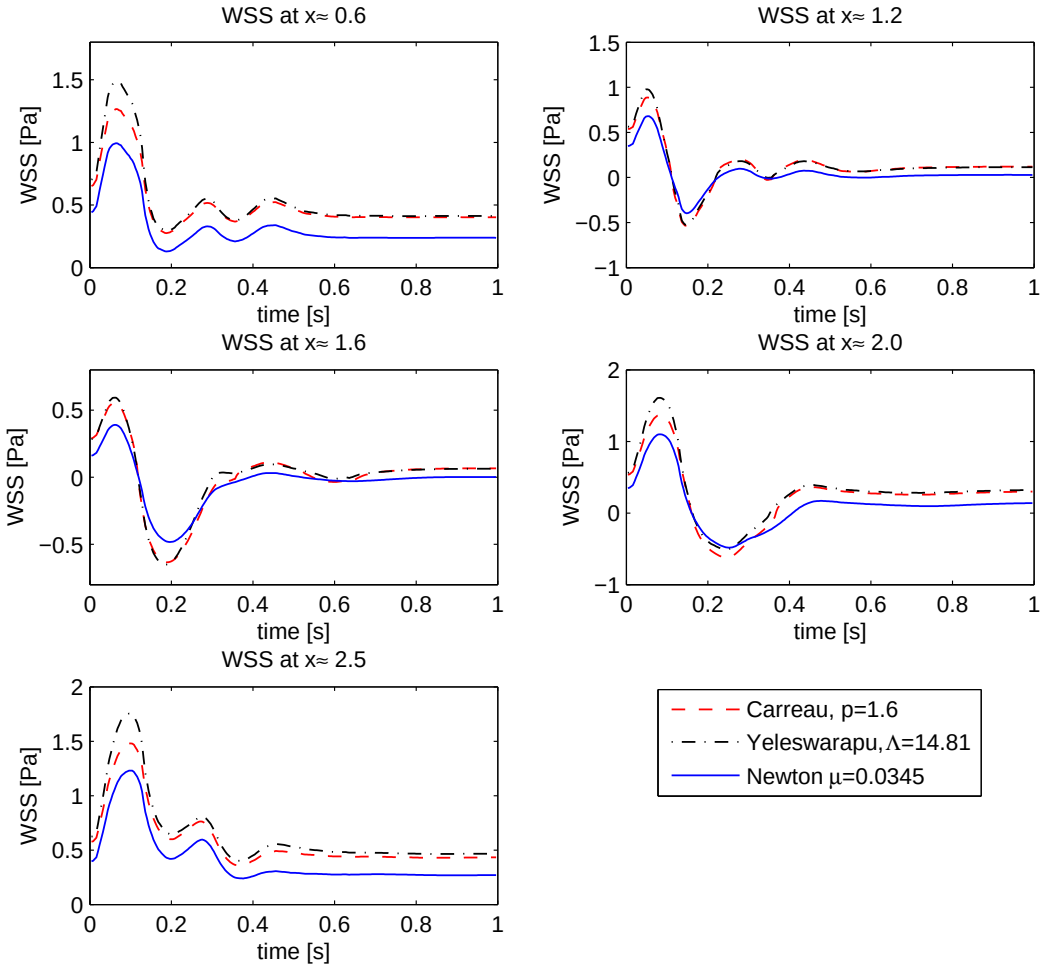

Figure 7.24: WSS at five different positions along Γ^m_{wall} for the period of one heart beat; bifurcation geometry; mean Reynolds number Re $\approx$ 152.

Analysing the plots of the WSS evolution in sampling points for stenotic geometry, see Fig. 7.25, we can obtain the following information: the narrowed part of vessel corresponding to the point $x = 3$ cm yields higher values of WSS than at $x = 1.8$ cm and $x = 4.2$ cm (before and after the stenosis). Moreover, due to the large negative flow period in the iliac flow rate the values of WSS belong mostly to the athero-prone range (with exception of the systolic peak phase and the systolic minimum phase). Decreasing the Reynolds number, see Fig. 7.26, the extremal values of WSS decreased twice. However, analogous behaviour as in Fig. 7.25 has been observed. Similarly to the case of bifurcation, see Figs. 7.23 - 7.24, higher extrema in the peaks of the flow are followed by higher WSS for the non-Newtonian models.

The results shown in Figs. 7.19-7.25 confirm dependence of the shear stress distribution on a given geometry. Consecutively, the WSS is one of the important parameters for the prediction of stenotic danger.

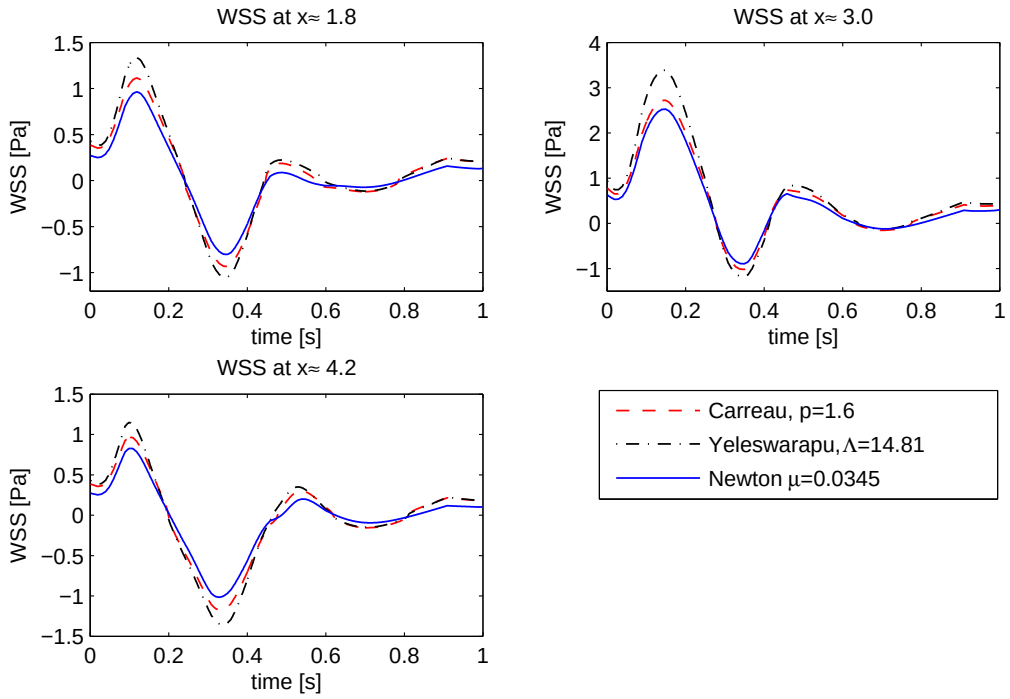

Figure 7.25: WSS at three different positions along Γ^m_{wall} for the period of one heart beat; stenotic geometry; mean Reynolds number Re $\approx$ 195.

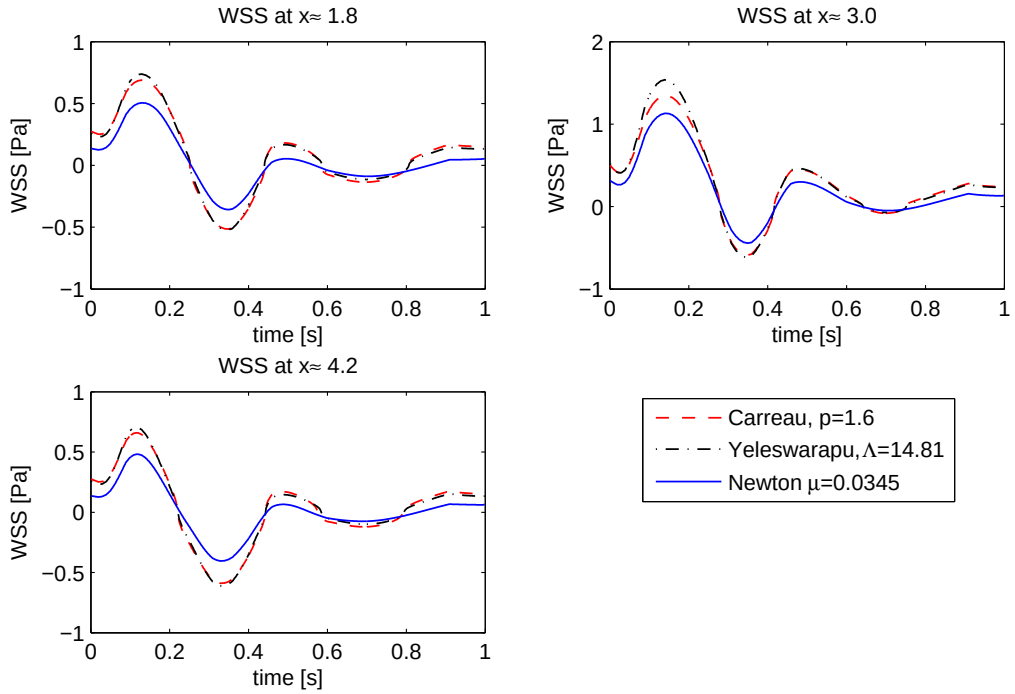

Figure 7.26: WSS at three different positions along Γ^m_{wall} for the period of one heart beat; stenotic geometry; mean Reynolds number Re $\approx$ 98.

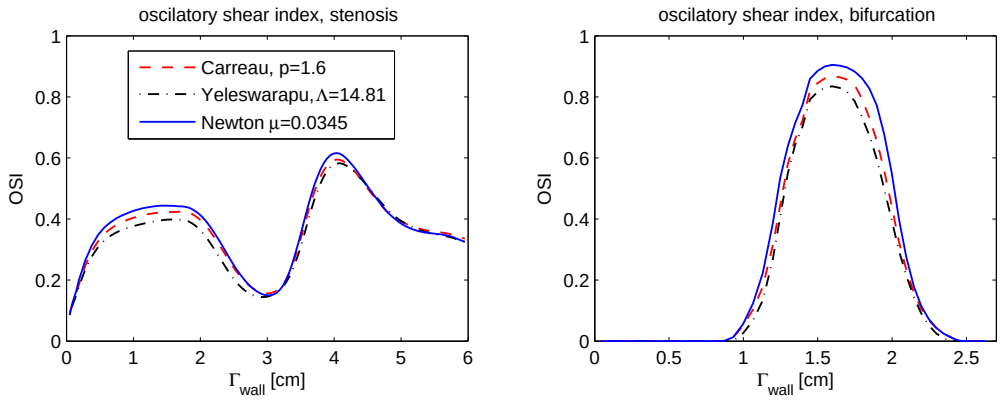

Figure 7.27: OSI along Γ_{wall}. Left: stenosed geometry (mean Re $\approx$ 304), right: bifurcation geometry (mean Re $\approx$ 195).

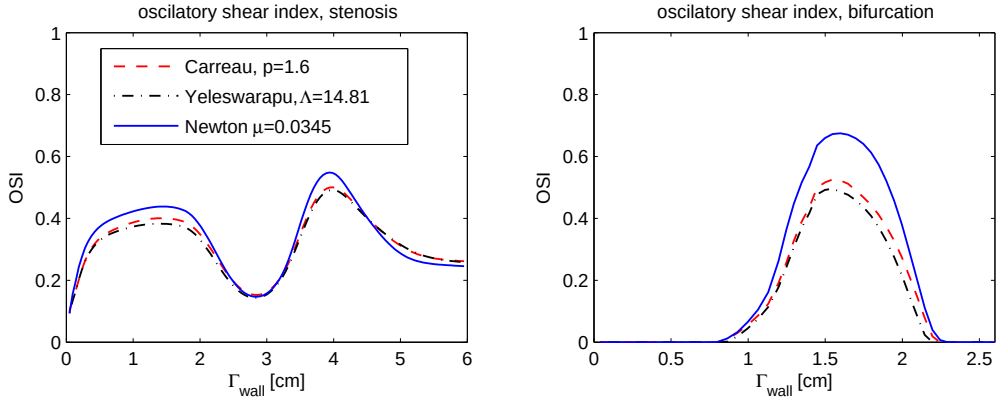

Figure 7.28: OSI along Γ_{wall}. Left: stenosed geometry (mean Re $\approx$ 152), right: bifurcation geometry (mean Re $\approx$ 98).

Finally, in Fig. 7.27-7.28 the dependence of the OSI index on position and rheology is presented.

Since the OSI measures the change of WSS with respect to the direction, high values of this index indicate regions with pulsatile WSS. Figs. 7.27(left)-7.28(left) confirm our assumption that in the case of the iliac stenosed artery the reversed flow occurs along the whole boundary. Due to the high-shear flow in the stenosed region, direction-varying WSS appears in particular behind the stenosed area. This is clearly visible in the measurements of the OSI. In Figs. 7.27 (right)-7.28 (right) it can be observed that the reversed flow appears preferentially in the carotid sinus. Indeed, the OSI index increases and the peak corresponds to the mid-carotid sinus point. Moreover, in both, the stenotic and the bifurcation reference geometry, the Newtonian rheology causes more oscillations of the WSS (for comparison see the areas of reversed flow in Figs. 7.21-7.22, points $x = 1.2\,\text{cm}$, $x = 1.6\,\text{cm}$, $x = 2.0\,\text{cm}$).

Chapter 8

Conclusions and future works

In this thesis we have studied mathematical aspects of the fluid-structure interaction with application in hemodynamics.

Firstly, we have introduced the mathematical model arising from the conservation laws with a special choice of a constitutive relation and from a linear elasticity theory. The model leads to the system consisting of the generalized Navier-Stokes equations and a generalized string model. Since we assume that our computational domain can be represented by a kind of channel with a rigid inflow and a rigid outflow parts and several movable parts a special technique to capture the dynamic mesh movement is needed. We have used the arbitrary Lagrangian-Eulerian mapping that represents a suitable description of the domain movement. With respect to this mapping, the time-derivative in the Eulerian frame changed to the ALE derivative and a new term, i.e. the ALE convective term with domain velocity, is arising. Then, we introduced a structural model, i.e. the generalized string model, which has been extended also to the non-constant reference radius domains. This is needed for our experimental studies, where the blood flow through stenotic vessels is investigated. In this part we have also presented the results on well-posedness of the mathematical model in both, the rigid and the moving domains, for Newtonian fluids.

Next, we were focused on the non-Newtonian rheology. We have explained differences between the Newtonian and non-Newtonian fluids and pointed out the non-Newtonian features observing in blood that categorized it to be a non-Newtonian fluid. This seems to be a natural assumption since blood is a suspension of several cells and plasma. Therefore its behaviour is very complex and shows the signs of non-Newtonian material. For our experimental study we have chosen two shear thinning viscosity models that enters the constitutive relation between the Cauchy stress tensor and the rate of the deformation tensor. We have introduced a power-law-type model, i.e. the Carreau model, and we have recalled the viscoelastic model of Yeleswarapu. Since we have been focused on shear-dependent behaviour so far, we have used from the Yeleswarapu viscoelastic model only the definition of the shear thinning viscosity function. Discussing briefly well-posedness of the generalized Navier-Stokes equations with non-Newtonian shear dependent viscosity, we have seen that results strongly depend on the power-law exponent q.

After we introduced the weak formulation of our fluid-structure interaction problem, we have discussed the numerical approximations of the coupled problem. It is well-know that fluid-structure algorithms are typically affected by the added mass effect, cf. [22, 37, 58, 89], that is very strong in the case of comparable densities between the fluid and the structure. We have introduced a new loosely coupled fluid-structure interaction algorithm based on the idea of kinematic splitting, see also the work of Guidoboni et al. [50]. It is designed in such a way that the coupling on the moving interface avoids the classical problems with added mass effect, see also [50].

The stability analysis of our fluid-structure interaction scheme was investigated in the energy norms. In order to find a suitable functional setting for the fluid field and the structure displacement, a priori estimates for the continuous problem have been derived. Using the energy estimates we have analyzed stability of the semi-discrete coupled fluid-structure interaction scheme and shown that it is stable without any subiterations. Indeed, using the implicit Euler time discretization we obtained conditional stability with the stability condition for the time step depending on the domain velocity. We have shown that if the ALE convective term is discretized using the mid-point rule, then the semi-discrete kinematic splitting scheme is unconditionally stable. We would also like to point out that our analysis generalizes the result from [50]: we take explicitly the domain movement into account, apply the ALE formulation and point out the role of geometric conservation law. Moreover, we have assumed the nonlinearities in the convective as well as in the diffusive term.

Convergence analysis of the kinematic splitting fluid-structure interaction problem has been performed for a simplified fluid model. We assumed divergence-free fluid velocities that are given by the equation of the Oseen type. We would like to point out that even if the model is simplified the idea of convergence analysis for our fluid-structure interaction algorithm has been still included. The convergence study is based on the finite element approximation. We have introduced the finite element discretization, the interpolations operators for fluid and structure variables and derived the corresponding approximation errors. Assuming the functional spaces that have sufficient regularity we have derived the error equations for the operator A and the operator B. Summing up both contributions and using the Gronwall lemma we have obtained the error equation for the difference between an approximated fluid and structure variables and their interpolants. This equation has been then easily rewritten into the error equation between the exact and the numerical solutions and the accuracy in space of first order has been shown. Finally, we have discussed several extensions concerning the domain definition and the fully non-linear governing equations including the pressure contribution.

The coupled fluid-structure interaction problem was investigated also experimentally. The resulting system of equation was solved with the UG software toolbox, where the numerical approximation of the generalized Navier-Stokes equations is based on the finite volume method. We have presented the discretization of the fluid as well as the structure equations. The kinematic splitting scheme was based on the Marchuk-Yanenko operator splitting, which is of the first order in time, and the Strang operator splitting, which gives the second order convergence in time. We have compared our kinematic splitting scheme with the global iterative method developed by Hundertmark and Lukáčová [58]. This was done for a non-stenosed geometry, sinus pulsatile inflow and model data for non-Newtonian viscosity. We have seen that the kinematic splitting method yields a numerical scheme that is more efficient than the global iterative scheme while no subiterations are needed. The experimental order of convergence tests have indicated similar order of accuracy and even shown smaller global error. The experimental order of convergence in time has been improved using the Strang splitting scheme.

We have also simulated blood flow in a stenotic iliac artery and a carotid bifurcation artery and analysed some hemodynamic control quantities, i.e. the wall shear stress and the oscillatory shear index. The blood was modelled as a shear thinning non-Newtonian fluid with physiologically relevant viscosity parameters and the pulsatile inflow describing the flow rate in the heart with its systolic and diastolic parts. Numerical experiments have confirmed dependence of the WSS and the OSI on the vessel geometry. Moreover, a significant influence on the non-Newtonian rheology has been shown. Although the qualitative character for both the Newtonian and non-Newtonian fluids was similar, the results were quantitatively different. In particular, it has been observed that the non-Newtonian viscosity models, that are assumed to describe better the blood flow, indicate the areas with extremal values of

WSS later than the Newtonian viscosity model. In addition, the areas of the oscillatory WSS were larger assuming the Newtonian rheology. Hence, it has been demonstrated that the Newtonian model overestimates problematic areas both in time and space. Moreover, it has been shown that also the OSI depends strongly on the geometry. The maximal values of OSI are larger for the Newtonian fluid. Such high OSI values at the end of stenotic occlusion indicate a large oscillatory nature of the wall shear stress and could yield further to additional stenotic plug.

The study presented in the thesis can be extended to the following main areas:

- First extension that would be interesting to do considers the structural model. Here, the extensions to the more realistic models would need the wall deformation in both directions, x_1 as well as x_2, using e.g. the Koiter shell model. This would bring more freedom in design of the vessels since no restriction due to the axial symmetry would appear.

- The constitutive relation expressing dependence of viscosity on the Cauchy stress tensor (or the extra stress tensor) and the rate of the deformation tensor can be extended to the case of viscoelastic viscosity function as it is presented in the Oldroyd-B model, see Tab. 3.3. Even if shear thinning behaviour is the most relevant in the blood flow modelling, also the viscoelasticity plays an important role. Here, the place is seen for e.g. the full viscoelastic Yeleswarapu model, which is the model of the Oldroyd-B type including shear thinning properties in the viscosity function.

- From the numerical analysis the correction can be done in terms of outflow boundary conditions, which should reflect the rest of the circulatory system. Similarly as proposed in Vignon-Clementel et al. [104] this can be realized using the boundary conditions that incorporate memory-effects like the impedance condition and couples the fluid equations with some less dimensional model, i.e. 1D or 0D lumped model.

- Extension of the convergence analysis for the generalized Navier-Stokes equations as proposed in Remark 6.5 and for the situation, when $\Omega_t \neq \Omega_{h,t}$, $\Omega_t \neq \Omega_{h,0}$ discussed in Remark 6.3.

Bibliography

[1] Adams R.A.: *Sobolev Spaces*, Academic Press, New York, 1975.

[2] Anand M., Rajagopal K., Rajagopal K.R.: A model incorporating some of the mechanical and biochemical factors underlying clot formation and dissolution in flowing blood, *J. Theor. Med.* 5(3-4): 183–218 (2003).

[3] Ardakani S.S.J., Jafarnejad M., Firoozabadi B., Saidi M.S.: Investigation of wall shear stress related factors in realistic carotid bifurcation geometries and different flow conditions, *Scientia Iranica, Transaction B: Mech. Eng.* 17: 358–366 (2010).

[4] Astorino M., Chouly F., Fernandez M.: Robin based semi-implicit coupling in fluid-structure interaction: stability analysis and numerics, *SIAM J. Sci. Comput.* 31(6): 4041–4065 (2009).

[5] Astorino M., Grandmont C.: Convergence analysis of a projection semi-implicit coupling scheme for fluid-structure interaction problems, *Numer. Math.*, 116: 721–767 (2010).

[6] Badia S., Nobile F., Vergara C.: Robin-Robin preconditioned Krylov methods for fluid-structure interaction problems, *Comput. Meth. Appl. Mech. Eng.* 198: 2768–2784 (2009).

[7] Bastian P., Johannses K., Reichenberger V.: *UG tutorial*, Heidelberg, 1999.

[8] Bastian P., Birken K., Johannsen K., Lang S., Eckstein E., Neuss N., Rentz-Reichert H., Wieners C.: UG - A flexible software toolbox for solving partial differential equations, *Comput. Visual. Sci.* 1: 27–40 (1997).

[9] Behbahani M., Behr M., Hormes M., Steinseifer U., Arora D., Coronado O., Pasquali M.: A review of computational fluid dynamics analysis of blood pumps, *Eur. J. Appl. Math.* 20: 363–397 (2009).

[10] Behbadani M., Behr M., Nicolai M., Probst M.: Towards shape optimization for ventricular assist devices using parallel stabilized FEM, *In: Proceedings of the NIC Symposium*, Jülich, 325–331 (2008).

[11] Beirao da Veiga H.: On the existence of strong solutions to a coupled fluid-structure evolution problem, *J. Math. Fluid Mech.* 6(1): 21–52 (2004).

[12] Bellout H., Bloom F., Nečas J.: Young measure-valued solutions for non-Newtonian fluids, *Comm. Part. Differ. Equat.* 19: 1763–1803 (1994).

[13] Besov O.V.: On coercivity in nonisotropic Sobolev spaces, *Math. USSR Sb.* 2: 521–534 (1967).

[14] Bodnár T., Sequeira A., Prosi M.: On the shear-thinning and viscoelastic effects of blood flow under various flow rates, *Appl. Math. Comput.* 217: 5055–5067 (2011).

[15] Bodnár T., Sequeira A.: Numerical study of the significance of the non-Newtonian nature of blood in steady flow through a stenosed vessel, In: Rannacher R. et al. (Eds.), *Advances in Mathematical Fluid Mechanics*, 83–104, Springer, 2010.

[16] Boulakia M., Cazeau S., Fernández Varela M.A., Gerbeau J.F., Zemzemi N.: Mathematical modeling of electrocardiograms: a numerical study, *Ann. Biomed. Eng.* 38(3): 1071–1097 (2010).

[17] Broser P.J.: *Simulation von Strömungen in Blutgefäsen*, Master's Thesis, Heildelberg, 2003.

[18] Burman E., Fernández M.A.: Stabilization of explicit coupling fluid-structure interaction involving fluid incompressibility, *Comput. Meth. Appl. Mech. Eng.* 198: 766–794 (2009).

[19] Caffarelli L., Kohn R., Nirenberg L.: Partial regularity of suitable weak solutions of the Navier-Stokes equations, *Comm. Pure Appl. Math.* 35: 771–831 (1982).

[20] Calvez V., Huout J.G., Meunier N., Raoult A., Rusnáková G.: Mathematical and numerical modeling or early atherosclerotic lesions, *ESAIM: Proceedings*, 30: 1–14 (2010)

[21] Čanić S., Tambača J., Guidoboni G., Mikelić A., Hartley C.J., Rosenstrauch D.: Modeling viscoelastic of arterial walls and their interaction with pulsatile blood flow, *SIAM J. Appl. Math.* 67(1): 164–193 (2006).

[22] Causin P., Gerbeau J.F., Nobile F.: Added-mass effect in the design of partitioned algorithms for fluid-structure problems, *Comput. Meth. Appl. Mech. Eng.* 194: 4506–4527 (2005).

[23] Chambolle A., Desjardin B., Esteban M.J., Grandmont C.: Existence of weak solutions for unsteady fluid-plate interaction problem, *J. Math. Fluid Mech.* 7 (3): 368–404 (2005).

[24] Cheng A., Shkoller S.: The interaction of the 3D Navier-Stokes equations with a moving nonlinear Koiter elastic shell, *SIAM J. Math. Anal.* 42(3): 1094–1155 (2010).

[25] Ciarlet P.G.: *The Finite Element Method for Elliptic Problems*, In: O'Malley E. et al. (Eds.), SIAM's Classics in Applied Mathematics, Vol. 40, North-Holland, Amsterdam, New York, Oxford, 1978.

[26] Ciarlet P.G.: *Mathematical Elasticity, Volume II: Theory of Plates*, North-Holland, Amsterdam, 1997.

[27] Ciarlet P.G.: *Mathematical Elasticity, Volume III: Theory of Shells*, North-Holland, Amsterdam, 2000.

[28] Coleman B.D., Noll W.: Foundations of linear viscoelasticity, *Rev. Mod. Phys.* 33(2): 239–249 (1961).

[29] Deutsch S., Phillips W.M.: Towards a constitutive equation for blood. *Biorheology* 12: 383–389 (1975).

[30] Diening L., Prohl A., Růžička M.: Semi-implicit Euler scheme for generalized Newtonian fluids, *SIAM J. Numer. Anal.* 44(3): 1172–1190 (2006).

[31] Diening L, Růžička M., Wolf J.: Existence of weak solutions for unsteady motions of generalized Newtonian fluids, *Ann. Sc. Norm. Super. Pisa*, Classe di Scienze, Vol. IX: 1-46 (2010).

[32] Donea J., Giuliani S., Halleaux J.P.: An arbitrary Lagrangian-Eulerian finite element method for transient dynamic fluid-structure interactions, *Comput. Meth. Appl. Mech. Eng.* 33: 689–723 (1982).

[33] Evans L.C.: *Partial Differential Equations*, AMS: Graduate Studies in Mathematics, Vol. 19, 2010.

[34] Farhat C., Lesoinne M., Maman N.: Mixed explicit/implicit time integration of coupled aeroelastic problems: three-field formulation, geometric conservation and distributed solution, *Int. J. Numer. Meth. Fluid.* 21: 807–835 (1995).

[35] Fefferman Ch.I.: Existence and smoothness of the Navier-Stokes equation, *Official statement of the problem*, Clay Mathematics Institute.

[36] Feistauer M.: *Mathematical Methods in Fluid Dynamics*, Chapman and Hall, London, 1993.

[37] Fernández M.A.: Coupling schemes for incompressible fluid-structure interaction: implicit, semi-implicit and explicit, *Bol. Soc. Esp. Mat. Apl.* 55: 59–108 (2011).

[38] Fernández M.A., Gerbeau J.-F., Grandmont C.: A projection algorithm for fluid-structure interaction problems with strong added-mass effect, *C. R. Acad. Sci. Paris ,Ser. I* 342: 279–284 (2006).

[39] Fernández M.A., Gerbeau J.-F., Grandmont C.: A projection semi-implicit scheme for the coupling of an elastic structure with an incompressible fluid, *J. Numer. Meth. Eng.* 69: 794–821 (2007).

[40] Fernández M.A., Moubachir M.: A Newton method using exact Jacobians for solving fluidstructure coupling, *Compos. Struct.* 83: 127-142 (2005).

[41] Formaggia L., Nobile F.: A stability analysis for the arbitrary Lagrangian Eulerian formulation with finite elements, *East. W. J. Numer. Math.* 7(2): 103–131 (1999).

[42] Formaggia L., Quarteroni A., Veneziani A.: *Cardiovascular Mathematics*, Springer, Milano, 2009.

[43] Förster Ch., Wall W.A., Ramm E.: The artificial added mass effect in sequential staggered fluid-structure interaction algorithms, *ECCOMAS Computational Fluid Dynamics*, 2006.

[44] Frehse J., Málek J., Steinhauer M.: *On existence results for fluids with shear dependent unsteady flows*, Partial differential equations (Praha, 1998), 121129, Chapman & Hall/CRC Res. Notes Math., 406, Chapman & Hall/CRC, Boca Raton, FL, 2000.

[45] Galdi G.P., Rannacher R., Robertson A.M., Turek S.: *Hemodynamical Flows. Modelling, Analysis, Simulation.* Oberwolfach-Seminars, Vol. 37, Birkhäuser, 2008.

[46] Gastaldi L.: A priori error estimates for the Arbitrary Lagrangian Eulerian formulation with finite elements, *East. W. J. Numer. Math.* 9(2): 123–156 (2001).

[47] Gerbeau J.-F., Vidrascu M.: A quasi Newton algorithm interaction in blood flows on geometries based on medical imaging, *Compos. Struct.* 83(2-3): 155-165 (2005).

[48] Glowinski R.: Numerical Methods for Fluids (Part 3), In: Ciarlet P.G. et al. (Eds.) *Handbook of Numerical Analysis*, Vol. VI, Elsevier, Amsterdam, 2003.

[49] Guidorzi M., Padula M., Plotnikov P.I., Bellomo N.: Hopf solutions to a fluid-elastic interaction model, *Math. Model. Meth. Appl. Sci.* 18(2): 215–270 (2008).

[50] Guidoboni G., Glowinski R., Cavallini N., Čanić S.: Stable loosely-coupled-type algorithm for fluid-structure interaction in blood flow, *J. Comput. Phys.* 228(18): 6916–6937 (2009).

[51] Guidoboni G., Glowinski R., Cavallini N., Čanić S., Lapin S.: A kinematically coupled time-splitted scheme for fluid-structure interaction in blood flow, *Appl. Math. Lett.* 22(5): 684-688 (2009).

[52] Gresho P.M., Sani R.L.: On pressure boundary conditions for the incompressible Navier-Stokes equations, *Int. J. Numer. Meth. Fluid* 7: 1111–1145 (1987).

[53] Hademenos G.J., Massoud T.F.: Biophysical mechanisms of stroke. *American Heart Association* 28: 2067–2077 (1997).

[54] Hanke-Bourgeois M.: *Grundlagen der numerischen Mathematik und des wissenschaftlichen Rechnens*, B. G. Teubner, Stuttgart, 2002.

[55] Heil M.: An efficient solver for the fully-coupled solution of large-displacement in fluid-structure interaction problems, *Comput. Meth. Appl. Mech. Eng.* 193: 1–23 (2004).

[56] Hopf E.: Über die Anfangswertaufgabe für die hydrodynamischen Grundgleichungen, *Math. Nachr.* 4: 213–231 (1951)

[57] Hron J., Turek S.: A monolithic FEM/multigrid solver for an ALE formulation of fluid-structure interaction with applications in biomechanics, *In: Fluid-structure interaction, Lect. Notes Eng. Comput. Sci.*, Vol. 53: 146-170 (2006).

[58] Hundertmark-Zaušková A., Lukáčová-Medviďová M.: Numerical study of shear-dependent non-Newtonian fluids in compliant vessels, *Comput. Math. Appl.* 60: 572–590 (2010).

[59] Hundertmark-Zaušková A., Lukáčová-Medviďová M., Nečasová Š.: On the existence of fluid-structure interaction of non-Newtonian shear-dependent fluid in compliant vessels, *Preprint University of Mainz*, 2011.

[60] Hundertmark-Zaušková A., Lukáčová-Medviďová M., Rusnáková G.: Fluid-structure interaction for shear-dependent non-Newtonian fluids, In: Kaplický P. (Ed.) *Topics in Mathematical Modeling and Analysis* Vol.7, 109–158, 2012.

[61] Janela J., Moura A., Sequeira A.: A 3D non-Newtonian fluid-structure interaction model for blood flow in arteries, *J. Comput. Appl. Math.* 234: 2783–2791 (2010).

[62] Karimian S., Schneider G.: Pressure-based control-volume finite-element method for flow at all speeds, *AIAA Journal* 33: 1611–1618 (1995).

[63] Ladyzhenskaya O.A.: *The Mathematical Theory of Viscous Incompressible Flow*, Gordon and Breach, New York, 1969.

[64] Ladyzhenskaya O.A.: On finite dimensionality of bounded invariant sets for the NavierStokes equations and some other dissipative systems, *Zap. Nauch. Sem. Leningrad. Otdel. Mat. Inst. Steklov (LOMI)* 115: 137–155 (1982).

[65] Leeson P.: *Cardiac Imaging*, Oxford University Press, 2011.

[66] Leray J.: Etude de diverses équations intégrales nonlinéaires et de quelques problémes que pose l'hydrodynamique, *J. Math. Pure. Appl.* 12: 1-82 (1933)

[67] Leray J.: Sur le mouvement d'un liquide visqueux emplissant l'espace, *Acta Math.* 63: 193-248 (1934)

[68] Lesoinne M., Farhat Ch.: Geometric conservation laws for flow problems with moving boundaries and deformable meshes, and their impact on aeroelastic computations, *Comput. Meth. Appl. Mech. Eng.* 134(1-2): 71–90 (1996).

[69] LeVeque R.J.: *Finite Volume Methods for Hyperbolic Problems*, Cambridge University Press, 2002.

[70] Lions J.L.: *Quelques mèthodes de rèsolution des problèmes aux limites non lineàires*, Dunod, Paris, 1969.

[71] Lions J.L., Prodi G.: Un thèorème d'existence et unicitè dans les èquations de Navier-Stokes en dimension 2, *Compr. Rendus. Acad. Sci. Math.* 248: 3519–3521 (1959).

[72] Malek A.M., Alper A.L., Izumo S.: Hemodynamic shear stress and its role in atherosclerosis, *J. Am. Med. Assoc.* 282: 2035–2042 (1999).

[73] Málek J., Nečas J., Rokyta M., Růžička M.: *Weak and Measure-valued Solutions to Evolutionary Partial Differential Equations*, Chapman and Hall, London, 1996.

[74] Málek J., Nečas J., Růžička M.: On weak solutions to a class of a non-Newtonian incompressible fluids in bounded three-dimensional domains. The case $p \geq 2$. *Adv. Differ. Equat.* 6: 257–302 (2001).

[75] Málek J., Rajagopal K.R., Růžička M.: Existence and regularity of solutions and the stability of the rest state for fluids with shear-dependent viscosity, *Math. Model. Meth. Appl. Sci.* 5: 789–812 (1995).

[76] Nägele S.: *Mehrgitterverfahren für die inkompressiblen Navier-Stokes Gleichungen im laminaren und turbulenten Regime unter Berücksichtigung verschiedener Stabilisierungsmethoden*, PhD Thesis, Ruprechts-Karl University Heidelberg, 2003.

[77] Nägele S., Wittum G.: On the influence of different stabilisation for incompressible Navier-Stokes equations, *J. Comput. Phys.* 224: 100–116 (2007).

[78] Nečas J.: *Les Méthodes Directes en Théorie des Equations Elliptiques,* Masson, Paris, 1967.

[79] Neff P.: On Korn's first inequality with non-constant coefficients, *Proc. R. Soc. Edinb.: Section A Mathematics*, 132(1): 221–243 (2002).

[80] Nobile F.: *Numerical approximation of fluid-structure interaction problems with application to haemodynamics*, PhD Thesis, EPFL Lausanne, 2001.

[81] Nobile F., Vergara C.: An effective fluid-structure interaction formulation for vascular dynamics by generalized Robin conditions, *SIAM J. Sci. Comput.* 30(2): 731–763 (2008).

[82] Noll W.: A mathematical theory of the mechanical behavior of continuous media, *Arch. Ration. Mech. Anal.* 2(3): 197–226 (1958).

[83] Perego M., Veneziani A., Vergara C.: Variational approach for estimating the compliance of the cardiovascular tissue: an inverse fluid-structure interaction problem, *SIAM J. Sci. Comput.* 33(3): 1181–1211 (2011).

[84] Perktold K., Rappitsch G.: Mathematical modeling of local arterial flow and vessel mechanics. In: Crolet J., Ohayon R. (Eds.), *Computational Methods for Fluid Structure Interaction. Pitman Research Notes in Mathematics No. 306*, 230–245, Harlow: Longman, 1994.

[85] Perktold K., Resch M., Reinfried O.P.: Three-dimensional numerical analysis of pulsatile flow and wall shear stress in the carotid artery bifurcation, *J. Biomech.* 24(6): 409–420 (1991).

[86] Perktold K., Thurner E., Kenner T.: Flow and stress characteristics in rigid walled and compliant carotid artery models, *Medic. Biol. Eng. Comput.* 32(1): 19-26 (1994).

[87] Prohl A., Růžička M.: On fully implicit space-time discretization for motions of incompressible fluids with shear-dependent viscosities: the case $p \leq 2$, *SIAM J. Numer. Anal.* 39 (1): 214–249 (2001).

[88] Quaini A., Quarteroni A.: A semi-implicit approach for fluid-structure interaction based on an algebraic fractional step method, *Math. Model. Meth. Appl. Sci.* 17(6): 957-983 (2007).

[89] Quarteroni A., Formaggia L.: Mathematical Modelling and Numerical Simulation of the Cardiovascular System, In: Ciarlet P.G. et al. (Eds.), *Handbook of Numerical Analysis (Computational models for the human body)*, Vol. XII, Elsevier, 2004.

[90] Quarteroni A., Tuveri M., Veneziani A.: Computational vascular fluid dynamics: problems, models and methods, *Comput. Visual. Sci.* 2: 163–197 (2000).

[91] Quarteroni A., Valli A.: Numerical Approximation of Partial Differential Equations, *Springer Series in Computational Mathematics*, Springer, 2008.

[92] Raw M.: *A New Control-Volume-Based Finite Element Procedure for the Numerical Solution of the Fluid Flow and Scalar Transport Equations*, PhD. Thesis, University of Waterloo, 1985.

[93] Råback P., Ruokolainen J., Lyly M., Järvinen E.: Fluid-structure interaction boundary conditions by artificial compressibility, *ECCOMAS Computational Fluid Dynamics*, Swansea, 2001.

[94] Serrin J.: The initial value problem for the Navier-Stokes equations, Nonlinear Problems, In: Langer R. (Ed.) *Nonlinear Problems Proc. Sympos.*, 69–98, University of Winsconsin Press, Madison, 1963.

[95] Sequeira A., Santos R.T., Bodnár T.: Blood coagulation dynamics: mathematical modelling and stability results, *Math. Biosci. Eng.* 8(2): 425–443 (2011).

[96] Schmidt-Schönbein H., Volger E., Klose H.J.: Microrheology and light transmission of blood. II Photometric quantification of red cell aggregation formation and dispersion in flow, *Pflüggers Arch. Springer* 333: 140–155 (1972).

[97] Soulis J.V., Giannoglou G.D., Chatzizisis Y.S., Seralidou K.V., Parcharidis G.E., Louridas G.E.: Non-Newtonian models for molecular viscosity and wall shear stress in a 3D reconstructed human left coronary artery, *Med. Eng. Phys.* 30(1): 9–19 (2008).

[98] Sváček P., Feistauer M., Horáček J.: Numerical simulation of flow induced airfoil vibrations with large amplitudes, *J. Fluid. Struct.* 23: 391–411 (2007).

[99] Steinman D.A., Loepping T.L., Tambasco M., Rankin R.N., Holdsworth D.W.: Flow pattern at the stenosed carotid bifurcation: effect of concentric versus eccentric stenosis, *Ann. Biomed. Eng.* 28: 415–423 (2008).

[100] Tambača J., Kosor M., Čanić S., Paniagua D.M.D.: Mathematical modeling of vascular stents, *SIAM J. Sci. Comput.* 70(6): 1922–1952 (2010).

[101] Taylor C.A., Hughes J.R., Zarins C.K.: Effect of exercise on hemodynamic conditions in the abdominal aorta, *J. Vasc. Surg.* 29(6): 1077–1089 (1999).

[102] Teman R.: *Navier-Stokes Equations: Theory and Numerical Analysis*, Elsevier North-Holland, Amsterdam, New York, Oxford, 1977.

[103] Truesdell C., Noll W.: *Non-linear Field Theories of Mechanics.* Springer, 1965.

[104] Vignon-Clementel I., Figueroa C.A., Jansen K.E., Taylor C.A.: Outflow boundary conditions for three-dimensional simulations of non-periodic blood flow and pressure fields in deformable arteries, *Comput. Meth. Appl. Mech. Eng.* 13(5): 625–640 (2010).

[105] Yeleswarapu K.K.: *Evaluation of continuum models for characterizing the constitutive behavior of blood*, PhD Thesis, University of Pittsburgh, 1996.

[106] Yeleswarapu K.K., Kameneva M.V., Rajagopal K.R., Antaki J.F.: The flow of blood in tubes: theory and experiment, *Mech. Res. Comm.* 25(3): 257–262 (1998).

[107] Zaušková A.: *2D Navier-Stokes Equations in a Time-Dependent Domain*, PhD Thesis, Comenius University Bratislava, 2006.